The University of Nottingham

MAGNETIC FIELD MODELLING OF MACHINE AND MULTIPLE MACHINE SYSTEMS USING DYNAMIC RELUCTANCE MESH MODELLING

By Li Yao
BEng (Honours), Msc (Engineering)

Thesis submitted to the University of Nottingham
for the degree of Doctor of Philosophy
May 2006

ABSTRACT

This thesis concerns the modified and improved, time-stepping, dynamic reluctance mesh (DRM) modelling technique for machines and its application to multiple machine systems with their control algorithms. Improvements are suggested which enable the stable solution of the resulting complex non-linear equations. The concept of finite element (FE) derived, overlap-curves has been introduced to facilitate the evaluation of the air-gap reluctances linking the teeth on the rotor to those on the stator providing good model accuracy and efficient computation. Motivated industrially, the aim of the work is to develop a fast and effective simulation tool principally for evaluating salient pole generator system designs including the generator, exciter and the automatic voltage regulator (AVR). The objective is to provide a modelling system capable of examining the detail of machine operation including saturation of main and leakage flux paths, slotting and space harmonics of the windings. Solutions are obtained in a sufficiently short computational time to facilitate efficient iterative design procedures in an industrial design office.

The DRM modelling technique for electrical machines has been shown in this thesis to be a fast and efficient tool for electrical machine simulation. Predicted results for specific machine and system designs have been compared with FE solutions and with experimental results showing, that for engineering purposes, the technique yields excellent accuracy.

The DRM method has a great advantage in multiple machine simulations. This is because magnetic field calculations are limited to evaluating only the most important information so saving computation time. A brushless generating system including the excitation system and control scheme has been modelled. Additionally a cascaded, doubly fed induction generator for wind generator applications has also been modelled. These different applications for the dynamic reluctance mesh method have proved that this approach yields an excellent machine and machine-system evaluation and design tool.

ACKNOWLEDGEMENTS

Firstly, I would like to express my sincere gratitude to my supervisors, Dr. Keith Bradley and Professor Phil Sewell for their invaluable assistance and guidance with my research study during the past three and a half years at the University of Nottingham. Also, I would like to express my appreciation to Newage AVK SEG UK for the financial support and their sincere help with the experimental data.

I would like to thank all my colleagues in the PEMC group, at the University of Nottingham, for their encouragement, support and friendship throughout the years. In particularly to Ungku Anisa Ungku Amirulddin and Chris Gerada, with whom I had very helpful conversations related to my research. Thanks also go to my friends and housemates in Nottingham over these years for their help and the fun moments that we shared.

Finally, I would like to express my deepest gratitude to my parents, family who have relentlessly supported me in every possible way throughout my study in the UK, and for their never ending love and encouragement.

LIST OF SYMBOLS

A	area of airgap reluctance element (m^2)
B	flux density (Tesla or Wb/m^2)
b , b_p	width for salient pole shoes and poles (m)
c_s , c_p	distance between parallel salient pole shoes and poles (m)
D	machine windage
$\frac{de_a}{d\phi_i}, \frac{de_b}{d\phi_i}, \frac{de_c}{d\phi_i}$	terms representing the change of the emf induced in phase A , B or C due to a change of flux in tooth i
E_i	energy stored in each air gap element (J)
E_{af} , E_{bf} , E_{cf}	generated emf of stator three phase (V)
E'_d , E'_q	added d and q axis voltages represent transient voltage in the generator (V)
E''_d , E''_q	added d and q axis voltages represent sub-transient voltage in generator (V)
$F(\mathbf{x})$	matrix of state equations solved by the DRM software
F_k	mmf source (A)
F_l	mmf source value for salient rotor windings (A)
f_i	mmf at node I (A)
f_1 , f_2 , f_3 , f_4	frequencies for side 1,2,3 and 4 in cascaded doubly fed induction machine system (Hz)
f_m	rotor rotating mechanical frequency (Hz)
H	flux field intensity (A/m)

h_s, h_p	height for salient pole shoes and poles (m)
i_a, i_b, i_c	three phase current (A)
i_f	synchronous machine field current (A)
I_s	leakage current for diode (A)
J	machine inertia (Kg m$^{2)}$
$\vec{J}$	current density (A/m^2)
$\mathbf{J}$	jacobian matrix
K_g	carter's factor used in extended air gap length calculations
k_o	carter's factor referenced from carter's curve
l_g	air gap length (m)
l'_g	extended air gap length (m)
L_{ld}, L_{lq}	d and q axis leakage inductance (H)
L_{md}, L_{mq}	d-axis and q-axis magnetization inductance (H)
L_r, λ_r	rotor inductance and flux linkage for synchronous machine (H, Wb)
L_s, L_p	length for salient pole shoes and poles (m)
L_{lfd}	field winding leakage inductance in salient pole synchronous machine (H)
L'_{lkd}, L'_{lkq1}	referred damper winding d-axis and q-axis leakage inductance in salient pole synchronous machine (H)
N_{node}	number of node in the reluctance mesh in DRM
N_{bar}	number of damper bars in the induction machine
n_p	number of parallel paths in stator winding

N_s	number of stator slots
P	Park's transformation matrix
$\mathbf{p}$	Newton step in Newton-Raphson algrithm
p_A, p_B	number of pole pairs in cascaded doubly fed induction machine system
P_{mech}	mechanical power of the shaft (J)
$P_{converter\ electrical}$	power flowing out of the converter side machine's stator (J)
$P_{generated\ electrical}$	power flowing out of the grid side machine's stator (J)
P_{loss}	power loss (J)
R_a, R_b, R_c	phase resistance of A, B and C (Ω)
R_f	synchronous machine field resistance (Ω)
R_{sd}, R_{sq}	salient pole synchronous machine stator d and q axis resistance (Ω)
R'_{fd}	referred salient pole synchronous machine field resistance (Ω)
R'_{kd}, R'_{kq1}	referred damper winding d-axis and q-axis resistance in salient pole machine (Ω)
S	number of stator teeth
T_e	electrical torque in the machine (N.m)
T_{load}	mechanical load torque in the machine (N.m)
T_c	turns per coil for stator
T_{ph}	turns per phase
V	volume (m^3)

v_A, v_B, v_C	three phase voltage (Volts)
v_f	synchronous machine field voltage (Volts)
w_o	slot opening (m)
w, l, d	width, length and depth of the reluctance elements (m)
w_{sl}, w_{pl}	effective width for leakage reluctance between pole shoes and poles in a salient pole rotor (m)
$w_{effective\ width}$	air gap reluctance effective width when taking fringing into account (m)
$\mathbf{x}$	vector of state variables
$\mathbf{x}_{old}, \mathbf{x}_{new}$	vector of state variables at initial value and solving value fron Newton-Raphson method
X_{sa}, X_{sb}, X_{sc}	synchronous reactance for synchronous machine (Ω)
X_a, X_b, X_c	magnetizing reactance for synchronous machine (Ω)
X_l	leakage reactance for synchronous machine (Ω)
X_d, X_q	direct- and quadrature- axis synchronous reactances for salient pole machine (Ω)
X_{ls}	stator leakage reactance (Ω)
X_{md}, X_{mq}	magnetizing reactance for d and q axis for salient pole synchronous machine (Ω)
y_s	slot pitch (m)
$\lambda\mathbf{p}$	line searched Newton step
μ_0	permeability of vacuum (H/m)
μ_r	relative permeability
$\mu = \mu_0\mu_r$	permeability of an element (H/m)

α_{ij}	factor for i^{th} stator or rotor teeth determines the presence or absence of the j^{th} phase current in the slot
ω_r	Shaft speed (rad/sec)
ϕ	flux (wb)
λ	flux linkage (Wb)
θ_{mech}	mechanical angle of the shaft (rad)
ϕ_m	main flux between the stator and rotor in a salient pole generator (Wb)
ϕ_1, ϕ_2	leakage flux between salient pole shoes (Wb)
ϕ_3, ϕ_4	leakage flux between salient poles (Wb)
$\Re$	reluctance (m/H)
δ	load angle (deg)

LIST OF FIGURES

CONTENTS

CHAPTER 1 INTRODUCTION

1.1 Background

The material presented in this thesis is primarily concerned with the investigation and development of a dynamic reluctance mesh field modelling and simulation tool for electrical machines and machine systems, specifically salient pole synchronous generators, small brushless synchronous generating systems and cascaded doubly fed induction machine systems. This simulation technique stems from the magnetic equivalent circuit modelling method for electrical machines by Carpenter [1] and Haydock [2], which was further developed and specifically applied to induction machine modelling as the dynamic reluctance mesh method by Sewell [3].

In 1968, Carpenter [1] introduced and explored the possibility of modelling eddy-current devices using magnetic equivalent circuits, which are analogous to electric equivalent circuits. Magnetic terminals are introduced which provide a useful means of describing the parameters in electromagnetic devices, particularly those whose operation depends upon induced current behaviour. The virtual-work [4] [5] principle was suggested for torque calculations and exploited in [3]. Generally, the magnetic equivalent circuit modelling method can be used to analyse many types of electrical machine in terms of physically meaningful magnetic circuits. For example, Ostovic' evaluated the transient and steady state performance of squirrel cage induction machines by using this magnetic equivalent method [6] [7], taking into account the machine geometry, the type of windings, rotor skew, the magnetising curve etc. In a later investigation by Ostovic' [8], a set of differential equations describing saturated electrical machine states was developed which simplified the solution process for saturated machines. In the past two decades, magnetic equivalent circuit modelling method for electrical machines has been further developed and applied to modelling many other types of machines, apart from induction machines: synchronous machines by Haydock [2], inverter–fed synchronous motors by Carpenter [9], permanent magnet motors and claw-pole alternators by Roisse [10], and 3-D Lundell alternators, which are a main source of electric energy in internal combustion engine automobiles, by Ostovic' [11]. From the simulation results presented in these papers, the magnetic equivalent circuit method has been proven to be an efficient and fast simulation tool for a variety of electrical machine types.

Sewell developed Dynamic Reluctance Mesh software for simulating practical induction machines based on the previous work using magnetic circuit models for electrical machines [3]. This algorithm was developed from rigorous field theory. Combined with prior known knowledge of electrical machine behaviour determined from practical experience, this model is simplified in a physically realistic manner and results in a procedure that can efficiently simulate 3D machines within an iterative design environment without requiring extensive computational resources. Its computation time was minimised by direct computation of the rate of change of flux, thus the evaluation of time and rotor position dependent inductances are avoided. A practical and effective approach to model skewed rotor and iron saturation effects were also implemented in the algorithm. The magnetic, electrical and dynamic models of the machine are coupled so that the simulation determines both steady state and transient behaviour including the effects of saturation and high order torque harmonics due to the rotor and stator teeth. The work in this thesis concerns the simulation of machines and multiple machines systems based upon this dynamic reluctance mesh modelling method, with some additional model developments in modelling and improvements in the solution process. Further details of the dynamic reluctance mesh method will be discussed later in chapter 2.

1.2 Industrial Motivation and Aim of The Work Described in The Thesis

The research work implemented in this thesis is motivated by an industrially funded project “Development of software package for design and performance prediction of new and conventional generators”. Its aim is to develop a fast and effective simulating software package, for evaluating the designs and performances of new and conventional generators with non-uniform air gap geometry under different operating conditions.

Large synchronous generators are driven by steam turbines and gas turbines to generate electricity and over the past hundred years synchronous generators have provided nearly all the world’s electrical power needs. A typical structure of a power station is shown in Figure 1.2.1.

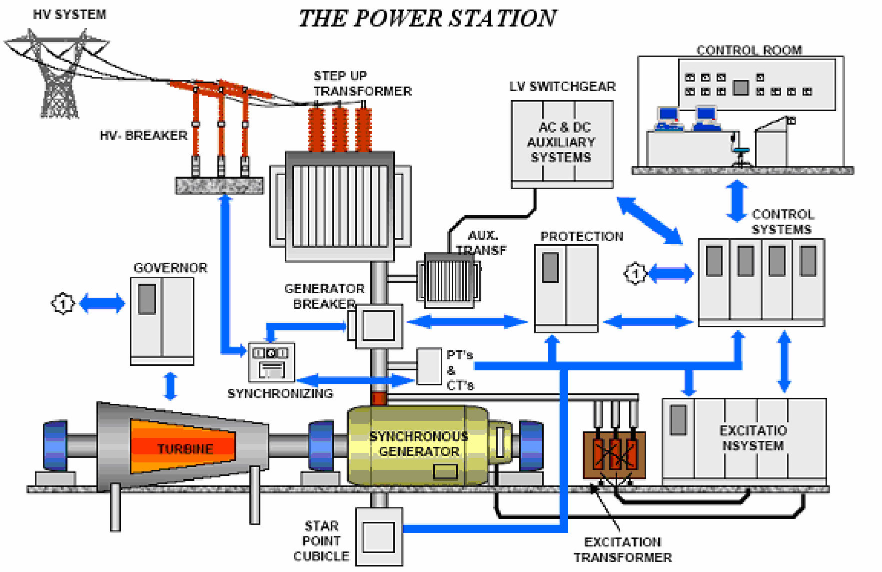

Figure 1.2.1 [12] Typical topology structure of a power station

Figure 1.2.1 shows the basic structure for a coal-fired steam turbine or gas turbine power plant, which utilises steam or pressured gas as the energy source to drive the synchronous machine, and converts the rotary mechanical motion into the electrical energy that the plant is designed to provide. Economically motivated by the fact, that coal and other fossil fuels are cheap and abundant in the world, 38% of the world's electricity is generated by coal-fired power plants [13]. Gas turbines have the particular advantage that they offer the facility for rapid speed up and thus by the end of the twentieth century the gas turbine had become one of the most widely used prime movers for new power generation applications [13]. These power plants utilise solid pole rotor synchronous machines due to the high shaft rotation speed. As we can see from Figure 1.2.1, there are control systems to ensure that this mechanical-electrical system is operating under controlled conditions: governor for control of the turbine and excitation control for the control of the field excitation of the generator.

However, in the generator family, there are other industrial generators, which can be utilised in various other industry scenarios. These generating sets can supply power to remote communities or isolated commercial facilities, such as industrial, marine/offshore, construction, combined heat and power, parallel operation, telecommunications, mining, and other standby or continuous power applications. At present the most common solution for providing electrical power below 200 kW is to use a fixed speed diesel engine in conjunction with a synchronous generator and associated controls to form a generating set. The power generation rating of diesel engines is also enormously variable. Small units can be used for standby power units or for combined heat and power in homes and offices. Larger units are often used in situations where a continuous supply of power is critical; in hospitals or to support highly sensitive computer installations such as air traffic control. Many commercial and industrial facilities use medium-sized piston-engine-based combined heat and power units for base-load power generation. Large engines meanwhile can be used for base-load, grid-connected power generation while smaller units form one of the main sources of base load power to isolated communities with no access to an electricity grid.

From the machine design point of view the difference between the synchronous generators used in power plants and industrial applications is that the latter is more variable, both in terms of the geometry and performance. As a manufacture of these diesel engine driven small and medium synchronous generators, the sponsor of this work is interested in performance evaluation of the small and medium range of industrial generators with consideration of their associated controls and power electronics and would like to evaluate different generator system designs. Thus a fast and effective machine performance evaluation tool for different generators and system designs is essential for their activity.

The previous work described above has led to the conclusion that the dynamic reluctance mesh modelling of electrical machines provides a tool, which with additional development and investigation, can be further applied to multiple machine system modelling and in conjunction with control scheme evaluation.

In this thesis, the research work will be concentrated on an improved dynamic reluctance mesh model of a pragmatic small brushless synchronous generating system, and subsequently this is further extended to the case of multiple machines, specifically cascaded doubly fed induction machines.

The small brushless synchronous generating system to be modelled in the thesis is an industrial generating system, driven by a diesel engine is shown in Figure 1.2.2.

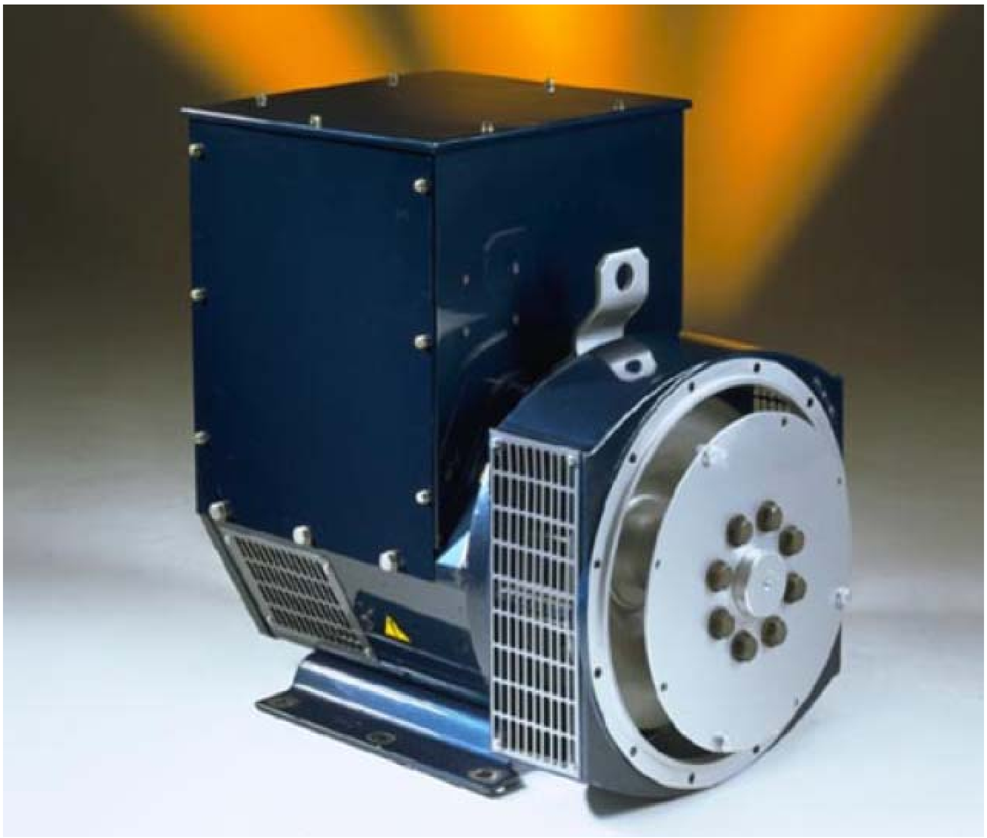

Figure 1.2.2 Appearance of a typical small industrial brushless generating system

Details of the brushless generating system will be explained later in chapter 5 of this thesis. The internal structure of this type of generating system is shown in Figure 1.2.3. The shaft is driven by a diesel engine with the exciter rotor, rotating diodes and the main rotor fixed to this shaft. An excitation voltage is fed to the exciter stator side, which has been regulated by the automatic voltage regulator (AVR). Main generator excitation is provided by the d.c. voltage rectified by the rotating diodes. Later in the thesis, chapter 5 will describe more details of the operating theory.

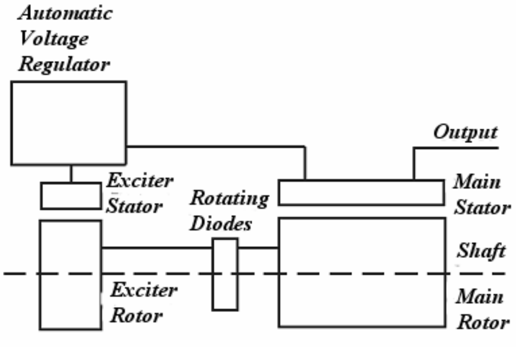

Figure 1.2.3 Internal structure of a typical small brushless generating system

Apart from the traditional source of energy for power generation, mentioned previously, steam turbines, gas turbines and diesel engines, there has been increased interest in renewable and distributed power generation systems in recent years, such as wind generation systems. Wind energy is viewed as a clean, renewable source of energy from an environmental point of view, which produces no greenhouse gas emissions or waste products. Although, there are other sources of renewable energy, wind energy is currently viewed as the lowest risk and most proven technology which is capable of providing significant levels of renewable energy in the world [14].

Most of wind power generation systems demand low cost reliable generators suitable for variable speed operation. Moreover, in modern wind generation systems, turbine designs are moving towards variable speed architectures to increase energy capacity [15]. As turbine power ratings have steadily increased over the years, electrical generator technology has also adapted and developed from the early fixed-speed generators in order to improve drive train dynamics and increase energy recovery. Modern vertical turbines are normally variable-speed units and this requires the generator to be interfaced to the grid through an electronic power converter. Conventional generators such as the induction or synchronous options are viable but these require the grid side converter to be rated to match the generator. For very large turbines, these converters are complex and expensive at today’s prices. Therefore, one of the present preferred options for large turbines in excess of a 2MW rating is the variable-speed doubly fed induction generator (DFIG) with the rotor converter connected to the rotor via slip rings [16][17]. A detailed description of a doubly fed induction generating system will be given later in chapter 6.

The advantage of DFIG is that the power electronic equipment only needs to handle a fraction (20%-30%) of the total system power [18] [19]. However, a typical doubly fed induction machine design has to include slip rings to connect the power converter to the rotor of the induction generators, which causes wear and tear and increases the cost of maintenance. Many kinds of machine design for doubly fed induction generators have been investigated and deployed in order to replace the slip rings needed in doubly fed induction generating systems. Cascaded doubly fed induction machines is one of these alternatives [20] and further details of these will be given later in chapter 6.

A cascaded doubly fed induction machine is a multiple machine system, and therefore a suitable multiple machine simulation and analyse tool has to be adopted to design and optimise this kind of system. Dynamic reluctance mesh modelling can be considered as one of the choices for this purpose. The advantage of dynamic reluctance mesh method is that it can model electrical machines with non-uniform air gaps and its associated controls and power electronic equipment, and can also model multiple machine systems in sufficient detail within a reasonable time. Thus, DRM models of cascaded doubly fed induction machine systems, used computationally in the wind energy industry are also under consideration and investigation in this thesis.

1.3 Overview of The Thesis

The thesis employs an improved dynamic reluctance mesh method to model and simulate small salient pole synchronous generators, small brushless generating systems, and multiple machine systems of cascaded doubly fed induction generators for wind energy applications. The contents of the remaining chapters in the thesis are summarised below:

Chapter 1 introduced the background of the dynamic reluctance mesh modelling technique and the research motivation of the work completed in this thesis.

In chapter 2, the basic dynamic reluctance mesh modelling method and its software implementation for induction machines by previous researchers is described. The creation of the reluctance mesh, the state variables, state equations and also the numerical solution techniques employed in the DRM software are presented.

Chapter 3 gives the improvements and developments in the modelling and solution techniques of the basic DRM method described in chapter 2 for a typical induction machine model. A more accurate and stable model with robust numerical solving techniques has been implemented using the modifications made in chapter 3, which supplied a good numerical computation platform for the later research and investigations in the thesis.

In Chapter 4, a modelling technique based on DRM modelling method for salient pole synchronous generators with non-uniform air gap geometry is proposed. Reluctance mesh discretisations of the iron and air gap parts and also the damper bars is presented. The state variables and state equations are also given which are then solved to reveal the behaviour of the machine. Other models for synchronous machines such as the mathematical model and finite element models are also described and a comparison between the results obtained from the DRM and finite element methods is given. In the last part of the chapter, comparison is made between the DRM results and experimental values.

Chapter 5 models the full brushless small generating system described in the introduction, which includes modelling of the exciter, rotating rectifiers and AVR controller. The main generator model has already been described and validated in chapter 4 and emphasis is laid on the electrical connection modelling between the multiple machines, and modelling of the power electronic components and control algorithms. Simulation results and analysis of the full system are given in comparison with experimental results.

To further the DRM modelling technique to other multiple machine systems, cascaded doubly fed induction generator systems for wind energy generation are modelled and simulated in Chapter 6. Power flow and variable frequency phenomena in the system are investigated.

Chapter 7 investigates how different reluctance mesh discretisation affects the DRM simulation results. Subsequently, comparisons of the results obtained with different mesh topologies are made and discussed, for the exciter, main generator and full brushless generating system respectively.

Finally in Chapter 8, a conclusion of the modelling and simulation studies of small brushless generating systems and multiple machine systems using DRM, including the main findings of the work in this thesis, is presented. Possible areas in which future work can be directed will also be proposed.

CHAPTER 2 DYNAMIC RELUCTANCE MESH MODELLING

2.1 Introduction

The simulation of electrical machines and multiple machine systems in this thesis is based upon the Dynamic Reluctance Mesh Modelling method. As the foundation of later research work in the thesis, a description of the basic theory and methodology of the Dynamic Reluctance Mesh modelling method, as well as its software implementation will be given in this chapter. Further developments and improvements to this modelling technique will be introduced in chapter 3.

Computer simulations of electrical machines can help electrical machine designers to design machines more efficiently. As various machine designs and variations can be simulated and validated, this reduces the traditionally expensive and time-consuming trial and error process in the electrical machine design industry. Furthermore, technological developments in power electronics and control techniques have widened the field of application of electrical machines and thus more detailed and advanced models are needed to accommodate these changes in simulations. For example, more detailed and sophisticated models are needed for multiple machine system simulations with which current commercial Finite Element software can not deal, and in the scenarios where high switching frequency converters and complicated control schemes are being applied.

Although the inductance model (or the winding coil model) is sufficient for some designs and purposes, in other cases, more detailed and comprehensive models are needed to simulate a machine's performance. For example, the distortion of the generated voltage in a generator due to stator slotting could not be inspected by using the inductance model. However, with the ongoing development of numerical simulations in the field of engineering, the finite element method has been used in an ever-broader raise of circumstances. Commercial software is now widely available for a variety of disciplines, including for the analysis of electrical machinery. The finite element method is founded on rigid numerical approaches and can supply accurate and complete solutions for machine performance in terms of both detailed field behaviour and global performance measures [21]. However a substantial amount of computational resources are needed for finite element analysis of realistic 3D machine geometries and this limits its usage for electrical machine design and assesment.

Another way of modelling electrical machines, the Dynamic Reluctance Modelling method, was developed and validated through experiment by Carpenter [1], Ostovic' [6][7][8] and Sewell [3], and a significant quantity of work focused upon this kind of magnetic equivalent circuit based method had been undertaken [9][10][11]. The Dynamic Reluctance Modelling method is really a different way of encapsulating the key physical processes. It is based upon the simple concept of a reluctance mesh, in which the magnetic field behaviour is mapped onto an equivalent lumped element circuit. The key to the efficiency of this approach is that in most parts of the machine, both the principal direction and the spatial distribution of the magnetic fluxes are known from experience and can be well approximated by the behaviour of simple lumped equivalent circuit parameters. Combined with prior knowledge, this DRM method can considerably save both in terms of computation time and memory use and thus high efficiency is obtained without compromising the accuracies. Results from Sewell [3] have shown that DRM results provide very good agreement with experimental results. However, the limitation of this method is that the accuracy of the local field calculations is discretised by the local reluctances, thus, with a coarse reluctance mesh some detailed field information is inevitably omitted compared with FEM results, which may cause some inaccuracy in machine transients. A sensible engineering balance has to be made between the computation accuracy and computation time for dynamic reluctance mesh modelling calculations.

A basic description of dynamic reluctance mesh modelling will be given in this chapter, taking a typical induction machine as an example. Reluctance mesh creation, system variables and solution algorithms will also be introduced here. Developments and improvements of the DRM method will be presented in the next chapter. Detailed result comparisons between the DRM and experimental work will not be presented here as this has already been presented and validated by Sewell [3].

2.2 Reluctance Mesh of Electrical Machines

The Dynamic Reluctance Mesh modelling method is based upon the concept of equivalent magnetic circuits. To understand how the Dynamic Reluctance Mesh is set up for electrical machines, basic magnetic circuit theory will be presented first and then the specific discretisation method for electrical machines will be introduced.

2.2.1 Magnetic circuit

Magnetic circuits are a way of simplifying the analysis of magnetic field systems which can be represented by a set of discrete elements, in the same way that electric circuits do. Thus, many laws and analysis methods could be analogous to those of electric circuit theory.

In electric circuits, the fundamental elements are sources, resistors capacitors and inductors, and these elements are connected together through ideal ‘wires’ and their behaviour is described by network constraint, such as Kirkhoff’s voltage and current laws, and their constitutive relationships are described by, for example, Ohm’s law. In magnetic circuits, the fundamental elements are called reluctances (the inverse of reluctance is permeance). The analog to a ‘wire’ is considered to be a high permance magnetic material, in which flux is totally confined, analogous to a high conductivity material in an electric circuit.

By describing the magnetic field system as lumped parameter elements and using the network constraint and constitutional relationships the analysis of such system can be performed.

Now, the magnetic circuit laws analogous to those of electric circuits will be introduced.

1. Kirkhoff’s Current Law (KCL)

Guass’s law is [22]:

$$\oint\!\!\oint \vec{B} \cdot \vec{n} da = 0 \tag{2.2.1}$$

which embodies the fact that the total flux passing through a closed surface in space is always zero, i.e. magnetic flux density is conserved.

The magnetic flux crossing a surface is defined as:

$$\phi_k = \iint \vec{B} \cdot \vec{n} da \tag{2.2.2}$$

which is the surface integral of the normal component of the flux density B .

In most of the cases of interest in machines, flux is primarily carried by high permeability iron material, analogous to wires of high conductivity material which carry current in an electric circuit. Due to the high permeability, most of the flux follows the path the magnetic material rather than leaking “laterally” out to the surrounding air.

By analogy to electric circuits in which the elements are connected through wires with interconnection points called nodes, where Kirkhoff’s Current Law holds; in magnetic circuits, the reluctances are connected through high permeability iron material and the interconnection points represent small closed region of space which can also be called nodes and which, according to equation 2.2.1 and 2.2.2, flux conservation is satisfied:

$$\sum_k \phi_k = 0 \tag{2.2.3}$$

This is Kirkhoff's Current Law for magnetic circuits.

2. Kirkhoff's Voltage Law (KVL)

Ampere's law is [22]:

$$\oint \vec{H} \cdot d\vec{l} = \iint \vec{J} \cdot \vec{n} da \tag{2.2.4}$$

which states that the line integral of the tangential component of magnetic field intensity H around a closed contour is equal to the total current passing through the surface surrounded by the contours.

If a magnetomotive force (mmf), analogous to the electromotive force (voltage in an electric circuit) is defined as:

$$F_k = \int_{a_k}^{b_k} \vec{H} \cdot d\vec{l} \tag{2.2.5}$$

then, the source for the magnetic circuit is the magnetomotive force. If the current enclosed by a loop is defined to be:

$$F_0 = \iint \vec{J} \cdot \vec{n} da \tag{2.2.6}$$

then, according to equation 2.2.4 and 2.2.5, Kirkhoff's Voltage Law for magnetic circuits analogous to that of electric circuits is:

$$\sum_k F_k = F_0 \tag{2.2.7}$$

The direction of mmf sources in magnetic circuits can be determined by using the right hand rule with the current direction.

3. Ohm's law: Reluctances

Consider a magnetic material with permeability μ, its length width and depth are l, w and d respectively, as shown in figure 2.1.1.

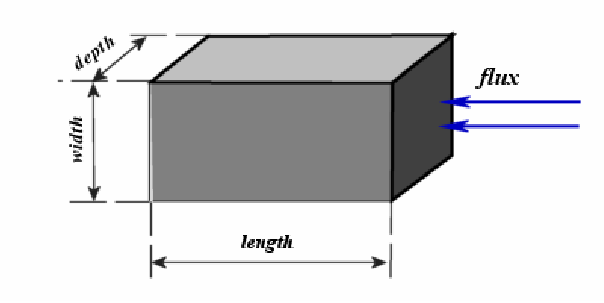

Figure 2.2.1 Reluctance in magnetic circuit

Assume that flux flow through this magnetic material along its length and the flux density B is uniform in the cross sectional area, thus the flux flowing through this magnetic material is:

$$\phi = BA \tag{2.2.8}$$

where A is the cross-sectional area, $A = w \cdot d$. The magnetic field intensity, H related to the flux density B through the permeability characteristic of the material (here taken to be linear for clarity):

$$H = \frac{B}{\mu} \tag{2.2.9}$$

According to the definition of the mmf, the mmf drop across this block of material is:

$$\Delta F = H \cdot l \tag{2.2.10}$$

thus,

$$\Delta F = \frac{B}{\mu} l = \frac{\phi}{\mu w d} l \tag{2.2.11}$$

It can be seen that the mmf is the driving force in the magnetic circuit, as the voltage is the driving force in an electric circuit, and magnetic flux is analogous to the current in an electric circuit. Extending the analogy between equation 2.2.11 and Ohm's law in an electric circuit, the reluctance plays the same role as the resistance in an electric circuit.

$$\Re = \frac{l}{\mu w d} \tag{2.2.12}$$

2.2.2 Dynamic Reluctance Mesh creation of electrical machines: iron part

The Dynamic Reluctance Mesh modelling method is basically a method that models the electrical machine as coupled magnetic circuits and electric circuits, and models the air gap as a ‘dynamic’ reluctance mesh within the magnetic circuit, reflecting the fact that the air gap reluctance mesh changes with the rotation of the rotor.

Having briefly introduced the magnetic circuit as analogous to an electric circuit, the basics of the dynamic reluctance mesh discretisation of electrical machines will now be described, taking an induction machine as an example application to achieve the magnetic circuit.

First the reluctance mesh topology for the time invariant part of the machine will be discretised, and then the dynamic modelling of the air gap will be introduced.

The induction machine is discretised into a number of reluctance element cells, each of which has its own length, width and depth as shown in Fig 2.2.1. Nodes where magnetic potential (mmf) values were sampled connect adjacent reluctances. Two adjacent reluctances in the magnetic circuit are shown in figure 2.2.2

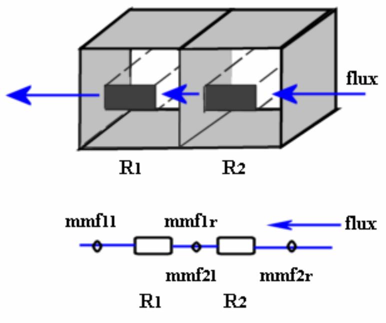

Figure 2.2.2 Reluctances in DRM reluctance mesh

In these cells, flux is realistically assumed to flow only perpendicularly to the inter-cell boundaries, and is uniformly distributed in the cross-section. Based on Ohm's law in the magnetic circuit, the total flux flowing through each reluctance is given by

$$\phi_i = \frac{\Delta F_i}{\Re} = \frac{mmf_r - mmf_l}{\Re} \tag{2.2.13}$$

where mmf_r and mmf_l are the magnetic potentials at the left and right ends of the element and ΔF_i is the mmf drop across the reluctance. In figure 2.2.2, the mmf drops for each of reluctance $\Re_1$ and $\Re_2$ are:

$$\varDelta F_1 = mmf_{1r}\text{-}mmf_{1l} \tag{2.2.14}$$

$$\varDelta F_2 = mmf_{2r} - mmf_{2l} \tag{2.2.15}$$

clearly here, $mmf_{2l} = mmf_{1r}$.

In practice, the permeability, μ, of the iron elements is a non-linear function of the mmf drop across the reluctance, as expressed in equation 2.2.16.

$$B = \mu(H) = \mu\left(\frac{\Delta F}{l}\right) \tag{2.2.16}$$

Moreover, in the magnetic material used in electrical machines, the relationship between B and H for a ferromagnetic material is both nonlinear and multileveled due to the hysteresis effect of the material, which causes notable difficulties in engineering simulations. These multilevel and nonlinear curves are called B-H curve or hysteresis loops. However, for many engineering applications, it is sufficient to describe the material by a single valued curve obtained by plotting the locus of the maximum values of B and H at the tips of the hysteresis loops [22], which is known as the d.c. or normal magnetisation curve. A simplified B-H curve for one of material, Losil 800, is shown in figure 2.2.3.

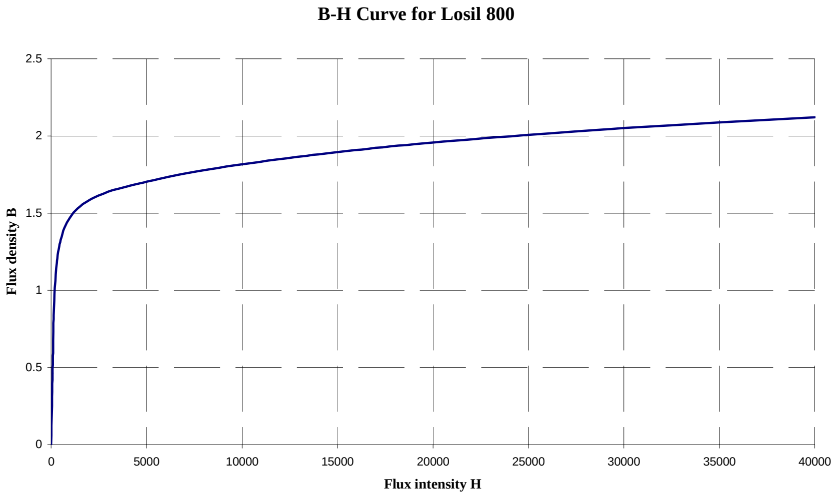

Figure 2.2.3 Simplified B-H curve for ferromagnetic material Losil 800

This simplified B-H curve clearly shows the nonlinearity of the material, but neglects the hysteresis nature of the material. In dynamic reluctance mesh modelling, this kind of simplified B-H curve is applied.

In order to embed the nonlinearity of the B-H curve within a computer code, cubic spline interpolation [23] is adopted. Cubic splines provide an interpolation formula that is smooth in the first derivative, and continuous in the second derivative, which is necessary for our purpose as shall be seen later. Due to its smooth and accurate interpolation characteristic, cubic spline interpolation is widely used in a range of engineering applications and it is utilised in the dynamic reluctance code to get the magnetic material’s B-H curve at any desired point.

Mmf sources are added to the magnetic circuit of the Dynamic Reluctance Mesh model, close to the location of the stator and rotor windings, as shown in figure 2.2.4.

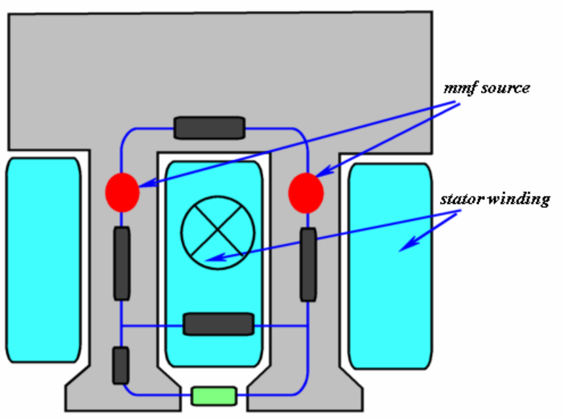

Figure 2.2.4 Mmf source placing by DRM method for electric machine

These mmf sources in both the stator and rotor teeth magnetic circuits are shown by the solid circles in figure 2.2.4, are decided by Ampere's law locally, as shown in equation 2.2.17.

$$N \cdot i = \Delta F = mmf_l - mmf_r \tag{2.2.17}$$

where i is the winding current enclosed by the magnetic loop, and ΔF is the mmf source in the magnetic circuit.

In three phase stator windings, where each slot may contain conductors from more than one of the phases, the mmf sources are calculated by equation 2.2.18:

$$mmf_i = N \sum_{j=0}^{2} \alpha_{ij} \cdot i_j \tag{2.2.18}$$

where mmf_i is the mmf source in tooth i, i_j is the j^{th} phase current, N is the number of turns for each coil in the winding, and $\alpha_{ij} = 0{,}1$ determines the presence or absence of the j^{th} phase current in the slot. However, in a cage bar rotor model, each bar has an mmf value associated with it and it is regarded as a variable of the problem.

To calculate the flux inside the reluctances which are connected with the mmf sources, the presence of the source is now reflected in equation 2.2.19 and figure 2.2.5.

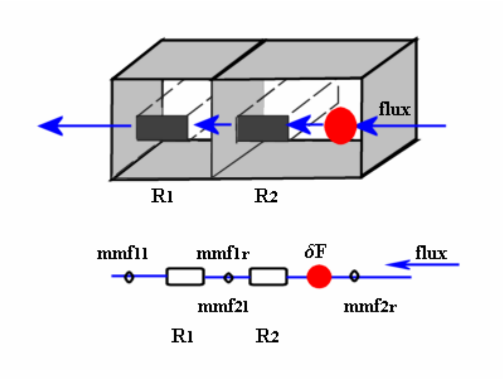

Figure 2.2.5 Reluctances connected with mmf source in DRM reluctance mesh

$$\phi_i = \frac{mmf_r + \Delta F - mmf_l}{\Re} \tag{2.2.19}$$

where ΔF denotes the mmf source.

Attention now is focused upon the creation of a suitable reluctance mesh for a typical induction machine. Initially, the simplest configuration that encapsulates the essential physics is used; more refined meshes will be examined later in chapter 7.

Given the stator and rotor geometry shown in Fig 2.2.6(a) and 2.2.7, a typical reluctance mesh (Fig 2.2.6(b)) for an induction machine can be created using equation 2.2.12 with the values given in table 2.1.

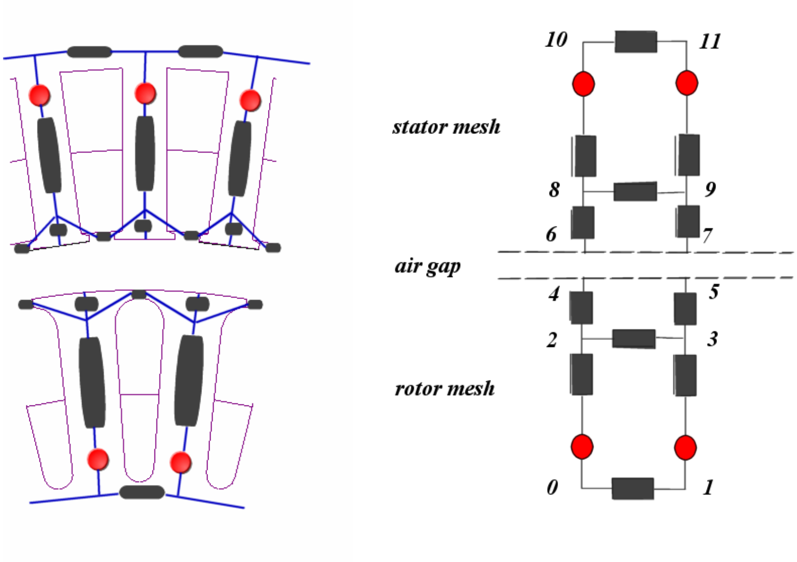

(a): a typical reluctance mesh discretisation. (b): mesh numbering

Figure 2.2.6 A typical induction machine reluctance mesh discretisation

Reluctance connections		Length (l)	Width (w)
8	6	Bridge depth	2* π *meshing radius/no. of stator teeth-slot opening
9	7	Bridge depth	2* π *meshing radius/no. of stator teeth-slot opening
10	8	Slot depth-bridge depth	Tooth width
11	9	Slot depth-bridge depth	Tooth width
10	11	2* π *(meshing radius +slot depth + 0.5*back iron) /no. of stator teeth	Back iron
8	9	Slot opening	Bridge depth

Table 2.1(a) dimensions of stator reluctance elements

Reluctance connections		Length (l)	Width (w)
4	2	Bridge depth	2* π *meshing radius/no. of rotor teeth-slot opening
5	3	Bridge depth	2* π *meshing radius/no. of rotor teeth-slot opening
2	0	Slot depth-bridge depth	Tooth width
3	1	Slot depth-bridge depth	Tooth width
0	1	2* π *(meshing radius -slot depth - 0.5*back iron) /no. of stator teeth	Back iron
2	3	Slot opening	Bridge depth

Table 2.1(b) dimensions of rotor reluctance elements.

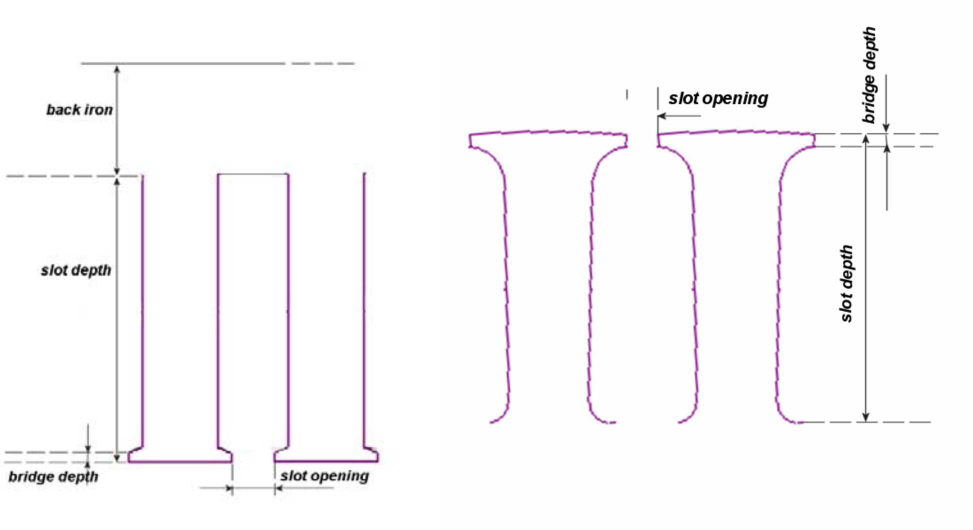

(a) stator dimensions (b) rotor dimensions

Figure. 2.2.7 Induction machine stator and rotor dimensions

Although this is the typical reluctance mesh used for induction machines, it could also be applied to other machine types that have similar rotor or stator geometries and flux distribution characteristics. A similar reluctance mesh will be employed for the stator of salient pole synchronous generators later in chapter 4.

2.2.3 Dynamic reluctance mesh creation of electrical machines: the air gap

In a simple magnetic circuit as shown in figure 2.2.8, where there is an air gap in the magnetic circuit, the equivalent magnetic circuit can be derived as shown in figure 2.2.8.

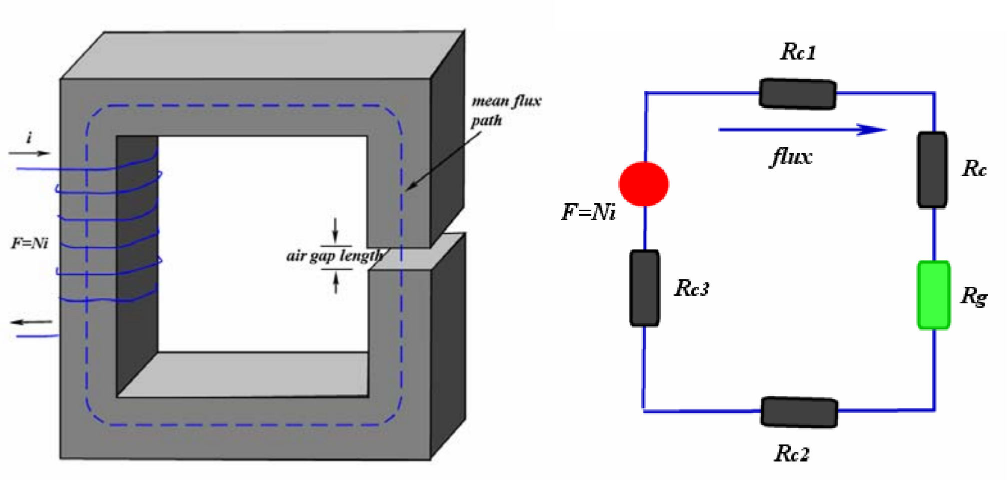

Figure 2.2.8 A simple air gap magnetic circuit includes air gap

Because the permeability of air is much smaller than that of iron, the flux is well confined to the iron path rather than leaking into air, as has been discussed in section 2.2.1. In a magnetic circuit where an air gap exists, as in figure 2.2.8, most of the flux enters the air gap from the iron perpendicularly to the iron surface. However, in practice, the magnetic field lines actually ‘fringe’ slightly outward as they cross the air gap [24], as shown in figure 2.2.9. This fringing field will increase the ‘effective’ cross-sectional area of air gap elements in a magnetic circuit analysis. There are several empirical ways of coping with this fringing effect and they will be introduced later in chapter 3. For the time being this fringing effect will be neglected and the area of the air gap element is taken to be equal that of the adjacent iron element.

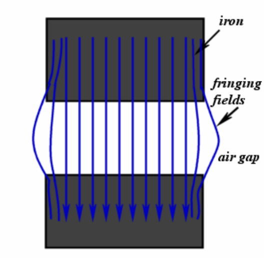

Figure 2.2.9 Air gap in a simple magnetic circuit

The air gap plays a very important role in magnetic circuit analysis, because most of the mmf is dropped across the air gap. This is because the permeability of air is very small and thus the air gap reluctance is large compared to the iron reluctances. In electrical machines, the air gap is paramount in determining the energy conversion processes and thus modelling the air gap properly is a key factor in simulating electrical machine performance accurately.

To properly represent the flux paths between each pair of stator and rotor teeth, air gap reluctances connecting each pair of stator and rotor teeth are introduced in the magnetic circuit of electrical machines, as shown in figure 2.2.10.

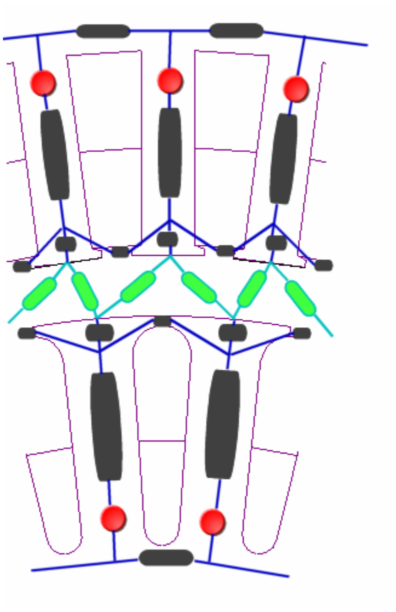

Figure 2.2.10 Air gap reluctances in electrical machine magnetic circuit

Air gap reluctances are created for all pairs of stator and rotor teeth which are, physically linked by magnetic flux. The green elements in figure 2.2.10 are air gap elements. In this manner, the flux connection between the stator and rotor for a specific rotor position is modelled properly. However, in dynamic simulations this method encounters a problem in that these air gap reluctances change as the rotor rotates, because the instantaneous coupling between each pair of teeth is different for different rotor positions.

The dynamic reluctance mesh method solves this problem by recreating all the air gap elements for every instantaneous rotor position. This is also the reason why the 'dynamic' reluctance mesh method is so named for electrical machine simulations. As shown in figure 2.2.11, a set of air gap reluctances has been determined for one specific rotor position and in the next sampled rotor position the previous set of air gap reluctances is deleted and a new set created. By this recreation of the connectivity between the rotor and stator magnetic circuits, the dynamic flux behaviour can be well simulated in the machine.

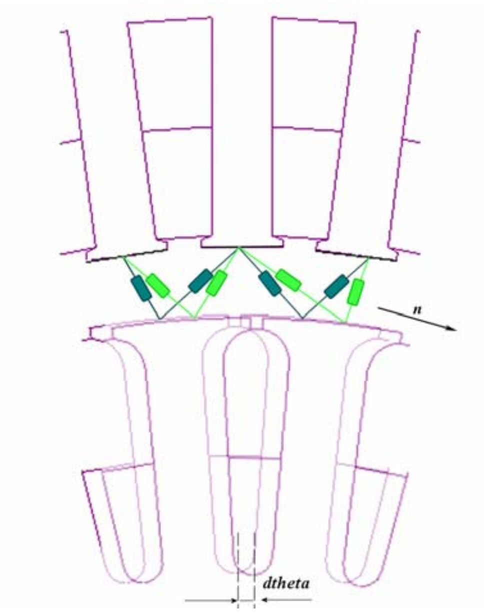

Figure 2.2.11 Dynamic creations of air gap reluctances in DRM method

For other types of machines, which have non-uniform air gap geometry, such as salient pole synchronous generators, a different method of evaluating the air gap reluctances may be used, but the concept of dynamic creation – destruction of elements remains the same. Chapter 4 will discuss the non-uniform air gap reluctance calculations in detail.

2.2.4 Dynamic reluctance mesh method of electrical machines: torque calculation

In the DRM method, torque is calculated based on the principle of virtual work [3][4], that is flexible, easy to apply and does not require knowledge of the mutual flux components in the air gap. This is an alternative method to Maxwell’s tensor formulation. The force and torque are obtained from the derivatives of the energy (co-energy) versus the displacement of the movable part. Specifically for electrical machines, the torque is calculated by evaluating the net change in stored and supplied energy due to an incremental virtual rotation of the rotor if the fluxes remain constant over the change. In the DRM, this procedure is greatly simplified by noting that the only position-dependent elements are those in the air gap and therefore the net torque is given by

$$T_e = \sum_{i=0}^{N-1} \frac{\partial E_i}{\partial \theta} \tag{2.2.20}$$

where N is the number of air gap reluctances created in this specific rotor position, and E_i is the energy stored in each air gap element.

Energy stored in a magnetic field over the volume V [24]:

$$E = \int_V \left(\int_0^B H \cdot dB \right) dV \tag{2.2.21}$$

For soft magnetic material of constant permeability where $B = \mu H$ equation 2.2.21 evaluates to [24]:

$$E = \int_V \left(\frac{B^2}{2\mu} \right) dV \tag{2.2.22}$$

In DRM method, the stored magnetic energy in each air gap reluctance in which B is assumed uniform is:

$$E_{energy} = \frac{1}{2} \cdot B \cdot H \cdot Volumn = \frac{B^2}{2\mu_0} \cdot V \tag{2.2.23}$$

and therefore the total electrical torque is:

$$T_e = \sum_{i=0}^{N-1} \frac{\partial \left(\frac{B_i^{\,2}}{2\mu_0} \cdot V_i \right)_i}{\partial \theta} = \sum_{i=0}^{N-1} \left(\frac{1}{2} \cdot \frac{B_i^{\,2}}{\mu_0} \cdot \frac{\partial V_i}{\partial \theta} \right) = \sum_{i=0}^{N-1} \left(\frac{1}{2} \cdot \frac{B_i^{\,2} d_i l_i}{\mu_0} \cdot \frac{\partial w_i}{\partial \theta} \right) \tag{2.2.24}$$

where B_i is the flux density in the i^{th} air gap reluctance, and d_i, l_i, w_i, V_i are the depth, length, width and volume of this air gap reluctance.

2.2.5 Dynamic Reluctance Mesh method of electrical machines: skew modelling

In previous sections of this chapter, the creation of a typical reluctance mesh for induction machines has been implemented and now a further practical issue for machine simulations, namely skewed rotor simulations, will be introduced in this section.

Most cage induction motors have their rotor slots skewed by one slot-pitch to reduce space harmonics in the air gap flux density introduced by the slotting [25]. Because of its 3D nature, consideration of skew has generally involved significant computational effort in electrical machine simulations. The DRM uses a quasi-3D method to model skew. Dividing the whole machine into several sections along its axial length, each section is offset by a small angle with respect to the previous section to model the skew, as shown in figure 2.2.12. The DRM approach assumes that the axially directed flux is negligible such that the reluctances meshes of different axial sections are only coupled indirectly through the rotor and stator electrical circuits.

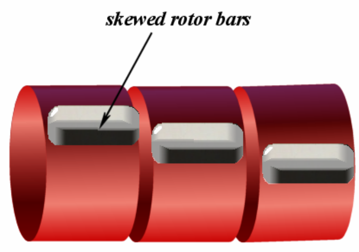

Figure 2.2.12 Skew model of cage rotor

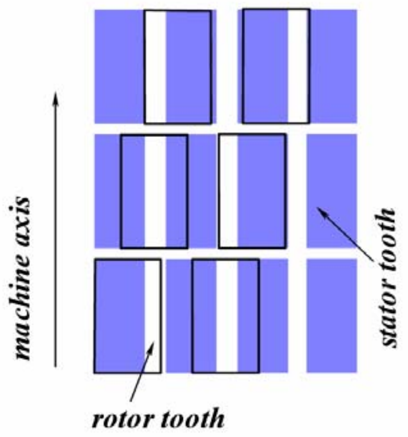

Figure 2.2.13 Trapezoidal rotor tip elements

Figure 2.2.13 shows the relative position of the stator and rotor in different skew sections. As stated above, the machine has been divided into several skew sections and the reluctance meshes for both the stator and rotor are separately generated for each section including air gap reluctances.

In figure 2.2.13, the overlapping area between pairs of stator and rotor teeth is rectangular in this case and thus the appropriate reluctance connects the corresponding stator and rotor nodes has a rectangular cross-section. However, this way of calculating air gap reluctance values has two disadvantages [3]. Firstly, it is clear that the more skew sections that are used; the more accurate the effects of skew are modelled. Unfortunately the more skew sections that are used the longer the calculation time. Secondly, when rotating at constant speed, the overlap area between a pair of rotor and stator teeth is a piecewise linear function of time. Unfortunately, the evaluation of the torque generated by the motor in equation 2.2.24 depends upon the rate of change of these reluctances with time and this causes discontinuous steps in the torque. Not only does this appear as unwanted numerical 'noise', but also it has a noticeable effect on the ease with which the simulation can predict the future state of the machine from the present one and hence the calculation time required for the simulation to go forward in time.

To address both of the issue, the DRM model uses trapezoidal shape rotor tip elements in the skewed rotor model, as shown in figure 2.2.14.

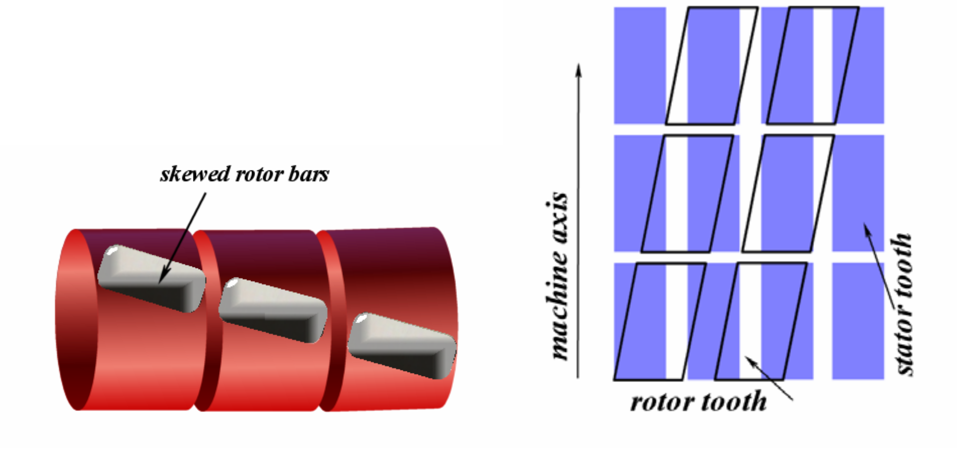

Figure 2.2.14 Trapezoidal air gap elements in DRM modelling

By using the trapezoidal elements for air gap elements in a skewed rotor machine, the rate of change of the air gap reluctances is always continuous and the problems caused by discontinuities in the torque are avoided. Figure 2.2.15 shows the torque ripple observed in the simulation of the direct on line start of an unloaded induction machine. It can be seen that the use of trapezoidal skew elements significantly reduces the unphysical torque ripple seen when using rectangular elements.

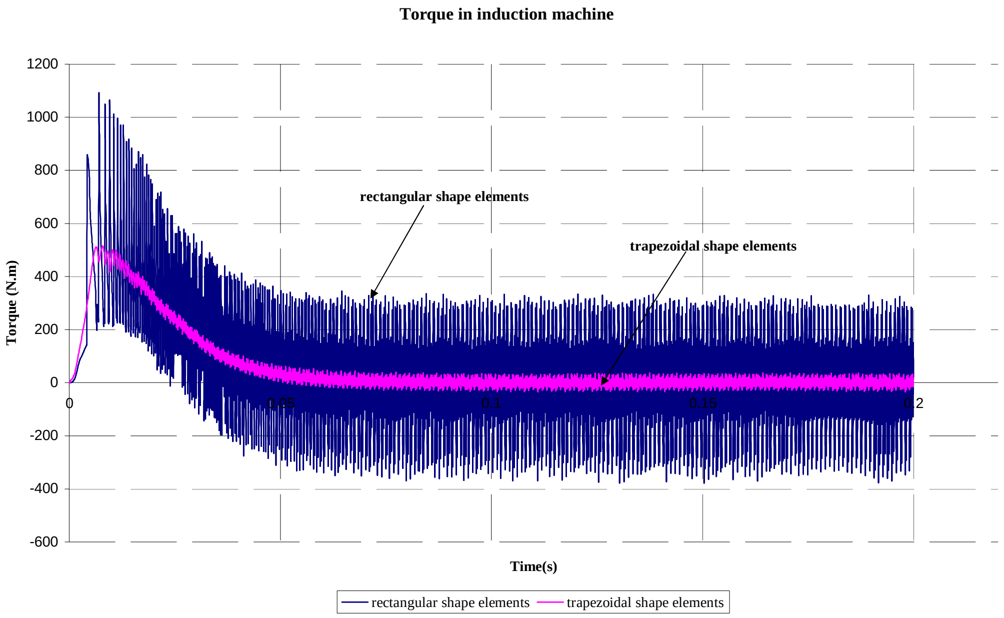

Figure 2.2.15 Torque ripple comparison for the result come from induction machine direct on line start no load condition simulation, with air gap modelled by rectangular and trapezoidal shape elements

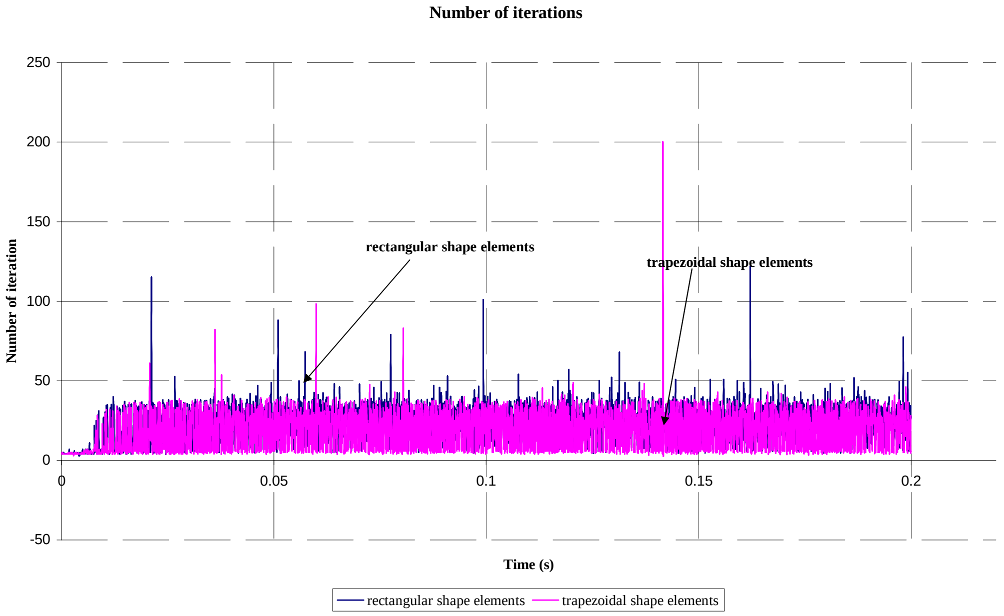

Figure 2.2.16 Number of iteration comparison for the results come from induction machine direct on line start no load condition simulation, with air gap modelled by rectangular and trapezoidal shape elements

Figure 2.2.16 shows the number of iterations required in the Newton-Raphson solver, which will be discussed later in this chapter. It can be seen that the use of trapezoidal shape elements requires slightly fewer iterations compared to the use of rectangular elements. Quantitatively, the average number of iterations for rectangular elements is 23.83, compared to 19.32 for trapezoidal elements. Employing trapezoidal shape elements reduces the unphysical numerical noise and total computational time of induction machine simulations.

Further details about the air gap modelling technique in skewed rotor induction machines will be presented in chapter 3 along with some other approaches for coping with skew.

2.3 State Variables and State Equations

In the previous sections of this chapter the methodology for discretising the induction machine geometry into reluctance meshes was discussed as well as the method to calculate torque and to deal with skewed rotors. This section will describe how the system state is defined and present the system equations, which govern the system's behaviour.

As discussed in section 2.2.1, flux conservation holds at a 'node' in a magnetic circuit in an analogous manner to KCL in an electric circuit. In a dynamic simulation, conservation of flux at each 'node' for every specific time instance should be enforced. As can be seen from equation 2.2.13, the magnetic flux flowing through the reluctance can be evaluated given the mmf drop across it and its reluctance value. The DRM model specifies each node's mmf value as a state variable and conservation of the rate of change of flux is enforced at each node. An initial condition for the mmf value, which is typically zero, is also given. For each node i, conservation of the net rate of change of flux entering it from all the elements connecting to this node holds, as shown in equation 2.3.1, and in figure 2.3.1:

$$\sum_{j=0}^{n-1} \frac{d}{dt} \phi_{ji} \left(mmf_{j2}, mmf_{j1} \right) = 0 \tag{2.3.1}$$

where n is the number of elements connected to this node, and ϕ_{ji} is the flux flowing through the j^{th} element to the i^{th} node as a function of the node potentials, mmf_{j2} and mmf_{j1}.

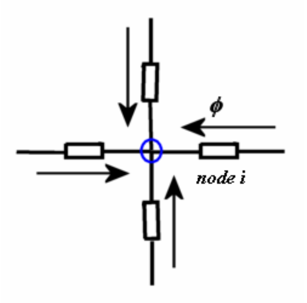

Figure 2.3.1 Conservation of rate of change of flux in one node

The instantaneous rate of change of flux through each mesh element is calculated from

$$\frac{d\phi}{dt} = \frac{1}{\Delta t} \left[\left(\frac{\Delta F(t + \Delta t / 2)}{\Re} \right) - \left(\frac{\Delta F(t - \Delta t / 2)}{\Re} \right) \right] \tag{2.3.2}$$

Equation 2.3.2 forms the basis for a non-linear set of equations, the source terms which are obtained by linking the above magnetic model with a lumped element electrical circuit model for the machine windings. Consider the simple electrical loop supplied by a voltage source as shown in figure 2.3.2 below.

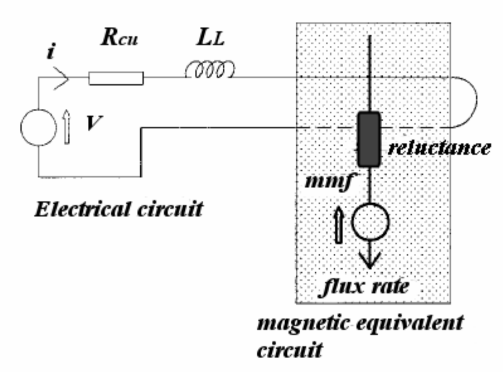

Figure 2.3.2 Coupling of a single turn electrical network with the reluctance mesh

The existence of the electrical current in the loop is incorporated into the magnetic circuit via the mmf source terms as discussed in the previous sections.

The induced electromotive (emf) in the loop is determined by the rate of change of flux in the corresponding mmf source (which clearly ensures conservation of power). Applying KVL around the electrical circuit loop yields

$$v(t) = R_{cu} i(t) + L_L \frac{di(t)}{dt} + \frac{d\phi(t)}{dt} \tag{2.3.3}$$

In equation 2.3.3, copper loss is incorporated as a resistor, R_{cu}, and an inductive term is introduced to allow for any end winding leakage reactances which are not explicitly modelled in the DRM. The driving term in equation 2.3.3 is the applied voltage.

Naturally, realistic windings for practical machines are not just simple loops but are specifically designed to obtain an mmf distribution in the air gap region which is as close to sinusoidal as possible. Thus, practical machine windings are usually singly or doubly wound. For example in a three-phase induction motor, the stator electrical equations would be of the form:

$$v_A = R_a \cdot i_a + \sum_{i=1}^{S} \frac{de_a}{d\phi_i} \cdot \frac{d\phi_i}{dt} \tag{2.3.4}$$

$$v_B = R_b \cdot i_b + \sum_{i=1}^{S} \frac{de_b}{d\phi_i} \cdot \frac{d\phi_i}{dt} \tag{2.3.5}$$

$$v_C = R_c \cdot i_c + \sum_{i=1}^{S} \frac{de_c}{d\phi_i} \cdot \frac{d\phi_i}{dt} \tag{2.3.6}$$

Where v_A, R_a and i_a are the applied voltage source, resistance and current of phase A respectively. S is the number of stator teeth. $\frac{de_a}{d\phi_i}$ is the term representing the change of the emf induced in phase A due to a change of flux in tooth i. These expressions account for the total flux linkage changes that are enclosed by the phase A electrical loop and implicitly involve the connectivity between the electrical network and the magnetic circuit as defined by the winding pattern.

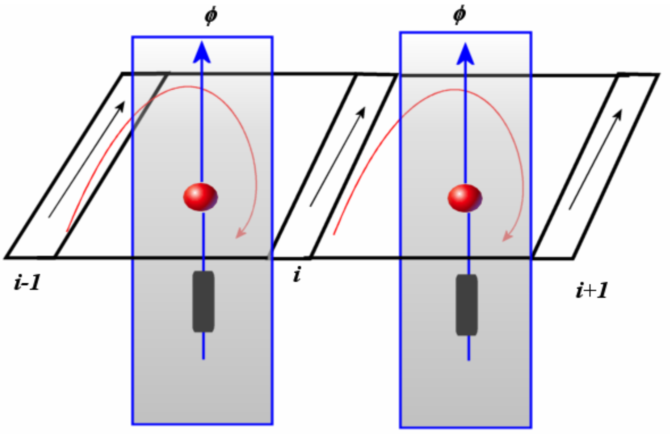

Figure 2.3.3 Coupling of electrical network and magnetic circuit in a cage rotor

In a cage rotor, as shown in figure 2.3.3, these electrical loop equations are modelled to $-i_i \cdot R_i + i_{i-1} \cdot R_{i-1} - \frac{d\phi}{dt} = 0$, where i_i and i_{i-1} are currents in bar i and bar $i-1$, and ϕ is flux passing between them. The relationship between the currents and the mmf is shown in equation 2.3.7. According to Ampere's law, the current flowing through each bar is determined by the mmf difference for adjacent bars.

$$i_i = mmf_{i+1} - mmf_i \tag{2.3.7}$$

Thus, these mmf sources, mmf_i in each bar are employed as state variables in the DRM model for induction machines, as shall be seen later in this chapter.

The above equations define the electrical and magnetic response of the machine. Dynamic simulations of a machine require consideration of the mechanical response, as defined by:

$$\omega_r - \frac{d\theta_{mech}}{dt} = 0 \tag{2.3.8}$$

$$T_e - J\frac{d\omega_r}{dt} - D\omega_r - T_{load} = 0 \tag{2.3.9}$$

where ω_r is the mechanical speed of the rotor and D and J are the associated machine windage and inertia respectively.

To summarize, the variables that characterise the machine's state and for which are solved are the nodal mmf $f_0 \cdots f_1$, the cage rotor bar mmfs $mmf_0 \cdots mmf_{Nbar-1}$, the three phase stator current i_a, i_b and i_c, and the position and velocity of the rotor.

$$\mathbf{x} = \left[f_0, \cdots, f_{Nnode-1}, mmf_0, \cdots mmf_{Nbar-1}, i_a, i_b, i_c, \theta_{mech}, \omega_r \right]^T \tag{2.3.10}$$

The system equations relating these variables are:

$$\mathbf{F}(\mathbf{x}) = \begin{bmatrix} \text{conservation of rate of change of flux at node 0} \\ \vdots \\ \text{conservation of rate of change of flux at node } \mathrm{N}_{\mathrm{node}} - 1 \\ \text{electrical loop equations for cage rotor, loop 0} \\ \vdots \\ \text{electrical loop equations for cage rotor, loop } \mathrm{N}_{\mathrm{bar}} - 1 \\ \text{electrical loop equations for stator phase A} \\ \text{electrical loop equations for stator phase B} \\ \text{electrical loop equations for stator phase C} \\ \text{speed equation 2.3.8} \\ \text{torque equation 2.3.9} \end{bmatrix} \tag{2.3.11}$$

The dimension of $\mathbf{F}(\mathbf{x})$ and $\mathbf{x}$ are $n = N_{node} + N_{bar} + 3 + 2$.

The system of equations that need to be solved are a set of coupled nonlinear first order differential equations. The nonlinearity in the system equations is caused by the nonlinearity of the iron.

$$\mathbf{F}\left(\mathbf{v}, \mathbf{mmf}, \mathbf{i}, \theta_{mech}, \omega_r, \frac{d\mathbf{mmf}}{dt}, \frac{d\mathbf{i}}{dt}, \frac{d\theta_{mech}}{dt}, \frac{d\omega_r}{dt} \right) = 0 \tag{2.3.12}$$

The method of solving this set of equations will be discussed in the next section.

2.4 Solving Process

To solve the machine’s state equations, which are first order, nonlinear, time dependent differential equations, they are first converted to a nonlinear set of algebraic equation, and then subsequently an iterative linearisation procedure is applied which makes them easier to solve. In this chapter, a brief description of the Crank-Nicolson differencing scheme will be introduced first, which converts the nonlinear differential equation to nonlinear algebraic equations, and then the Newton-Raphson method, which linearises these nonlinear equations, will be introduced. The overall solution procedure will be given finally in this section on a flow chart.

2.4.1 Crank-Nicolson differencing scheme

The Crank-Nicolson differencing scheme is adopted here to convert the differential equations into algebraic equations. The Crank-Nicolson method is an implicit differencing scheme with second-order accuracy that allows larger time steps [23] than explicit schemes. It is a compromise between the Forward Time Centre Space (FTCS) method [23] and the Fully Implicit method. The FTCS differencing scheme is first-order accurate but only stable for sufficiently small time steps, whereas the Fully Implicit scheme is stable for arbitrary large time steps, is only first-order accurate, but generally requires matrix solvings.

The reason why the Crank-Nicolson has been chosen for the DRM code is due to its well-proven stability and accuracy. There is a parameter α in the differencing scheme which balances the scheme between implicit and explicit. The factor $\alpha = 0.5$ corresponds to the Crank-Nicolson scheme. For each time step the Crank-Nicolson approach approximates the variables' value and time derivatives:

$$\mathbf{x}\left(t+\frac{\Delta t}{2}\right) = \alpha\mathbf{x}(t) + (1-\alpha)\mathbf{x}(t+\Delta t)$$

$$\frac{d\mathbf{x}}{dt}\left(t+\frac{\Delta t}{2}\right) = \frac{\mathbf{x}(t+\Delta t)-\mathbf{x}(t)}{\Delta t} \tag{2.4.1}$$

Although choosing α =0.5 provides the most accurate results it is on the stability limit. In practice, a slightly different lower value for α, such as 0.495, is used to make the system slightly implicit which overcomes any instability caused by numerical noise such as rounding errors.

Applying the differencing scheme of equations 2.4.1 yields

$$\underline{\underline{\mathbf{A}}}\begin{pmatrix}\mathbf{V}(t+\Delta t)\\ \mathbf{F}(t+\Delta t)\\ \mathbf{I}(t+\Delta t)\\ \theta(t+\Delta t)\\ \omega(t+\Delta t)\end{pmatrix}=\underline{\underline{\mathbf{B}}}\begin{pmatrix}\mathbf{V}(t)\\ \mathbf{F}(t)\\ \mathbf{I}(t)\\ \theta(t)\\ \omega(t)\end{pmatrix} \qquad (2.4.2)$$

where $\underline{\underline{\mathbf{A}}}$ and $\underline{\underline{\mathbf{B}}}$ are sparse, as yet nonlinear, matrix. Given the present value of the state variables those at the next time step can be found from equations 2.4.2.

The rest of the section will describe how the nonlinear behaviour is iteratively linearised.

2.4.2 Newton-Raphson multidimensional nonlinear solving technique

Multi-dimension simultaneously nonlinear equations are difficult to solve, in that it is difficult to find the solution that sets all of the system equations to zero. For example, consider two dimensional nonlinear equations which need to be solved simultaneously,

$$\begin{aligned} f(x,y)&=0\\ g(x,y)&=0 \end{aligned} \qquad (2.4.3)$$

The functions $f(x,y)$ and $g(x,y)$ are two arbitrary nonlinear equations and they both divide the xy plane into positive and negative parts, as shown in figure 2.4.1.

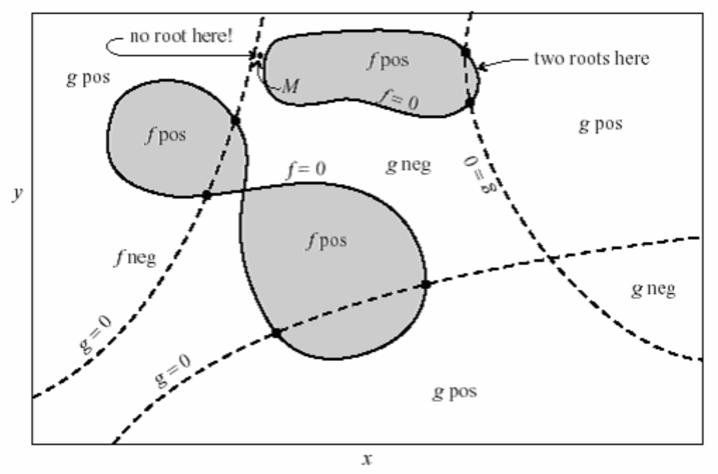

Figure 2.4.1 [23] Solutions of two nonlinear equations. The grey regions are the positive regions for the function f and the dashed lines divide the plane into positive and negative regions for the system

From figure 2.4.1 it can be seen that to solve the system with two equations, the intersections of the zero contour lines of the function f and g have to be found. Since normally function f and g are unrelated, this is not a simple task.

For multi-dimensional equations this task becomes even more complicated. Our aim is to find the common solutions, the roots to all of the equations, i.e. the intersection of all the zero contours in N-dimensional space which is generally difficult if no insight into the nature of the problem can be obtained in advance.

In the DRM modelling the simplest multi-dimensional solving technique, the Newton-Raphson method, is used. This method provides a very efficient means of converging to a root if an initial guess is sufficiently good.

For example consider one-dimensional nonlinear root-finding problem solved by Newton-Raphson. To solve the problem $f(x)=0$, a taylor series for $f(x)$ is expanded in the neighbourhood of an estimation (x) to the solution x_0:

$$f(x+\delta) = f(x) + f'(x)\delta + \frac{f''(x)}{2}\delta^2 + \cdots \tag{2.4.4}$$

where x is the current estimation to the solution x_0, and δ is the distance between the current estimation and the next estimation. For sufficiently small enough values of δ and a well-behaved function, terms higher than linear are not important, and thus if the root occurs at $x+\delta$

$$f(x+\delta) = 0 \tag{2.4.5}$$

which gives:

$$\delta = -\frac{f(x)}{f'(x)} \tag{2.4.6}$$

If the function value $f(x)$ and its derivative $f'(x)$ at the estimation point are known, where x is a suitable estimate to solution x_0, then δ is evaluated from equation 2.4.5 and a better estimate of x found. Geometrically speaking, as can be seen from figure 2.4.2, Newton's method extends the tangent line at point x until it cross the x axis which becomes the next predicted value of the system solution; this procedure continues until the function value is small enough to be regarded as zero, as shown in figure 2.4.2.

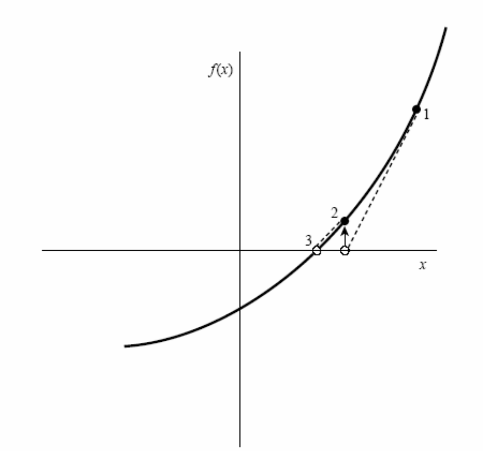

Figure 2.4.2 [23] Newton method in one dimensional to find the next predicted value

However, although Newton's method for one-dimensional problems is fast and effective, it will fail to converge if the initial point is not close enough to the solution (figure 2.4.3), or the system function has local extremes (figure 2.4.4) where high order terms in equation 2.4.4 are important.

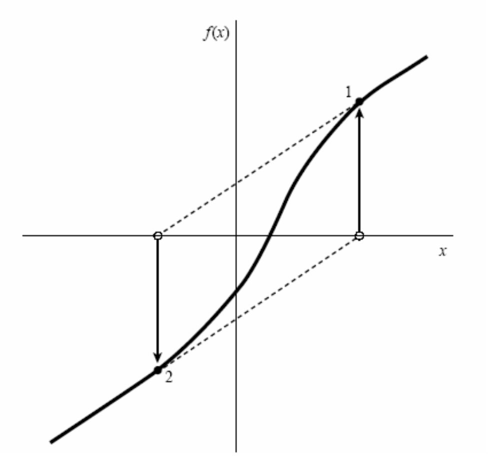

Figure 2.4.3 [23] Initial guess is not close enough to the solution and nonconvergence situation happened in Newton-Raphson method

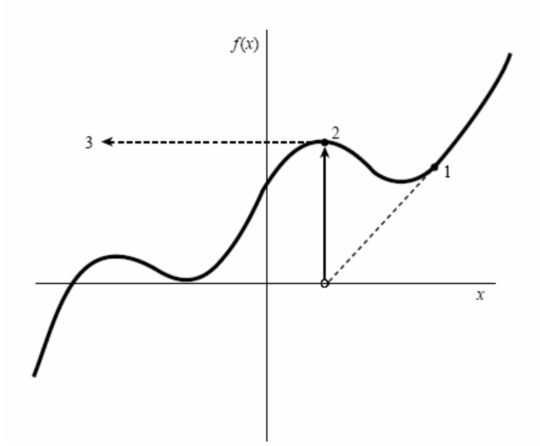

Figure 2.4.4 [23] Newton-Raphson method encounters a local extreme where high order terms are important and cannot be neglected

The Newton-Raphson method can be used in multidimensional root finding problem and is very efficient to converge to a root, if the initial guess is sufficiently good [23]. An improved Newton-Raphson solving technique will be introduced later in chapter 3, which gives a global convergent Newton-Raphson method no matter where the initial guess is.

In a one-dimensional problem, the function value $f(x)$ and its derivative $f'(x)$ at point x are needed in order to calculate the next predicted root. In multi-dimensional problems the value of the equations for a system state $\mathbf{x}$ and the system Jacobian matrix at $\mathbf{x}$ are needed. The Jacobian matrix is the first partial derivative matrix of the system equations with respect to the state variables as given in equation 2.4.7.

$$J_{ij} \equiv \frac{\partial F_i}{\partial x_j} = \begin{bmatrix} \frac{\partial f_1}{\partial x_1} & \frac{\partial f_1}{\partial x_2} & \cdots & \frac{\partial f_1}{\partial x_n} \\ & & \cdots & \\ \frac{\partial f_2}{\partial x_1} & \frac{\partial f_2}{\partial x_2} & \cdots & \frac{\partial f_2}{\partial x_n} \\ \vdots & \vdots & & \vdots \\ \frac{\partial f_n}{\partial x_1} & \frac{\partial f_n}{\partial x_2} & \cdots & \frac{\partial f_n}{\partial x_n} \end{bmatrix} \tag{2.4.7}$$

where $\mathbf{x}$ denotes the vector value of system variants and $\mathbf{F}$ denotes the vector of function values.

Consider the multi-dimensional system equations in the DRM modelling, as shown in equation 2.4.8. The Newton-Raphson expansion for the i^{th} equation is:

$$F_i\left(x_i + \delta x_i, x_j + \delta x_j, \cdots\right) = F_i\left(x_i, x_j, \cdots\right) + \sum_{j=0}^{N-1} \frac{\partial F_i}{\partial x_j} \delta x_j + \mathrm{O}\left(\delta x^2\right) \tag{2.4.8}$$

In matrix notation, the above function is:

$$\mathbf{F}(\mathbf{x} + \delta\mathbf{x}) = \mathbf{F}(\mathbf{x}) + \mathbf{J} \cdot \delta\mathbf{x} + \mathrm{O}\left(\delta\mathbf{x}^2\right) \tag{2.4.9}$$

where J is the Jacobian matrix defined in equation 2.4.7.

If terms of order $\delta\mathbf{x}^2$ and higher terms are neglected, and the root occurs at $\mathbf{x} + \delta\mathbf{x}$, then the correction $\delta\mathbf{x}$ that moves the solution toward the root is:

$$\mathbf{J} \cdot \delta\mathbf{x} = -\mathbf{F} \tag{2.4.10}$$

$\mathbf{x}_{\mathbf{new}} = \mathbf{x}_{\mathbf{old}} + \delta\mathbf{x}$ is the process to be iterated to converge.

Thus application of the Newton-Raphson scheme linearises the system equations. In the next section, the approach used to solve these linear equations will be discussed.

2.4.3 Linearised equation solving method

The linear equations 2.4.10 above are inherently sparse because the majority are derived from the magnetic reluctance mesh circuit. Previous work [1][26] has solved these linearised equations by LU decomposition, a direct matrix method which becomes rapidly untenable as the size of the problem increases, i.e. with the number of reluctances used in the discretisation of the magnetic circuit of the electrical machine.

The alternative approach adopted in DRM modelling, is to use an iterative method such as the preconditioned Bi-Conjugate Gradient Stabilised (BiCGSTAB) algorithm in conjunction with efficient sparse matrix-vector multiplications [27]. Due to the irregular sparse matrix involved in the system equations, a simple pre-processing routine is included as a preconditioner to increase the convergence of the iterative process. The preconditioner used is a simple incomplete LU decomposition. The linear equations $\mathbf{J} \cdot \delta\mathbf{x} = -\mathbf{F}$ are preconditioned as

$$\tilde{\mathbf{J}}^{-1} \cdot \mathbf{J}\delta\mathbf{x} = -\tilde{\mathbf{J}}^{-1} \cdot \mathbf{F} \tag{2.4.11}$$

where $\tilde{\mathbf{J}}^{-1}$ is the approximate inverse matrix of $\mathbf{J}$ identified by incomplete LU decomposition, so that $\tilde{\mathbf{J}}^{-1} \cdot \mathbf{J} \approx \mathbf{I}$. Incomplete LU decomposition uses a partial decomposition scheme where the appearance of elements in the inverse matrix is controlled by a threshold, only those elements of magnitude above the threshold appear in the inverse matrix. By applying different thresholds, the program can vary the accuracy to the true inverse matrix of $\mathbf{J}$ which allows a balance between memory use and computation time. The smaller the threshold, the greater the memory usage, but the better preconditioned the matrix problem which requires fewer iterations of the linear solver i.e. the BiCGSTAB solver. However, insufficient preconditions may lead to a total failure to converge. A schematic relationship diagram between memory usage and the number of iterations in the BiCGSTAB linear solver with respect to the threshold is shown in figure 2.4.5.

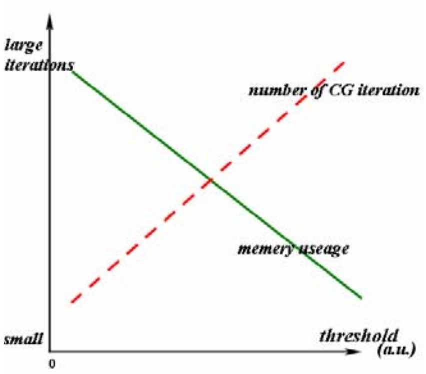

Figure 2.4.5 Schematic diagram shown the relationship between memory usage and the number of linear solver iteration with respect to threshold

After the nonlinear first order differential system equations are solved by the algorithms introduced above, the system state at a specific time is known. As the Newton-Raphson nonlinear solving scheme needs an initial guess for the solving process at each time instance, a prediction for next time step is calculated. This is based upon the present solution and it is different from the previous step.

$$\mathbf{x}_{\mathbf{predicted}} = \mathbf{x}_{\mathbf{present}} + (\mathbf{x}_{\mathbf{present}} - \mathbf{x}_{\mathbf{previous}}) \qquad (2.4.12)$$

However, as has been discussed in section 2.4.2 and shown in figure 2.4.3, the Newton-Raphson method is sensitive to the initial guess, and will fail to converge if the initial guess is not sufficiently good. In electrical machine simulations, most of the nonlinearity in the machine is due to the nonlinear characteristic of the iron material. If, at some time instance when the flux density value in a part of the iron is around the ‘knee’ area of its B-H curve, the system equations exhibit a dramatic degree of nonlinearity, which undermines the NR process.

To alleviate this, the DRM employs a simple scheme to try to ensure the robustness of solving process, the use of an adaptive time step method. If at one time step, the Newton-Raphson scheme fails, the system state will be reset to that of the previous time step and the time step used is halved and a new predicted value using the halved time step will be calculated. The Newton-Raphson scheme will then attempt to solve the system state in the new time step and, if it fails again, the same process continues until the Newton-Raphson succeeds. If, on successful convergence the time step is doubled and subject to remain less than a predefined maximum value.

The criteria used to decide whether the solution process for the current time step is unsuccessful is that:

1. The total equation error on iteration of the Newton-Raphson process increases compared to the previous iteration;
2. The conjugate gradient solver (BiCGSTAB) fails to solve the linear equations in a predefined number of iterations;

As just described the time step is then halved and the whole machine state will be recovered to the previous time step.

The total system error in the solving process is defined as

$$Error_{total} = \frac{\sqrt{\sum_{i=0}^{N-1} F^2{}_i(x)_{present}}}{N} \qquad (2.4.13)$$

2.4.4 The DRM program flow chart

In section 2.4, the system solving techniques have been discussed. Now the DRM system flow chart will be given to show a clear view of the program structure, as shown in figure 2.4.6.

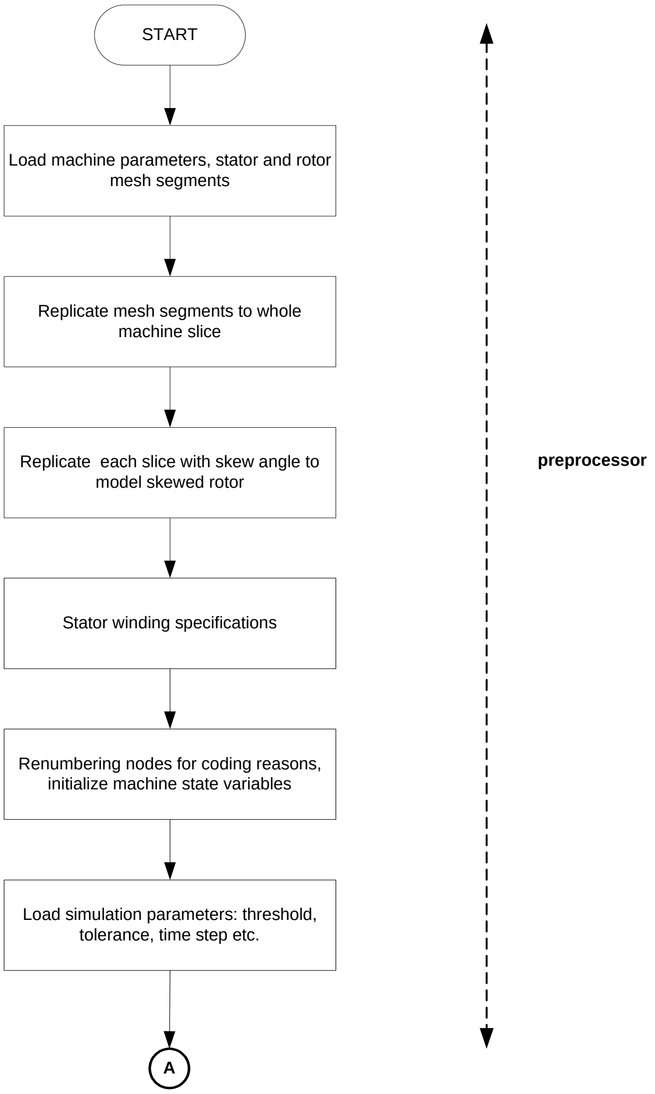

(a) DRM Preprocessor flow chart

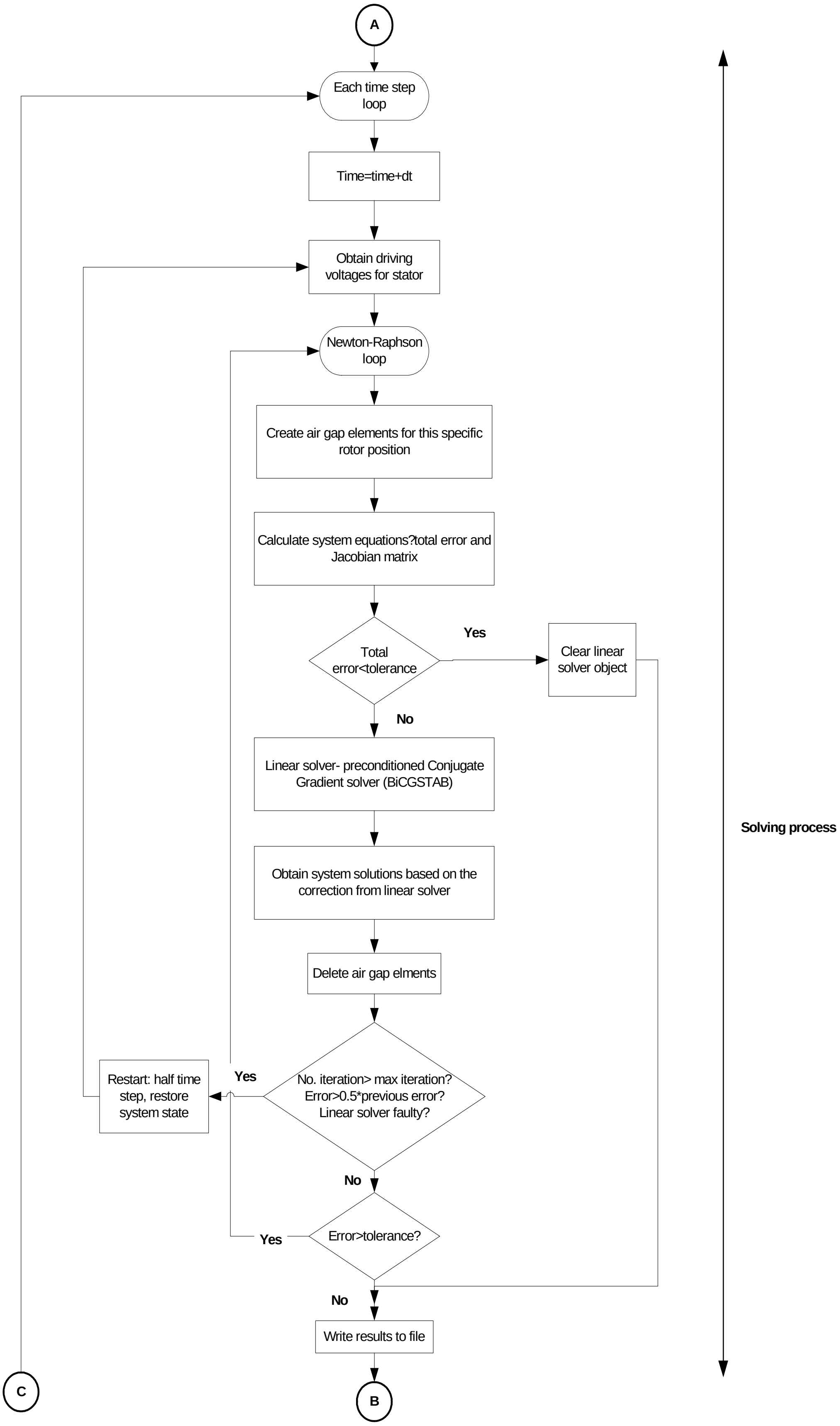

(b) DRM solving core flow chart

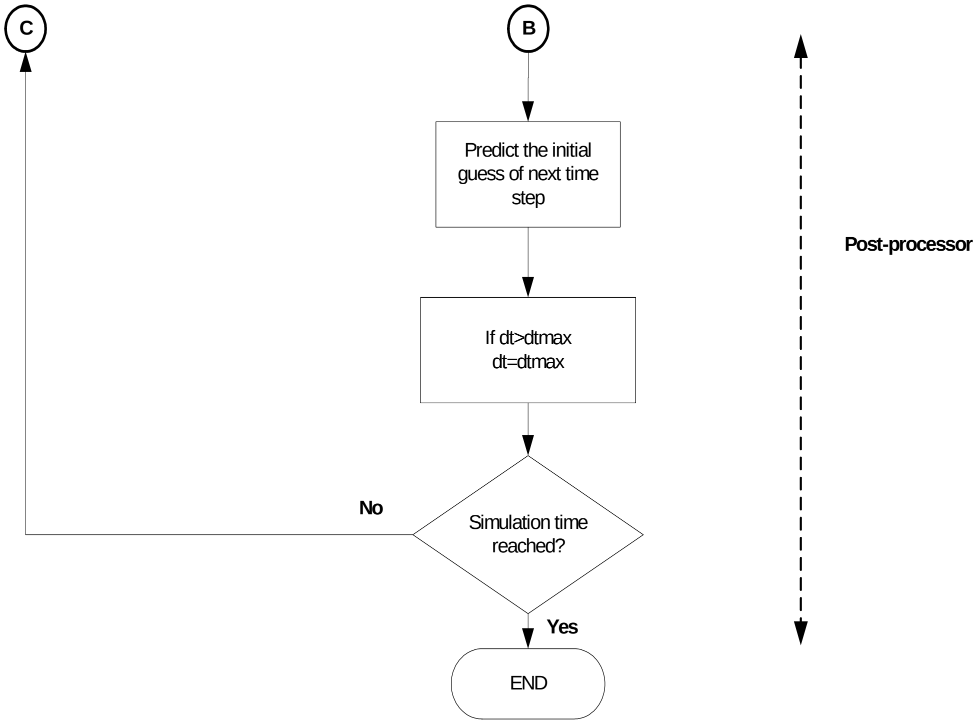

(c) DRM post-processor flow chart

Figure 2.4.6 DRM program flow chart

The total system flow chart is shown in figure 2.4.6. It can be seen that the whole DRM program is divided into three parts, which are the pre-processor, the solving core and the post-processor.

The pre-processor sets up the dynamic magnetic reluctance mesh model of the machine. It reads in the machine geometry, the winding arrangements and the simulation parameters, such as the threshold and maximum simulation time step. In creating the reluctance mesh, the pre-processor reads the mesh topology of one pair of stator teeth first and then replicates these through the whole machine to get the complete reluctance mesh. The same replication procedure happens to create the rotor reluctance mesh. Skewed rotor is also implemented by replicating the reluctance mesh in one skew section to the other skew sections with the appropriate angular offsets. Due to the dynamic creation of air gap elements which depends upon the specific position of the rotor, and thus vary for each time step, the DRM leaves these to the solution phase.

In the main solving core, the system state is solved for each time step. It can be seen that in each time step, air gap reluctances for this specific rotor position are created and the system state equations are evaluated. If the current system state is close enough to the exact system solution, i.e. total system error are smaller than the tolerance, solving process for the current time step will be stopped and the current state will be taken as the exact solution, and the program carries on to next time step solving process. However, if the system equation error for the current time step is not small enough, the preconditioned iterative linear solver (BiCGSTAB) will be invoked to solve for the next Newton-Raphson solution in current time step. After solving for the next Newton-Raphson solution for current time step, air gap elements will be deleted. After that, the system will check to see if the Newton-Raphson solving process has failed. If the Newton-Raphson fails, the time step will be reduced and the whole system state will be restored to the previous time step, then a new system state prediction will be generated based on the reduced time step. If the Newton-Raphson solving process is healthy in the current step, the total system error is checked to decide if this next Newton solution coming out of the linear solver is accurate enough, by applying the criteria given in section 2.4.3. This procedure will continue until the total system equation error is smaller than the tolerance, i.e. to find the exact system solution for this current time step.

The postprocessor writes out the simulation results and predicts the solution of the next time step which is regarded as the initial guess for the Newton-Raphson algorithm.

2.5 Conclusion

This chapter described the Dynamic Reluctance Mesh modelling method for electrical machines. Since it is based upon magnetic circuit theory, a brief introduction of the basic theory of magnetic circuits was first given, and then the procedure for creating dynamic reluctance meshes for electrical machines taking the induction machine as an example, was presented. The description of the DRM emphasised the descritisation method of the iron and air parts of the machine and the way the DRM deals with skewed rotors and torque calculations are also described. After the reluctance model has been defined for the induction machine, the chapter summarised the system state variables and system equations describing the induction machine electro-mechanical system. Section 2.4, detailed how the system state is solved in the DRM, including the Crank-Nicolson scheme, Newton-Raphson iterations and the preconditioned BiCGSTAB linear solver. The flow chart for the solution process is also given.

CHAPTER 3 DEVELOPMENTS OF THE DYNAMIC RELUCTANCE MODELLING SOFTWARE

3.1 Introduction

Dynamic Reluctance Modelling is a fast and effective method of modelling electrical machines as has been described and validated by Sewell [3] for cage induction machines. However, with the increased requirements upon simulations of electrical machines, more detailed models are needed to accommodate the complex flux distributions in the air gap regions due to the complicated tooth geometry and fringing effects. Thus, some improvements have been made to enhance the modelling of the air gap elements.

Moreover, scheme solving the system equations using Newton-Raphson iterations coupled with the Crank-Nicolson technique works well for a single cage induction machine, as has been described in chapter 2 where the nonlinearity only exists in iron materials. However, the situation becomes more complicated if there are other nonlinear components involved in the system, such as the rotating rectifiers which exist in brushless generating systems. Some modifications have to be made to strengthen the Newton-Raphson solving process, in order to cope with the higher degree of system nonlinearity and the deficiency of the Newton-Raphson algorithm already presented in chapter 2.

This chapter states the modifications that have been made to the original version of the Dynamic Reluctance Modelling software and why these changes have been made. Section 3.1 describes the detailed modelling method of air gap elements; section 3.2 describes the changes of nodal flux equations;

chapter 3.3 presents the modified globally convergent Newton-Raphson nonlinear solver. Finally, further modifications were made to the induction machine model to make it more precise and a comparison of results between Finite Element models and the Dynamic Reluctance Mesh models is also given.

3.2 Representing Air Gap Reluctances Precisely

Magnetic equivalent circuits are more difficult to derive than electrical equivalent circuits from the field point of view due to the relatively large leakage phenomenon in magnetic paths: in electrical circuits, most of the current caused by moving electrons can be constrained within electrical conducting materials and components, because the electrical conduction of air is extremely small compared to that of metals. In magnetic circuits, things are quite different. The permeability of air is not insignificant compared to that of magnetic materials and therefore the flux paths are difficult to predict and calculate as flux can ‘leak’ out of the magnetic path, as depicted in chapter 2 by the air gap fringing effect shown in figure 2.2.9. This leakage of flux in the air gap region causes difficulties for modelling in electrical machines and these fringing effects are reflected as a modified air gap reluctance width or length.

There are several ways of dealing with these air gap reluctance issues in a computer code, either taking the fringing effect into account or not. These options will be introduced in turn.

3.2.1 Method 1

The method of calculating the air gap reluctance element values, which has been introduced in chapter 2, is called Method 1 in this thesis. It utilises a relatively simple way of modelling the air gap elements assuming that the flux across the air gap region between the stator and rotor is normal to both the stator and rotor tooth surfaces and calculates the area of air gap elements using the direct overlap area of each pair of stator and rotor teeth, as shown by the shadowed area in figure 3.2.1.

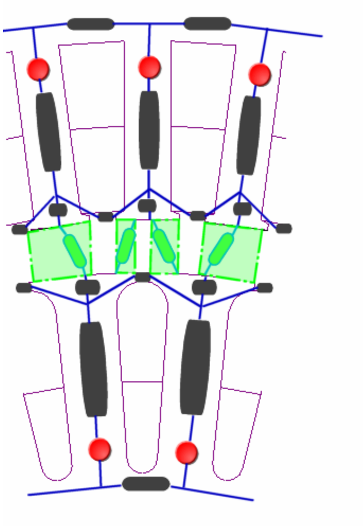

Figure 3.2.1 Air gap modelling in DRM: method 1

When allowing for skewed rotors, the air gap reluctance values in each skew section are evaluated for a trapezoidal overlap area, for reasons which are already explained in chapter 2.

Now a detailed analysis of how the overlap area is calculated in each skew section will be given. Figure 3.2.2 (a) shows the overlapped air gap area for a non-skewed rotor which is the rectangular area between a pair of rotor and stator teeth.

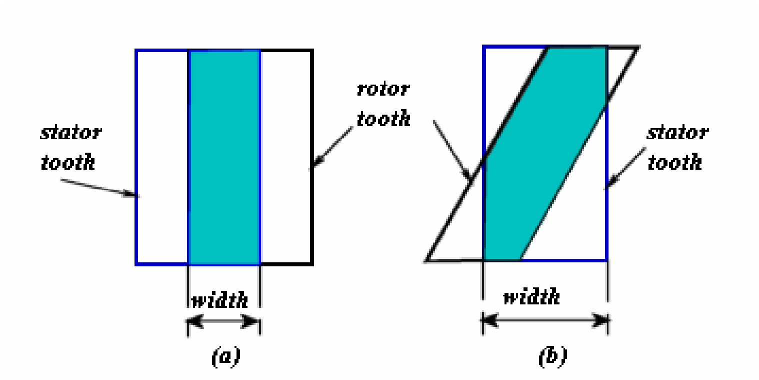

Figure 3.2.2 Air gap elements calculated by method 1
(a) non-skewed rotor; (b) skewed rotor

However, for the skewed section of induction machine shown in figure 3.2.2

(b), the overlap area between the stator and rotor teeth are more difficult to calculate. The air gap reluctance area is evaluated from the irregular overlap area shown in figure 3.2.3(b).

As mentioned in chapter 2, the air gap reluctance effective width is a piece-wise linear function of time. The width changes as the rotor rotates. The figures shown in figure 3.2.3 encompass the possible configurations.

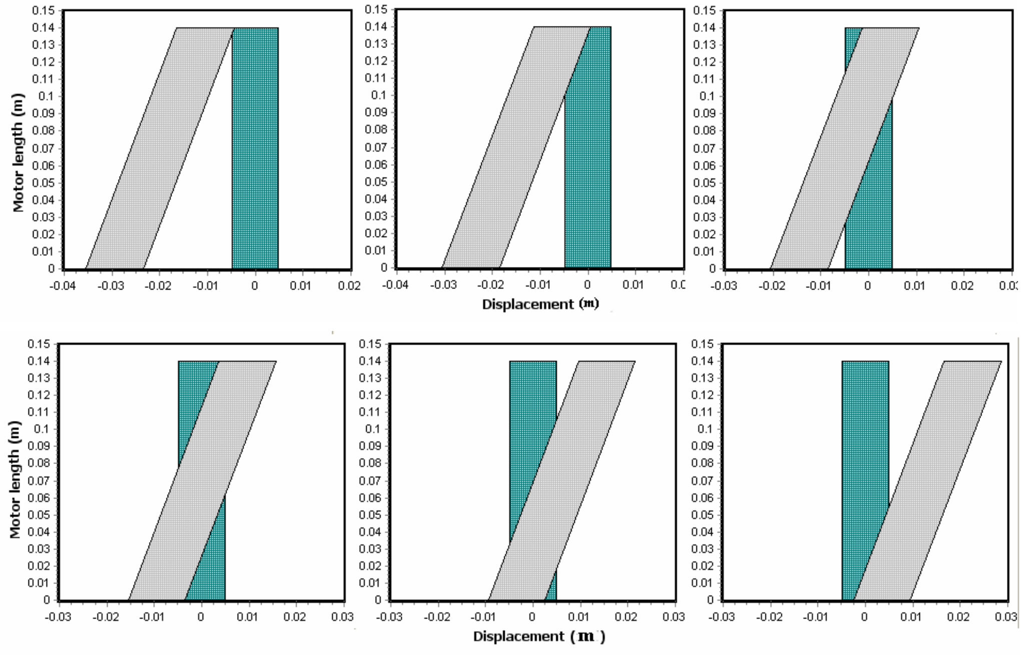

Figure 3.2.3 Different stator and rotor overlap conditions in a skewed rotor section

Figure 3.2.4 plots the effective air gap reluctance width between a pair of stator and rotor teeth plotted with respect to their relative position. It can be seen from these curves that, the more the displacement (relative position between a pair of stator and rotor teeth), the less the width of the air gap reluctance connecting this pair of teeth. There are five curves in figure 3.2.4, each of them has a skewed rotor with different rotor skew angles, from 0.01 mechanical degree to 15 degree.

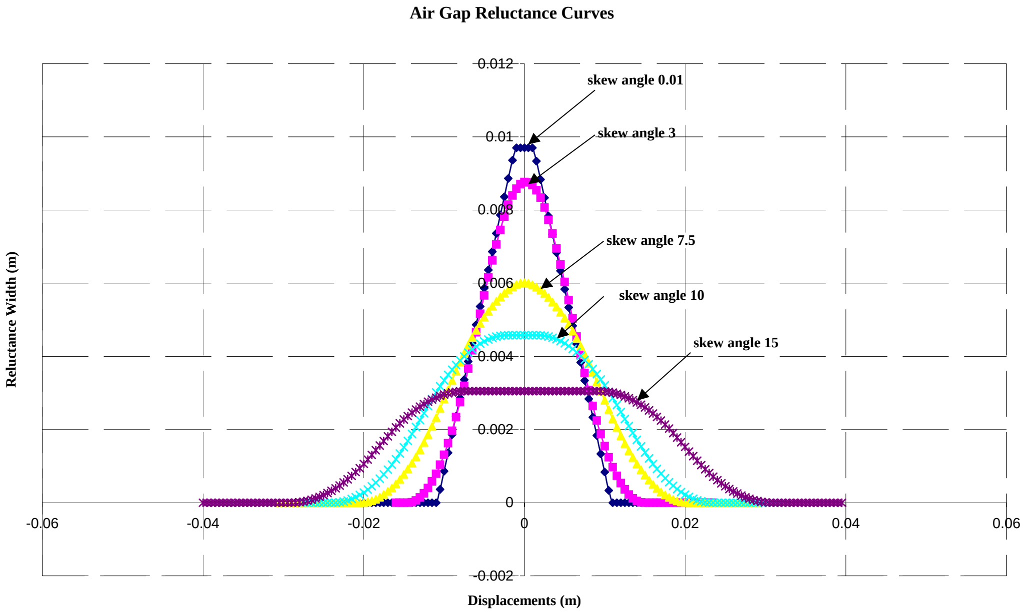

Figure 3.2.4 Air Gap reluctance effective width curves for a specific type of induction machine with different skew angles with method 1

In figure 3.2.4, it can be seen that for large skew angles, the curves tend to be flat and broad, but the maximum value is less. This is because with increasing skew angle, the flux coupling between one skewed rotor tooth with the stator teeth tends to be spread wider around the air gap circumference and thus the peak value of this flux coupling is weaker. This also explains the aim of machine designers use of a skewed rotor in induction machine designs, a properly skewed rotor should reduce cogging effects caused by the very strong flux coupling between rotor and stator teeth, as can be seen from the curve named 'skew angle 0.01' in figure 3.2.4. The shape of that curve is narrow and its magnitude is relatively high compared to the others. Thus with the skew angle to be 0.01 degrees, the flux coupling between stator and rotor teeth will also be narrow and strong which will cause cogging in induction machines.

Displacement in figure 3.2.4 means the distance (in meters) between the stator and rotor teeth centre for each teeth pair.

Method 1 is a fast and effective way of modelling the flux coupling between stator and rotor teeth in induction machines and can handle the skewed rotor, as has been validated in chapter 2. However, it is still a coarse way of modelling the air gap reluctances as it neglects the effect of fringing flux between the stator and rotor teeth. Indeed, the precise flux pattern between stator and rotor depends upon the saturation condition of the iron tooth tip which changes with the magnetic field intensity in the iron.

3.2.2 Method 2

To account for fringing effects between the stator and rotor teeth in the air gap region some empirical methods have been introduced. Dr. F. W. Carter analytically evaluated the magnitude of the fringing fluxes in open slot stator and rotor teeth [28] by solving Laplace's equation governing the flux distribution in the air, and in that region. The gap permeance (the reciprocal of reluctance) can be solved using his analytical results [28] and is less than the value obtained if the slot opening is ignored (b), but greater than if the slot opening is assumed to be a magnetic insulator (c), as shown in figure 3.2.5.

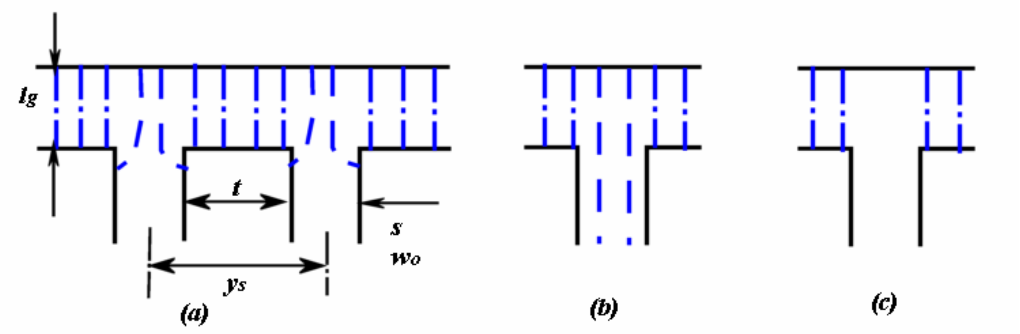

Figure 3.2.5 Air gap surface opening

Dr. Carter's approach deals with slot fringing effects by using either an effective length or an effective width for the air gap. Compared to neglecting the fringing (c), the effective air gap width would be wider or the effective length would be shorter when considering fringing effects. Given the ratio of slot opening to air gap length $\frac{s}{l_g}$, Carter's factor for the effective air gap length can be derived according the Carter's coefficient curve [25][28].

Carter's factor K_g :

The effective length of the air gap is described by:

$$l'_g = K_g l_g . \tag{3.2.1}$$

here Carter's factor is defined as:

$$K_g = \frac{y_s}{y_s - k_o \cdot w_o} \tag{3.2.2}$$

l'_g is the extended (effective) air gap length, l_g is the air gap length, y_s is the slot pitch, w_o is the slot opening, k_o is Carter's factor which depends upon the ratio of slot opening to air gap length and is obtained from Carter's curves. The effective air gap tooth width modified by Carter's factor can be derived if the reluctance remains the same, instead of using the effective length of air gap. The effective tooth width w_e according Carter's evaluation is:

$$w_e = y_s - k_o w_o \tag{3.2.3}$$

The extended air gap length or width formulae given in the previous statement only hold when one side, either the stator or the rotor is, slotted. If there are slot openings on both sides of the air gap, then the effective air gap length or effective width is the product of the air gap length and the product of the two fringing factors or Carter factors.

$$K_g = K_{g1} \cdot K_{g2} = \frac{y_{s1}}{y_{s1} - k_{o1} \cdot w_{o1}} \cdot \frac{y_{s2}}{y_{s2} - k_{o2} \cdot w_{o2}} \tag{3.2.4}$$

Where y_{s1}, y_{s2} are the stator and rotor slot pitches respectively, w_{o1}, w_{o2} are the stator and rotor slot openings and k_{o1}, k_{o2} are the Carter coefficients which depend on the ratio of the slot opening to the air gap length and are determined from Carter’s lookup curve. However, in this case for doubly slotted surfaces all that are required is to evaluate the effective tooth width of the stator and rotor independently.

It can be seen that the two sets of formulae that take slot fringing effects into consideration actually have the same form; the effective air gap length multiplied by a coefficient which represents the flux passing ratio between the stator and rotor teeth with respect to the full slot pitch area. The derivation of this coefficient has been based on rigorous field calculations. Thus, by using the fringing coefficient or Carter’s factor, fringing fluxes can be taken into account and this is called Method 2 to model the air gap reluctance and consequently the machine’s dynamic response can be modelled more accurately. Unfortunately, in its present form it cannot model the air gap reluctances whilst fully taking into account any tooth tip saturation effects.

3.2.3 Method 3

In order to take skewed rotors into account, as well as the fringing effects between the stator and rotor teeth which behave differently for different saturation levels, and also for coding convenience, air gap reluctance curves derived from accurate finite element analysis are applied in different small axial sections of the machine.

Application of FE analysis to the air gap region in induction machines permits detailed flux distribution patterns to be derived, as shown in figure 3.2.6. A variety of information is available from this comprehensive and detailed analysis. However, here only the flux distribution in the air gap region is of interest. When considering the fringing effects caused by slotting of the stator and rotor, only the amount of flux leaving or entering the rotor and stator teeth surfaces are of interest, in order to represent the fringing effect in terms of an effective air gap reluctance width. The effective air gap width modelling method that is obtained by interpolating curves calculated from FEM analysis is called method 3 in this thesis.

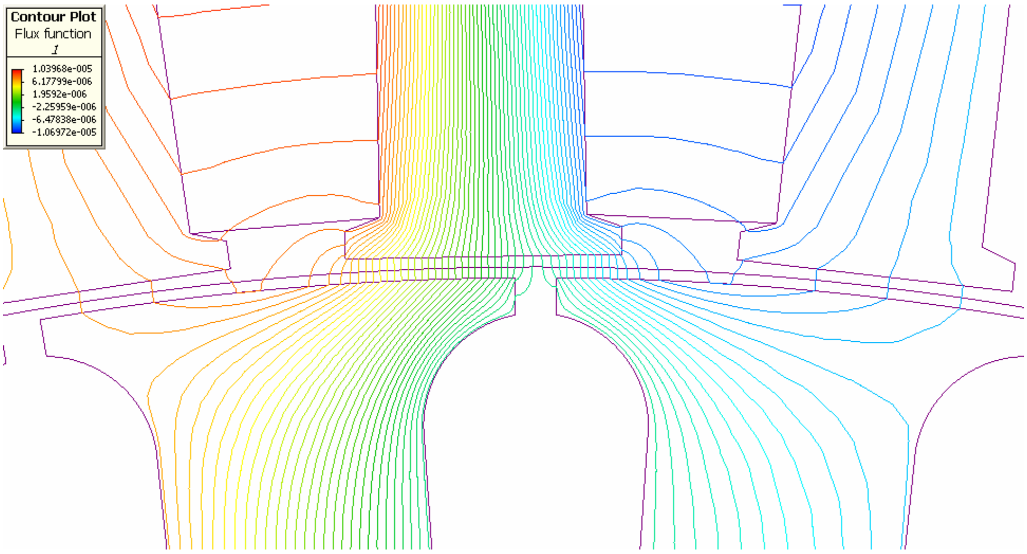

Figure 3.2.6 Overlap curves model for induction machine for method 3

If a single excitation coil carrying a unity current is set on one of the stator teeth, as shown in figure 3.2.6, then the flux pattern for this specific air gap geometry can be found by FEM analysis. It shows that, as expected, the majority of the flux crosses the air gap region to the rotor tooth directly, but that there is some flux leakage to the adjacent stator teeth. In method 3, the effective width of air gap reluctances are calculated by deriving the amount of flux entering the rotor surface, as shown in equation 3.2.6.

Assuming the iron permeability is sufficiently large so that the mmf drop in the iron can be neglected, the mmf drop only occurs across the air. From an engineering point of view if the winding current is small (unity current) and the iron is not saturated, leakage flux to other stator teeth can be neglected as well, then according to Ohm’s law in a magnetic circuit:

$$mmf = \phi_{rotor} \cdot \Re_{airgap} \qquad (3.2.5)$$

where the air gap reluctance is:

$$\Re_{airgap} = \frac{l_{airgap}}{\mu_0 w_{effectivearea} d} . \tag{3.2.6}$$

Using unity motor length in the FEM analysis, gives:

$$\frac{l_{airgap}}{\mu_0 * w_{effectivewidth} *1} = \frac{mmf}{\phi_{rotor}} \tag{3.2.7}$$

so that the effective air gap reluctance width is given by:

$$w_{effective\ width} = \frac{\phi_{rotor} \cdot l_{airgap}}{\mu_0 \cdot mmf} . \tag{3.2.8}$$

From equation 3.2.8, the effective width of the air gap reluctance for this specific rotor position and machine geometry can be determined, provided that the quantity of flux flowing into the rotor surface is known.

By rotating the rotor relative to the stator for a small angle, the air-gap effective width for a different rotor position can be identified from the FEM analysis. Repeating this process gives the air gap effective width curve with respect to the offset between the rotor and stator teeth, as shown in figure 3.2.7 for method 3. This curve can be used in the DRM simulations.

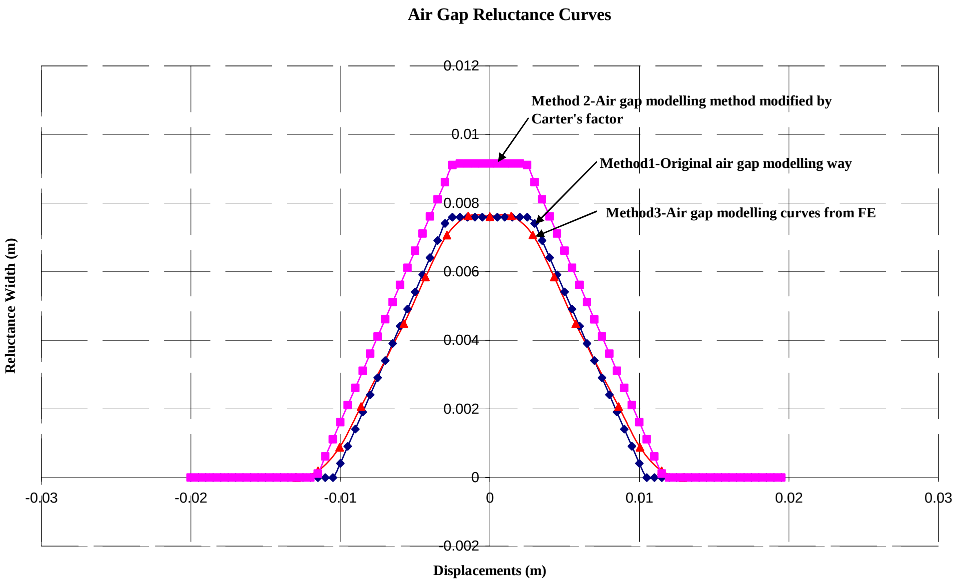

Figure 3.2.7 Air gap overlap curves for a specific geometry of induction machine with different methods

Figure 3.2.7 shows the air gap curve comparison for the air gap modelling methods, namely method 1, method 2 and method 3. It can be seen that when the displacement is big, i.e. when the tooth centres are not aligned, air gap reluctance effective width from method 3 is more than that of method 1 because of the fringing between the stator and rotor tooth pair. However, in the centre region of the air gap reluctance curve, air gap reluctance width from method 3 is slightly less than that of method 1. This is due to the leakage flux between the stator teeth, that some of the flux lines from the excited stator tooth come into the adjacent stator teeth. The curve for method 2 is wider and the magnitude is bigger than method 1 and method 3; and in the ‘tail’ of the curves, curve from method 2 comes closer to that of method 3, indicating a more accurate modelling of fringing effects. The magnitude of the curve from method 2 is bigger than the others, because the effective width of the stator and rotor teeth has been expanded by Carter’s factor thus widening the overlapping area for the tooth pair when they are aligned.

However, it is necessary to remember, when using this method, that unity excitation current in the stator coil is used to obtain the effective reluctances which neglects iron saturation and hence the flux pattern is only valid for non-saturated stators and rotors. Saturation will alter the flux distribution and hence the air gap reluctances curves.

As the focus will be on steady state analysis of induction machines, which do not heavily saturate under normal running conditions, the fact that this non-saturated air gap reluctance curve is used is acceptable. Even when the tooth tips are driven into saturation by the large slot leakage flux during the acceleration phase of a direct on line start simulation, results using this approach will show only a minor discrepancy between the DRM and FEM results. However, there will be a significant saving in time and computational effort thus increasing the computational efficiency.

For modelling skew, the DRM method described in chapter 2 cuts the rotor length into several skew sections, to account for the change in flux distribution along the axis. Rectangular and trapezoidal shape air gap overlap reluctances are used in a skewed rotor, as seen in figures 2.2.12 to 2.2.14, and the results shows that the trapezoidal shape air gap reluctances produces less torque ripple and requires fewer iterations of the solving process. The air gap reluctance curve in method 3 is obtained from FEM results of a non-skewed rotor machine. To extend this to a skewed rotor requires that additional techniques be employed.

As has been described in chapter 2 each of the sections has their own reluctance mesh and these reluctance meshes are only connected electrically through the winding coils. Now, each of these sections is further divided into subsections in order to obtain a more accurate value for the air gap reluctance effective width. The subsections that are used for calculating effective air gap width are shown in figure 3.2.8.

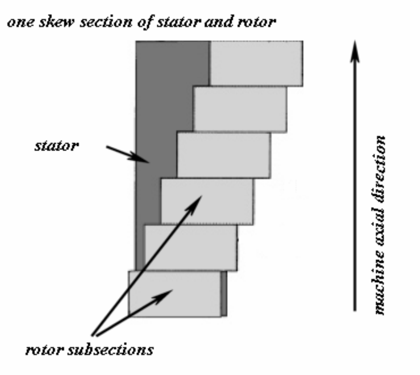

Figure 3.2.8 Sub skew sections for effective air gap reluctance calculation in a skewed rotor induction machine

The effective air gap reluctance width between each subsection of the rotor and stator is calculated from the effective air gap reluctance curve shown in figure 3.2.7 for this machine geometry, given the offset distance between the stator tooth centre and the subsection rotor centre. To identify the overall air gap effective width in this skew section, the average value of the effective widths in each subsection is calculated.

$$w_{effective} = \frac{1}{N}\sum_{i=1}^{N} w_i \tag{3.2.9}$$

where, N is the number of sub sections in one skew section, and w_i is the effective air gap reluctance width of the i^{th} sub section. Higher numbers of subsections provides more accurate skew simulations, noting that the number of subsections does not affect the simulation speed, since each subsection does not introduce additional reluctance meshes. Thus, the total number of reluctances is the same for the machine compared to the use of trapezoidal shape elements described in chapter 2. A comparison of the results of different skew modelling methods will be given later in this chapter.

Thus, method 3 accounts for both the tooth fringing effect and the skewed rotor, and an accurate dynamic induction machine model is now ready for use in analysis and design.

3.2.4 Comparison of the results for induction machines using Methods 1, 2&3 for modelling the air gap

Three methods for modelling the air gap reluctances in the Dynamic Reluctance Model of induction machines have been introduced and discussed. Method 1 correctly accounts for skew and method 2 for tooth fringing effects. Method 3 can account for both fringing effects and a skewed rotor at the same time. A comparison of results and discussion will be given in this section.

These simulations are based on a wound induction machine with 48/36 stator/rotor slots, rated power 15kW, rated voltage 415V and skewed one rotor bar. Machine specifications can be found in Appendix 1. The simulation scenario is a direct on line start. In order to see the difference between these methods in coping with skewed rotors, results are given for 1 and 3 skew sections in the DRM model. Comparison of these three methods with FEM analysis is also made to assess the ability to model the fringing effects.

1. Results with a skewed rotor induction machine

The speed versus time curve for an induction machine direct on line start is shown in figure 3.2.9.

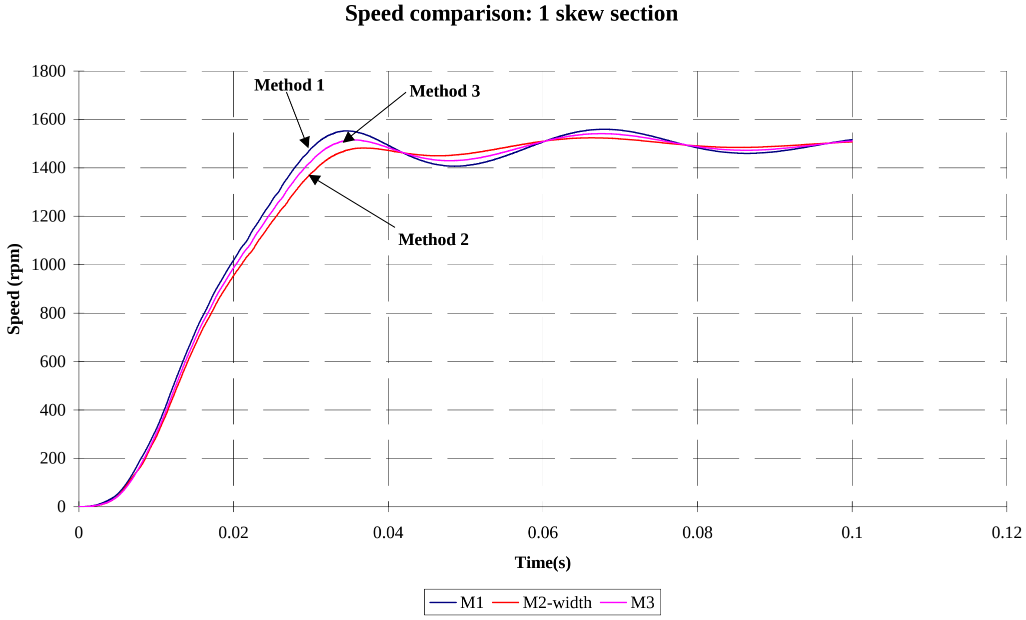

Figure 3.2.9 Comparison of speed curve for a skewed rotor induction machine, simulated with one skew section

The results show that with only one skew section, a difference is observed for the speed with the three different methods. Method 1 rises faster than method 3 and so does method 3 to method 2. It is the machine reactance that determines the induction machine's rotor acceleration, and the machine reactance is determined by the leakage reactance and air gap reluctance. In this simulation, all three methods use the same slot leakage flux model, and the only difference is the way they model the air gap reluctance, specifically the tooth fringing effects, which affect the flux passing between stator and rotor tooth surfaces. The one (method 3), which most correctly accounts for tooth fringing effects and leakage flux, rises slower than the one that neglects them (method 1). This is because method 1 underestimates the air gap leakage flux (Zig-Zag flux [28]). Results from method 2 rise slower than that from method 3 because method 2 overestimates air gap leakage flux, which slows down the building up of the flux field inside the machines thus reducing the torque and speed in the machine. Both method 2 and method 3 have taken fringing effects into account thus providing more accurate air gap modelling for the induction machine.

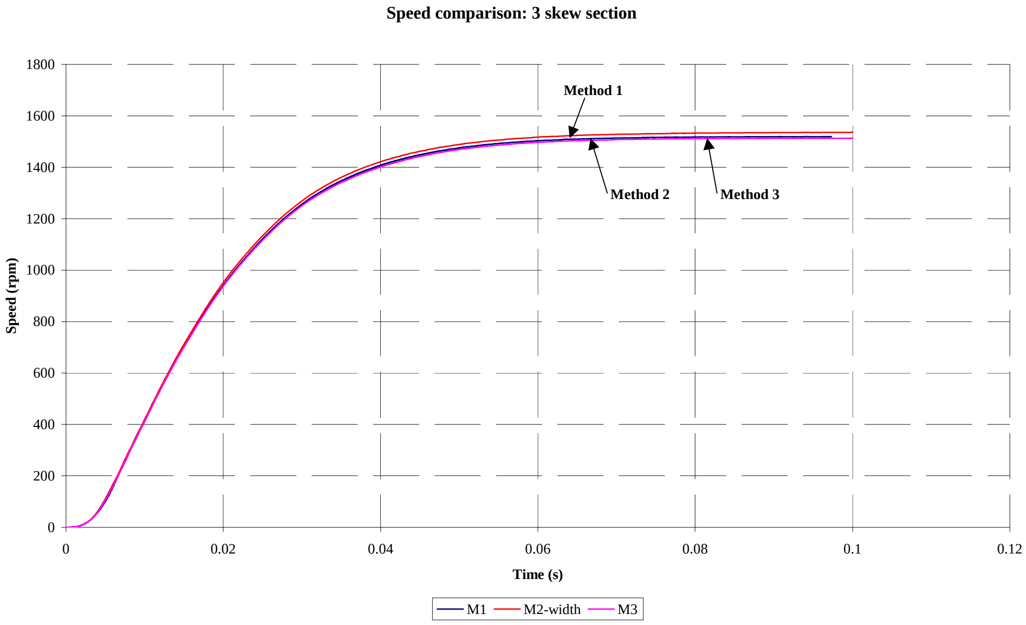

Figure 3.2.10 Comparison of speed curve for a skewed rotor, simulated with three skew section

Figure 3.2.10 show that with three skew sections, the three methods agree well. With the increase of the number of skew sections in the simulation, the difference between these three methods is further reduced. Essentially, all the curves are smoother because the cogging torque is greatly reduced.

2. Results with a non-skewed rotor induction machine

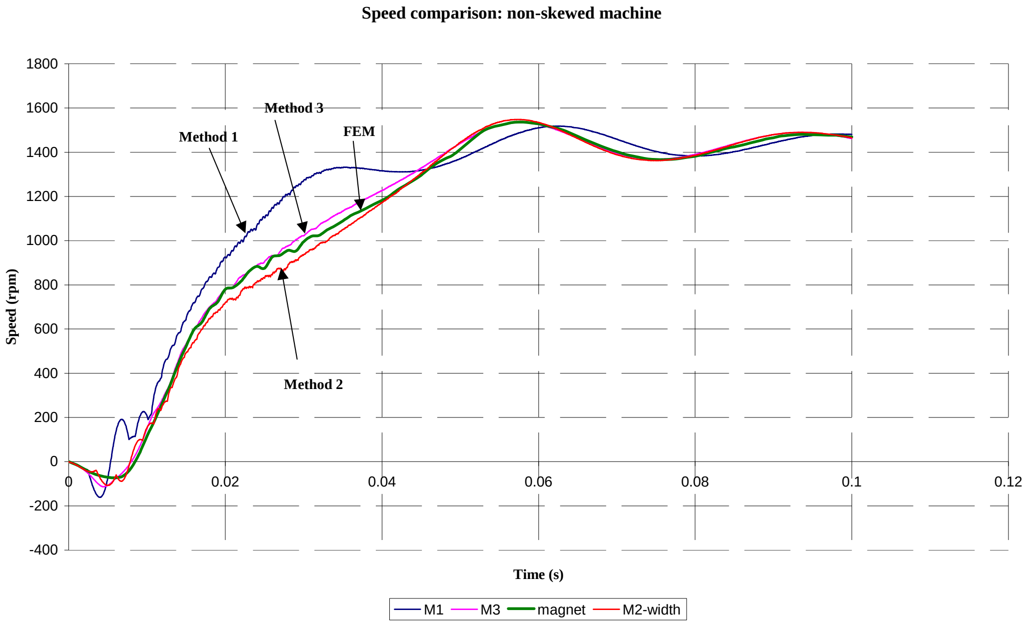

Figure 3.2.11 Speed curve comparison with a non-skewed rotor induction machine

Figure 3.2.11 shows that the speed curves from air gap modelling method 2 and 3 agree with the FEM (MagNet) results better than method 1. Because the flux connection modelled by method 2 and 3 come from rigid field calculations, thus tooth-fringing effects is accounted for more accurately than for method 1. Again, it can be seen that method 1 underestimates the air gap leakage flux between stator and rotor in this specific induction machine simulations, while method 2 overestimates the air gap leakage flux a little. Also, some cogging effects due to non-skewed rotor can also be observed in figure 3.2.11. Air gap modelling method 3 gives the most accurate result compared to FE simulation results.

3.3 Solving For Conservation of Flux

In the previous section the air gap reluctance modelling method in the DRM technique has been improved. Additional improvements to the nodal mmf formulation and equation solving will now be made.

This improvement is provoked by the fact that some flux offset is seen when calculating the flux linkage in the stator and rotor, as described in [29]. The reason for the flux offset is the accumulation of rounding errors when solving the equations that force the net rate of change of flux entering each node to be zero. Forcing of the net change in flux to be zero at each node does not necessarily mean that the net flux flowing into this node is zero as a small and pseudo-random node mmf offset produced by rounding errors might accumulate causing the flux offset seen in the solution.

To overcome this problem, the mmf node potential in the equation 2.3.1: is enforced

$$\sum_{j=0}^{n-1} \phi_j\left(f_{j2}, f_{j1}\right) = 0 \tag{3.3.1}$$

Changing form equations 2.3.1 to equation 3.3.1 does not alter the physical basis of the modelling process for electrical machines; it is just a numerical modification to the code which can reduce effect of the rounding on the results.

The equations that define the induction machine electro-magnetic system are now:

$$\mathbf{F}(\mathbf{x}) = \begin{bmatrix} \text{conservation of flux at node 0} \\ \vdots \\ \text{conservation of flux at node } \mathrm{N_{node}} - 1 \\ \text{electrical loop equations for cage rotor, loop 0} \\ \vdots \\ \text{electrical loop equations for cage rotor, loop } \mathrm{N_{bar}} - 1 \\ \text{electrical loop equations for stator phase A} \\ \text{electrical loop equations for stator phase B} \\ \text{electrical loop equations for stator phase C} \\ \text{speed equation 2.3.8} \\ \text{torque equation 2.3.9} \end{bmatrix} \tag{3.3.2}$$

3.4 Globally Convergent Non-linear Solver

3.4.1 Introduction

The Newton-Raphson (NR) iterations coupled with the Crank-Nicolson (CN) scheme solves the machine state well for both the linear and nonlinear iron machine models. If the nonlinearity is not too large, it is remembered that the system's current state is used as the basis for predicting the state in the next time step, which is used to seed the NR method. NR iterations repeat until the system simulation error is less than the acceptable tolerance, as described in chapter 2.

Unfortunately, the NR method has the disadvantage that it might proceed to a local minima if the initial guess is not close enough to the actual solution when solving nonlinear equations [23]. This phenomenon presents itself in the DRM solving process in that for certain time steps, nonconvergence occurs and repeatedly halving the time step eventually leads to program overflow. Figure 3.4.1 shows a DRM simulation scenario for a generator system, which includes the exciter, rotating rectifiers and main salient pole generator. It can be seen that whenever process could not converge at a certain time step the time step was halved and the whole system state is recovered to that at the previous time step. The left curve corresponding to the left vertical axis shows the reducing time step and even when reduced to a very small value after a number of restarts, the solution still could not be found.

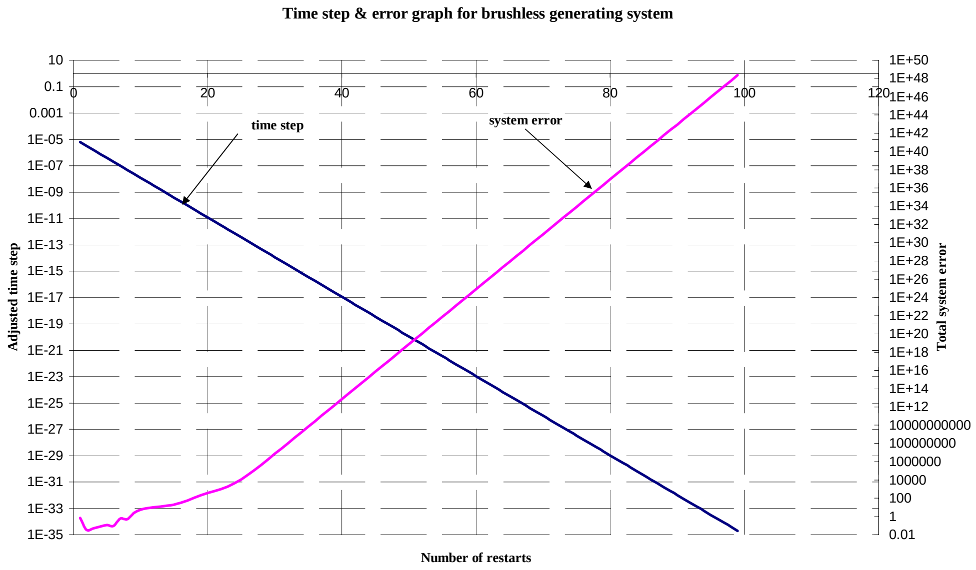

Figure 3.4.1 The adjusting of time step and the changing of system error with respect to the number of restart times in a synchronous machine generating system

The right hand side curve on figure 3.4.1 shows the system error with the reducing time step. It can be seen that the error becomes larger, which indicates that the prediction is too far from the system state solution. As the time step becomes very small numerical rounding dominates the Crank-Nicolson process and completely undermines the process. This phenomenon is caused by the significant nonlinearity in this system, in particular due to the nonlinear diode behaviour. Further detail about the system modelling and its simulation will be discussed in later chapters. With such a degree of nonlinearity, an initial prediction that is not close enough to the system solution will cause NR iterations to fail, as shown in figure 3.4.1.

To solve this, an algorithm that combines the rapid local convergence of Newton's method with a globally convergent strategy, which will guarantee some progress towards the solution at each iteration, is developed [23].

3.4.2 Globally convergent solver for nonlinear systems

As has been described in Chapter 2, the Newton-Raphson step for the set of nonlinear system equations

$$\mathbf{F}(\mathbf{x}) = 0 \tag{3.4.1}$$

is

$$\mathbf{x}_{new} = \mathbf{x}_{old} + \delta\mathbf{x} \tag{3.4.2}$$

where

$$\delta\mathbf{x} = -\mathbf{J}^{-1} \cdot \mathbf{F} \tag{3.4.3}$$

$\mathbf{J}$ is a Jacobian matrix, and $\mathbf{F}$ is the system equation values at a trial solution $\mathbf{x}_{old}$. The original Newton-Raphson scheme, as was described in chapter 2, accepts $\mathbf{x}_{new}$ without condition, as long as it is calculated from equation 3.4.2. However, in the case of system equations with significant nonlinearity, if the initial guess $\mathbf{x}_{old}$ is not close enough to the system solution, $\mathbf{x}_{new}$ will actually more further away from the system solution than $\mathbf{x}_{old}$, in this case the Newton-Raphson algorithm will never converge to the system solution, and this is a process that one could not control.

If a criterion is used to decide whether to accept the $\mathbf{x}_{new}$ or not, the situation improves. Unacceptable $\mathbf{x}_{new}$, i.e. $\mathbf{x}_{new}$ that are further from the solution than $\mathbf{x}_{old}$, can be rejected so that the Newton-Raphson process is more controlled to make it a globally convergent algorithm.

But, how does one decide whether to accept the Newton step $\delta\mathbf{x}$? A reasonable strategy is to require that the step decreases $|\mathbf{F}|^2 = \mathbf{F} \cdot \mathbf{F}$, which is the same requirement that would be imposed if one were trying to minimise

$$f = 0.5\mathbf{F} \cdot \mathbf{F} \tag{3.4.4}$$

(0.5 is for later convenience) Every solution to equation 3.4.1 minimises the function f in 3.4.4, but f may also possess local minima that are not solutions of equation 3.4.1. Thus, simply applying minimum searching algorithms is not a robust approach.

To develop a better strategy, note that the Newton step is a descent direction for f:

$$\nabla f \cdot \delta\mathbf{x} = (\mathbf{F} \cdot \mathbf{J}) \cdot (-\mathbf{J}^{-1} \cdot \mathbf{F}) = -\mathbf{F} \cdot \mathbf{F} < 0 \tag{3.4.5}$$

Thus the strategy is quite simple: the full Newton step will be tried first, because once the guess is sufficiently close to the solution quadratic convergence will be achieved. However, checking the proposed step reduces f is performed at each iteration. If not, a backtrack along the Newton direction is undertaken until an acceptable step is found. Because the Newton step is a descent direction for f, it is guaranteed to find an acceptable step by backtracking. This method can still occasionally fail by landing on a local minimum of f, but this is quite rare in practice [23]. The backtrack searching scheme will be introduced in the following section.

3.4.3 Line search algorithm for globally convergent solving scheme

The line search (backtracking search) algorithm is to search for the proper Newton-Raphson step that reduces the system error in function 3.4.4 sufficiently along the Newton direction.

When the initial guess is close enough to the minimum of f, taking the full Newton step would help one to find the system solution with quadratic convergence. When it is not close enough to the minimum of f, the move might be too far for the full Newton step $\mathbf{p} = \delta\mathbf{x}$ to decrease the function as the quadratic approximation is not valid here. So the goal is to move to a new point $\mathbf{x}_{new}$ along the direction of the Newton step $\mathbf{p}$, but not necessarily all the way:

$$\mathbf{x}_{new} = \mathbf{x}_{old} + \lambda \mathbf{p} \tag{3.4.6}$$

where,

$$0 < \lambda < 1 \quad . \tag{3.2.7}$$

The aim is to find λ so that $f(\mathbf{x}_{old} + \lambda \mathbf{p})$ has decreased sufficiently. If $f(\mathbf{x}_{new})$ does not meet our acceptance criteria, we backtrack along the Newton direction, trying a smaller value of λ, until a suitable point is found. Since the Newton direction is a descent direction, it is guaranteed to decrease f for sufficiently small λ.

But, how is it possible to tell if $f(\mathbf{x}_{old} + \lambda \mathbf{p})$ has decreased sufficiently? The suggested criteria for accepting a step, by W. H. Press [23], to require that the average rate of decrease of f is at least some fraction α of the initial rate of decrease $\nabla f \cdot \mathbf{p}$:

$$f(\mathbf{x}_{new}) \le f(\mathbf{x}_{old}) + \alpha \nabla f \cdot (\mathbf{x}_{new} - \mathbf{x}_{old}) \tag{3.2.8}$$

Here the parameter α satisfies $0 < \alpha < 1$. Then, the λ value in each iteration needs to be found.

A strategy for a practical backtracking routine is as follows:

Define:

$$g(\lambda) \equiv f(\mathbf{x}_{old} + \lambda \mathbf{p}) \tag{3.2.9}$$

such that:

$$g'(\lambda) = \nabla f \cdot \mathbf{p} \tag{3.2.10}$$

Here, the algorithm begins with a step multiplier of 1 (full Newton step) and then backtracks until an acceptable reduction in the performance is obtained. On the first step the value of performance at the current point $g(0)$ is used, and a step multiplier value of $g(1)$. Use of the value of the derivative of the performance at the current point $g'(0)$ is also made to obtain a quadratic approximation to the performance function along the search direction, hence $g(\lambda)$ can be modelled as a quadratic:

$$g(\lambda) \approx [g(1) - g(0) - g'(0)]\lambda^2 + g'(0)\lambda + g(0)\,, \tag{3.2.11}$$

then the minimum of the quadratic is found as:

$$\lambda = -\frac{g'(0)}{2[g(1) - g(0) - g'(0)]}\ . \tag{3.2.12}$$

This minimum of the quadratic approximation becomes a trial point for where the function $f(\mathbf{x}_{old} + \lambda\mathbf{p})$ has its minimum value, and the performance at this point is tested. If f_{new} is not sufficiently reduced, on the second and subsequent backtracks, a cubic model of $g(\lambda)$ is obtained and the minimum of the cubic interpolation becomes the new trial point. The cubic model of $g(\lambda)$ is:

$$g(\lambda) = a\lambda^3 + b\lambda^2 + g'(0)\lambda + g(0) \tag{3.2.13}$$

where,

$$\begin{bmatrix} a \\ b \end{bmatrix} = \frac{1}{\lambda_1 - \lambda_2}\begin{bmatrix} \frac{1}{\lambda^2{}_1} & -\frac{1}{\lambda^2{}_2} \\ -\frac{\lambda_2}{\lambda^2{}_1} & \frac{\lambda_1}{\lambda^2{}_2} \end{bmatrix} \cdot \begin{bmatrix} g(\lambda_1) - g'(0)\lambda_1 - g(0) \\ g(\lambda_2) - g'(0)\lambda_2 - g(0) \end{bmatrix} \tag{3.2.14}$$

The minimum of this cubic occurs at:

$$\lambda = \frac{-b + \sqrt{b^2 - 3ag'(0)}}{3a} \tag{3.2.15}$$

This process is continued until sufficient reduction in the performance error is obtained. The line search algorithm flow chart is shown in figure 3.4.2.

Figure 3.4.2 shows the flow chart of the line search scheme, which is entered after the BiCGSTAB solver solves for the full Newton step. As described above the aim of this line search function is to find a proper step that minimises the error function f. The slope is calculated after the full Newton step is made and then a scheme for detecting small changes is applied to avoid too close a distance between $\mathbf{x}_{new}$ and $\mathbf{x}_{old}$. Subsequently, parameter λ is set to be 1 (a full Newton step) when the algorithm starts and the error function value f at that time is evaluated. If it is decreased sufficiently, as defined by equation 3.2.8, the line search ends; if not, the line search function will model the function $g(\lambda)$ by a quadratic in the first searching step, as described in equation 3.2.11; and by a cubic in the subsequent backtracks, as described in equation 3.2.13. The λ value when this minima of $g(\lambda)$ occurring is derived from the cubic and quadratic models. The error function value is evaluated again to see if it is decreased sufficiently. This line search iteration process will continue until sufficient decrease in the error function f is achieved.

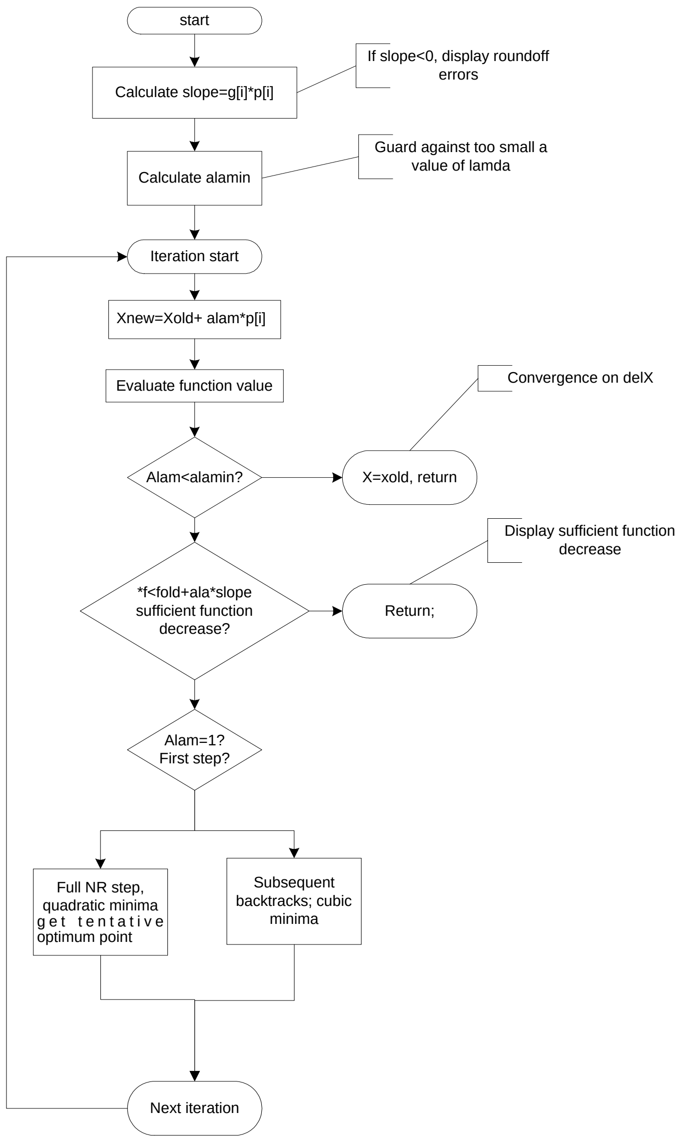

Figure 3.4.2 Flow chart of line search backtrack algorithm

3.4.4 Global convergent technique flow chart

After modification with the line search backtracking algorithm, the Newton-Raphson method provides a nonlinear multi-dimensional solving technique with global convergence. Figure 3.4.3 shows the core routine of this global convergent solver, the pre- and post-processor are the same as described previously at chapter 2.

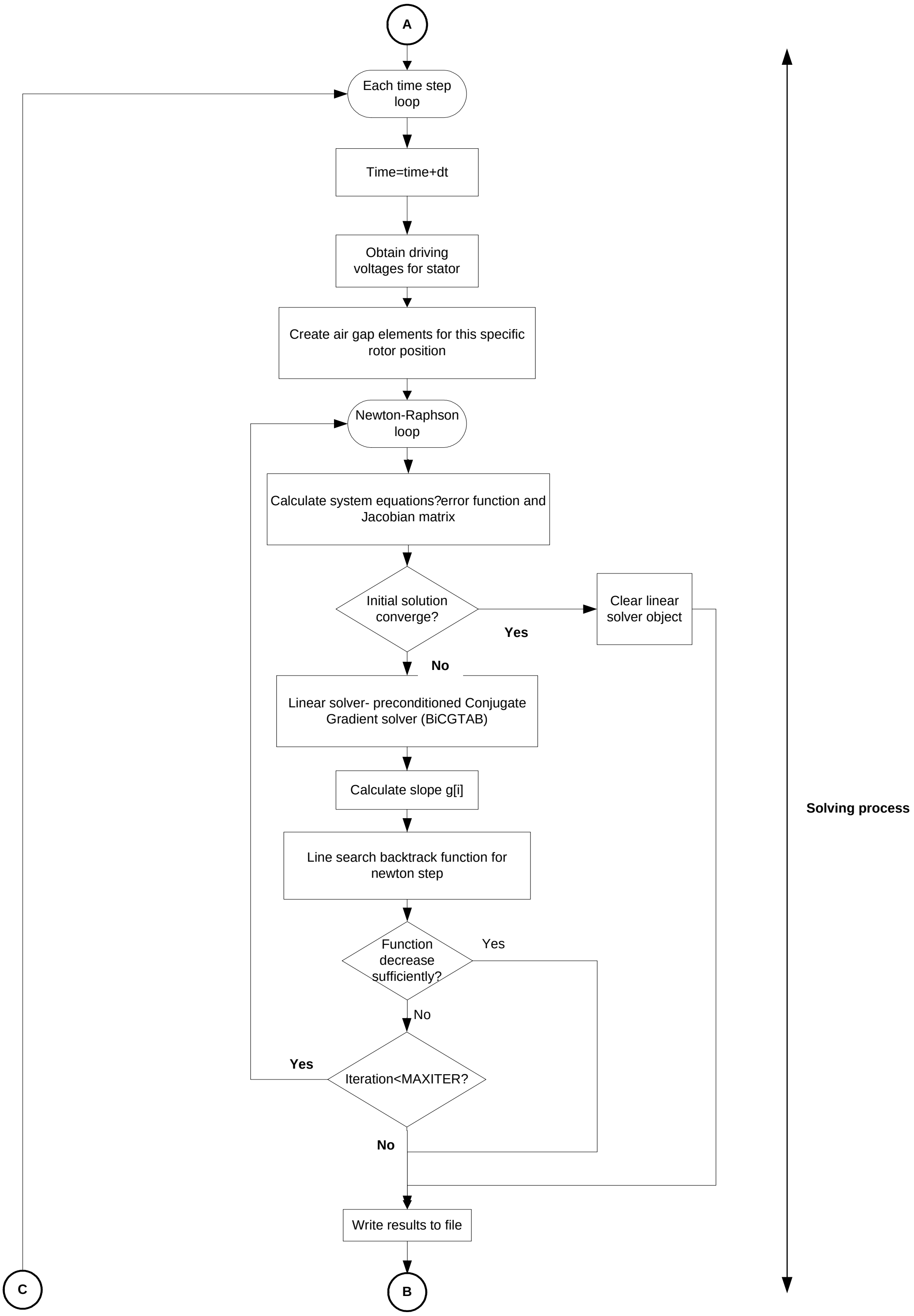

Figure 3.4.3 Solving process of a globally convergent Newton-Raphson solver

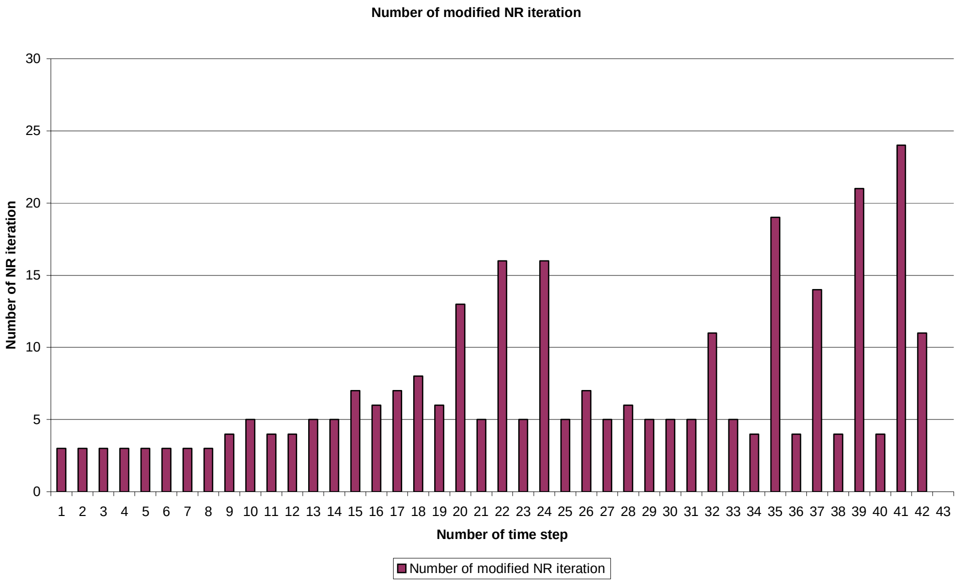

Figure 3.4.4 Number of NR iteration for globally convergent nonlinear solver vs. time step

Figure 3.4.4 shows how a system with significant nonlinearity (rectifier), is solved with the modified globally convergent NR solver. It solves the same systems as the original NR solver with which nonconvergence happens, as shown in figure 3.4.1. These two simulations use the same simulation parameters, i.e. time step, threshold and tolerance etc. and it can be seen that this nonlinear system is solved properly with the new NR solver.

The core solving technique has been modified to use an algorithm which can deal with nonlinear, sparse, first order differential equations and is globally convergent. The DRM now provides a powerful tool for systems with significant nonlinearities and other complexities, such as control loops. This solver will be utilised throughout the simulations in this thesis.

3.5 Detailed Slot Leakage Model for Induction Machine

In section 2.2.2, a typical induction machine reluctance mesh is given for the stator and rotor, including for the air gap region. It is quite a coarse mesh, and becomes inadequate when one wants to accurately assess a machine’s transient behaviour, such as the direct on line start of an induction machine.

In starting conditions, the winding currents in an induction machine are large and thus leakage fluxes between the stator and rotor slots are large as well. The leakage and working fluxes in machines are defined by Steven [30]:

‘The total flux in a machine has components, viz:

(a) Working flux, which links both the stator and rotor windings;

(b) Leakage flux, which links one winding only and generally, gives rise in an equivalent circuit interpretation to a component leakage reactance. The leakage inductance is an important parameter in calculations concerned with analysis of a.c. machines. In d.c. machines, it is of importance in relation to commutation, and in field estimation.’

These leakage fluxes play an important part in machine transients. In order to model the induction machine more accurately, as well as to improve the accuracy of other machine transient models, such as the short circuit condition in generators, reluctances that represent leakage fluxes have to be added to the dynamic reluctance mesh model. Only slot leakage inductances in electrical machines are considered here, although end winding leakage inductance could also be added as lumped inductors in the stator and rotor electrical circuit.

In the typical reluctance mesh model for an induction machine given in chapter 2, shown in figure 2.2.6, there is reluctance across the air gap region representing the slot leakage flux. However, there is also leakage flux existing in the space occupied by the winding, as shown in figure 3.5.1 named the winding region. To model the induction machine behaviour accurately, the slot leakage reluctance representing the winding region leakage flux has to be added into the induction machine reluctance mesh. This section will discuss how this reluctance is calculated.

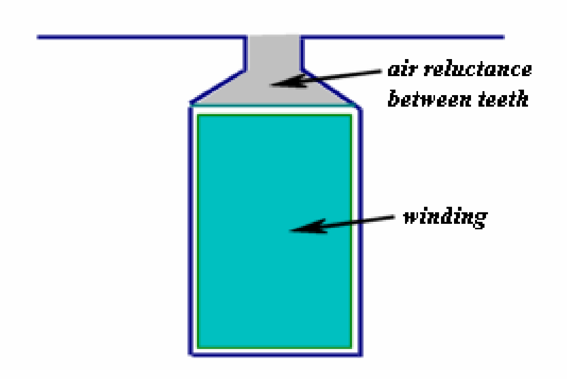

Figure 3.5.1 Air gap reluctances between stator and rotor teeth

When the windings carry current, they set up a slot-leakage flux pattern with a complex shape [28], as shown in figure 3.5.2. If there is a relative large space below the bottom conductor and its width is substantially less than that of the slot, then the field pattern is that shown in (a).

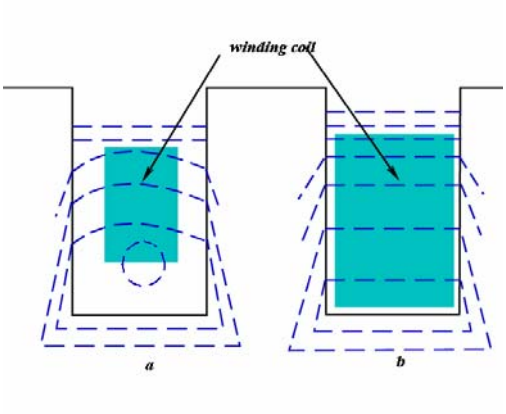

Figure 3.5.2 Slot leakage flux pattern in parallel slots, accommodating one rectangular conductor

However, the proportions are more usually those of (b), in which the field pattern is very nearly in the form of straight lines across the slot. This pattern is readily analysed, and is adequate for steady currents or those of low frequency, but fails (unless the conductors are subdivided and transposed) for frequencies approaching normal industrial supply values. The straight-line model is adopted here as it is sufficient for our industrial purposes.

For different slot shapes, different ways of calculating the leakage reluctances are adopted. Two commonly used induction machine slot shapes will be discussed in the following section.

3.5.1 Semi-closed rectangular slot

This semi-closed rectangular slot shape is usually used for induction machine stators. Considering the dimensions in figure 3.5.3, the permeance coefficient per unit axial length is the ratio (area/length) of the air path considered. The air gap regions above the conductors are $\frac{h_3}{w_0}$ for the lip and $\frac{2h_2}{w_s + w_0}$ for the wedge portion immediately above the conductor.

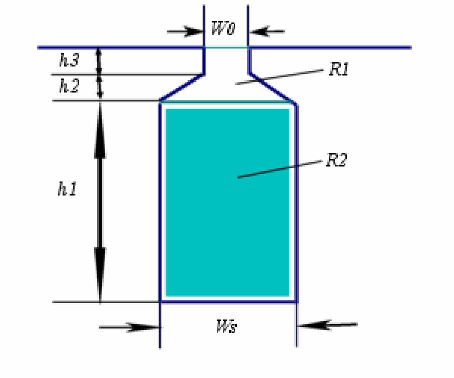

Figure 3.5.3 Semi-closed slot profiles

The slot region occupied by the conductor has to be treated differently. All the leakage flux above the conductor links the conduction wholly, but the flux at a height x, shown in figure 3.5.4, only links the lower part of the conductor and contributes only partial linkage. Thus, such flux has a lower density as only the fraction $(\frac{x}{h_1})$ conductor, uniformly distributed, and is linked by the point where is considered, as shown by x in figure 3.5.4.

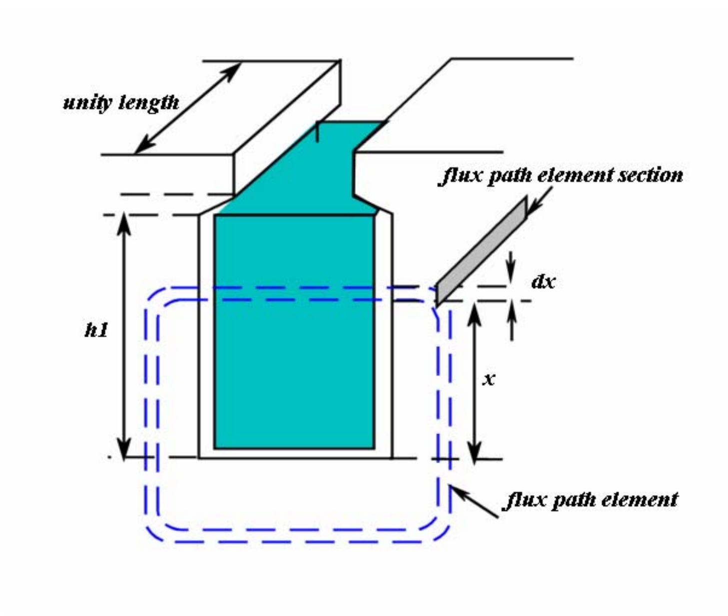

Figure 3.5.4 Schematic plot of slot leakage reluctance calculation

Consider the flux path loop shown in figure 3.5.4 whose top is x above the bottom of the conductor, the mmf enclosed is:

$$mmf = \frac{x}{h_1}(Ni) \tag{3.5.1}$$

so that the flux in the elemental path dx is:

$$d\phi = \frac{mmf}{\Re_x} = \frac{mmf}{\dfrac{w_s}{\mu_0 \cdot dx \cdot 1}} = \mu_0 \frac{(Ni)}{w_s} \cdot \left(\frac{x}{h_1}\right) \cdot dx \tag{3.5.2}$$

which links the proportion $\frac{x}{h_1}$ of the conductor. Therefore, the flux linking this part of elemental dx is:

$$d\lambda_s = \left[N\left(\frac{x}{h_1}\right)\right] \cdot \mu_0 \frac{Ni}{w_s}\left(\frac{x}{h_1}\right) \cdot dx \tag{3.5.3}$$

and hence the total coil-side flux linkage is:

$$\lambda_c = \int_0^{h_1} \mu_0 \frac{N^2 i}{w_s}\left(\frac{1}{h^2{}_1}\right) x^2 \cdot dx = \mu_0 N^2 i \frac{h_1}{3w_s} \tag{3.5.4}$$

from which the reluctances of the air gap reluctances representing leakage flux are derived as:

$$\Re_c = \frac{mmf}{\phi} = \frac{mmf \cdot N}{\lambda_c} = \frac{N^2 i}{\lambda_c} = \frac{w_s}{\mu_0 \left(\frac{h_1}{3} \right)} \quad . \tag{3.5.5}$$

It can be seen that by considering slot leakage flux, the width of the slot leakage reluctance is actually one third of the slot depth. This leakage reluctance can be used in the DRM to account for slot leakage fluxes in semi-closed shape induction machine modelling.

Instead of using one discrete reluctance element representing the slot leakage effects between stator and rotor slots in induction machines, two reluctances can also be used, in a more complicated reluctance mesh. Further discussion regarding the reluctance mesh topology will be presented in chapter 7.

3.5.2 Round slots

Round slot shapes are usually used in cage rotor induction machines. The cage bars on the rotor are round bars, deep bars, or double bars. The machine under investigation for time being has round slots as shown in figure 3.5.5.

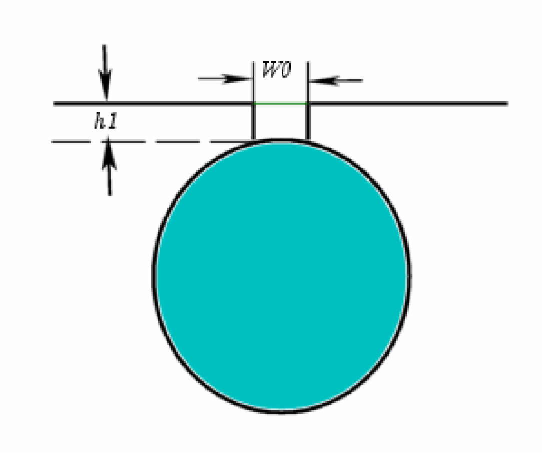

Figure 3.5.5 Round slot profiles

Assume that the flux crosses the slot in straight lines; the slot leakage reluctance for this type of slot is independent of the slot diameter. An empirical formula suggested for the leakage reluctance is [28]:

$$\Re_c = \frac{w_0}{\mu_0\left(0.66w_0 + h_1\right)} \tag{3.5.3}$$

i.e., the width of the slot reluctance reduced by $\left(0.66w_0 + h_1\right)$. Neglecting the slot opening the equivalent reluctance $\Re_c$ is:

$$\Re_c = \frac{1}{\mu_0\left(0.66\right)} \quad . \tag{3.5.4}$$

Employing the slot leakage reluctances to both the stator and rotor sides in the dynamic reluctance mesh method as shown in figure 3.5.6, provides a more accurate reluctance mesh for induction machines.

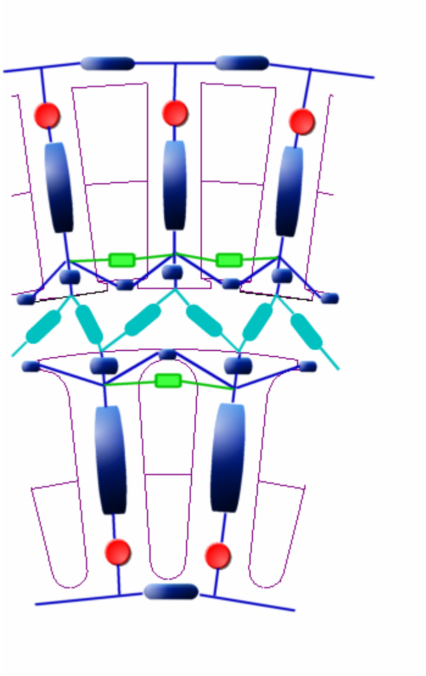

Figure 3.5.6 Modified dynamic reluctance mesh for induction machine which accounts for slot leakage flux

It is observed that the reluctances in light colour between the stator slots and rotor slots represent the slot leakage flux calculated from the previous method. With the modification of these reluctances to the reluctance mesh of induction machines, the simulation of the direct on line start of an non-skewed rotor induction machine becomes even closer to the FEM results, as shown in figure 3.5.7.

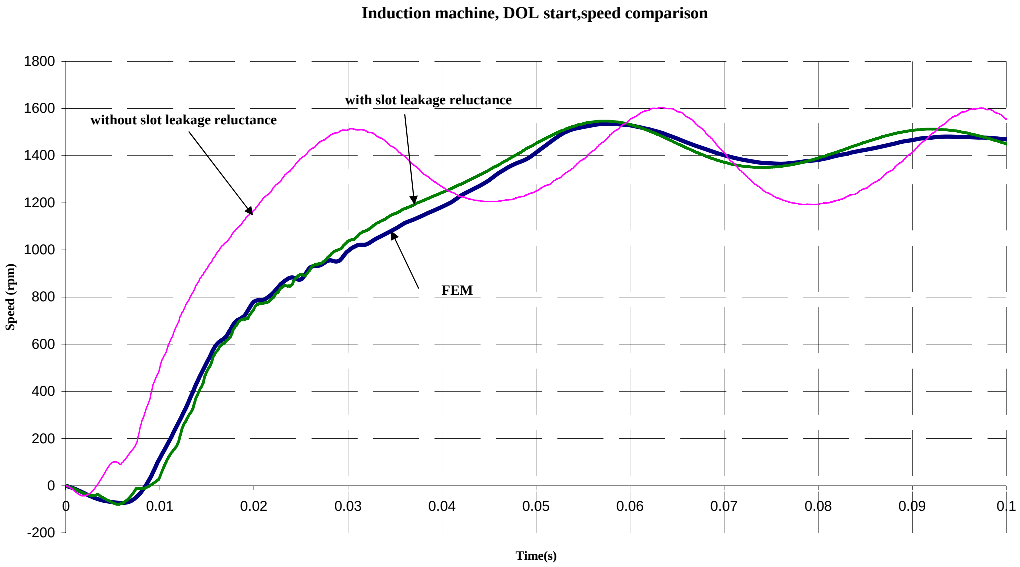

Figure 3.5.7 Induction machine direct on line start speed curve, with and without slot leakage reluctance modelled, in comparison to FEM results

3.6 Conclusion

This chapter describes the notable improvements made to the original Dynamic Reluctance Mesh modelling software, which makes the DRM simulations more accurate and stable.

First, modifications of the air gap reluctance models are introduced and results are given in comparison with FEM results which show the improvement in modelling of induction machines.

Modifications were also made for solving the system state equations. Solving for the conservation of flux in each node is applied rather than solving for the rate of change of flux, in order to eliminate the residual flux caused by computational round off errors.

In order to overcome the nonconverge problems, which happen when solving systems with significant nonlinearity, a modified globally convergent

Newton-Raphson nonlinear solver is applied, which incorporates line searching schemes to identify a proper Newton step.

Also, simulating an induction machine direct online start, the modelling of slot leakage inductance is known to be important. The reluctances that represent the leakage flux between the stator and rotor slots have been added to the reluctance mesh for induction machines previously described in chapter 2. The results show that these slot leakage reluctances improve transient performance modelling in comparison with FEM results.

With all these modifications and improvements made to the DRM simulations, other machines with more complicated geometries can be modelled. These include salient pole synchronous machines with nonlinear circuit components. Complex control schemes can also be incorporated in the simulation.

CHAPTER 4 MODELLING AND SIMULATING SALIENT POLE SYNCHRONOUS GENERATORS

4.1 Introduction

Three phase synchronous generators are the primary source of all the electric energy we consume today. Some of these machines are the largest energy converters in the world with ratings of up to 1500 MW. There are relatively small numbers of very large generators which include turbo-generators, driven by steam turbines and hydro generators, driven by water turbines. The majority of industrial generators have ratings up to 1000 kVA, and are driven by gas turbines and diesel engines. They are used for small power systems e.g. oil platforms, ships and remote industrial sites as well as for combined heat and power and standby cases, for such as transportation systems or hospital backup power supplies.

Turbo-generators usually have a forged, cylindrical rotor to reduce the effect of centrifugal force on the rotor structure due to their low pole number and high rotational speed together with their relatively large diameter resulting from the high power rating. Large gas turbine generators also follow this basic design form. However, for the relatively low speed, or low power prime movers, rotor specifications usually define a salient-pole structure. This covers hydro generators and small rating industrial generators driven by diesel engines.

After a long period of stability of the development in electrical power systems in the UK, there has recently been increasing development resulting in greater complexity and increasing scale of the power system. Local generation in the UK means that it becomes more and more important to simulate power system behaviour under different circumstances, such as fault conditions, in order to make the whole power system more efficient and stable and to develop correct protection strategies. Among the simulation models required of the power system components, one key model is the electric generator. From a power system standpoint, this may not need to be too complex. However, the generator manufacturer's standpoint is different.

Small power systems are increasingly common and pose problems in terms of reliable operation. The ability to clear faults effectively without the generator voltage sagging to the point where discrimination is compromised is a key requirement. Additionally, it is not uncommon for small systems to have large, key pieces of motor driven plant which must be able to be started even when not all of the paralleled generators are available. Such cases impose high transient load currents though the power required will be within the generator's capacity. These systems need to be modelled carefully from the generator manufacturer's point of view to ensure high customer satisfaction.

Thus, for both large, complex and for small power systems the generator manufacturer requires a detailed model of his product which can facilitate the development of machines that are both profitable to make and reliable in operation. The key features required for this situation are the ability to model, in detail, the excitation, the generation and the voltage regulation control systems. The model should also be capable of incorporating dynamic machine loads and simple power system loads. Additionally, the model must be sufficiently computationally efficient so that several "what if" scenarios or different design changes can be examined in a reasonable time scale.

Various models of small salient pole generators have been proposed [2][31], and the Dynamic Reluctance Mesh model is one of these. The advantage of the DRM approach is that it includes an essentially 2D model of saturation and slotting in the machine. This can be extended to pseudo 3D to incorporate skew. However, it is not a very difficult step to extend the model to include the exciter, the rotating rectifier and the automatic voltage regulator (AVR). This can be difficult and very computationally intensive if attempted with Finite Element software, though more detailed modelling of the electromagnetic operation of the machine would be expected. Simple dynamic modelling based on Park’s approach [32] and generalised machine theory is much more rapid than either of the magnetic-field based approaches but is much less able to model the detail of saturation and slotting in the machine.

This chapter is concerned purely with modelling the generator itself and not with the exciter and AVR. Initially the standard generalised machine model suitable for Matlab based analysis will be developed both to introduce the transient coupled circuit approach and to show the simplifications inherent in this approach. The magnetic field based models, FEM and DRM, will then be introduced. The first objective of the chapter is to show that a suitable DRM model gives excellent results for predicting machine performance. The second objective is to define the degree of complexity of the DRM model required to give that excellent performance. The third objective is to show that the DRM can provide excellent, though less detailed, results much more rapidly than the equivalent FEM approach. To do this, results for open circuit and short circuit transients predicted by both FEM and DRM approaches will be compared, not only with respect to each other but also with practical results obtained on an experimental machine. A typical industrial salient pole generator is used as an example, whose basic specifications are three phase, four poles, four hundred volts, fifty Hz, 68kW. The stator has a conventional winding. The field winding on the rotor is fed via slip rings. Full details of this machine are presented in Appendix 1.

4.2 Equivalent Circuit and Generalised Machine, Mathematical models of Salient-pole Synchronous Machines

The basic synchronous machine models are already well established, as are termed equivalent circuit models. The model shown in the equivalent circuit has several assumptions:

1. The synchronous rotor speed is constant, which is usually fixed at synchronous speed.
2. Leakage reactance only exists on the stator side.
3. Winding inductances are independent of current, which means this is an unsaturated machine in respect of leakage flux paths.

Under these assumptions, a synchronous machine can be modelled as a voltage behind impedance, and the per phase equivalent circuit for synchronous machine under steady state conditions could be derived, as shown in figure 4.2.1.

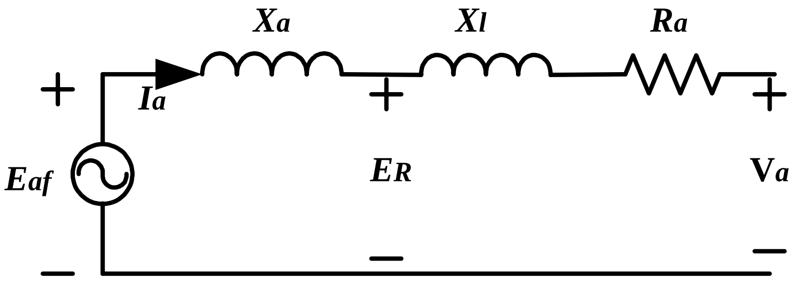

Figure 4.2.1 Equivalent circuit of cylindrical synchronous generator

One phase of the three phase equivalent circuit is shown in figure 4.2.1. X_a is the armature reactance which is responsible for generating the stator main flux field. X_l is the stator leakage reactance, representing leakage flux in the stator, and R_a is the stator phase resistance, representing copper loss in the stator. E_{af} is the generated voltage, or speed emf, produced by the relative motion of stator and rotor main flux ϕ_f. E_R is the voltage generated by resultant air gap flux ϕ_R. Part of the input mechanical energy is stored as magnetic energy represented by X_a, and V_a is the phase terminal voltage, i.e. output voltage of phase A of the generator.

Figure 4.2.2 shows the phasor diagram of the cylindrical synchronous generator in a steady state, over-excited condition.

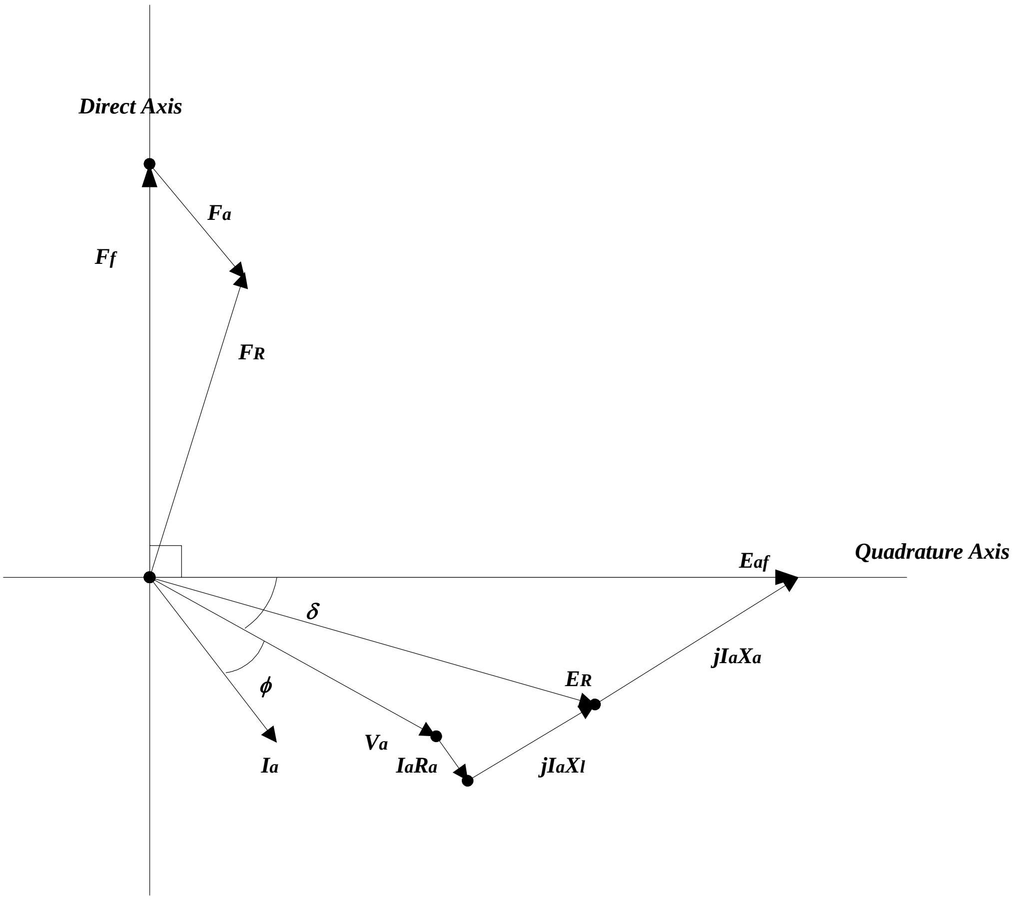

Figure 4.2.2 Phase diagram of cylindrical synchronous generator in steady state under excited

The angle δ is the load angle, which is the angle between the flux produced by the rotor and the resultant flux. Figure 4.2.2 shows quite clearly how the machine operates in steady state, for a generator E_{af} leads V_a. In general, for a lagging power factor the machine is over excited and for a leading power factor it is under excited.

The three phase electrical equations for simulating a simplified cylindrical rotor machine in the steady state condition is:

$$E_{af} = V_a + jX_{sa}I_a + I_aR_a \tag{4.2.1}$$

$$E_{bf} = V_b + jX_{sb}I_b + I_bR_b \tag{4.2.2}$$

$$E_{cf} = V_c + jX_{sc}I_c + I_cR_c \tag{4.2.3}$$

where $X_{sa} = X_a + X_l, X_{sb} = X_b + X_l, X_{sc} = X_c + X_l$ individually.

The salient pole rotor synchronous generator is different from the machine with cylindrical rotor in that there is a preferred magnetising direction in the salient rotor machine because of the non-uniform air gap. Thus, for analytical convenience, currents, voltages and fluxes are resolved in the d and q axis, where the d axis is the preferred flux magnetising direction, while the q is the axis perpendicular to the d axis electrically.

In salient pole generator analysis, it is more convenient to transform the currents and voltages from the stationary ABC frame to the rotating dq frame, which rotates synchronously with the rotor normally at synchronous speed. Park's transformation [32] is used when transforming from the stationary stator frame to the rotor frame, as shown in Equation 4.2.4. Assume:

$$x_{0dq} = P \cdot x_{abc}$$

where x denotes the variables in each reference frame, such as currents, voltages etc.. and P is Park's transformation matrix:

$$P = \sqrt{\frac{2}{3}} \cdot \begin{bmatrix} \frac{1}{\sqrt{2}} & \frac{1}{\sqrt{2}} & \frac{1}{\sqrt{2}} \\ \cos\theta & \cos(\theta - 2\pi/3) & \cos(\theta + 2\pi/3) \\ \sin(\theta) & \sin(\theta - 2\pi/3) & \sin(\theta + 2\pi/3) \end{bmatrix} \tag{4.2.4}$$

After transformation to the dq frame, the equations describing the salient-pole synchronous generator in steady state are:

$$E_f - V_q = R_a I_q + jX_d I_d$$

$$-V_d = R_a I_d + jX_q I_q \tag{4.2.5}$$

where $X_d = X_{ls} + X_{md}$, $X_q = X_{ls} + X_{mq}$, the direct- and quadrature- axis synchronous reactances, according to d-axis and q-axis theory, and X_{ls} is stator d and q axis leakage reactance, and X_d and X_q are magnetising reactance for d and q axis.

The transformed phasor diagram for the synchronous generator is shown in figure 4.2.3, when the salient pole generator running in the steady state condition, over excited.

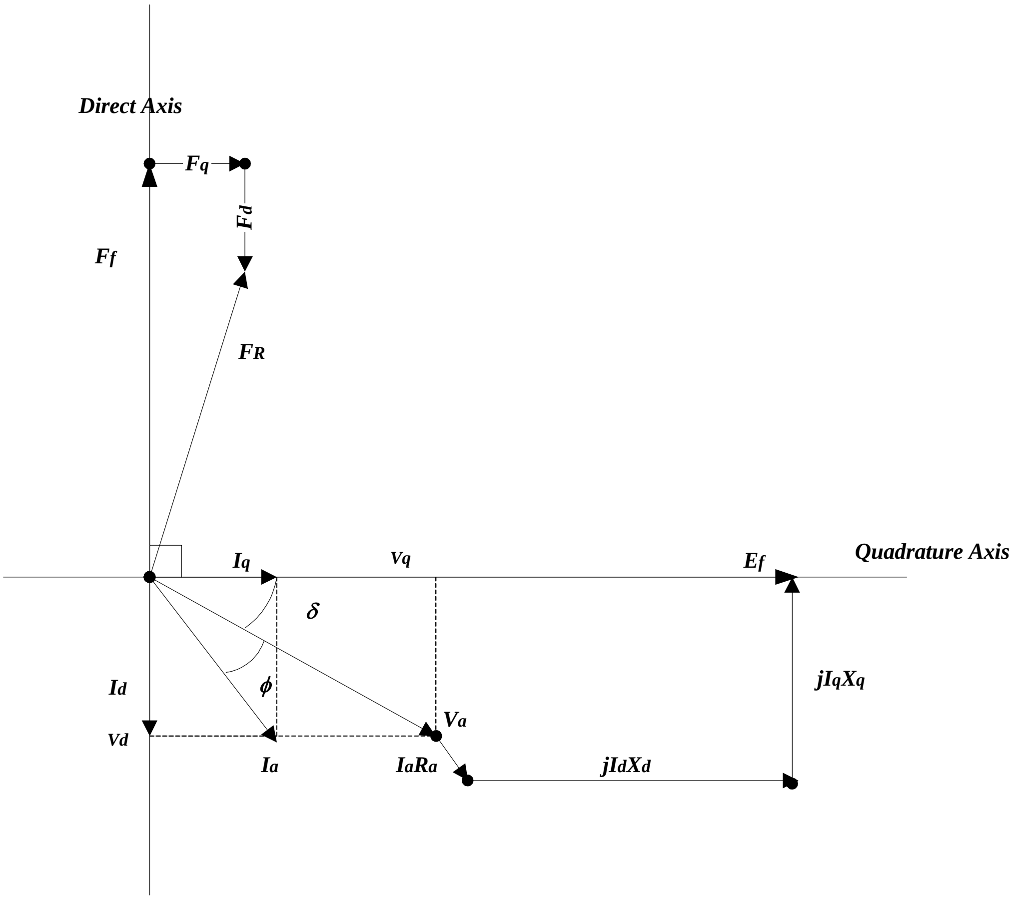

Figure 4.2.3 Phase diagram for salient-pole synchronous generator

The transformed dq model has been mentioned in previous context, however, in a typical salient pole synchronous machine, there are damper windings positioned on the surface of the salient pole, and these need to be considered in the generator’s dq mathematical model as well. Normally these are also resolved onto d and q axes for the convenience of analysis. A two pole, three-phase wye-connected salient pole synchronous machine with damper windings is shown in figure 4.2.4.

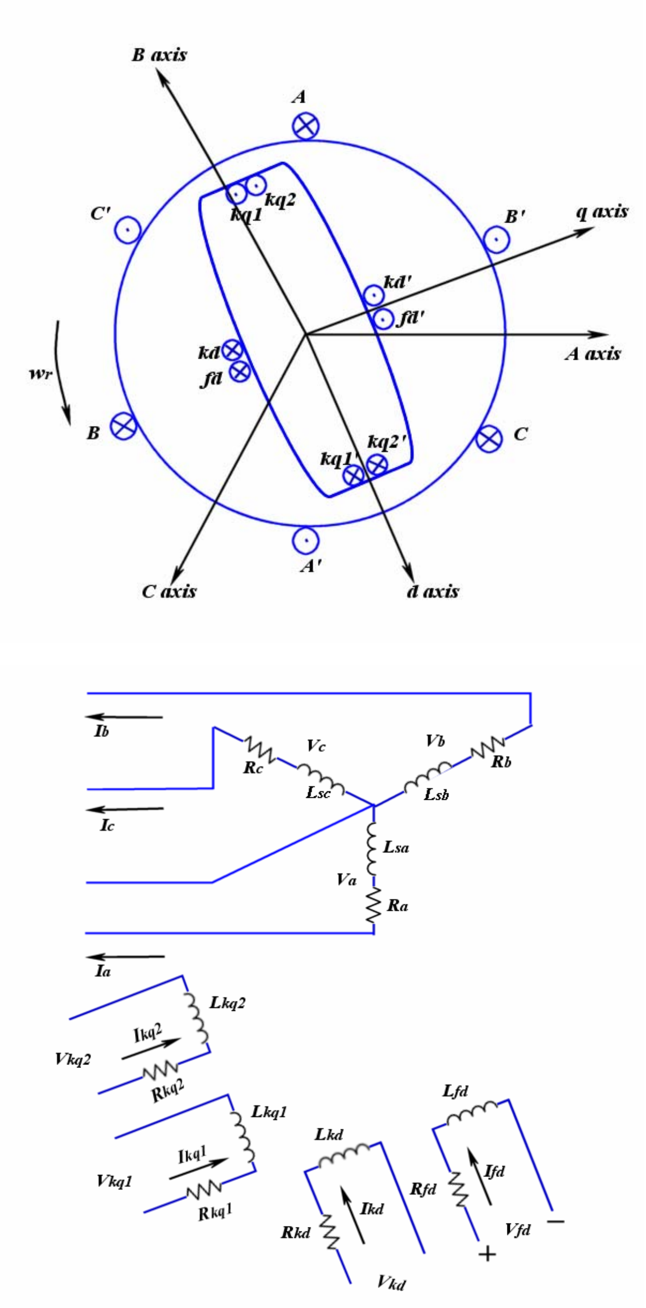

Figure 4.2.4 Two pole, three phase, salient pole synchronous machine windings arrangements

A, B and C are in the three phase stationary frame, d- and q- are in the two phase rotating rotor frame. The rotor is equipped with a field winding (fd winding), and three damper windings (kd , $kq1$ and $kq2$). One damper winding is in the same magnetic axis as the field winding, and the magnetic axis of the second and third damper windings is displaced 90° ahead of the magnetic axis of field winding. Also, the assumed direction of the positive stator current is out of the terminals convenient to describe generator action.

After Park’s transformation, the complete synchronous machine equivalent circuit including both stator and rotor is shown in figure 4.2.5.

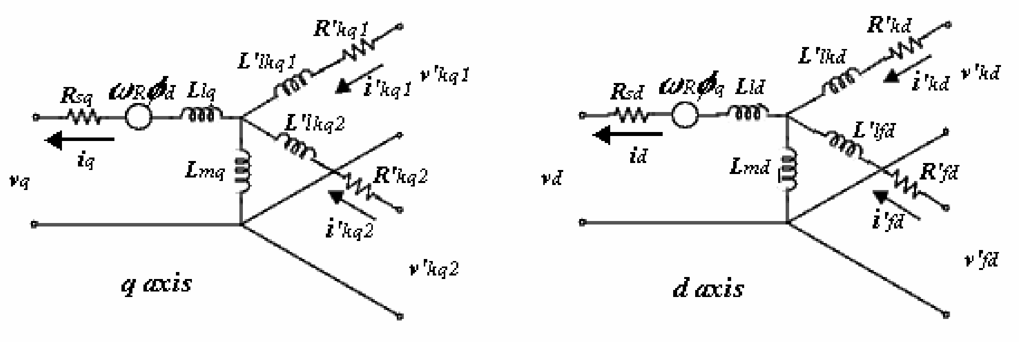

Figure 4.2.5 Complete synchronous machine d- and q- axis equivalent circuit

Where subscripts in figure 4.2.5 mean,

- *d,q*: d and q axis quantity
- *R,s*: Rotor and stator quantity
- *l,m*: Leakage and magnetiing inductance
- *f,k*: Field and damper winding quantity

The circuit equations are:

$$v_d = -R_{sd} i_d + \frac{d}{dt}\lambda_d - \omega_R \lambda_q$$

$$v_q = -R_{sq} i_q + \frac{d}{dt}\lambda_q + \omega_R \lambda_d$$

$$v'_{fd} = R'_{fd} i'_{fd} + \frac{d}{dt}\lambda'_{fd}$$

$$v'_{kd} = R'_{kd} i'_{kd} + \frac{d}{dt}\lambda'_{kd}$$

$$v'_{kq1} = R'_{kq1} i'_{kq1} + \frac{d}{dt}\lambda'_{kq1}$$

$$v'_{kq2} = R'_{kq2} i'_{kq2} + \frac{d}{dt}\lambda'_{kq2}$$

where:

$$\lambda_d = -L_d i_d + L_{md}(i'_{fd} + i'_{kd})$$

$$\lambda_q = -L_q i_q + L_{mq}(i'_{kq1} + i'_{kq2})$$

$$\lambda'_{fd} = L'_{fd} i'_{fd} + L_{md}(-i_d + i'_{kd})$$

$$\lambda'_{kd} = L'_{kd} i'_{kd} + L_{md}(-i_d + i'_{fd})$$

$$\lambda'_{kq1} = L'_{kq1} i'_{kq1} + L_{mq}(-i_q + i'_{kq2})$$

$$\lambda'_{kq2} = L'_{kq2} i'_{kq2} + L_{mq}(-i_q + i'_{kq1})$$

and,

$$L_q = L_{lq} + L_{mq}$$

$$L_d = L_{ld} + L_{md}$$

$$L'_{kq1} = L'_{lkq1} + L_{mq}$$

$$L'_{kq2} = L'_{lkq2} + L_{mq}$$

$$L'_{fd} = L'_{lfd} + L_{md}$$

$$L'_{kd} = L'_{lkd} + L_{md} \,.$$

With these equations derived, the synchronous generator machine state could be solved with commercial simulating software, such as Matlab. Matlab provide a machine library, which has some synchronous machine models with different units and parameter inputs.

As for the other complicated characteristics such as saturation and transient state, there are various models accounting for these.

For simulating the transient and sub-transient conditions, Arrillaga [33] and Saccomanno [31] mentioned the salient-pole synchronous machine mathematical model under transient and sub-transient conditions. Additional fictitious voltages E'_d and E'_q are added which represent the flux linkages due to the 'inertia' of flux change in the rotor winding during transient conditions. Thus, two additional rotor circuits (equations) are added, one of which acts magnetically along the direct axis, and the other along the quadrature axis. For sub-transient conditions, voltages E''_d and E''_q, and another two voltage equations are added for the same reason.

Saturation is a part of synchronous machine modelling but there is still uncertainty as to what is the best method of simulation. The degree of saturation is not the same throughout the machine because the flux density varies for different parts of the machine due to the design of the geometry of the machine. The saturation in the direct and quadrature axes are different.

For the mathematical synchronous machine model, saturation may be taken into account by modifying the value of the reactance used in representing the machine [33], including both the d and q reactances for the cylindrical machine and the salient-pole machine. Various methods have been adopted to account for saturation in both modification of the technique and in the representation of the saturation characteristic of the machine, such as the classical saturation model, salient-pole saturation model, which modify the synchronous reactances, the simple saturation representation, and the Potier reactance [33]. Saccomanno [31] considered saturation in the stator side and the rotor side separately and then combined the effects.

Overall, the models developed so far are simple. Park's transformation assumes sinusoidal flux distribution and winding distributions and so neglects slotting and phase belt harmonics [32]. Saturation is included in various ways but rarely with any detail since leakage flux paths are not separately identified and so the dependence of leakage reactances on winding current levels is imperfectly modelled, or ignored. Main flux saturation is treated in some methods with more detail yet secondary effects of armature reaction in terms of cross saturation are not well modelled and more normally neglected [32]. Not least of the problems with this method is the need for machine inductance values as well as speed emf constants and saturation data if the model is able to cope with it. This data can be determined experimentally for existing machines but if the approach is used to analyse new designs there is a consequent need for an additional machine design program to determine these values. It is very much apparent that this type of model is aimed more at systems analysis than at detailed machine behaviour analysis. However, the approach is very widely used.

4.3 Finite Element Models of Salient Pole Synchronous Machines

The finite element method (FEM) is a widely used field calculation method, which can be used in many engineering fields, including mechanical, material, structural, thermal, fluid, and electromagnetic field calculations. It can supply very detailed and accurate field information to meet user requirements, thus quite often, it is the benchmark of many engineering numerical simulation results. However, although generally speaking, the FE method is accurate, the accuracy and reliability depends on the discretising of the intended calculation objects and the polynomial order for interpolation. Results would be different using different solving parameters and discretising method, and interpolation techniques.

Due to the advantage of the FE method, it has been an effective method of investigating complicated electrical apparatus, such as electrical machines, which includes detailed flux field distribution, inductances calculations although the calculation time may be vast. There are also commercial software packages developed for each kind of specific application, such as MagNet^{TM} for the calculation of electrical machines or ANSOFT^{TM} for combined calculation of structure analysis, mechanical analysis etc.

One type of salient pole synchronous generator was modelled with commercial FEM software package. The machine rating was 68kw, 4 poles with 0.8 power factor. By using a time stepping method, the transients of the generator in the open circuit condition were calculated, where the field excitation voltage is added on the rotor circuit terminal, and the rotor is driven by prime mover at a constant synchronous speed. The generated stator terminal voltage and field current, and also the air gap flux density distribution are examined. A comparison of results between FEM and DRM is given in the flowing discussion.

Figure 4.3.1 shows the solution mesh from FE calculations at a specific time step. Automatic mesh adaption method is used at each time step calculation, so that the program will optimise the topology of the mesh in preparation for the next time step for a more accurate solution.

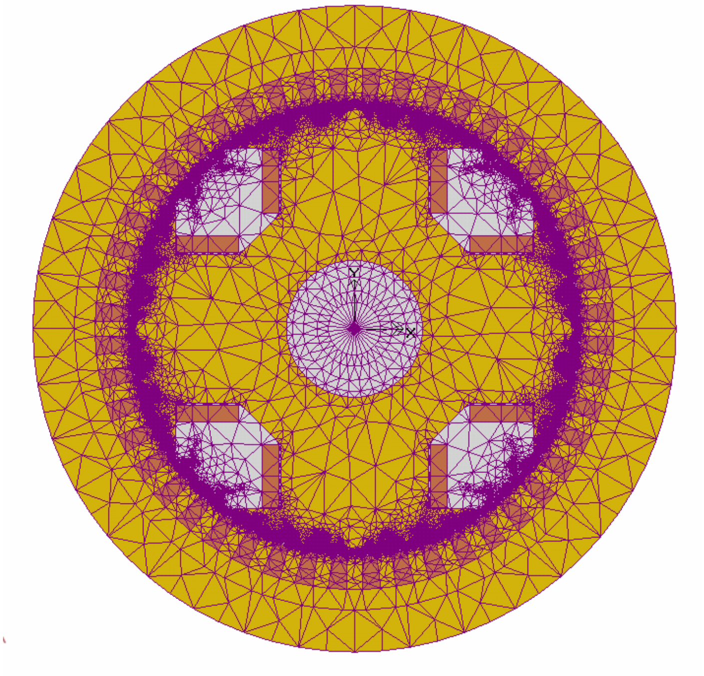

Figure 4.3.1 Solution mesh of the salient-pole synchronous machine in a specific time step @100ms

As can be seen from the figure, the meshed elements close to the air gap and in the stator slot and rotor surface region are denser than the others. This is due to the air gap geometry, which is more irregular compared with that of an induction machine, and is more important from the machine modelling point of view, because it is the air gap that carries the flux field between stator and rotor. In the solution mesh, there are 72,076 triangles in total.

The machine stator winding is a double layer concentric winding with a coil pitch of eight, parallel circuits, forty-eight slots and five number of turns. The winding was formed in each phase from four coils. As normal in four wire generators, to eliminate the harmful third harmonic, the stator three phases are star connected with a 120 degree coil pitch. The circuit in figure 4.3.2 shows the simulated winding coil connections in the FEM model of this type of generator. It simulates an open circuit condition, with a very large resistance value connected to the stator terminals to simulate an open circuit condition numerically. Rated value d.c. voltage source is applied to the rotor side as the excitation. All the damper bar windings are connected together as for the rotor of a cage induction machine.

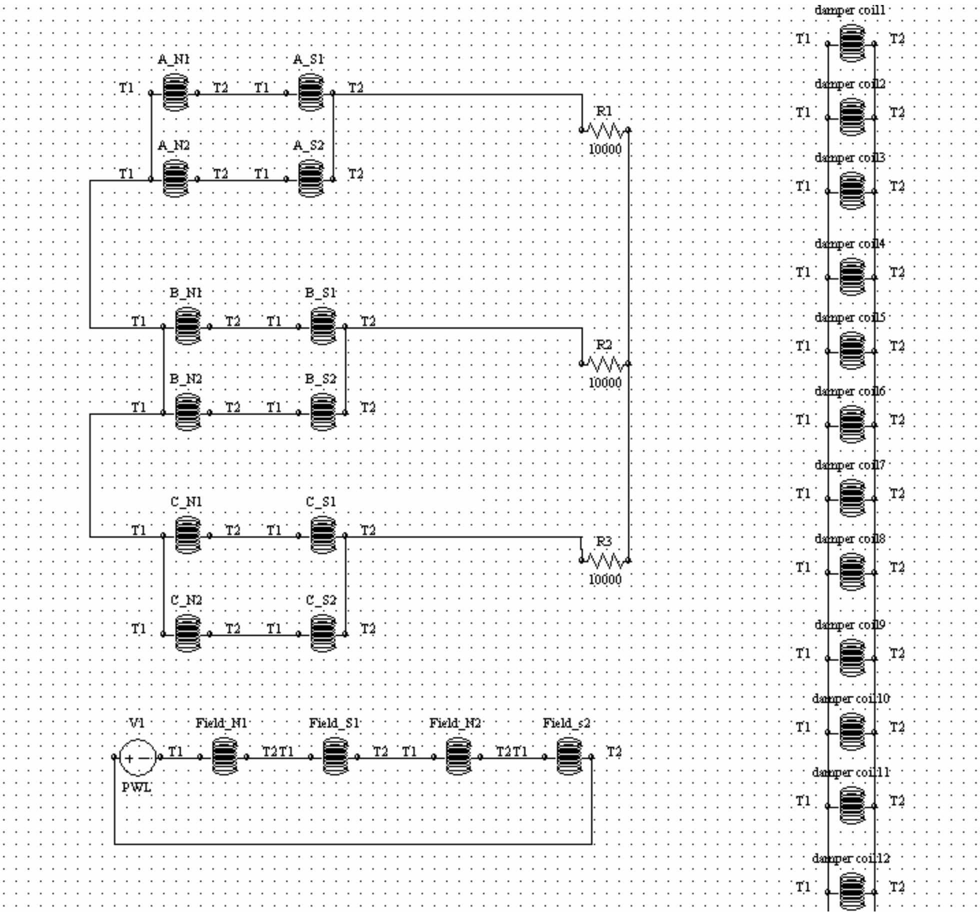

Figure4.3.2 Electrical circuit connection model of a type of salient-pole synchronous generator simulated in FEM software

For the nonlinear iron material, Losil 800 as stated in the generator datasheet, is selected in the FE model from the material database in the finite element software. Thus, the b-h curve is used in simulation to represent the nonlinear relationship between the field intensity and the actual flux density in the material.

For the rotating, transient magnetic field calculation, it normally takes days or weeks to achieve the results, depending on the problem scale and accuracy requirements. In the simulations in this chapter, a time step of 1ms was used, simulation time was 300ms, adaptive h-adaption was used for the meshing process, CG tolerance was 0.001 and Newton tolerance was 0.01. The total simulation time for the full FE model was 576 hours. While for a DRM simulation, for a time stepping method with time step to be 0.00001, solving tolerance to be 10e-8, the solution time for 1s would be taken for 10 hours. The simulation time comparison between FE and DEM is shown in table 4.3.1.

	Time step	Newton tolerance	Simulation time	Time take for simulations	Calculation time for each time step
FEM	0.001s	0.01	0.3s	576 hours	0.52 hour/step
DRM	10e-5s	10e-8	1s	10 hours	1e-4 hour/step

Table 4.3.1 Simulation time comparison between FEM and DRM

Figure 4.3.3 shows the detailed flux function distribution result in one specific time step for the whole machine.

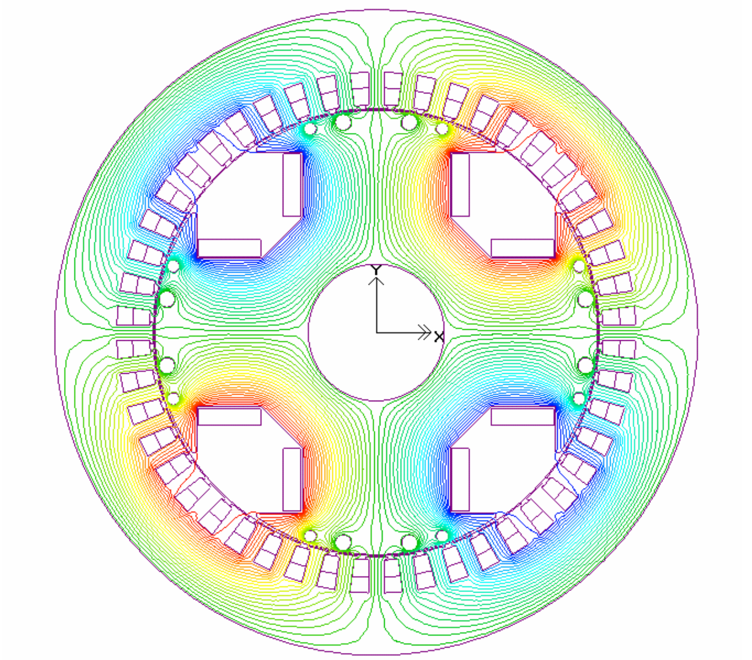

Figure 4.3.3 Flux function distribution in a salient-pole synchronous machine calculated by FEM software, results taken @100ms

Figure 4.3.4 to figure 4.3.6 show the results for the rate of growth of field current following initial switch on as calculated from FEM software for this type of salient pole synchronous machine.

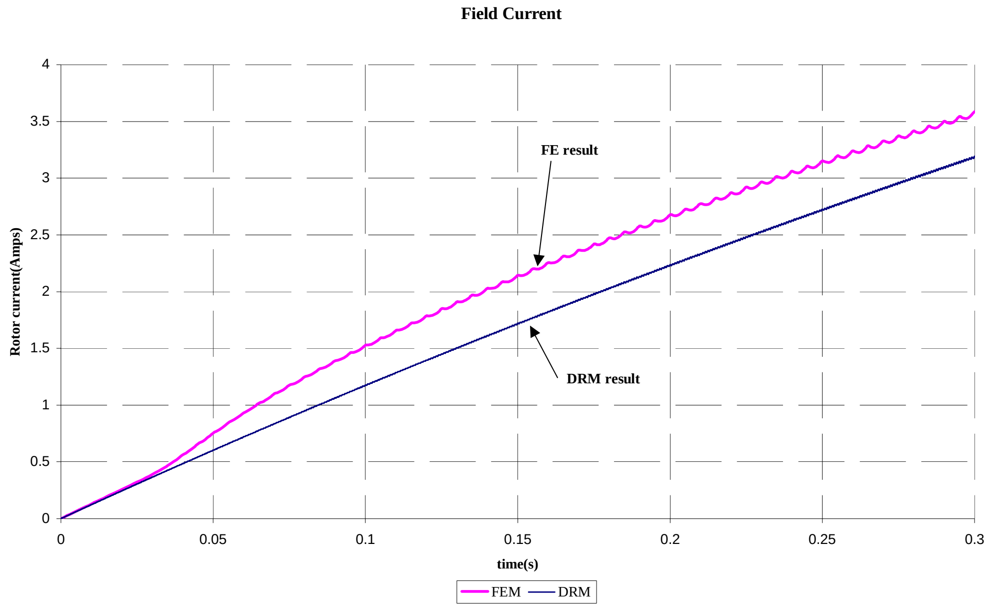

Figure 4.3.4 Field current comparison between FEM and DRM calculations

There is some difference in the rise of the field current using FEM and DRM calculation methods. This difference is due to different rotor resistance values in the two simulations. FEM calculated the rotor resistance based on the winding drawings and material resistivity in the software, where end winding resistance is not included, while DRM uses the rotor resistance supplied by the company datasheet, where there is an experimental data including all the field winding resistance. Thus FEM current rises faster initially than DRM because of the relatively small resistance it uses compared to the DRM result. The nonlinearity in the FEM curve is a concern. At such low currents in open circuit there would not be any saturation problems.

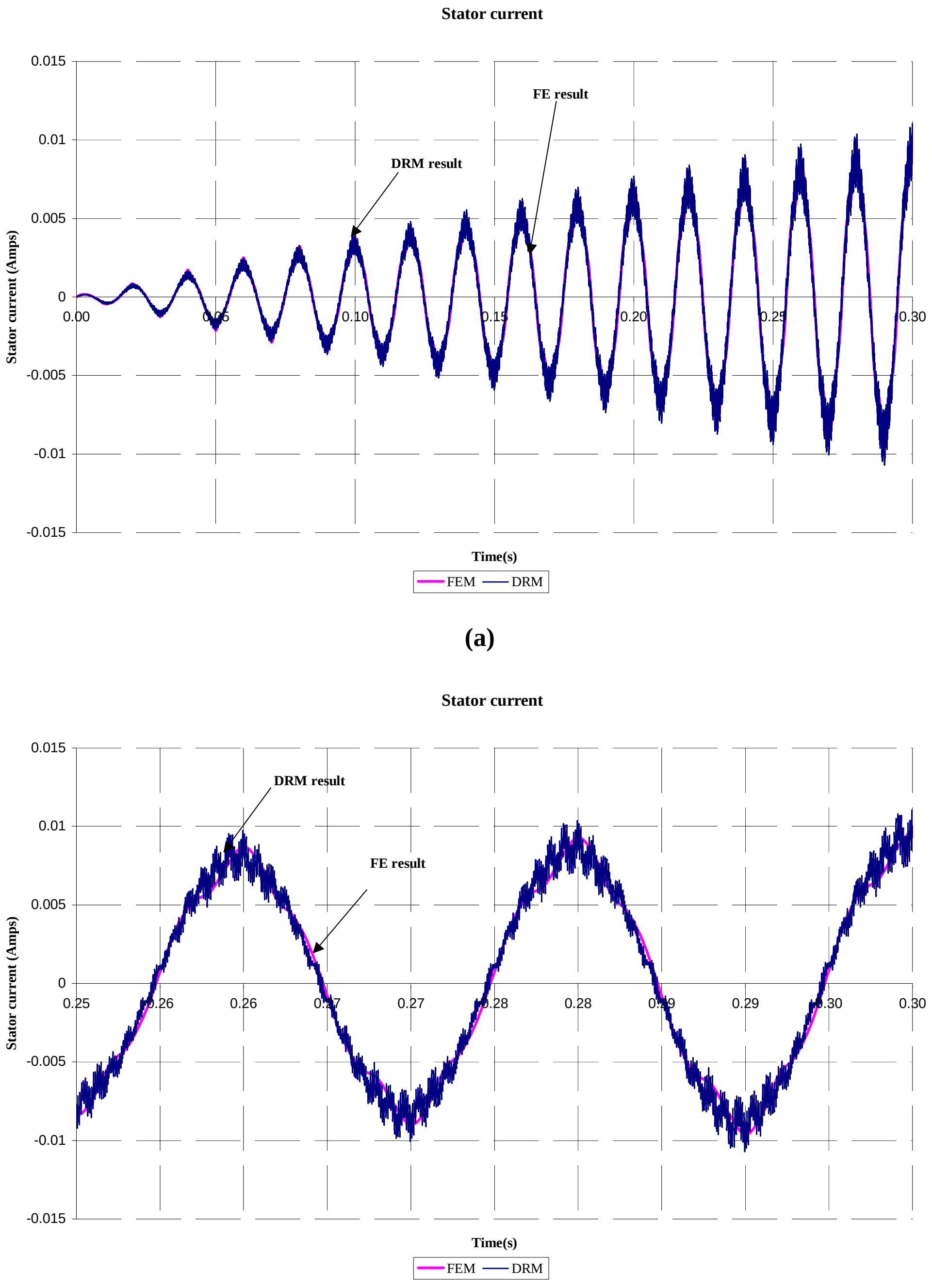

(a)

(b)

Figure 4.3.5 Stator current comparison between FEM and DRM results

Figure 4.3.5 shows the stator current comparison between FEM and DRM results. Although the open circuit condition is simulated here, where there should be no stator current, small stator current exists because the circuit is not actually open circuited but a very big value resistance was put in to limit the stator current to a very small range to simulate the open circuit condition. It can been seen from figure 4.3.5 that the FEM result and DRM result agree with each other very well, both in phase sequence and in magnitude. The DRM result has more ripples in the stator current because of the much smaller time step used in DRM simulations, which is 1e-5, a hundred times smaller than the FEM. figure 4.3.5 (b) is a zoom out picture of (a).

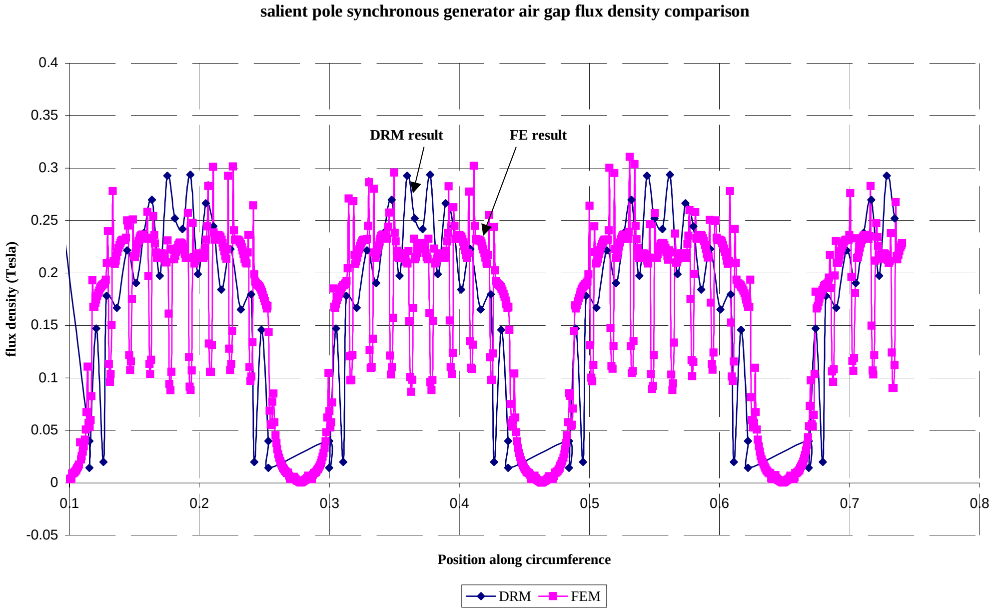

Figure 4.3.6 Torque and air-gap flux density (magnitude) of this type of machine simulated by FEM software

Comparison between the air gap flux density (magnitude) for the two simulation methods is given in figure 4.3.6. This air gap flux density value is derived from the iron type reluctances on the salient rotor surface for the DRM method, while it is derived from the flux density value along the pole surface for FEM. Thus, flux density values are taken and compared for the same place in the machine. From the graph it can be seen that the air gap flux density distributions shape along the air gap circumference are similar to each other for the two modelling methods. But more peak points were found in FEM results due to the denser element mesh for the stator and rotor surface discretisation in the finite element method than the dynamic reluctance mesh method, so that more peak values for flux density are sampled in the simulation.

4.4 Dynamic Reluctance Mesh Modelling of Salient Pole Synchronous Generator

In previous sections of this chapter, the modelling of salient pole synchronous machines using a basic mathematical method and finite element method have been introduced. This section will describe the modelling and simulation method of a salient pole synchronous generator using the Dynamic Reluctance Mesh method.

The Dynamic Reluctance Mesh method could simulate salient-pole synchronous generators in a way between the mathematical method and the finite element method; it has fewer number elements involved in the calculation process and fewer machine state variables when compared with the finite element method, but more than the mathematical method. Based on the induction machine's DRM model given in chapter 2 and chapter 3, a salient-pole generator DRM model will now be created with some developments. Due to its different geometry and flux distribution characteristics, DRM model for a salient pole synchronous generator is different from an induction machine in a number of ways.

From the computational model's point of view, the main differences are:

1. the rotor geometries are different; an induction machine has either a cage or a wound rotor. Both have a certain number of teeth, and the teeth geometry is similar to the teeth on the stator side, while a salient pole synchronous generator has salient teeth, which are equal to the number of poles. An air gap overlap curve which was applied for the induction machine in previous chapters only works for teeth pairs where the tooth width is in the same range. Some modifications of the air gap modelling method have to be made in order to accommodate this method to salient

pole synchronous generator modelling.

2. the rotor flux distributions are different. Due to the quite different geometry of the induction machine and salient pole generator, flux distribution inside the salient rotor is quite different from that of induction machines. Because the discretisation of the reluctance mesh in the DRM method is based on the knowledge of flux field distribution in the machine, the creation of reluctance mesh in a salient rotor has to be quite different from that of an induction machine.
3. there are damper windings on the rotor surface to reduce oscillations in salient pole synchronous generators. This makes the machine DRM modelling different from induction machines in that only have one set of windings on the rotor.

DRM modelling of these different aspects will be described one by one in the following text.

4.4.1 Air-gap modelling of a salient pole machine

The air gap is a key part in electrical machines because it is the intermediate component between the rotating rotor and the stationary stator, thus it is the essential component of electromagnetic energy transformation. For a generator, mechanical energy that comes in from the rotor is transferred through the air gap to the stator to become electrical energy based on electromagnetic energy conversion rules, e.g. Faraday’s law.

Due to the above reasons, modelling the air gap accurately and effectively is very important in the computer simulation of electrical machines, and an air gap model is always a very important part to be investigated in all kinds of machine simulation techniques. For a salient pole synchronous machine, the difficulty is the non-uniform air gap geometry and the irregular flux paths in the air gap region.

Dynamic Reluctance Mesh modelling uses a dynamic way to create air gap elements that connect to each pair of stator and rotor teeth depending on the rotor position, and achieves the effective air reluctance width based on the extracted information from FEM results so that the fringing effect could be accounted for. This method works well in the induction machine model, as shown and validated from the results evaluations in chapter 3.

Due to the non-uniform air-gap shape in a salient-pole generator, flux distribution is complicated, and would be different in different load conditions. figure 4.4.1 shows the flux distribution, which is from FEM software, for one type of salient pole machine when the rotor is excited with a rated voltage, and the stator terminals are open circuited. It can be seen that fringing effects exist in both the rotor pole tip region and the region between the stator teeth. The fringing is quite heavy in the pole tip region, where there is a great space between the adjacent poles.

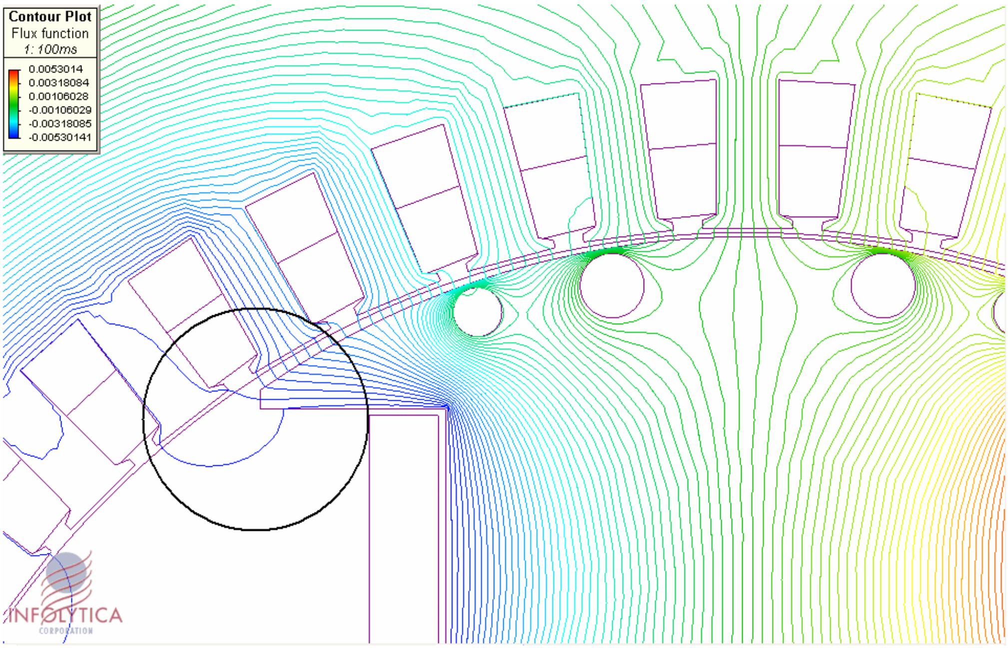

Figure 4.4.1 Flux distribution for a salient pole generator, rated field voltage excited and stator terminals are open circuited

However, for a salient-pole synchronous machine, the idea of the air gap overlap method for an induction machine could also be adopted, but with some modifications. In order to have the pair of stator and rotor teeth with a tooth width in the same range, some virtual teeth on the salient-pole rotor surface are created; each has its own air gap reluctance connected to the stator side.

To use the effective air-gap width method described in chapter 3, the salient-pole rotor surface is divided into several virtual rotor teeth that are adjacent to each other. There is no air in between these virtual teeth. The number of virtual teeth on the rotor surface is decided by the geometry of the salient pole, and also the stator tooth width. The virtual tooth width on the salient rotor surface should be the same size as the stator tooth. In figure 4.4.2, the iron type reluctances representing each of the virtual teeth on the rotor surface are shown by use of different shading. Reluctances perpendicular to the rotor surface represent the radial flux whilst tangential flux is represented by reluctances parallel to the rotor surface. The number of virtual teeth on a rotor surface should be selected with care in case of any cogging effects, as happens in induction machines [24].

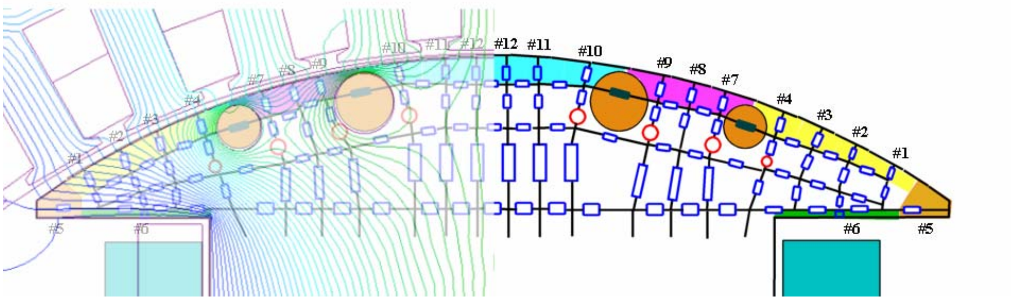

Figure 4.4.2 Virtual rotor teeth on the surface of salient-pole rotor

These ‘surface reluctances’ stay on the surface of the salient-pole rotor and exchange flux with stator teeth through the overlap curves for salient pole machines. Due to the non-uniform air gap shape of the salient-pole machine, overlap curves’ shape is different for the different virtual teeth by their different positions on the rotor surface. Methods of acquiring these effective overlap curves and the reason to do so have been explained in chapter 3. As shown in the left hand side of figure 4.4.2, virtual teeth #5 and #6 represent the flux relationship between the salient-pole rotor tip (#5) or the area under the rotor tip (#6) with the stator teeth to account for the fringing effect between the pole tip and stator tooth, as shown in the circle in figure 4.4.1. Derived from FE software, figure 4.4.3 shows these different overlap curves for different rotor virtual teeth.

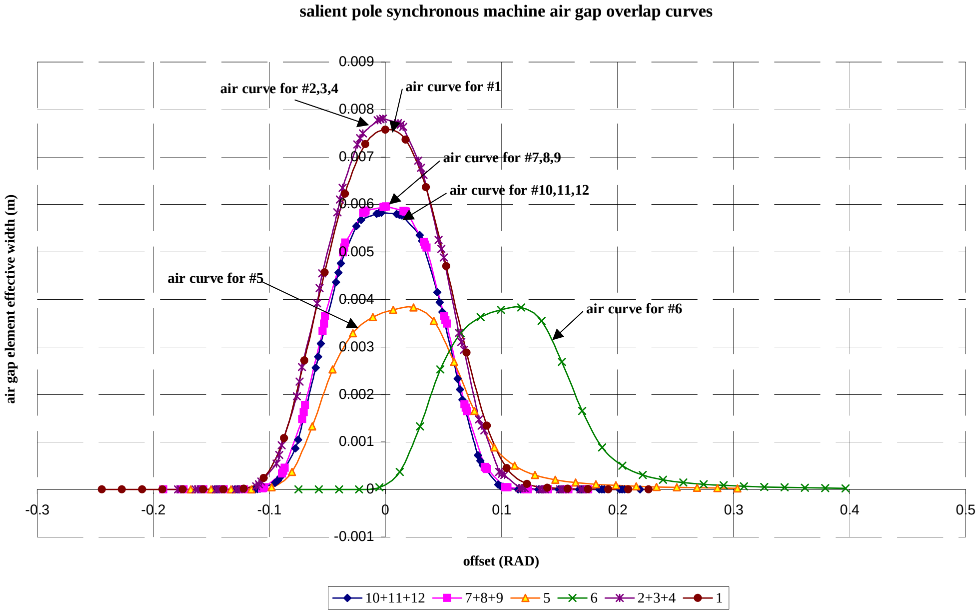

Figure 4.4.3 Overlap curves for salient-pole synchronous machines

Offset (displacement) in figure 4.4.3 means the angular displacement between the centres of each pair of teeth, as shown in figure 4.4.4.

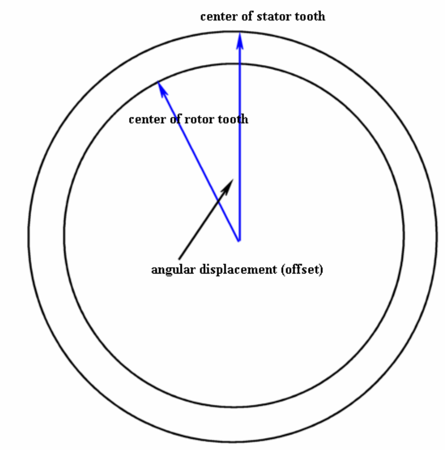

Figure 4.4.4 Angular displacement of salient pole synchronous machine

It can be seen from the overlap curves above that curves #5 and #6 are not symmetrical to the origin. The reason of this is that in the 0 offset point, when the centre of tooth #5, #6 and one of the stator tooth are aligned, flux is shed from coming into the rotor surface because the shape of the tip and the definition of the centre on the virtual tooth. Thus, especially for tooth #6, the maximum flux linkage happens in the position which has non-zero offset other than the origin offset point where tooth #6 and the stator tooth centre are aligned. The asymmetrical of curve #6 depends on how the centre of the virtual tooth #6 is defined. The closer the centre of tooth #6 to the pole tip, the less asymmetrical shape the air gap overlap curves have.

Another difficulty in air gap modelling is the non-uniform air gap length. The length of the air gap reluctances of these virtual teeth are different due to their different positions on the rotor surface. According to the usual pole geometry of a salient pole generator, in order to get a more sinusoidal shape flux density waveform on the air gap circumference, the salient pole shape is designed so that the further the distance from the teeth to the pole centre, the longer the air gap element length.

In the work discussed in this chapter, air gap lengths are calculated to be the average value of the left end and right end of each air gap element connecting each pair of virtual rotor teeth and stator teeth.

Virtual rotor teeth on the two sides of the salient-pole rotor are symmetrical due to the symmetry of the pole. Their overlap shapes are also symmetrical about the pole centre.

Flux distribution in electrical machines changes when the winding currents change, and more leakage flux exists when the winding currents are large due to the saturation characteristic of the iron material, such as in the transient of the direct on line starting of induction machine and short circuit condition of synchronous generator. In a synchronous generator, due to the large air gap in between adjacent poles, in some running conditions, such as short circuit testing, a certain leakage flux exists which could not be ignored. Some more air gap reluctances must be additionally added to account for tip area leakage fluxes between the pole tips, which are called inter-pole air gap reluctances in DRM. These leakage and inter-pole reluctances are shown in Fig. 4.4.5.

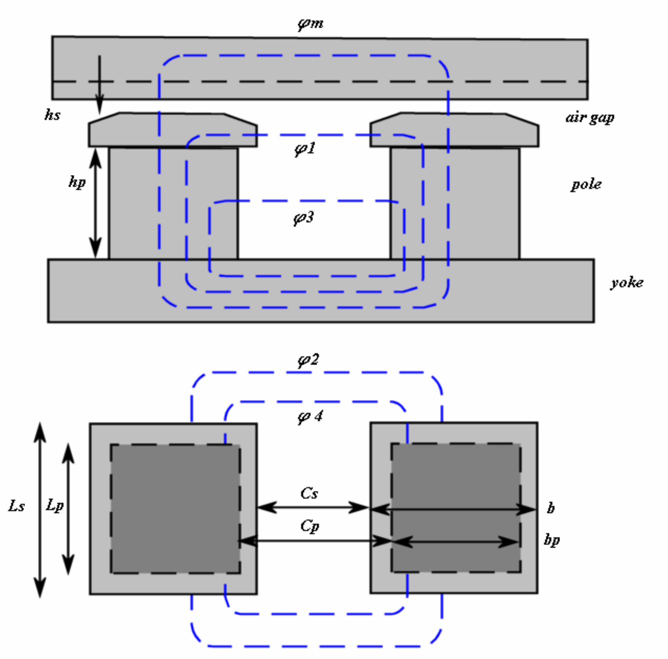

Figure 4.4.5 Reluctance mesh shows the leakage air-gap reluctance and inter-pole reluctances in salient-pole machine

M. G. Say suggests an empirical formula [27] of calculating leakage flux for a low speed salient pole synchronous machine, as shown in equations 4.4.1 and 4.4.2.

- Flux between shoes (for each pole pair): $\phi_{sl} = 2\phi_1 + 4\phi_2$

$$\phi_{sl} = \mu_0 F_l \left[2\frac{L_s h_s}{c_s} + 2.9 h_s \log_{10}\left(1+\frac{0.5\pi b}{c_s}\right)\right] \qquad (4.4.1)$$

- Flux between poles (for each pole pair): $\phi_{pl} = 2\phi_3 + 4\phi_4$

$$\phi_{pl} = \mu_0 F_l \left[\frac{L_p h_p}{c_p} + 1.5 h_p \log_{10}\left(1+\frac{0.5\pi b_p}{c_p}\right)\right] \qquad (4.4.2)$$

where F_l is the mmf of the winding, and parameter L_s, L_p, h_s, h_p, c_s, c_p b, b_p are shown in figure 4.4.5.

To fit the above equations representing leakage fluxes between salient poles and pole shoes, corresponding inter pole reluctances representing these leakage fluxes need to be added in to the Dynamic Reluctance Mesh modelling. Assume reluctance $\Re_1$ represents the leakage flux ϕ_1, $\Re_2$ represents the leakage flux ϕ_2, $\Re_3$ represents ϕ_3 and $\Re_4$ represents ϕ_4. From equation 4.4.1, following equations could be derived:

$$\phi_1 = \mu_0 F_l \cdot \frac{L_s h_s}{c_s} \tag{4.4.3}$$

$$\phi_2 = \mu_0 F_l \cdot 2.9 h_s \log_{10}\left(1 + \frac{0.5\pi b}{c_s}\right) / 4 \tag{4.4.4}$$

Considering the relationship between flux and reluctance: $\phi = F_l / \Re$,

$$\Re_1 = \frac{c_s}{\mu_0 L_s h_s} \tag{4.4.5}$$

$$\Re_2 = \frac{4}{2.9 \mu_0 h_s \log_{10}\left(1 + \frac{0.5\pi b}{c_s}\right)} \tag{4.4.6}$$

When considering the total leakage flux path between the pole shoes, based on the leakage flux calculating method from M.G. Say, there are three parallel leakage flux paths between each pair of pole shoes, as shown in figure 4.4.6, which could be represented by:

$$\Re_{sl} = \Re_1 // \Re_2 // \Re_2 \tag{4.4.7}$$

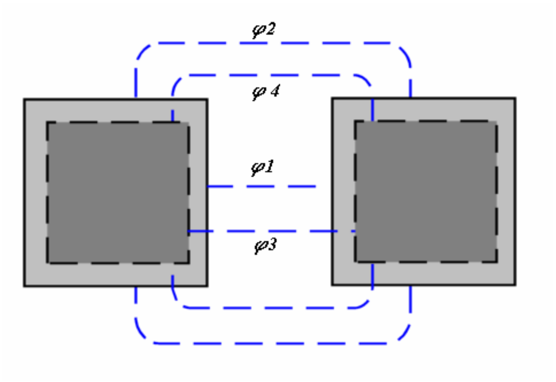

Figure 4.4.6 Parallel leakage flux path between each pair of pole shoes

thus, inter pole leakage reluctances for each between each pole pair is:

$$\Re_{sl} = \frac{1}{\mu_0 h_s} \cdot \frac{c_s}{L_s + 1.45 c_s \log_{10}\left(1 + \frac{0.5\pi b}{c_s}\right)} \tag{4.4.8}$$

Compare this equation to a typical air type reluctance equation: $\Re_{sl} = \frac{l_{sl}}{\mu_0 w_{sl} d_{sl}}$, where l_{sl}, w_{sl} and d_{sl} are the length, effective width and depth of the leakage reluctance between poles respectively. So the effective width, length and depth of the reluctance between pole shoes pairs taking the leakage flux effect into account would be:

$$l_{sl} = c_s \tag{4.4.9}$$

$$w_{sl} = h_s \tag{4.4.10}$$

$$d_{sl} = L_S + 1.45 c_s \log_{10}\left(1 + \frac{0.5\pi b}{c_s}\right) \tag{4.4.11}$$

If the same calculation process is applied to the leakage flux between poles, then ($F_l / 2$ is utilised because the this leakage is in the middle of the pole)

$$\phi_3 = \frac{1}{2}\mu_0 F_l \cdot \frac{L_p h_p}{c_p} \tag{4.4.12}$$

$$\phi_4 = \mu_0 F_l \cdot 1.5 h_p \log_{10}\left(1 + \frac{0.5\pi b_p}{c_p}\right) / 4 \tag{4.4.13}$$

and the reluctances are:

$$\Re_3 = \frac{c_p}{\mu_0 L_p h_p} \tag{4.4.14}$$

$$\Re_4 = \frac{2}{1.5\mu_0 h_p \log_{10}\left(1+\frac{0.5\pi b_p}{c_p}\right)} \quad , \tag{4.4.15}$$

the leakage reluctance representing the leakage flux between poles are:

$$\Re_{pl} = \Re_3 // \Re_4 // \Re_4 \tag{4.4.16}$$

$$\Re_{pl} = \frac{1}{\mu_0 h_p} \cdot \frac{c_p}{L_p + 1.5 c_p \log_{10}\left(1+\frac{0.5\pi b_p}{c_p}\right)} \tag{4.4.17}$$

and the effective width, length and depth for leakage reluctance between the poles are:

$$l_{pl} = c_p \tag{4.4.18}$$

$$w_{pl} = h_p \tag{4.4.19}$$

$$d_{pl} = L_p + 1.5 c_p \log_{10}\left(1+\frac{0.5\pi b_p}{c_p}\right) \tag{4.4.20}$$

With the inter pole leakage air gap reluctances modelled, the whole air gap reluctance mesh of a salient pole rotor is shown in figure 4.4.7.

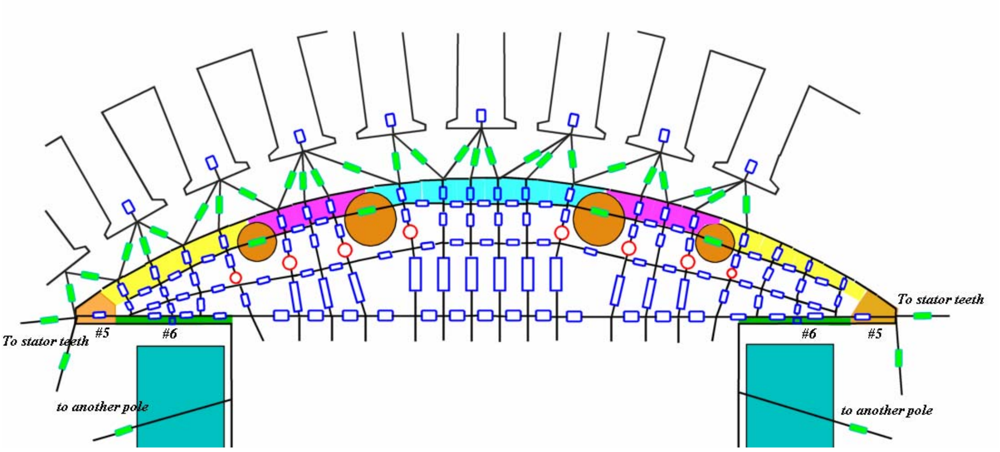

Figure.4.4.7 Whole air gap reluctance mesh for salient pole generator, including leakage and inter-pole reluctances

4.4.2 Meshing of salient pole rotor

After finishing the modelling of the air gap part of the machine, this section will continue to model the iron part of the generator. A salient pole synchronous generator stator has a similar geometry to an induction machine stator and the same reluctance mesh topology for induction machine could be adopted. However, this is not the case in rotor reluctance mesh creation. Because the rotor geometry for a salient-pole rotor generator and induction machine are so different, the rotor mesh has to be quite different to in order to account for the different flux distribution inside the rotor pole.

The advantage of Dynamic Reluctance Mesh is that the reluctance mesh could be simplified by the given prior-known knowledge of flux distribution in the machine. For a salient pole synchronous generator, the main flux distribution in the salient pole is known from experience, thus the salient pole could be discretised into the reluctance mesh based on empirical knowledge.

The main principle of dividing the iron part of a machine into reluctance mesh is that the direction of the reluctances should be in approximately the same direction as the flux direction, although some small displacements are allowed, and there have to be reluctances where there is flux path. Reluctances should lie in both radial and tangential directions in the iron to allow radial flux and tangential flux to pass through, and reluctances in different direction can be overlapped, because their fluxes have different directions.

Based on the discretisation principle given above, reluctance mesh for a salient-pole rotor can be created as shown in figure 4.4.8.

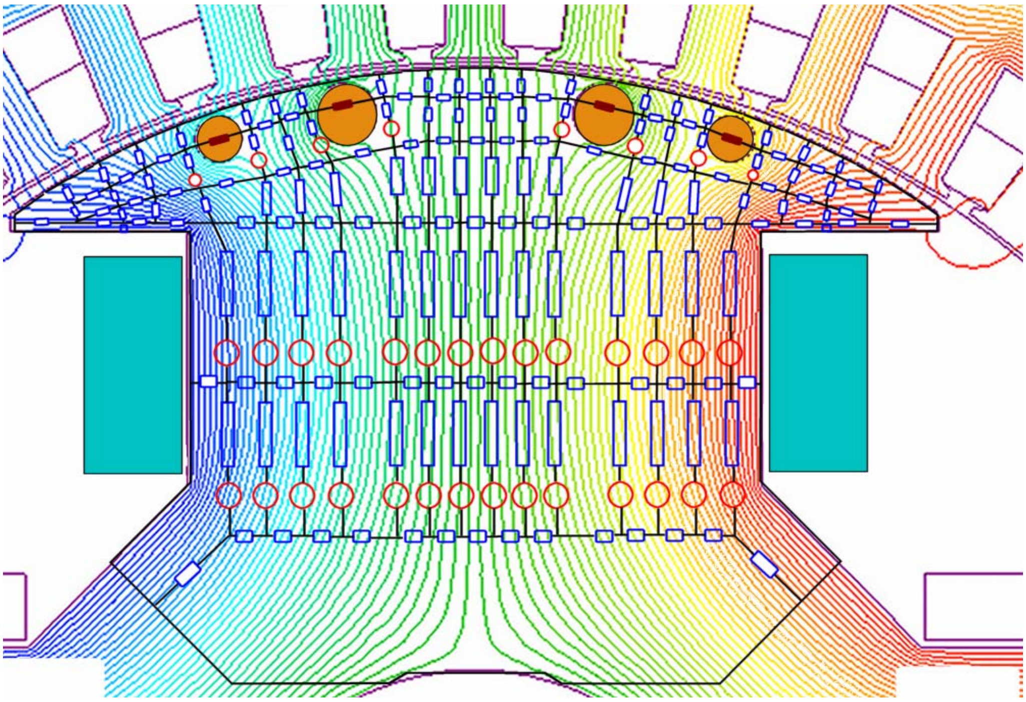

Figure4.4.8 A typical complete salient pole rotor reluctance mesh

In the rotor surface region of a salient pole, reluctance mesh is modified due to the presence of damper bars. A similar type of reluctance mesh for a cage rotor in the induction machine is adopted here in the damper bar regions. One reluctance represents the air gap element across the bar, and other elements represent iron around the damper bar. In order to take account of the surface flux in rotor, and also the flux flowing below the damper bar, two layers on the top of the rotor surface are added. There are three elements between each pair of damper bars because there might be some flux distortion between two damper bars, as can be seen from the damper bar region in figure 4.4.8, thus an additional central reluctance is added to account for the possible flux difference between bars. Mmf sources are modelled in the same way were done with the cage rotor induction machine.

In the meshing process, topology of the virtual teeth on the rotor surface decides the topology inside the rotor, and these all depend on the approximate flux distribution inside the pole. Thus, for the tangential direction, apart from the first two layers which are situated at the damper area, another tangential layer of reluctance mesh is needed which conduct the pole tip flux to the pole centre, representing tangential flux across the pole, although it is normally small. Also, a tangential path which accounts for the tangential flux path in the middle of the yoke and connects with the inter pole leakage reluctances in the leakage area, needs to be added to the reluctance mesh. In the shaft area, there is also a tangential path to account for the circular flux around the shaft, as can be seen in figure 4.4.8. The tangential reluctance mesh of the salient pole generator is shown in figure 4.4.8.

As to the radial flux in the salient pole, the meshing process could be created based on the discretisation of the virtual teeth on the salient rotor surface that have already have been set up. Each virtual rotor tooth on the salient pole rotor surface connects with one branch of reluctance mesh representing radial flux. These radial reluctance branches are divided into central branch and pole tip branch. Central branches will end up at the node around the shaft area, while pole tip radial reluctance branch will end up at the pole tip area facing the shaft. In central reluctance branches which represent the radial flux, two mmf sources exists in each branch in the pole yoke area. This is due to the fact that one tangential path separates the radial branch and thus there has to be two reluctances in each of the radial branches. Since two mmf sources are situated in each radial branch, the winding magnetomotive force has to be split evenly between the two mmf sources. The radial flux reluctance mesh of a salient pole generator could be shown in figure 4.4.8. Given the reluctance mesh shown in figure 4.4.8 for the salient rotor pole, the flux in the pole tip area could flow to anywhere inside the pole through the radial and tangential network, if mmf potential difference exists.

4.4.3 Damper winding modelling

In previous sections, the dynamic reluctance mesh for the salient rotor synchronous machine as well as the non-uniform air gap modelling has been introduced. This section will concentrate on the modelling of the damper bars in the salient pole. Some modelling approaches different to the methods that have been adopted for induction machines will be used to model the damper bar electrically and magnetically, because of the irregular spacing of these damper bars on the salient rotor surface. Details of damper bar modelling for a salient pole synchronous rotor will be given in this section.

Damper bars are acknowledged as one of the most important method to reduce the instability during synchronisation or rapid change in load for salient pole generators. Thus damper bar modelling is a very important aspect in simulating a practical salient-pole synchronous machine.

Damper bars here are different from that of induction machines in that they are not equally spaced and the reluctances between each damper bar is not just one. The DRM principle of modelling mmfs is that: a magnetic loop requires that no 'fake' internal loop should exist, so that no 'fake' flux would exist in the proposed reluctance meshing solution. Thus, if one mmf source were added for each damper bar, as shown by the circles in the radial direction flux branch, in figure 4.4.9, there would be 'fake' internal flux circulating around the bars, as shown by the arrow in figure 4.4.9. To eliminate these 'fake' internal fluxes, other reluctance mesh topology for damper bars has to be proposed.

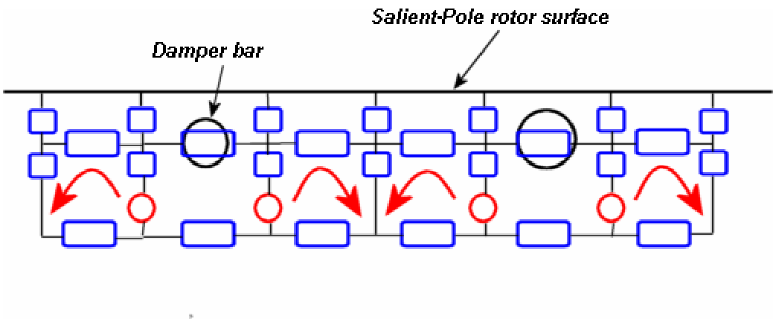

Figure 4.4.9 Reluctance mesh topology for modelling of damper bars which has 'fake' internal flux loop

To solve this, some virtual damper bars are added, as the way done to virtual rotor teeth for the salient pole. Thus, there is one damper bar associated with each virtual tooth on the salient pole rotor surface, some of the damper bars are real and some are virtual ones, as shown in figure 4.4.10.

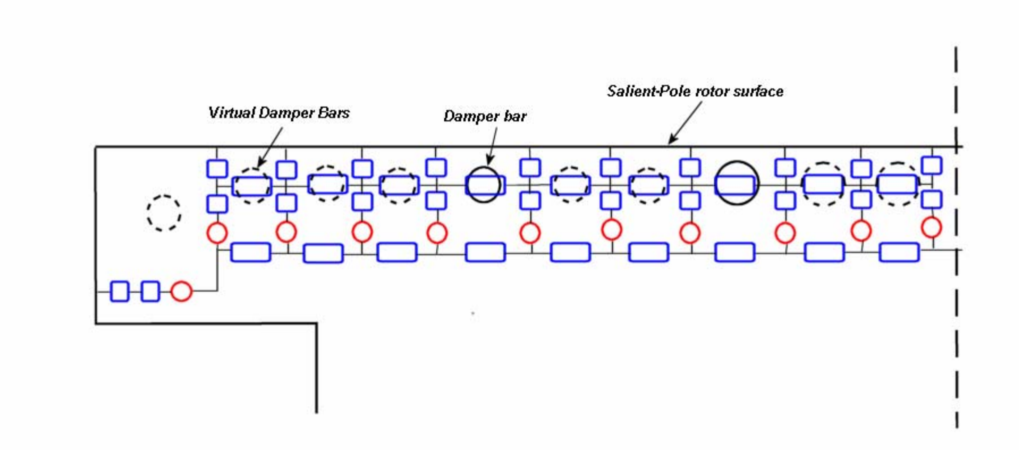

Figure 4.4.10 Virtual Damper Bars and mmfs

By modelling the damper bars as shown in figure 4.4.10, there is no possible fake internal flux circulation existing in the reluctance mesh. In the DRM simulations, the real damper bars and virtual damper bars are discriminated by their resistance: real ones have normal bar resistance, while virtual ones have a very big resistance to stop the current flowing through, such that there is no physical influence by the adding of these virtual damper bars.

Each virtual rotor tooth has a damper bar associated with it now, either a real damper bar or a virtual one. Thus, a salient-pole rotor dynamic reluctance model is unified with an induction machine rotor dynamic reluctance model, and the same electrical loop model could be applied from the induction machine.

As to the right-most flux branch in the salient pole rotor mesh, the virtual damper bar is positioned between two poles. This is a realistic assumption because damper bars on one pole are physically connected with the damper bars on another pole by the short circuit straps [27]. These are made with copper, as show in figure 4.4.11. The DRM model for virtual bars between the two poles can be shown in figure 4.4.12.

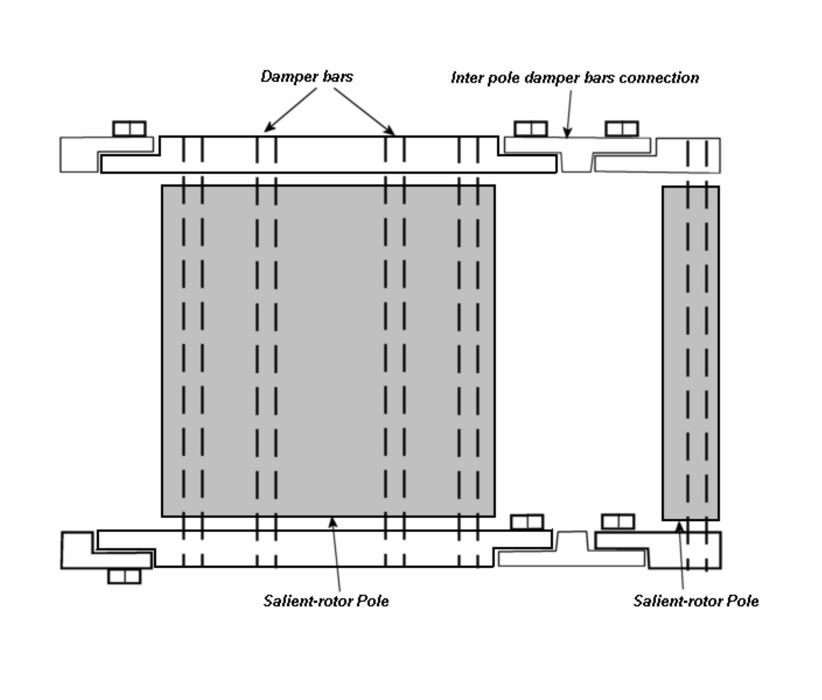

Figure 4.4.11 Real damper bar construction between two poles

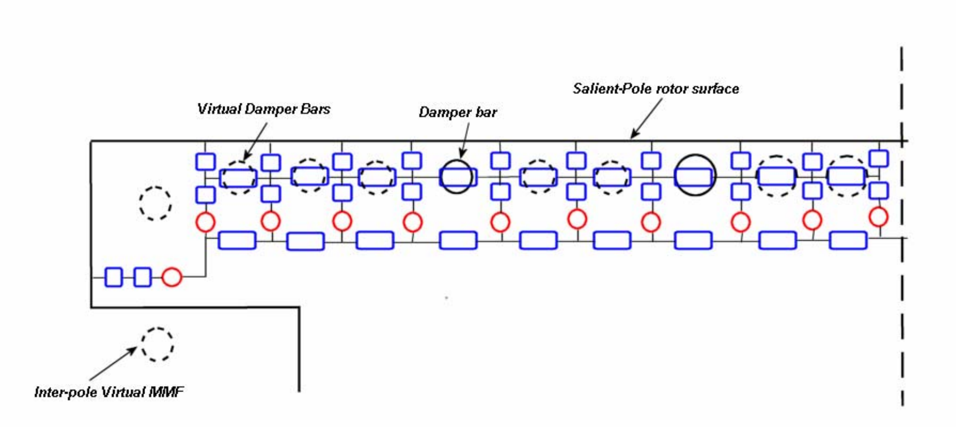

Figure 4.4.12 Virtual damper bar modelling between two salient-poles

With the models of damper bars that have been set up, a DRM model creation of the whole salient-pole synchronous generator could be completed. A complete salient-rotor reluctance mesh is shown in figure 4.4.13.

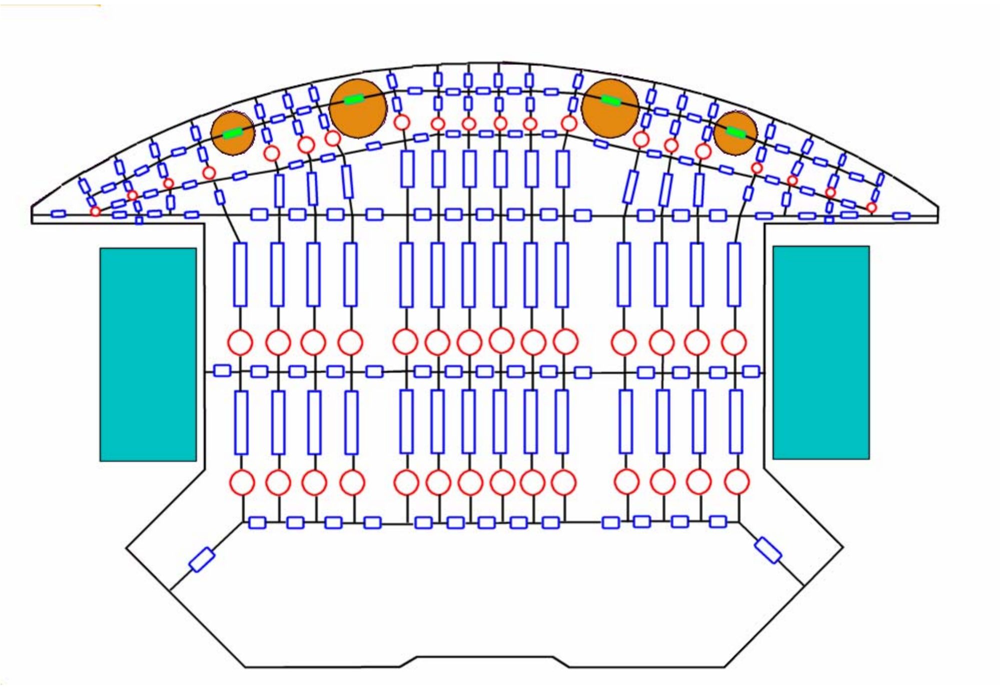

Figure 4.4.13 Proposed complete salient pole rotor reluctance mesh

After completing the creation of the reluctance mesh and the modelling of the damper bars and air gap, a complete DRM model for the salient pole rotor and air gap were set up. The stator reluctance mesh could be similar to that of an induction machine, due to the similar geometry and flux distribution inside the stator. In the following section, the state equations and state variables for the single salient pole synchronous generator will be given, to simulate the machine behaviour.

4.4.4 Equations and state variables for salient pole machine

The operating condition of a usual synchronous machine is that the shaft, to which the salient pole rotor is connected, is driven by a prime mover rotating at synchronous speed. Excitation voltage is applied to the rotor terminals, and a.c. currents are generated on the stator side by the relative rotation of the flux fields and the stationary stator coils.

To solve for the system state, and thus calculate the machine performance, system equations have to be given out. This section will give the state variables describing the system state and the system state equations.

The equations describing the node mmf potentials are the same for different types of machine in a DRM modelling method, as long as they have magnetic circuits. Similar to that of induction machines, equation 4.4.21 is satisfied for each node connecting the reluctances for a salient pole synchronous generator.

$$\sum_{j=0}^{n-1} \phi_j \left(mmf_{j2}, mmf_{j1}\right) = 0 \tag{4.4.21}$$

The rotor electrical circuit equation is:

$$-v_f + i_f R_f + \frac{d\phi_f}{dt} = 0 \tag{4.4.22}$$

where v_f, i_f and R_f are the terminal voltage, field current and resistance of the rotor, and ϕ is the flux flowing through the field winding.

Damper bar circuit equations almost have the same format as that for induction machines cage bars, after the modification of the modelling by virtual damper bars. Thus, electrical equations for adjacent damper bars are:

$$-i_i \cdot R_i + i_{i-1} \cdot R_{i-1} - \frac{d\phi}{dt} = 0 \tag{4.4.23}$$

$$i_i = mmf_{i+1} - mmf_i \tag{4.4.24}$$

Parameters here have the same specification as that in chapter 2.

Stator three phase electrical equations are as same as that of induction machines:

$$-v_A + R_a \cdot i_a + \sum_{i=1}^{S} \frac{de_a}{d\phi_i} \cdot \frac{d\phi_i}{dt} = 0 \tag{4.4.25}$$

$$-v_B + R_b \cdot i_b + \sum_{i=1}^{S} \frac{de_b}{d\phi_i} \cdot \frac{d\phi_i}{dt} = 0 \tag{4.4.26}$$

$$-v_C + R_c \cdot i_c + \sum_{i=1}^{S} \frac{de_c}{d\phi_i} \cdot \frac{d\phi_i}{dt} = 0 \tag{4.4.27}$$

The research work in this thesis is to investigate the simulation of electrical generator's behaviour by using dynamic reluctance mesh simulation method. Thus, the mechanical feature of the machine would not be considered here, and the mechanical shaft speed will be set to a fixed value to be synchronous speed.

Therefore, dynamic rotating equation remains as:

$$\omega_r - \frac{d\theta_{mech}}{dt} = 0 \tag{4.4.28}$$

where ω_r is the shaft mechanical speed, that is a fixed value in the DRM simulations here in this thesis.

Another point that should be mentioned in the simulation model of a synchronous machine is that the number of turns per slot for stator winding is calculated. The following formula is used [33]:

$$N_s = \frac{3T_{ph}n_p}{T_c} \tag{4.4.29}$$

where n_p: number of parallel paths in stator winding; T_c: turns per coil for stator; N_s: number of stator slots; T_{ph}: turns per phase.

Given turns per phase in the machine data sheet, turns per coil for the stator winding will be calculated which will be used in DRM simulations.

4.5 Results

In this section, a typical salient-pole synchronous generator is simulated using the dynamic reluctance mesh modelling method for the salient pole machine described in previous sections. The machine is a four pole, 85KVA, 68KW, fifty Hz, with 0.8 power factor, three-phase, star connected synchronous generator. The schematic drawing of the machine electrical connection is shown in figure 4.5.1.

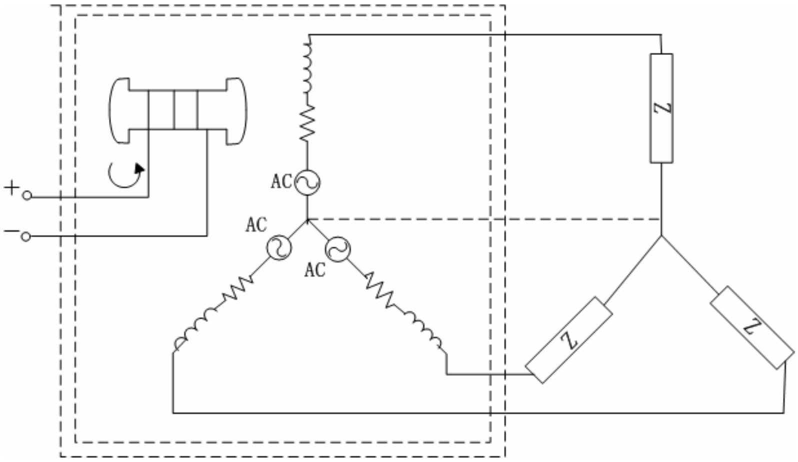

Figure 4.5.1 Schematic drawing of electrical connection for the generator to be simulated

In the testing that is done in this section, the rotor is excited by a d.c. voltage. In practise, a rotor terminal is usually fed by an exciter, which is actually another a.c. generator, through a rotating rectifier. However, it is excited directly through d.c. voltage in the tests in this chapter, for the reason that a single generator test is wanted, rather than a complicated system testing. Testing for the complete system will be performed in the next chapter.

An open circuit test and a short circuit test with the DRM model will be presented in this section, and also the results compared to the experimental results. System performance with and without damper bars in sudden short circuit condition is also simulated and investigated.

4.5.1 Open circuit & short circuit test

Testing conditions for open circuit test is: large resistive load is connected to the stator three-phase to simulate open circuit conditions. The big resistance virtually limits the phase current such that stator open circuit condition is simulated numerically. Different rotor excitation voltages are applied to rotor terminals, and stator terminal line-to-line voltages are recorded as the output voltage. The rotor speed is fixed to the synchronous speed numerically as mentioned in the previous section.

Experimental data of the open circuit and short circuit test is shown in figure 4.5.2.

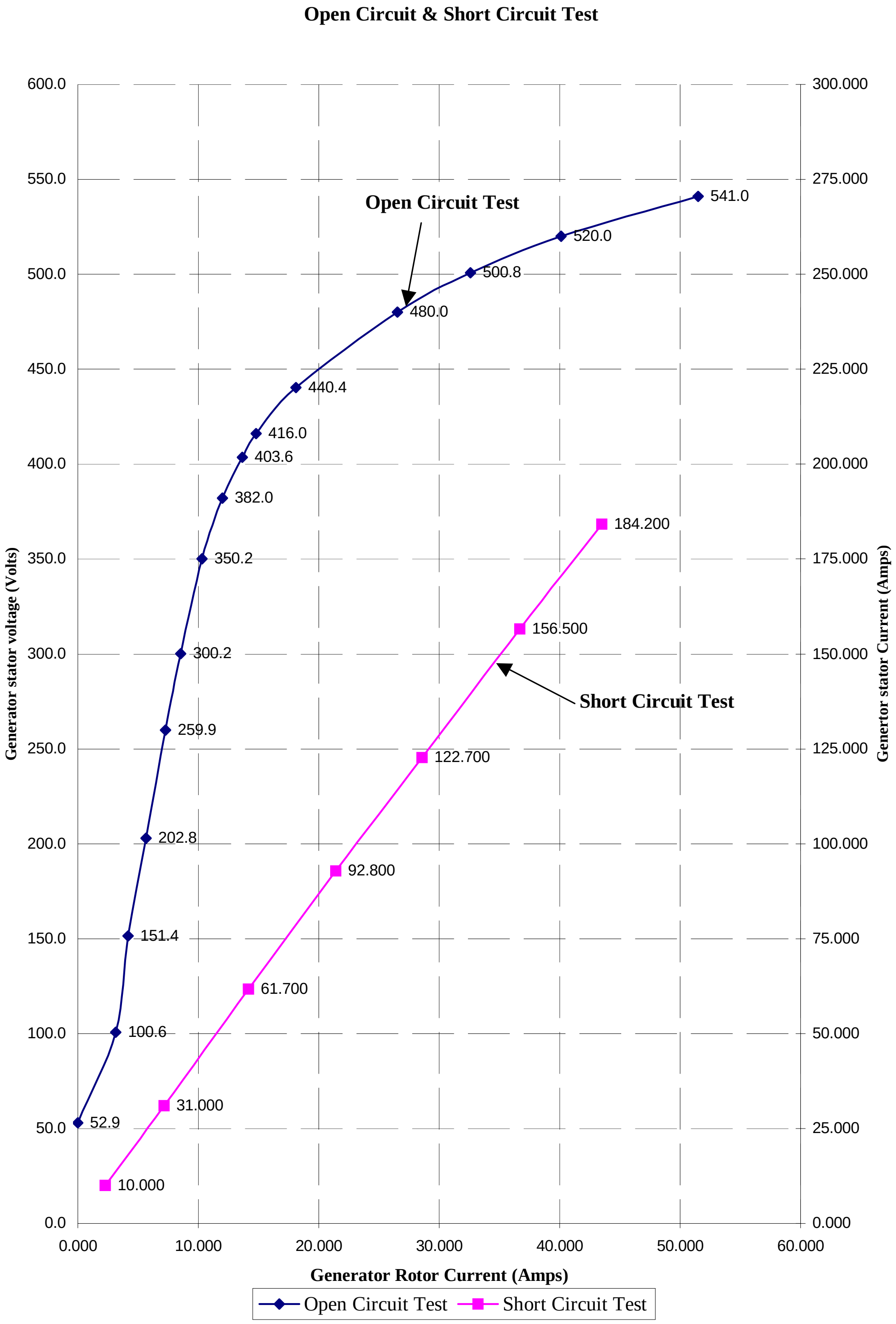

Figure 4.5.2 Experimental result of open circuit test and short circuit test

The DRM result for the open circuit test is shown in figure 4.5.3. As can be seen, the simulation result is quite close to the experimental results, especially in the rated generating voltage area, which is 400 volts. Maximum error in the result comparison is –8.7%, and the average error in percentage is 2.5%, which is excellent for engineering simulations. The relatively big error in the result with the increasing of field current is due to the material saturation. The material used in a DRM simulation is slightly different from that used in the experimental result. Thus, the small difference in material saturation characteristic can cause the result difference in figure 4.5.3. Iron material that has been used in DRM simulation is Losil 800 for both the stator and the rotor, while the material used in the real machine is Losil 800 for the rotor and DK70-65 for the stator.

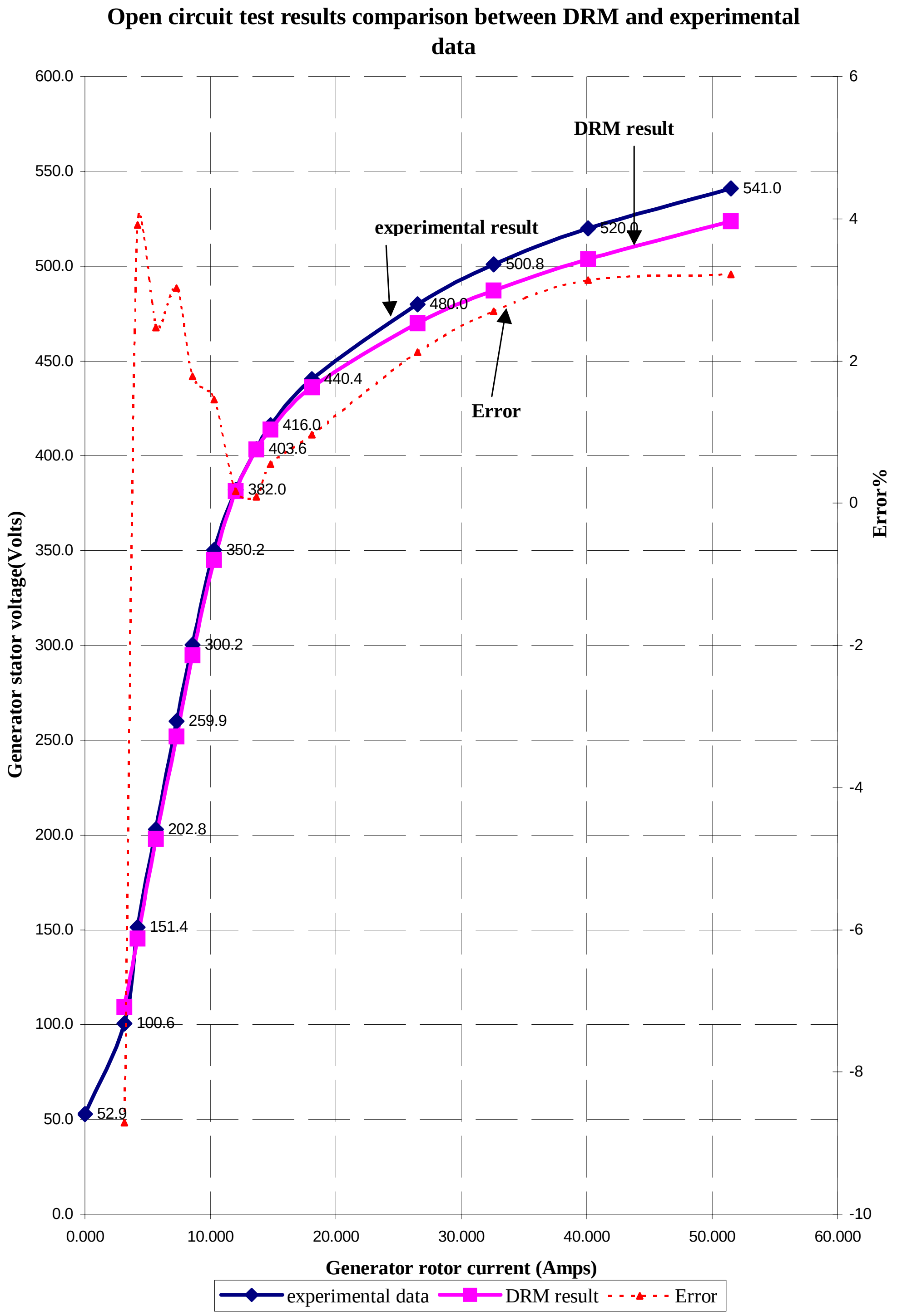

Figure 4.5.3 Open circuit result comparison for DRM and experiment data

In DRM simulations, rotor resistance rise with regards to temperature is also considered by using rotor resistance calculated from the experimental data sheet.

A short circuit test is also simulated by the DRM modelling technique. The testing condition for a short circuit is: zero electrical loads are connected to the stator terminals, and the rotor excitation d.c. voltage is varied to derive the full testing curve. Stator phase currents are recorded as the output.

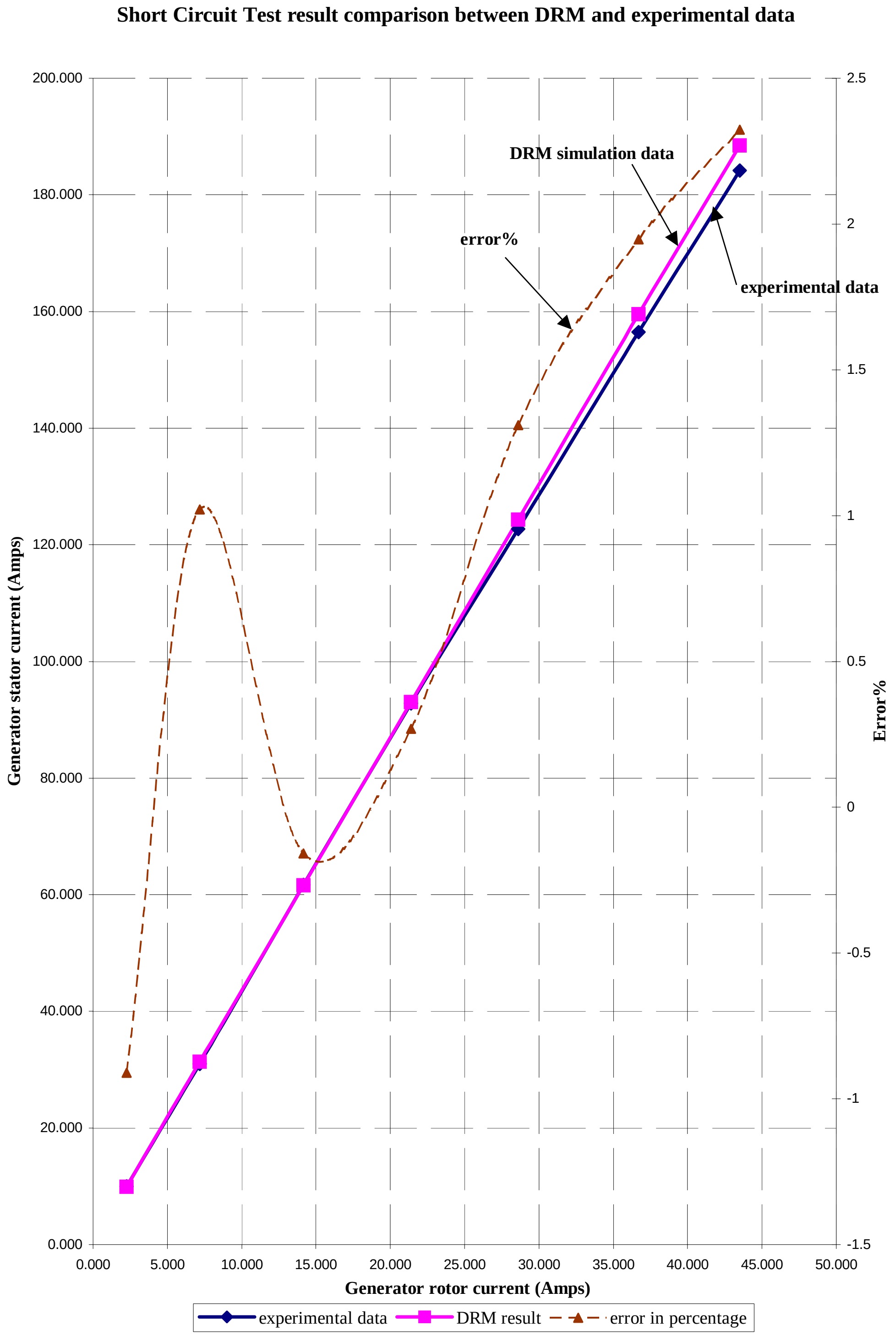

Figure 4.5.4 Short circuit test result comparison between DRM and experiment

Figure 4.5.4 shows the short circuit test result comparison between the DRM simulation result and the experimental result. They are quite close, and error is within 2.5%, with an average error of 1.135%, which is excellent for engineering simulations. Again, the relatively big error in the saturation region is due to the different material used in the DRM simulations compared to that used in the experiment.

4.5.2 Sudden short circuit test

Sudden short circuit conditions are important in generator performance evaluations, and could cause great damage if not properly treated. In this section, sudden short circuit condition of synchronous generators will be simulated, and the effect of damper bars during the sudden short circuit condition will be investigated, by using a DRM simulation tool.

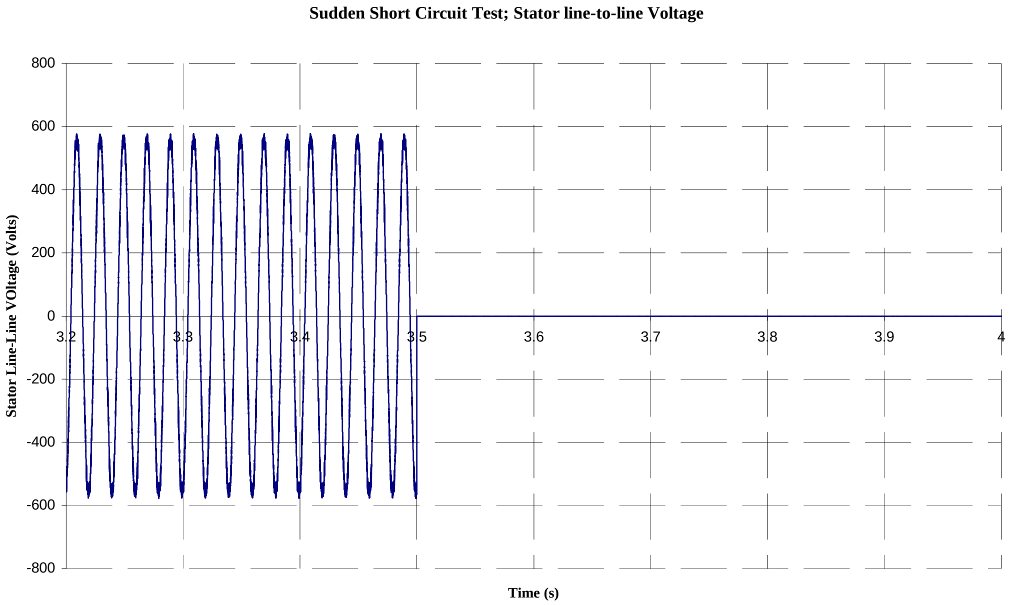

Figure 4.5.5 Sudden short circuit test, stator line-to-line voltage

Figure 4.5.4 shows the generator stator terminal voltage waveforms during sudden short circuit operating conditions. The short circuit happens at 3.5 seconds. It can be seen that the stator terminal line-to-line voltage value becomes very small as expected.

Figures 4.5.6 to 4.5.9 show the changing of stator phase current and field current during sudden short circuit transients. Due the theorem of constant linkage [27], flux linkage in an inductive magnetic circuit tends to remain the flux to be a constant level when there is a sudden flux change in the circuit. Thus, rotor current response to the sudden change of flux generated by sudden change of stator short circuit currents, and very large rotor current generated. Actually, these rotor current variations take place partly in the rotor winding, partly in other closed paths available for current flow, such as damper windings.

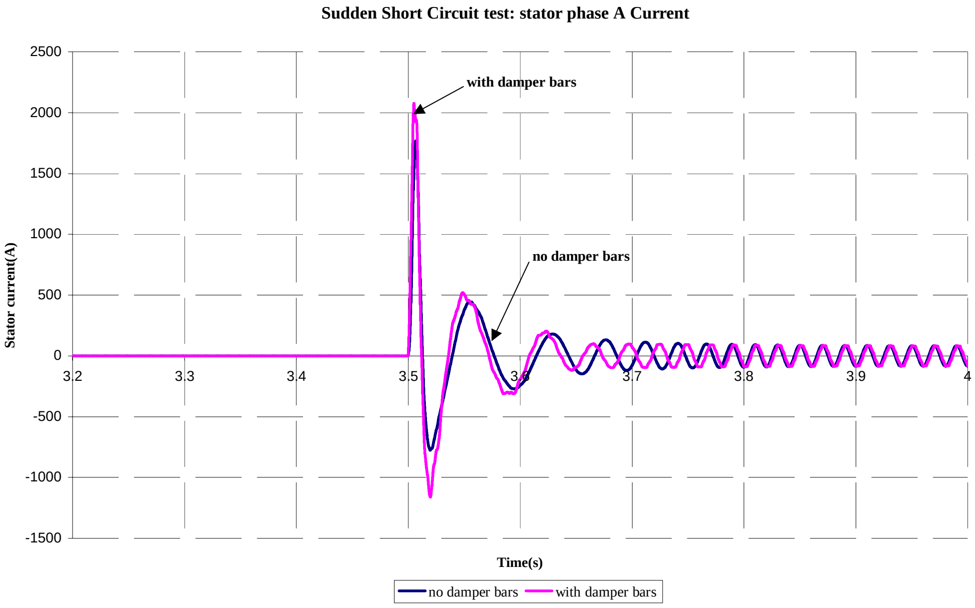

Figure 4.5.6 Sudden short circuit test stator phase current

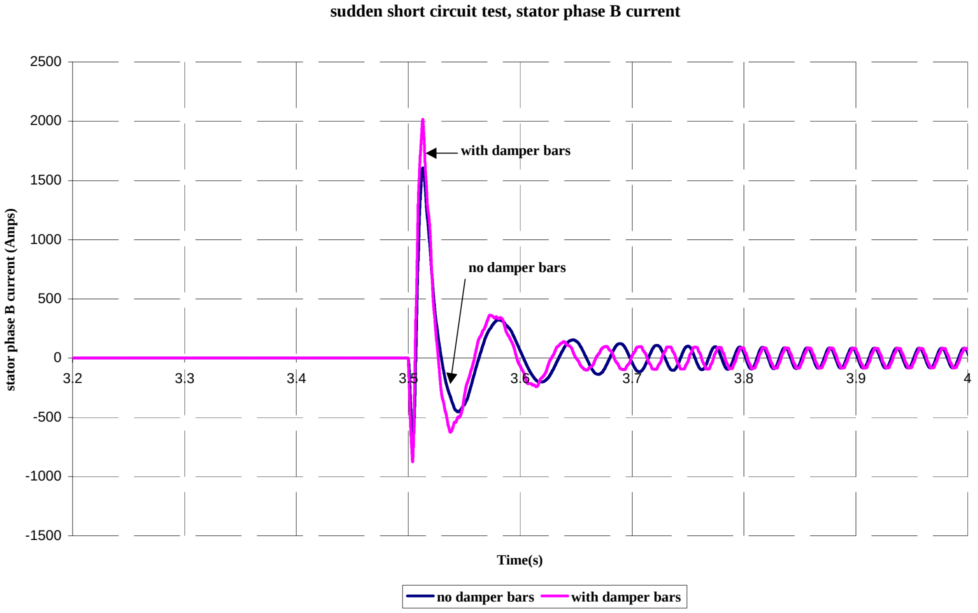

Figure 4.5.7 Sudden short circuit test, stator phase B current

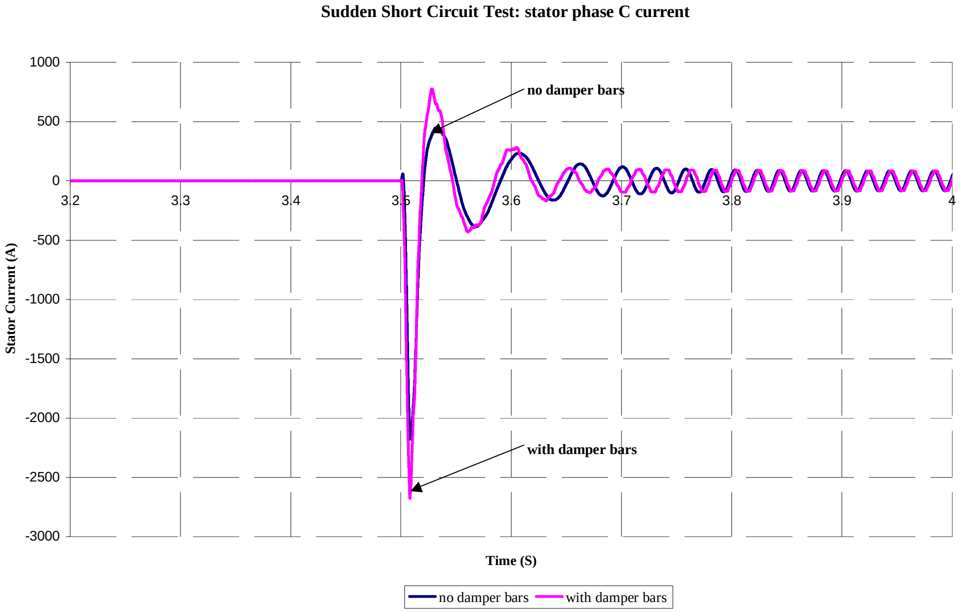

Figure 4.5.8 Sudden short circuit test, stator phase C current

At the moment of short circuit of a three-phase machine, the flux linking the stator from the rotor is caught and ‘frozen’ to the stator, giving a stationary replica of the main-pole flux. For this purpose each phase will, in general, carry a d.c. component, which will cause d.c. offset or asymmetry in the waveform of the stator current with respect to time, and will disappear with time. The quantity of d.c. offset depends the relative position of the stator and rotor in the instance of short circuit. As can be seen from figures 4.5.6-4.5.8, d.c offset is different for the stator three phase current.

The initial short circuit currents are limited by the transient reactance x'_d and sub-transient reactance x''_d, which characterises the effective leakage inductance. The steady state short circuit current, however, is limited by x_d, where x_d is the synchronous reactance of the generator.

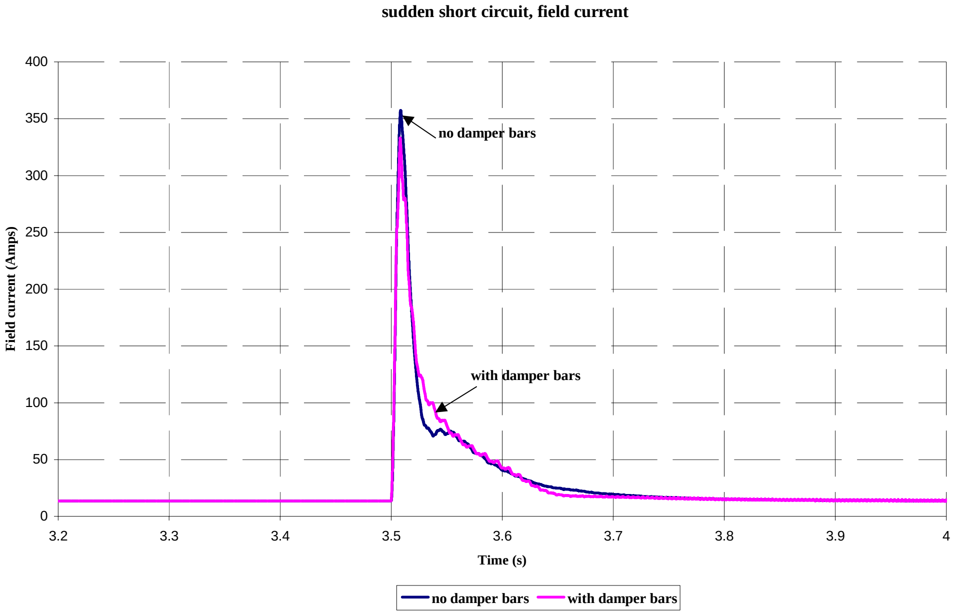

Figure 4.5.9 Sudden short circuit test, generator field current

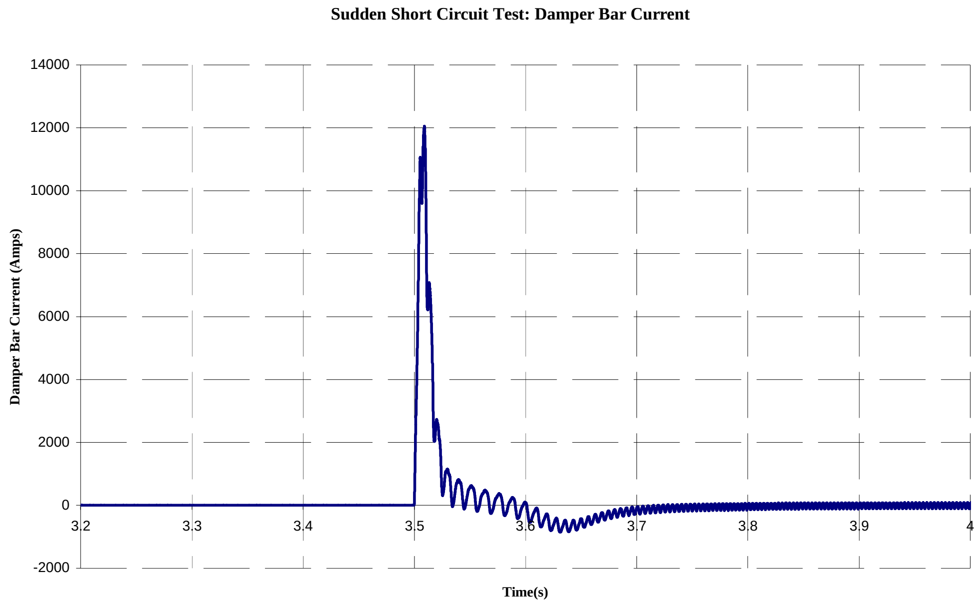

Figure 4.5.10 Sudden short circuit test, damper bar current

Damper winding plays an important part in synchronous machine transient. It reduces the oscillations in currents and helps maintain mechanical stability. As shown in figures 4.5.6-4.5.10, compared with the machine that has damper windings, stator phase currents of the generator that has no damper winding are lower and field current is more in a sudden short circuit case. This is because the damper bar is a part of the rotor windings, and it accounts for part of flux change in the whole rotor windings, apart from the field winding. A simple comparison for the current between the machine with damper bars and without damper bars is shown in table 5.1.

	Field current	**Stator phase current**
No damper bar generator	**more**	**less**
Damper bar generator	**less**	**more**

Table 5.1 Comparison of currents in generators with and without damper bars

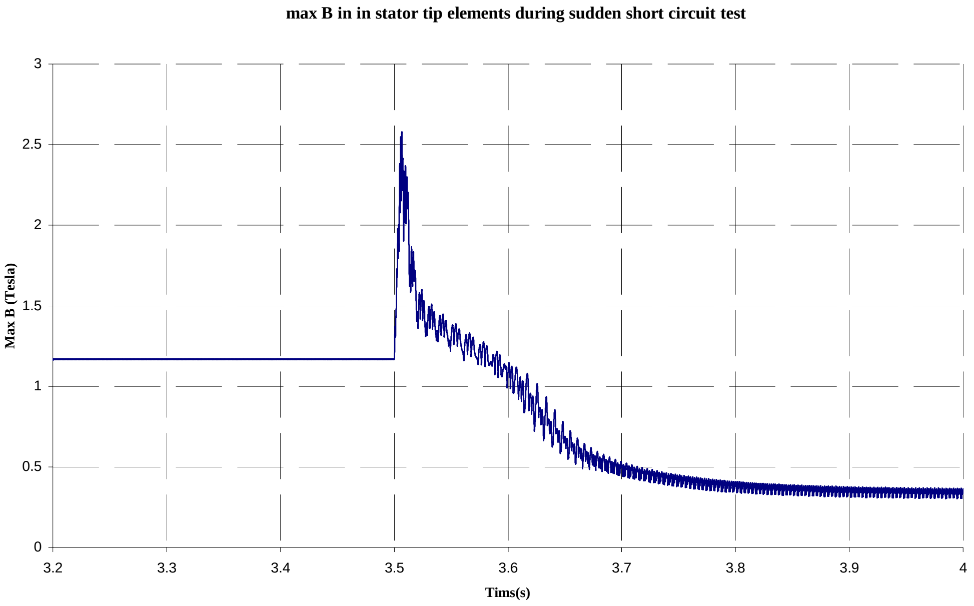

Figure 4.5.11 Sudden short circuit test, max B in stator tooth tip reluctances

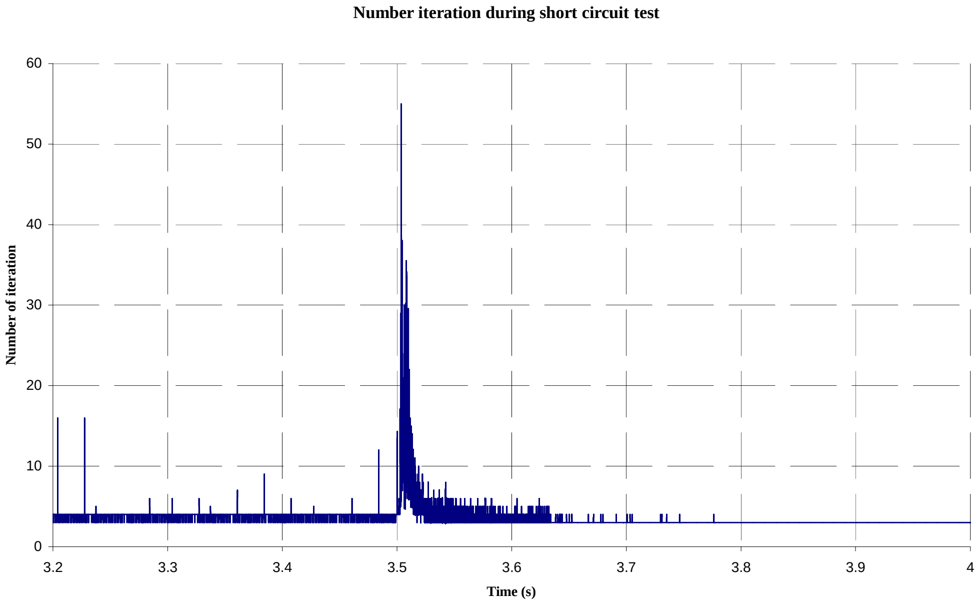

Figure 4.5.12 Sudden short circuit test, number of NR iterations

Figure 4.5.11 shows the maximum flux in stator tooth tip elements for a generator with a damper bar. It can seen that the stator tooth tip iron is saturated during short circuit transience. The number of Newton-Raphson iterations also increased during short circuit transience due to the sudden change of the machine system state, as can be seen in figure 4.5.12.

4.5.3 Damper bar investigation

With the help of DRM software, the damper bar effects in synchronous machines could be investigated. Figure 4.5.13 shows the damper bar currents in open circuit running conditions.

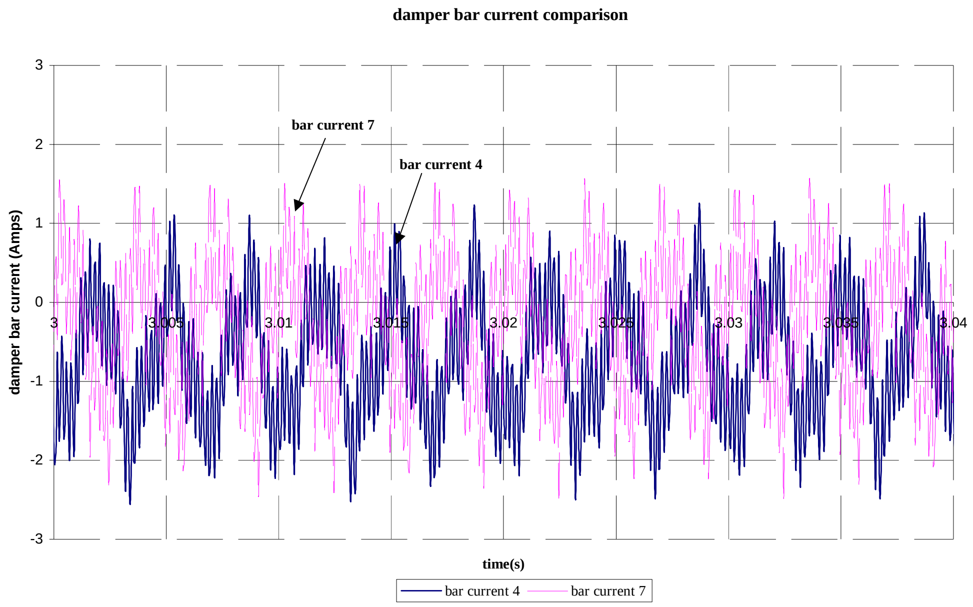

Figure 4.5.13 Adjacent Damper bar currents

Figure 4.5.13 shows the adjacent damper bar currents. As can be seen from the figure, there are phase offsets between the currents of adjacent bars. They are caused by the different damper bar positions on the salient rotor pole surface. Thus, current in one damper bar leads the current in the next bar following the rotating direction. The phase offset between the currents depends on both the speed of the rotor and the distance between the bars.

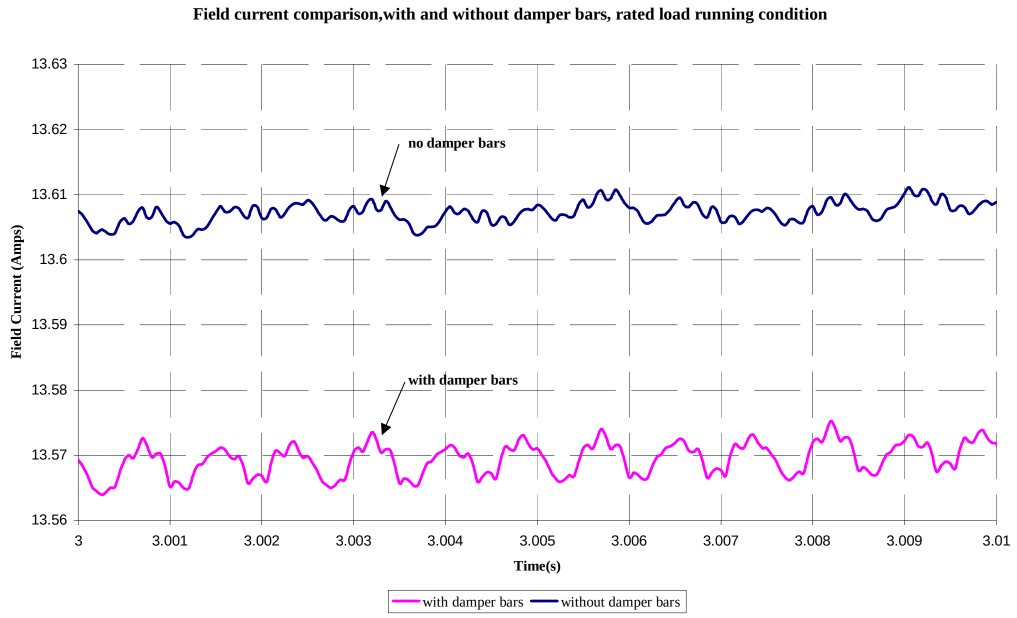

Figure 4.5.14 Field current comparison for generators with and without damper bars, at a rated load running condition

Darabi [32] mentioned the damper bar effect in genset alternators, that damper bar will introduce a slot harmonics to field current, as can be seen from figure 4.5.14. Field current for a machine with damper bars has more slot harmonics than the one with no damper bars. Figure 4.5.14 shows the damper bar current with slot harmonics in it, and the harmonics frequency is tooth passing frequency, which is 48*25=1200.

4.6 Conclusion

This chapter introduced and validated a way of modelling and simulating salient-pole synchronous generators efficiently based on the Dynamic Reluctance Mesh method. Details of the modelling method, including reluctance mesh creation, the modelling of the non-uniform air gap, virtual rotor teeth model in accordance with air gap meshing, and virtual damper bar model have been described. Open circuit test and short circuit test from the DRM model have been simulated and validated by experimental results. Results have shown that the DRM model could achieve excellent results compared with the experimental results. Sudden short circuit running conditions and the effect of damper bars have also been simulated and investigated.

Compared with the Finite Element Method, results that come out of the DRM model are quite satisfied, both with accuracy and speed. Thus this Dynamic Reluctance Mesh model could provide a faster and more effective way of simulating salient-pole synchronous generators in engineering solutions, which can be used in further analysis such as generator system simulations and investigations, where currently commercial FEM software was not able to cope. This will be mentioned further in later chapters.

CHAPTER 5 SIMULATION AND INVESTIGATION OF BRUSHLESS GENERATING SYSTEM

5.1 Introduction

In this chapter, the DRM models for brushless generating systems, including the models of the exciter, the rotating rectifiers, and the automatic voltage regulator (AVR) will be discussed. The DRM model for the main generator has been described and validated in chapter 4 and will not be given here.

This work is a significant advance on conventional methods of simulating a generator system. Normally, system models are analysed using programs like MATLAB^{TM} Simulink where conventional sinusoidal dq machine models are employed. Such machine models are very limited and neglect many saturation, harmonic and slotting effects inherent in a practical machine. Modelling using the detailed field models of machines is also normally confined to a single machine at a time such as a generator. That is system models are not examined. The work presented in this chapter includes detailed field models of both the generator and exciter as well as models covering the rotating rectifier and AVR all. That is the complete system is simulated at one time with the entire practical machine features included. This approach ensures that design of the system can be highly refined and critical operating conditions associated with voltage recovery following a fault can be optimised.

The work presented includes an initial examination of generator and exciter systems to show that the system chosen is the most appropriate for general study. Generator systems normally comprise the excitation systems, which supply d.c. current to synchronous generators field winding, although some small generators are sometimes built with permanent-magnet field excitations. Since the rotor is rotating, a special arrangement is required to get the d.c. power to its field windings. There are several common approaches to supplying this d.c. power [34] [35]:

1. Supply the d.c. power from an external d.c. generator to the rotor by means of slip rings and brushes, as shown in figure 5.1.1. D.c. current is generated by a d.c. generator whose rotor is mounted on the same shaft with the main generator rotor, and the generated d.c. voltage is connected to the main rotor field winding through the slip rings and brushes. This excitation method creates a few problems, when it is used to supply d.c. power to the field windings of a synchronous machine. It increases the amount of maintenance required on the machine and brush voltage drop can be the cause of significant power losses on machines with larger field currents. Despite these problems, slip rings and brushes were used on smaller synchronous machines, because no other method of supplying the d.c. field current was cost-effective.

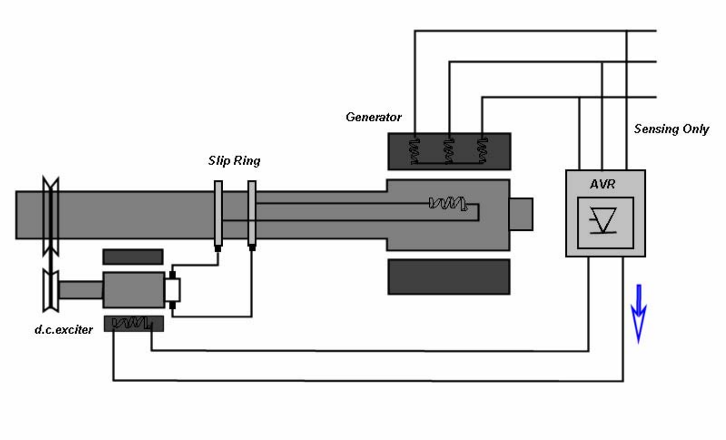

Figure 5.1.1 Conventional excitation of generator systems

2. There is also another choice, which is static excitation for the synchronous generator systems. There are no rotating parts in this excitation system, and the excitation power is supplied from the generated voltage itself, as shown in figure 5.1.2. Generated voltage from the main generator comes to a static

rectifier and also the AVR then d.c. current is fed into the main generator field windings. The advantage of this kind of system is that it is more compact than the first one in size, but it will lose excitation in the case of generator fault, and also slip rings and brushes are needed which increase maintenance.

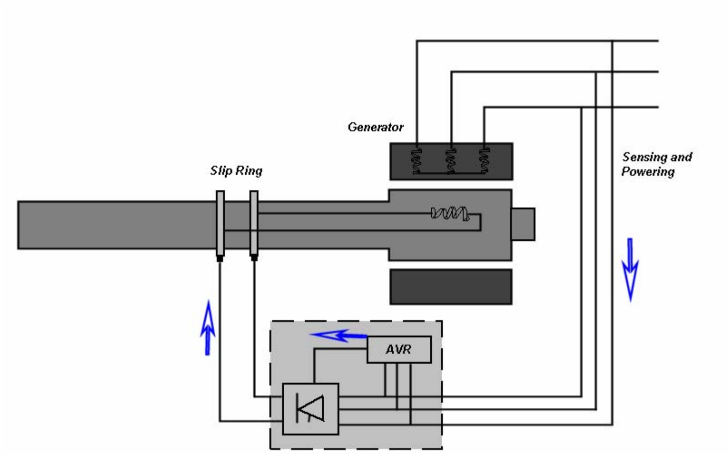

Figure 5.1.2 Static excitation of generator systems

3. Large synchronous generators and modern industrial generators are equipped with a brushless excitation systems, which means no slip rings and brushes are needed. Excitation is supplied by another a.c. generator, which is called an exciter. The exciter is a small a.c. generator with its field circuit mounted on the stator and its armature circuit mounted on the rotor shaft, as shown in figure 5.1.3. The three-phase output of the exciter generator is rectified to direct current by a three-phase rectifiers circuit also mounted on the shaft of the generator and is then fed into the main d.c. field circuit. Exciter field winding is supplied and controlled by the automatic voltage regulator, which senses the voltage that comes from the main generator stator. Since no mechanical contacts ever occur between the rotor and the stator, a brushless exciter requires much less maintenance than slip rings and brushes. However, in the case of generator short circuit fault, there would no excitation for the generator system, which is still a problem. Nevertheless, this configuration is the most common and is the one to be simulated in this chapter.

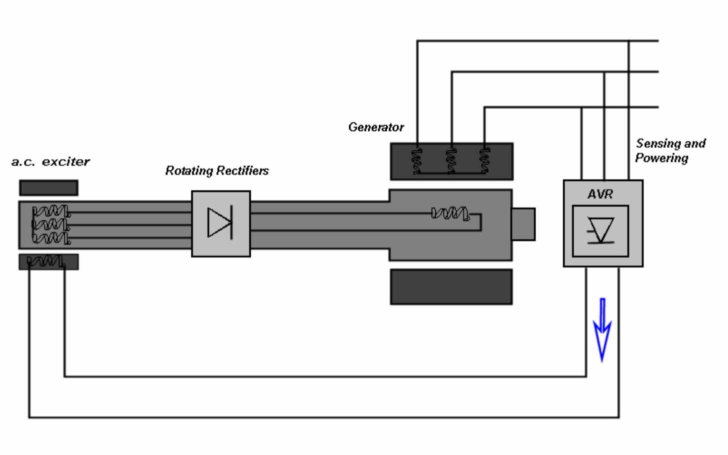

Figure 5.1.3 Brushless excitation of generator systems

4. To make the excitation of a generator completely independent of any external power sources, a small pilot exciter is often included in the system. A pilot exciter is a small a.c. generator with permanent magnets mounted on the rotor shaft and a three-phase winding on the stator. It produces the power for the field circuit of the exciter, as shown in figure 5.1.4, which in turn controls the field circuit of the main machine.

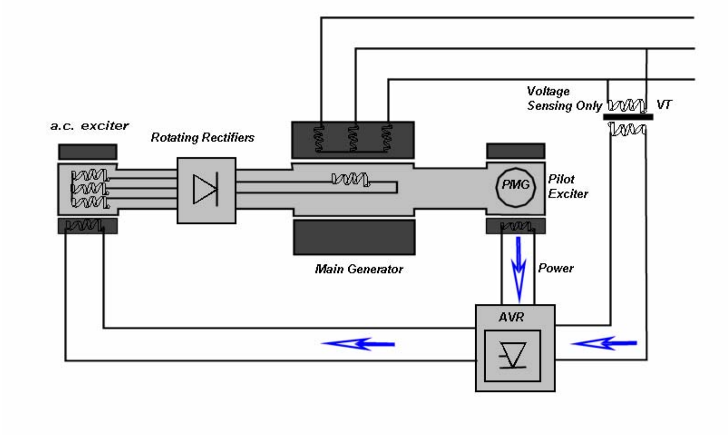

Figure 5.1.4 Brushless excitation with pilot exciter of generator system

It is not common for people to simulate the generating system including main generator, exciter and AVR altogether, because this involves two machines and also the power electronic components as the state equations need to be solved simultaneously. For a simple mathematical machine model, the whole system state equations may be solved. However, for the latest Finite Element technology, commercial software could not simulate two machines at the same time, although it might be possible in the near future. Darabi [36] simulated the brushless generator system with a small salient-pole synchronous machine and an exciter including AVR using FEM. However, the exciter model was not an FE model but a parametric model based on self and mutual inductances.

Due to the great flexibility and efficiency of Dynamic Reluctance Modelling technology, the complete brushless generating system including the exciter, the rotating rectifiers and the main generator, and voltage regulator, as the system shown in figure 5.1.3, can be simulate simultaneously. However, the AVR that is modelled here in this chapter is quite a simple model. It would not be a problem to utilize a more advanced AVR model and control algorithms into the generating system, so that the more realistic voltage regulation could be investigated. Even for the brushless generating system including the pilot exciter, the DRM could accommodate this kind of simulation without a great effort. It would all just require more work and the objective here is to show how the full field models of two or more machines can be incorporated with the control algorithm quite easily using the DRM approach.

In this chapter, the complete brushless generator system, including exciter, rectifiers and main generator and a simple automatic voltage regulator will be modelled. The generator model using the DRM has been described in chapter 4, and results have shown that the DRM model gives good accuracy from an engineering point of view. Exciter modelling will be described firstly in this chapter, and the rectifier model described next together with the system equations and state variables. Simulation results are given together with experimental results to justify this part of the model. Then the design and modelling of the AVR controller is described. Finally, the DRM simulations result of the complete brushless generating system are then described and discussed.

5.2 Exciter Modelling Scheme

The exciter is effectively a reversed synchronous machine with field winding staying on the stator and armature winding staying on the rotor side. The exciter geometry that is to be modelled in this chapter is shown in figure 5.2.1. Details of the exciter can be found in appendix 7.

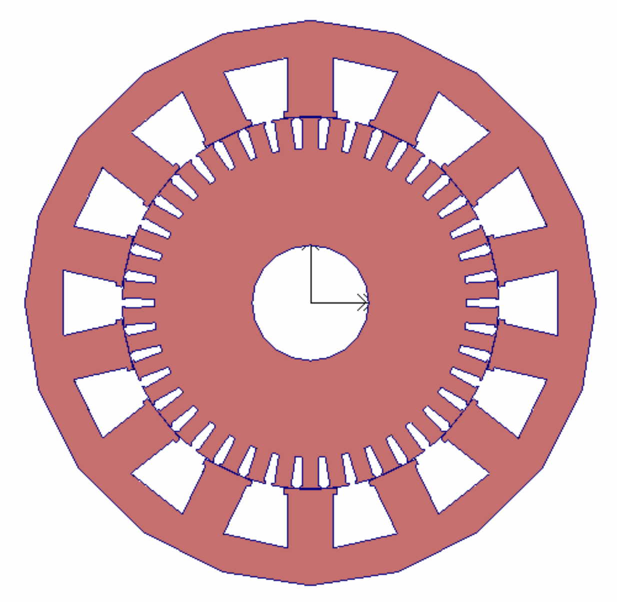

Figure 5.2.1 Exciter geometry, with field winding staying on the stator and armature winding on the rotor

5.2.1 Meshing the exciter

Based on the geometry of the exciter stator and rotor shown in figure 5.2.1, the same kind of meshing schemes for to the induction machine given in chapter 2 are applied to the exciter discretisation process. The only difference in the discretisation from that of the induction machine is that there is less number of stator teeth in the stator of exciter. Considering that there will be leakage flux flowing through the stator slots and rotor slots, for the reason described in chapter 3.5, and that saturation of the teeth will probably be high, one additional reluctance representing the leakage flux crossing the slots between the two teeth is included. The cross-section of the typical exciter reluctance mesh is shown in figure 5.2.2.

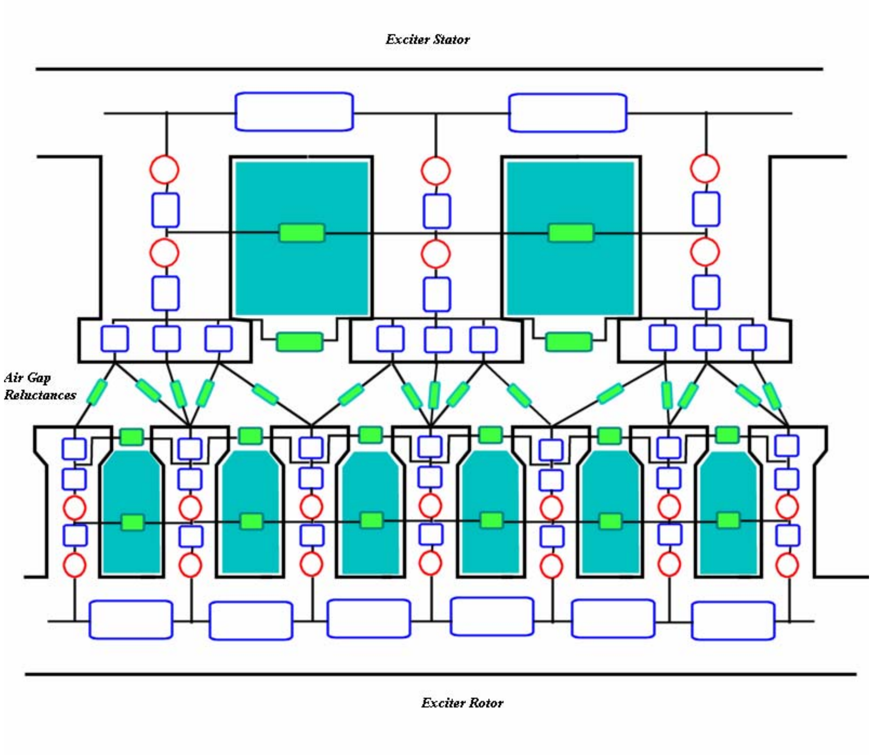

Figure 5.2.2 Sections of exciter reluctance mesh model

Hollow rectangles in figure 5.2.2 represent the iron reluctances, the circle is the mmf source due to winding currents, and filled rectangles are the air type reluctances, including leakage reluctances between slots and dynamic air gap reluctances connecting stator and rotor teeth. The method of calculating the reluctances is the same as described in chapter2.

5.2.2 Air gap reluctance curve of the exciter

Air gap reluctance curve method, which is named for method 3 in chapter 3, can be applied to different kinds of machines, and the number of reluctance curves depends on the detailed air gap geometry. There is only one air gap reluctance curve for the induction machine due to its uniformed air gap length and the similar width for the stator and rotor teeth. Several air gap reluctance curves are essential for salient pole synchronous machines due to their non-uniform air gap length design and the very big inter-pole area, which makes inter pole leakage flux significant.

By applying the method described in chapters 3 and 4, the air gap reluctance curves for the exciter machine can be derived. In deriving the air gap reluctance curve, the excitation coil is put on the rotor side, as has been done with both induction machine and synchronous machines. Fluxes entering into each virtual stator tooth are then evaluated. Thus the effective flux linkage between a virtual stator tooth and a rotor tooth can be calculated for different offset positions in the form of the effective width of uniform air gap reluctances. Figure 5.2.3 shows the air gap reluctance curve for this type of exciter machine.

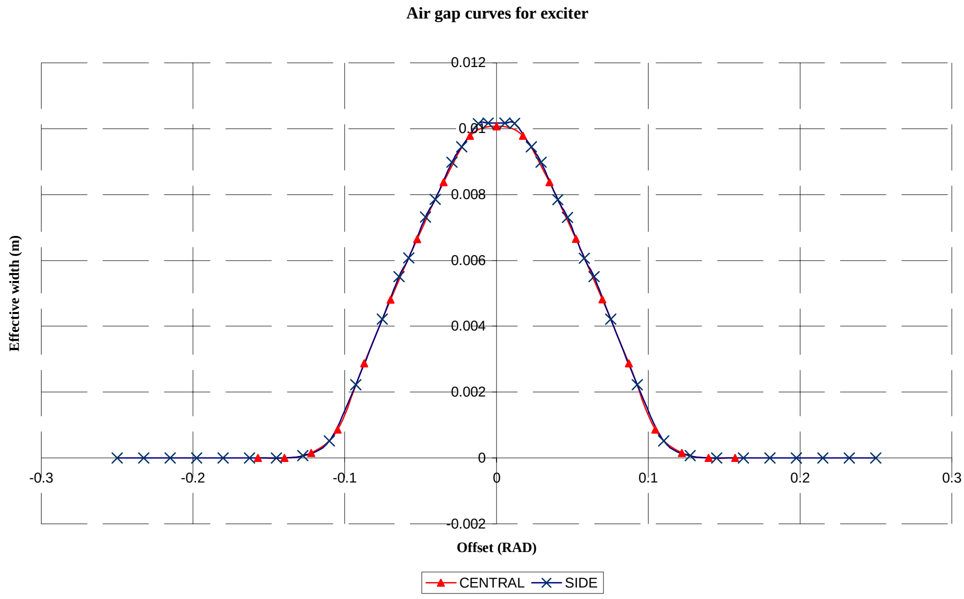

Figure 5.2.3 Exciter air gap reluctance curves

There are two curves in the figure, which are for the central and side virtual teeth for the stator respectively. 3 virtual teeth exist on the stator teeth of the exciter, for the reason that the relatively wider stator teeth width compared to that of the rotor. Comparison of the simulation results from different number of virtual teeth will be made in chapter 7 later.

5.2.3 Exciter machine system equations

In creating the system equations, the equations for the node mmfs are the same for all types of machines, independent of machine geometry.

$$\sum_{j=0}^{n-1} \phi_j \left(mmf_{j2}, mmf_{j1}\right) = 0 \tag{5.2.1}$$

Equation for the electrical circuit of the field winding, which is staying on the stator side for an exciter, is:

$$-V_f + i_f R_f + \frac{d\phi_f}{dt} = 0 \tag{5.2.2}$$

Equations for the electrical circuit of the armature windings, which are staying on rotor for an exciter, are:

$$-v_A + R_a \cdot i_a + \sum_{i=1}^{S} \frac{de_a}{d\phi_i} \cdot \frac{d\phi_i}{dt} = 0 \tag{5.2.3}$$

$$-v_B + R_b \cdot i_b + \sum_{i=1}^{S} \frac{de_b}{d\phi_i} \cdot \frac{d\phi_i}{dt} = 0 \tag{5.2.4}$$

$$-v_C + R_c \cdot i_c + \sum_{i=1}^{S} \frac{de_c}{d\phi_i} \cdot \frac{d\phi_i}{dt} = 0 \tag{5.2.5}$$

The dynamic equation for rotating angle is:

$$\omega_r - \frac{d\theta_{mech}}{dt} = 0 \tag{5.2.6}$$

5.2.4 Simulation results

With the dynamic reluctance mesh model set up for the exciter, simulations have been done to verify the functioning of this model. An open circuit condition for the rotor starting with zero field current and an applied field voltage has been examined and the results are shown in following figures.

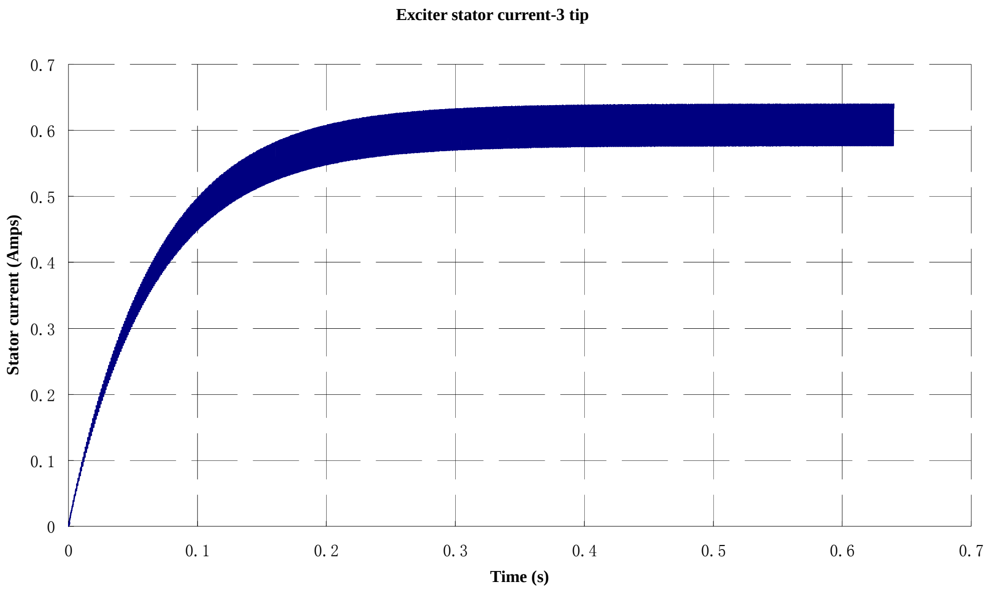

(a) Exciter stator current in open circuit condition

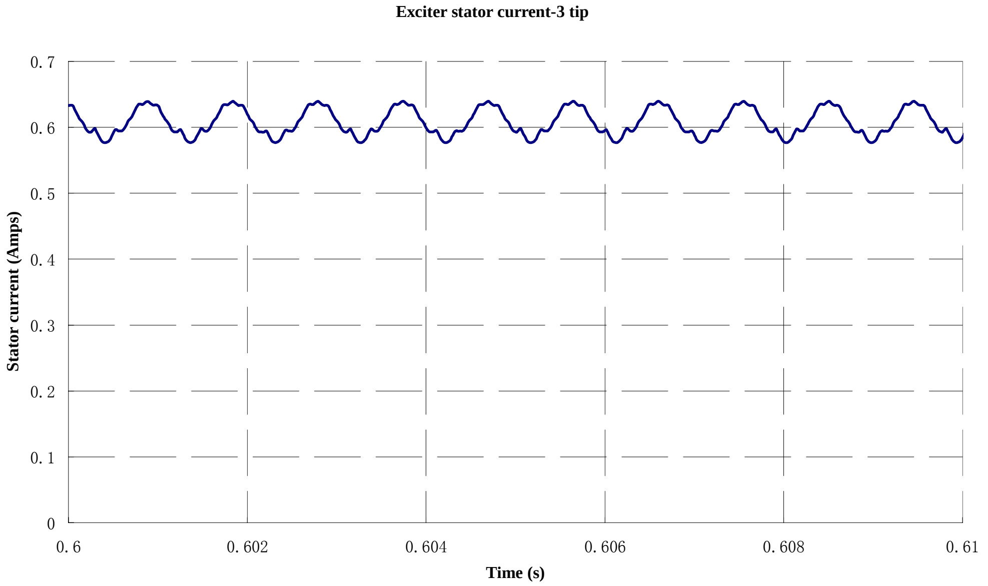

(b) Exciter stator current (zoom in view) in open circuit condition

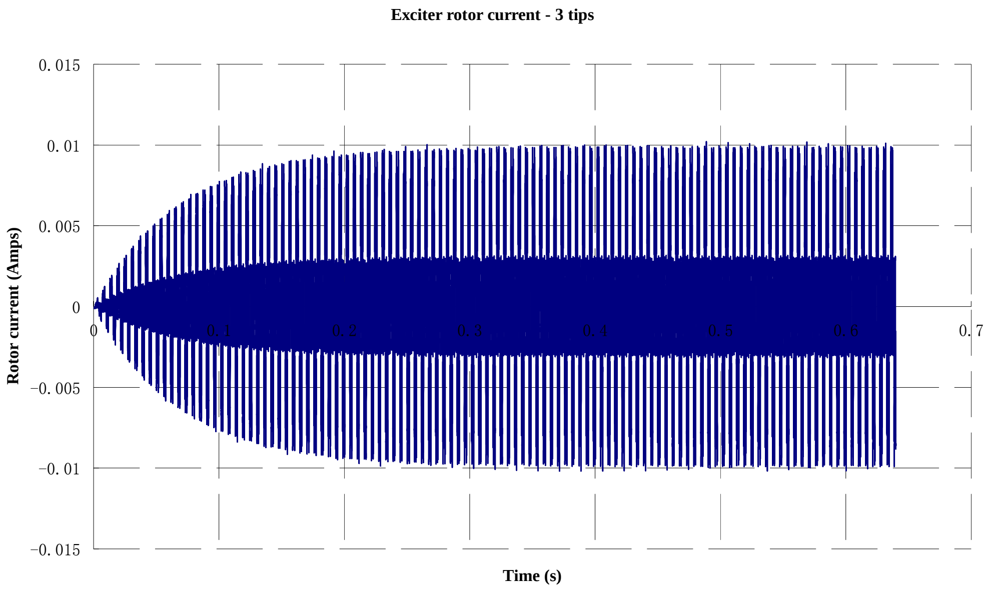

(c) Exciter rotor current in open circuit condition

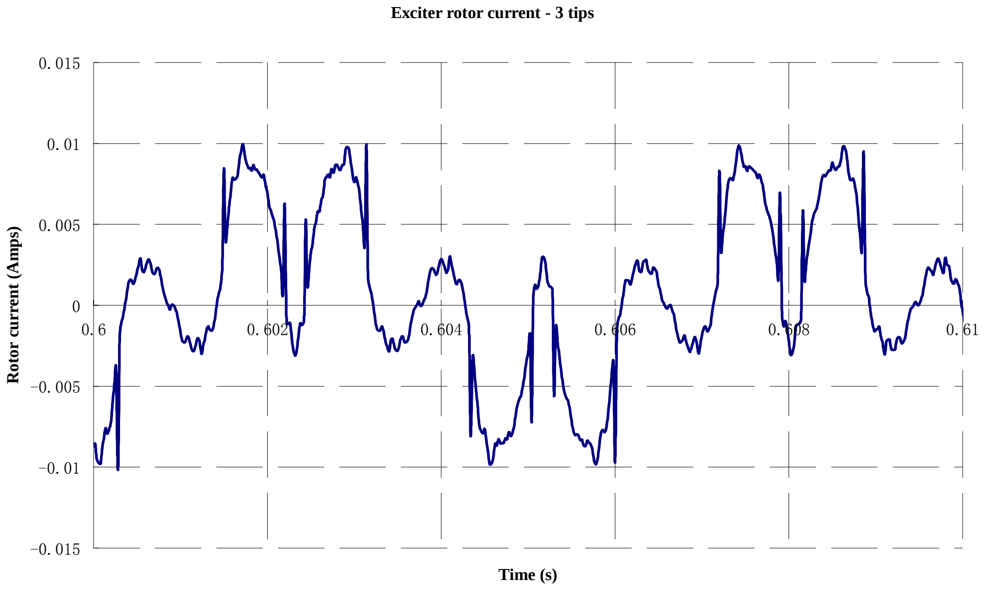

(d) Exciter rotor current (zoomed in) in open circuit condition

Figure 5.2.4 Exciter current waveforms in a numerical simulated open circuit condition

It can be seen from the result that there is d.c. current on the stator of the exciter, and the high frequency harmonics is caused by slotting on the rotor. The slotting harmonics frequency is 1050=25*42, where 25 Hz is the rotor's mechanical speed and 42 is the number of rotor teeth. There is a very small rotor current in this simulated open circuit rotor condition, because the open circuit condition is simulated numerically by adding a very big resistance load to limit the physical current. The slotting on the stator side causes the harmonics in the rotor current. The harmonics frequency is 175=25*7.

5.3 Rotating Rectifier Model

In generating systems, the rectifier converts a.c. current generated by the exciter to d.c. current which is fed into the field winding of the main generator. It is always mounted on the shaft and rotates together with the shaft.

In Industrial applications, where three-phase a.c. voltages are available, it is preferable to use three-phase rectifier circuits, compared to single-phase rectifiers, because of their low ripple content in the waveform and a higher power-handling capability. The three-phase, six-pulse, full-bridge diode rectifier shown in figure 5.3.1 is a commonly used circuit arrangement.

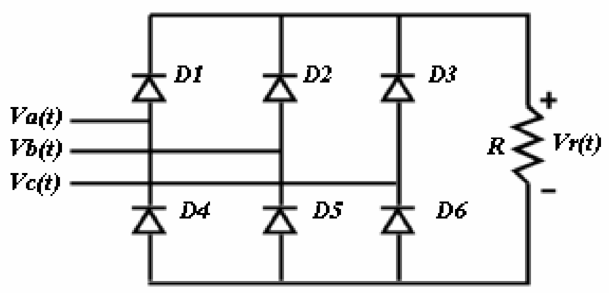

Figure 5.3.1 Six diodes full wave three-phase bridge rectifier

The small brushless generating system modelled in this chapter uses the full-bridge rectifier shown in the figure above. To model each single diode in the rectifier, different diode models can be used. The idealized model of a diode is shown in figure 5.3.2.

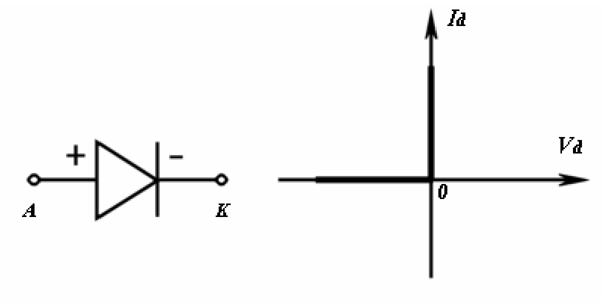

Figure 5.3.2 Ideal diode and its circuit symbol

When the diode is forward biased, it begins to conduct with only a small forward voltage across it, which is on the order of 1V. When the diode is reverse biased, only a negligibly small leakage current flows through the device until the reverse breakdown voltage is reached.

In the DRM modelling, each of the diode in the full wave bridge rectifier is modelled as a voltage function with diode input current [37], as shown in figure 5.3.3. The reason why this model is used in the DRM modelling instead of an ideal model is that the ideal model will cause numerical difficulties due to its complete non-linearity and the discontinuity of its first order derivative. By using the $v-i$ characteristic shown in figure 5.3.3, the diode $v-i$ characteristic becomes first order continuous which aids mathematical stability. The characteristic shown in figure5.3.3 is also the real $v-i$ characteristic of a practical diode.

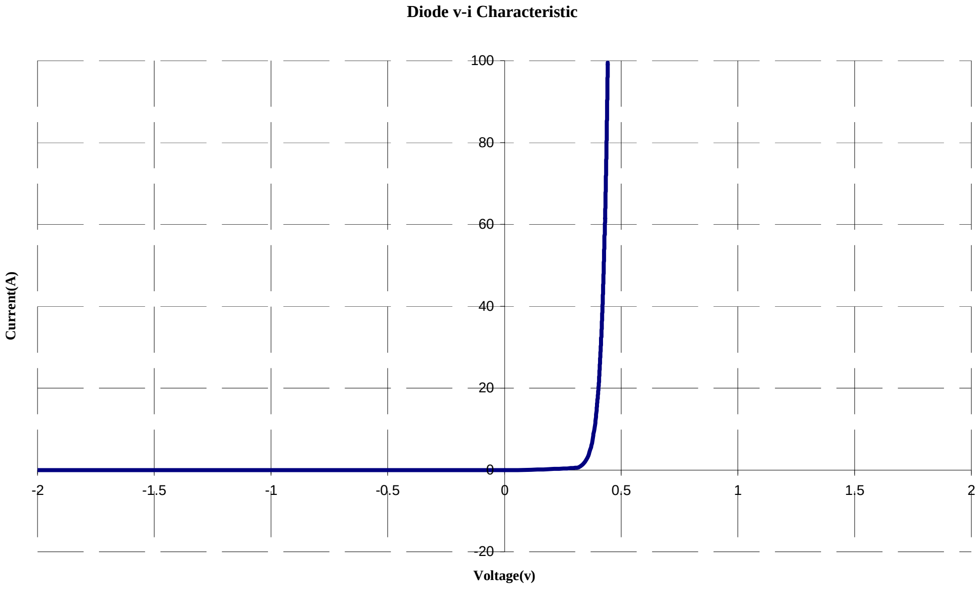

Figure 5.3.3 Practical diode $v-i$ Characteristic

In the first quarter of the practical diode function graph, the $v-i$ relation of a silicon diode is:

$$I = I_s\left(e^{eV/\eta kT} - 1\right) \tag{5.3.1}$$

where I_s is the leakage current which between the range of 10^{-4} to 10^{-9}, and factor η is approximately 2 for a silicon diode, but for silicon diode at high currents and for geranium diodes, $\eta \cong 1$. In room temperature (20^{o}C), $e/kT \cong 40V^{-1}$. Thus, equation 5.3.1 is converted into the form of equation 5.3.2 for a silicon diode under room temperature:

$$I = I_s\left(e^{20V} - 1\right) \tag{5.3.2}$$

For the negative voltage part of the practical diode function, due to its very big breakdown voltage the diode's $v-i$ characteristic is modeled by a very large resistance, which limits the physical reverse current in the diode model. The value of the resistance depends on the slope of the positive $v-i$ function at the origin to maintain a continuous slope change, thus reducing numerical solution difficulties.

The diode model finally used in the DRM system model is as shown in figure 5.3.4. It is build with a practical diode model shown in equations 5.3.2 in parallel with a very large resistance.

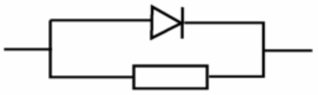

Figure 5.3.4 Diode model in the rotating rectifier model in the DRM Modelling

5.4 Equations and State Variables for the Power Generation Part of the System

Figure 5.4.1 shows the complete electrical connection of the generating system except the AVR control. It can be seen that there is only electrical connection between the exciter rotor windings and the rectifiers, and also between rectifiers and generator field winding. No magnetic flux link exists between the machines and the rectifiers. Thus, to model the complete system performance, only the electrical link between the two machines and the rectifiers need to be considered.

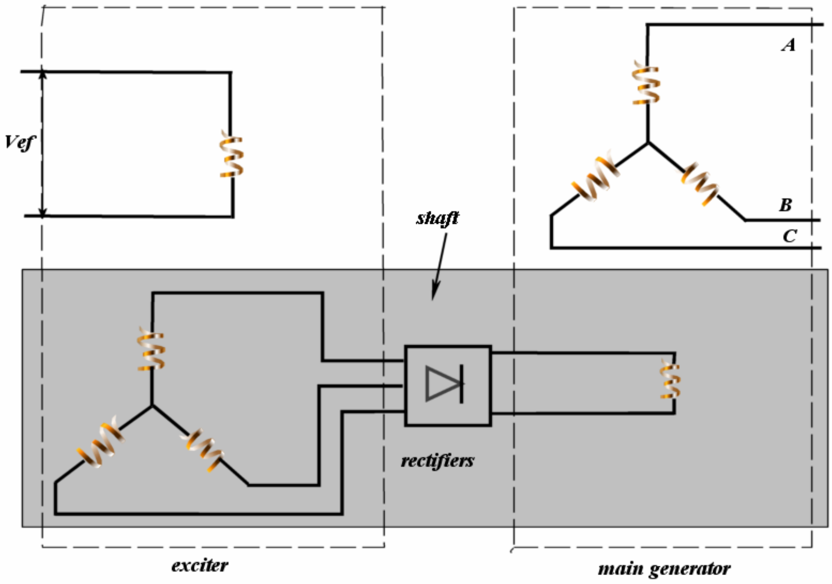

Figure 5.4.1 Schematic generating system diagram

To solve the current value flowing through each diode in the rotating rectifier, electrical circuit equations should be defined based upon the number of independent variables in the loops. Considering the star connected three-phase generator winding, the circuit loop of the complete generating system is shown in figure5.4.2.

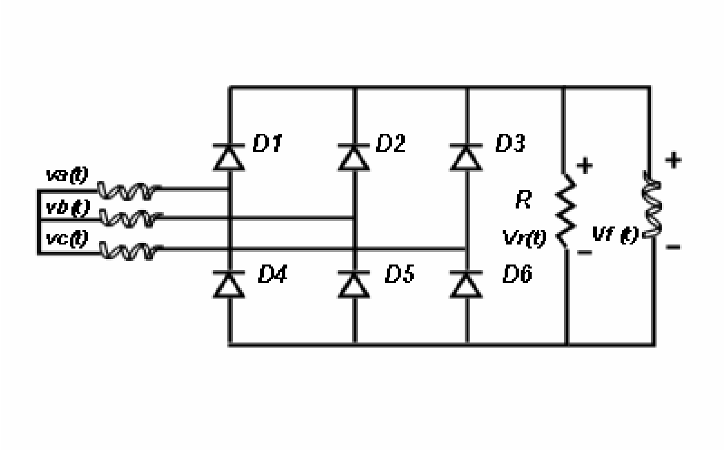

Figure 5.4.2 Electrical circuit diagram of generating system

As can be seen from figure 5.4.2, the circuit is actually a 3D topology circuit and there is more than one return loop for each a.c. winding. In order to get a clearer view of the electrical loops in figure 5.4.2, rearrangement is made to the electrical circuit in figure 5.4.2, shown in figure 5.4.3.

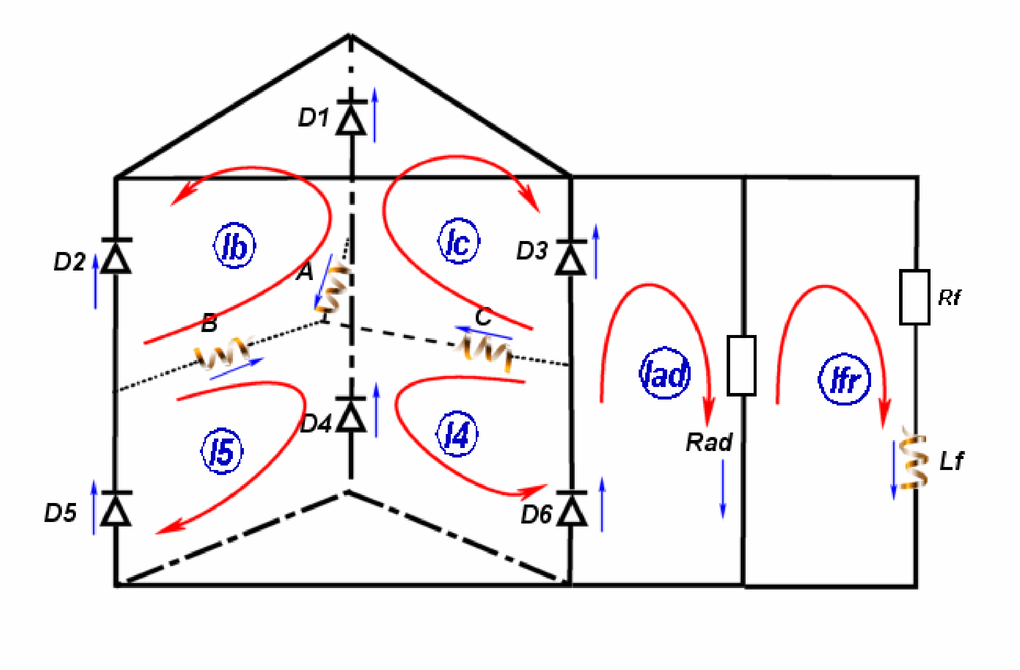

Figure 5.4.3 Rearranged electrical circuit of generating system

The arrow close to the element shows the reference current direction of each element in figure 5.4.3. Positive diode currents are taken to be from anode to cathode, and winding currents in the exciter rotor windings are taken to be flowing into the neutral point of the star connected windings.

To solve the electrical state of the expanded electrical network above, the independent solution variables have to be defined and the number of the variables should equal the number of independent electrical loops in the graph. It can be seen that from figure 5.4.3, the number of independent electrical loops is six, shown by the circulated arrows, and the loop associated with each independent variable is marked with circled character. All the other electrical loops are different combinations of these six electrical loops shown above.

Thus, the independent solution variables are assigned as: the currents flowing through diodes D_4, D_5; the rotor winding currents of the exciter phase B and C; the current flowing through additional resistance R_{ad}; and the d.c. current in the main generator rotor, as shown in Table 5.4.1.

Independent solving variables for currents	
Exciter rotor phase B winding current	i_b
Exciter rotor phase C winding current	i_c
Diode $D4$ **current**	i_4
Diode $D5$ **current**	i_5
Resistor R_{ad} **current**	i_{ad}
Main generator rotor winding current	i_{dc}

Table 5.4.1 Independent variables in solving electrical network in figure 5.4.3

The reason why the exciter rotor phase B and C’s currents are taken as the independent variables is because the rotor windings are star connected in this machine, thus two variables are sufficient.

Then, the currents in other elements can be derived easily by using simple additions, which are shown in Table 5.4.2.

Current Flowing through	
Diode $D1$ **current**	$i_4 + i_b + i_c$
Diode $D2$ **current**	$i_5 - i_b$
Diode $D3$ **current**	$i_{ad} + i_{dc} - i_4 - i_5 - i_c$
Diode $D6$ **current**	$i_{ad} + i_{dc} - i_4 - i_5$
Exciter rotor phase A winding current	$-i_b - i_c$

Table 5.4.2 Currents flowing through each element in electrical network

With the independent solution variables given, the electrical circuit equations in each independent loop can be derived, as shown in equation 5.4.1 to 5.4.6.

For exciter rotor winding phase B's loop i_b:

$$N_b \frac{d\phi_b}{dt} + R_b i_b - N_a \frac{d\phi_a}{dt} + R_a(i_b + i_c) + volt\_dio(i_4 + i_b + i_c) - volt\_dio(i_5 - i_b) = 0 \tag{5.4.1}$$

For exciter rotor winding phase C's loop i_c:

$$N_c \frac{d\phi_c}{dt} + R_c i_c - N_a \frac{d\phi_a}{dt} + R_a(i_b + i_c) + volt\_dio(i_4 + i_b + i_c) - volt\_dio(i_{ad} + i_{dc} - i_4 - i_5 - i_c) = 0 \tag{5.4.2}$$

For loop i_4:

$$N_c \frac{d\phi_c}{dt} + R_c i_c - N_a \frac{d\phi_a}{dt} + R_a(i_b + i_c) - volt\_dio(i_4) + volt\_dio(i_{ad} + i_{dc} - i_4 - i_5) = 0 \tag{5.4.3}$$

For loop i_5:

$$N_b \frac{d\phi_b}{dt} + R_b i_b - N_a \frac{d\phi_a}{dt} + R_a (i_b + i_c) - volt\_dio(i_4) + volt\_dio(i_5) = 0 \tag{5.4.4}$$

For loop i_{ad} :

$$R_{ad} i_{ad} + volt\_dio(i_{ad} + i_{dc} - i_4 - i_5) + volt\_dio(i_{ad} + i_{dc} - i_4 - i_5 - i_c) = 0 \tag{5.4.5}$$

For main generator rotor d.c. loop, loop i_{dc} :

$$N_f \frac{d\phi_f}{dt} + R_f i_{dc} - R_{ad} i_{ad} = 0 \tag{5.4.6}$$

where $volt\_dio(i)$ is the diode's $v - i$ characteristic function.

Then the solution variable vector will be:

$$\mathbf{x} = \begin{pmatrix} \text{exciter node 0 } mmf \text{ potential } f_{e0} \\ \cdots \\ \text{exciter node N}_{\text{enode}} - 1 \; mmf \text{ potential } f_{enode-1} \\ \text{exciter stator d.c. current} \\ \text{exciter rotor phase B winding current} \\ \text{exciter rotor phase C winding current} \\ \text{diode 4 current } i_4 \\ \text{diode 5 current } i_5 \\ \text{current in additional resistance } i_{ad} \\ \text{generator node 0 } mmf \text{ Potential } f_{g0} \\ \cdots \\ \text{generator node N}_{\text{gnode}} - 1 \; mmf \text{ potential } f_{gnode-1} \\ \text{generator field current } i_f \\ \text{generator damper bar 0 current} \\ \cdots \\ \text{generator damper bar N}_{\text{d}} \text{ -1current} \\ \text{generator stator phase B current} \\ \text{generator stator phase C current} \\ \text{rotating angle } \theta \end{pmatrix} \tag{5.4.7}$$

$$\mathbf{F(x)} = \left(\begin{array}{l} \text{conservation of flux at exciter node } 0 \\ \cdots \\ \text{conservation of flux at exciter node } \mathrm{N}_{\mathrm{enode}} - 1 \\ \text{exciter stator d.c. electrical loop equation} \\ \text{electrical loop equation for exciter rotor phase B, equation 5.4.1} \\ \text{electrical loop equaiton for exciter rotor phase C, equaiton 5.4.2} \\ \text{electrical loop equation for diode 4, equation 5.4.3} \\ \text{electrical loop equaiton for diode 5, equation 5.4.4} \\ \text{electrical loop equation for additional resistor, equation 5.4.5} \\ \text{conservation of flux at generator node } 0 \\ \cdots \\ \text{conservation of flux at generator node } \mathrm{N}_{\mathrm{gnode}} - 1 \\ \text{main generator rotor d.c. electrical loop equation 5.4.6} \\ \text{electrical equation for damper bar } 0 \\ \cdots \\ \text{electrical equation for damper bar } \mathrm{N}_{\mathrm{d}} - 1 \\ \text{electrical loop equation for generator phase B} \\ \text{electrical loop equation for generator phase C} \\ \text{speed equation} \end{array} \right) \qquad (5.4.8)$$

Given these equations and variables describing the brushless generating system, the system state can be solved by the technique given in chapter 2 and 3.

Simulation results from the system model described in this chapter will be given in next section, which include the exciter connected to the rectifier and also the main generator open circuit testing curves.

5.5 Simulation Results of the Complete System, Excluding AVR

Results will include the open circuit testing of the exciter, rectifier and as well as the main generator as a whole system.

Experimental result of the brushless system including the exciter, the rectifier and the main generator open circuit testing curves are shown in figure 5.5.1.

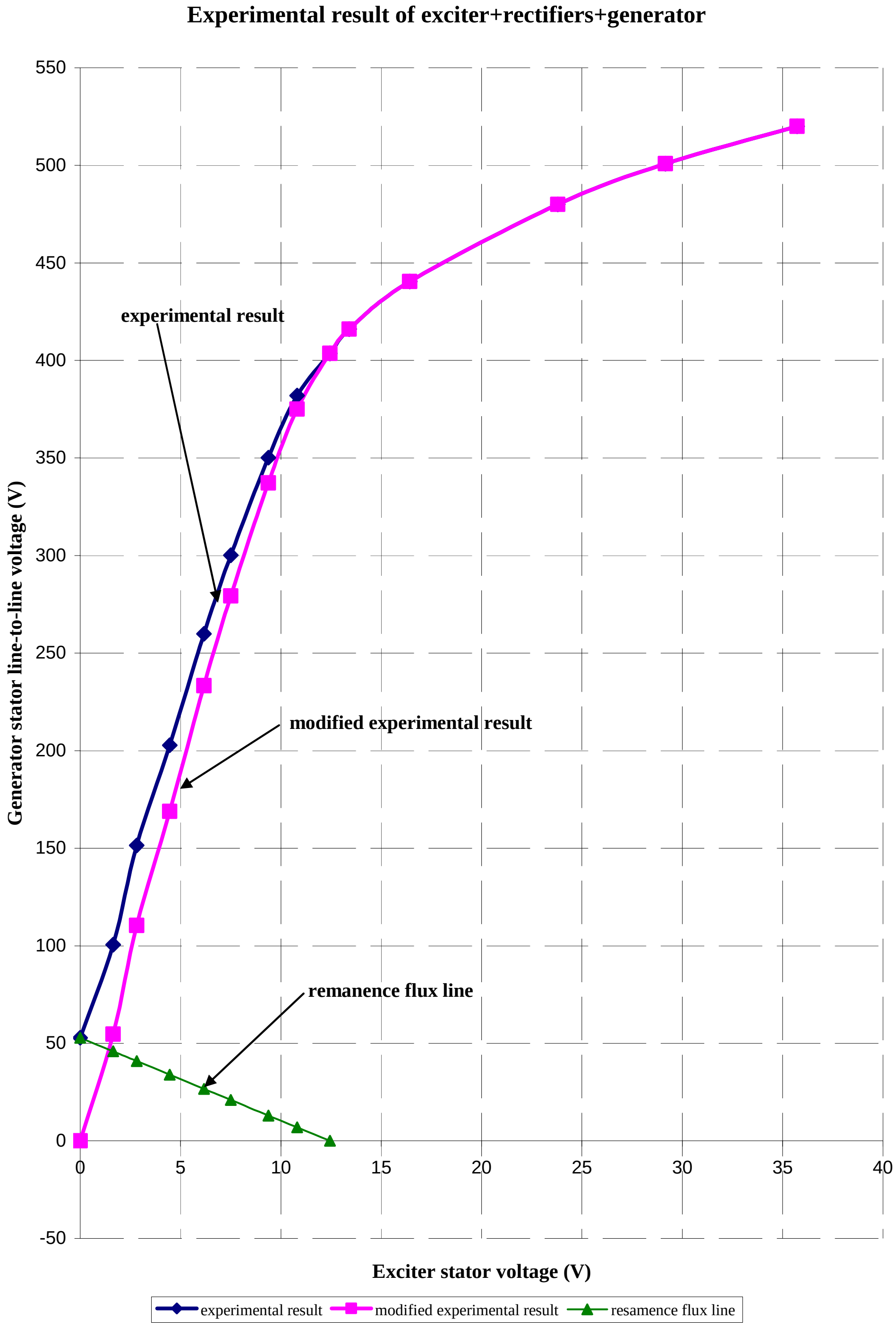

Figure 5.5.1 Experimental result for exciter+rectifiers+main generator

It can be seen that there is an assumed remanence flux line, shown by the line with triangle markers in the figure. This is because in the experiments, there is remanence flux remained in the iron material. Thus this causes a different open circuit saturation curve compared with the DRM simulation result where there is no modelled remanence flux in the material. The remenance effect is particularly noticeable in the low voltage section of the saturation curve. The small remanace in the exciter generate current in the field of the main generator. The exciter magnetic circuit uses a different magnetic material to the main generator and has in effect a shorter air gap thus maintaining the remanance flux more easily. It can be seen from the results of chapter 4 that there is little remanance effect in the generator itself.

The remanence flux line is derived by assuming that no remanence flux is present at the working point, e.g. the rated voltage, and zero generated voltage is assumed when the excitation voltage is zero. A linear variation of the remanence voltage is assumed. A modified experimental result after eliminating the remanence flux in the iron is shown in figure 5.5.1 by the line with rectangular markers. The generated voltage now starts from zero when there is no excitation. Now the comparison between this modified experimental result and DRM result is shown in figure 5.5.2.

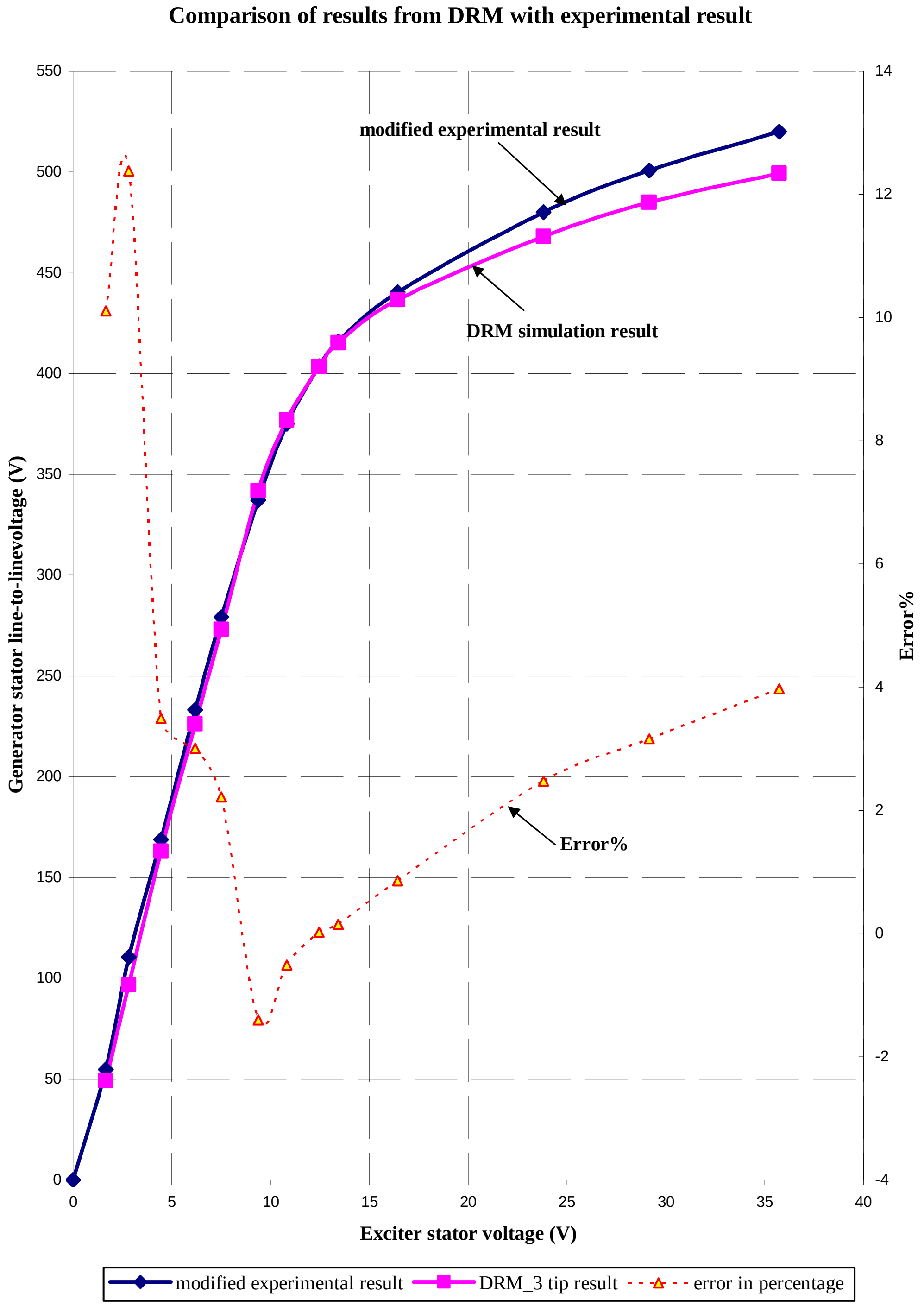

Figure 5.5.2 DRM simulation results in comparison to modified experimental results for open circuit testing

It can be seen from the result comparison in figure 5.5.2 that DRM result and modified experimental result show perfect agreement in the region below saturation. The bigger difference between the two results above the knee point is due to the slightly different material that have been used in the DRM simulation and experiment, this is the same reason for the difference in the open circuit test results in chapter 4.

5.6 AVR Controller Modelling

The DRM model of the exciter, rectifier and main generator have been investigated and validated in the previous in this chapter. To model the complete small brushless generating system, the excitation controller will now be modelled. The design and implementation of a digital excitation controller will be presented in this section, as well as the DRM simulations results.

5.6.1 Introduction

In a typical electrical power generation system, the excitation control system is essential and a key component to the power system stability and controllability. The functionality of the excitation control system in the structure of a power generating system is to supply the field voltage to the main generator, as well as to control the stability of the generating system. Normally, the excitation control system comprises the Automatic Voltage Regulator (AVR) and the Exciter a.c. generator, as shown in figure 5.6.1.

The first block in the middle row in figure 5.6.1 is a controller, which generates the excitation voltage needed by the exciter stator based on the voltage error between referenced voltage value and the main generator stator terminal voltage value. The field voltage of the main generator is fed by the exciter output through the rotating rectifiers.

The aim of the excitation system is to keep the stator terminal voltage of the generating system equal to the reference value V_{ref}. There are power stabilizers in figure 5.6.1. The aim of adding the power stabilizer is to add an additional torque component to reduce the rotor oscillations following transients. This is because the output power of the generating system is depend on the mechanical power of the shaft in steady state, but the transient power is decided partly by the control of the excitation system. In the case that there is a disturbance, the AVR control signal may have too many oscillations to react to the power swing. In certain conditions [41], this adjustment by the AVR to the field current of generator may have a negative effect on the rotor damping current. Thus the power stabilizers are added to adjust the time constant and transient response of the power system and to oscillations.

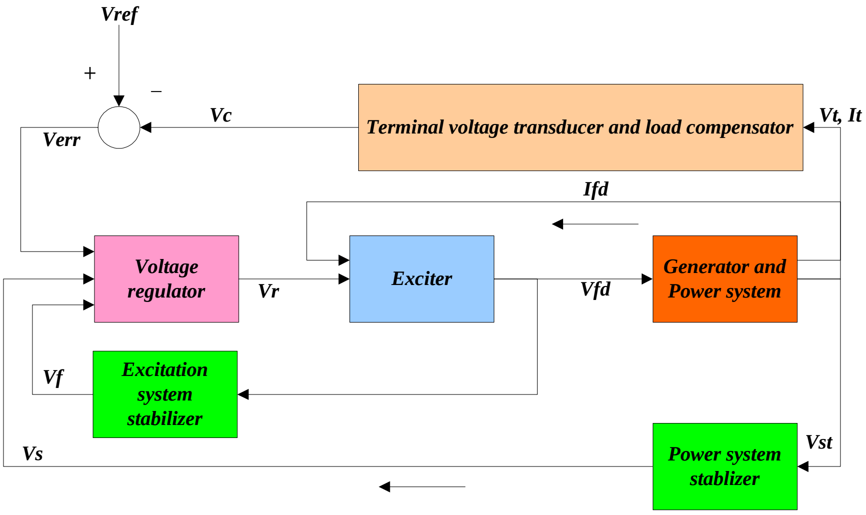

Figure 5.6.1 General functional block diagram for generator excitation control system

There have been a wide range of excitation system models, as can defined by the IEEE standard 421.5 [42] [43], and also some modified excitation models from IEEE committee report [44]. Figure 5.6.2 shows one of the simplified models of the excitation system.

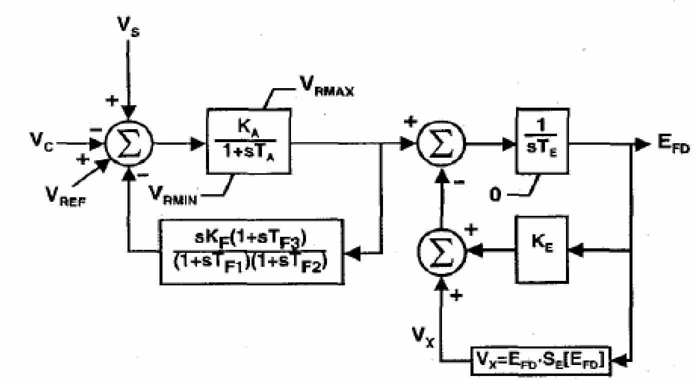

Figure 5.6.2 [44] IEEE std. 421.5 Type AC5A- simplified rotating rectifier excitation system representations

A practical excitation control system for the small brushless salient pole generating system described in the thesis is shown in the Simulink diagram of figure 5.6.3 [45].

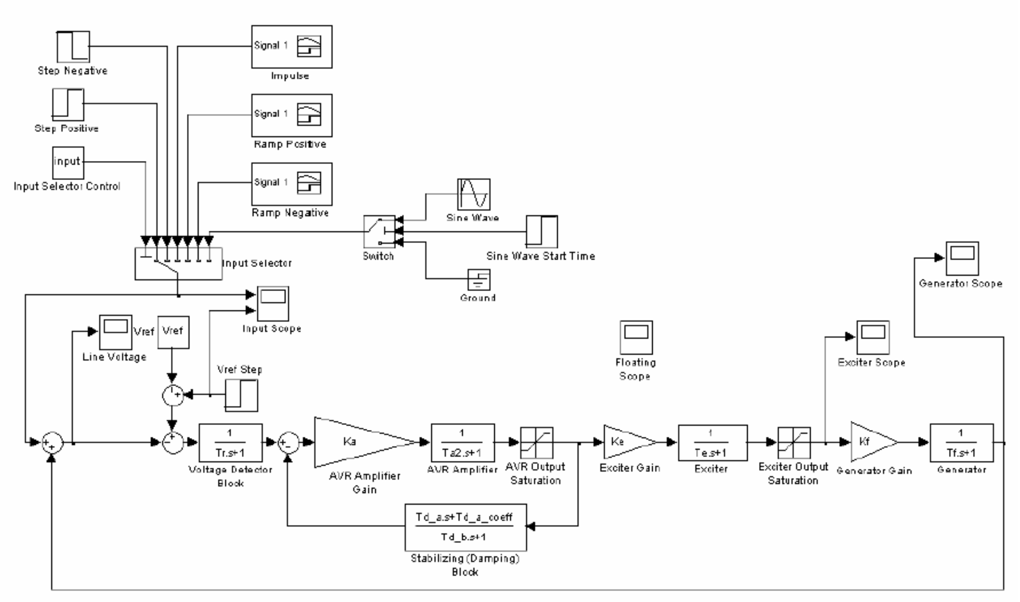

Figure 5.6.3 [45] The practical excitation system model for the generating system in the thesis

In figure 5.6.3, the automatic voltage regulator, exciter, generator and the stabilizer have all been modelled. There are other models that have been used for small salient pole generators [42].

However, for the brushless generating system simulations in this thesis, only the simplest excitation controls will be applied because the addition of the control is only to demonstrate that a full system may be modelled using the DRM method.

The structure of the whole small brushless synchronous generating system to be simulated in this thesis is shown in figure 5.6.4. A PID (Proportional, Integral and Derivative) controller was designed and implemented as the automatic voltage regulator. The DRM model for the exciter, rotating rectifiers and the main have been described and validated in previous sections. This section will concentrate on the controller design and implementation.

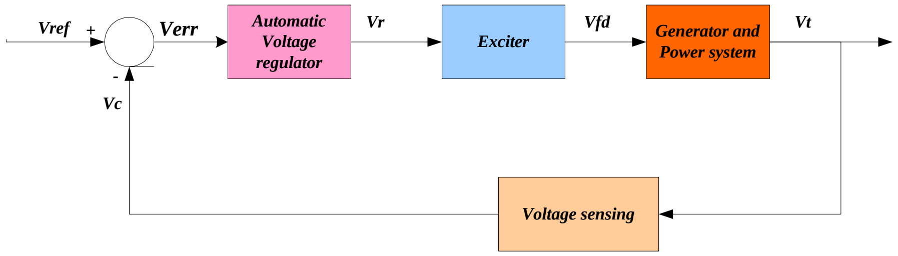

Figure 5.6.4 Excitation control model used in the simulation in this thesis

5.6.2 Transfer function of exciter and main generator

With the simplified model as shown in 5.6.4, the transfer function model of the system takes the form shown in figure 5.6.5.

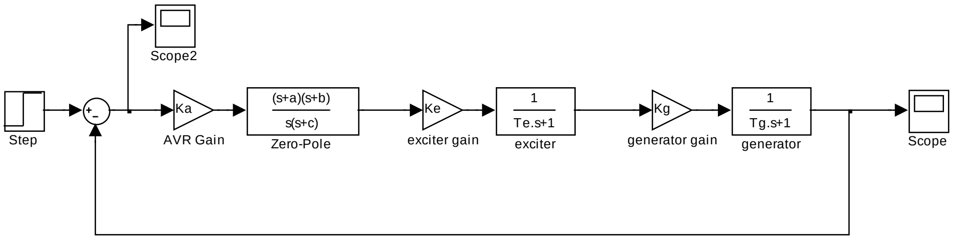

Figure 5.6.5 Transfer function model of excitation control system described in the thesis

The parameters are as shown in the graph. τ_e and τ_g are the first order time constants of the exciter and generator. τ_e represents the delay caused by the a.c. exciter in the brushless system due to inductances, capacitances and filters. It is value is normally between 0.1 and 1s depending on the size of the machine. τ_e can be derived based on the field current growth curve of the exciter, as shown in figure 5.6.6. The exciter time constant is the time taken for the exciter field current to reach 68% of the steady state value.

For a first order system, whose transfer function is as shown in figure 5.6.6:

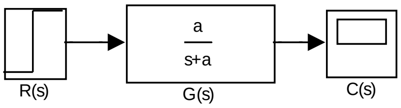

Figure 5.6.6 First order system transfer function

For a step input $R(s)=1/s$, the step response is given by:

$$C(s)=R(s)G(s)=\frac{a}{s+a}\cdot\frac{1}{s} \tag{5.6.1}$$

the step response in time domain is:

$$c(t)=c_f(t)+c_n(t)=1-e^{-at} \tag{5.6.2}$$

time constant for first order system is defined as: $\tau=\dfrac{1}{a}$, when:

$$c(t)\big|_{t=1/a}=\left(1-e^{-at}\right)\big|_{t=1/a}c_{in}=0.632c_{in} \tag{5.6.3}$$

Where $c(t)$ is system output signal, and c_{in} is system input value. Thus, the time constant for the exciter could be derived given the field rising curve in exciter stator, shown in figure 5.6.6.

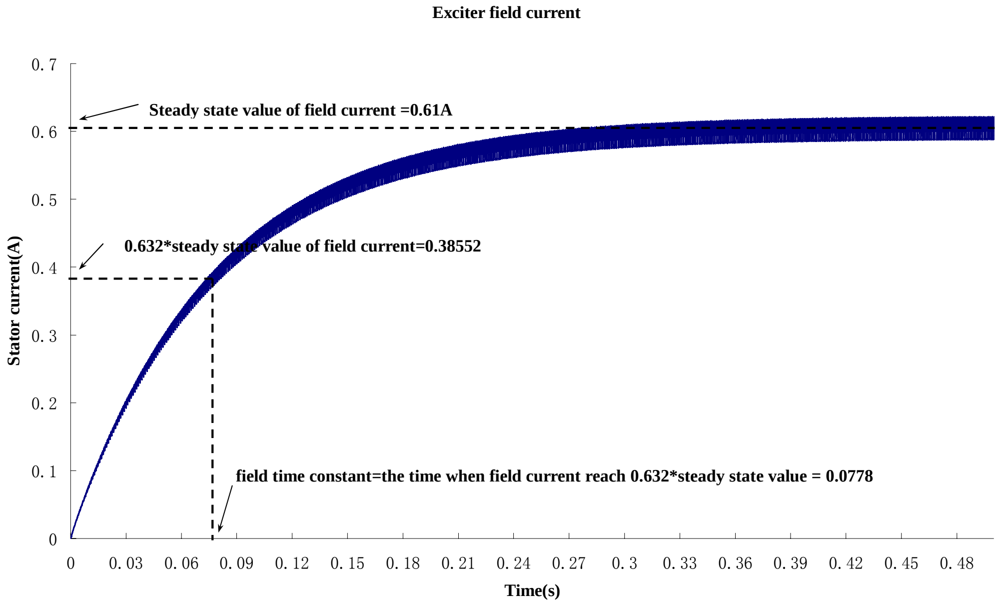

Figure 5.6.6 Deriving the field time constant of exciter

And τ_e is: $\tau_e=0.0778s$.

For the time constant of the generator, τ_g represents any delay caused by the generator main field winding due to its inductances (L/R time constants). Its value is dependent on the machine that the AVR is connected to and should be taken from available data and generator models. Its value is normally between

0.25 and 2s depending on the size of machine. Using the same method in deriving the time constant for the exciter, τ_g could be derived. The rising of field current of generator is shown in figure 5.6.7.

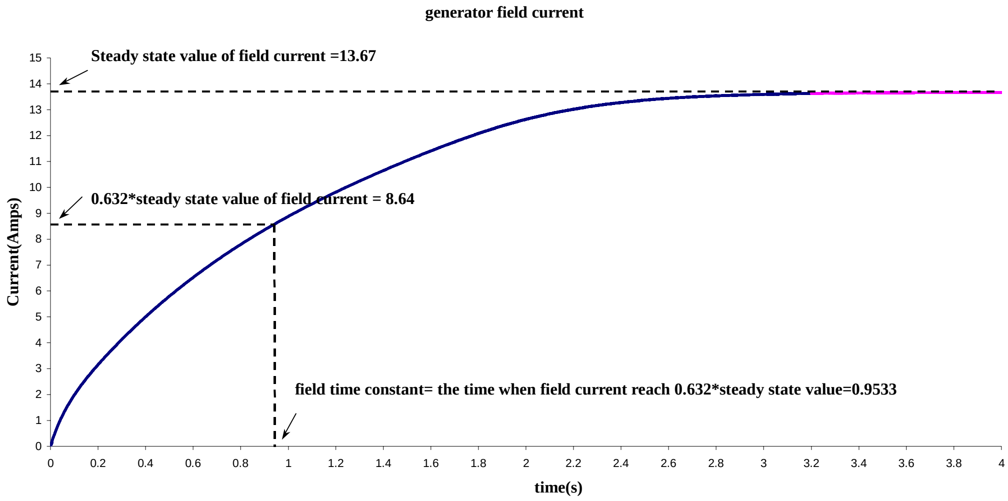

Figure 5.6.7 Deriving the field time constant of main generator

And τ_g is: $\tau_g = 0.9533s$

As for the loop gain, including K_e and K_g, based on the experimental data from the sponsor, the gain from the field voltage to stator terminal per phase voltage is:

$$K_e \cdot K_g = \frac{generator \quad stator \quad phase \quad voltage}{exciter \quad stator \quad field \quad voltage} = 18.73139619 \qquad (5.6.4)$$

In the feedback loop where the generator output voltage is sensed, the three-phase stator voltage value has to be transformed to a single value, in order to compare with the single reference value. In a practical AVR controller or complicated models, shown in figure 5.6.3, this is done by the voltage detector. Here in the simulations in this thesis, the stator terminal voltage needed by the controller was derived numerically by transformation using the commutator and three phase to two phase (α, β) transformations [32]. Thus the delay caused by the voltage detection was neglected.

The transformation in DRM program from the three phase (A, B, C) magnitude value to two phase (α, β) value is as shown below:

$$\begin{bmatrix} x_\alpha \\ x_\beta \end{bmatrix} = \sqrt{\frac{2}{3}} \cdot \begin{bmatrix} 1 & -1/2 & -1/2 \\ 0 & \sqrt{3}/2 & -\sqrt{3}/2 \end{bmatrix} \begin{bmatrix} x_a \\ x_b \\ x_c \end{bmatrix} \tag{5.6.5}$$

where x represents the stator voltage magnitude v_s.

The transformations yield the peak value of the a.c. voltage multiplied by $\sqrt{\frac{3}{2}}$.

The commutator transform converts the two phase a.c. representation into two phase direct voltage representation on the d and q axes and the peak value is extracted from by squaring these components, adding them and taking the square root. Thus $K_{32} = \frac{\sqrt{3}}{\sqrt{2}} \cdot \sqrt{2}$ =1.732.

Then this magnitude will be fed back to the controller, as shown in figure 5.6.8 below.

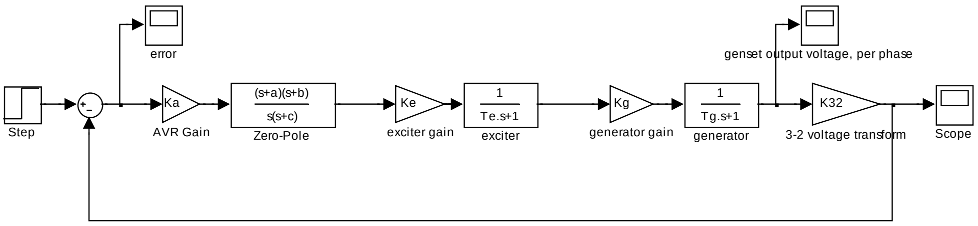

Figure 5.6.8 Simulated voltage sensing in DRM simulation

Considering all the gains included in the loop, the transfer function for the exciter and the main generator finally becomes:

$$G_p(s) = \frac{K_e K_g K_{32}}{(\tau_e s + 1)(\tau_g s + 1)} = \frac{437.4431167}{(s + 12.85347044)(s + 1.048987727)} \tag{5.6.6}$$

5.6.3 Design of PID controller

A typical structure of a digital PID controller [46] [47] [48] is shown in figure 5.6.9.

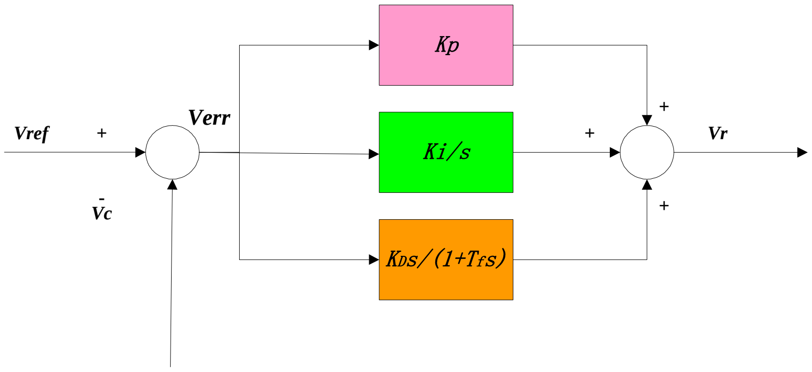

Figure 5.6.9 Digital PID controller used in this thesis

Where, K_p is the proportional gain; K_i is the integral gain; K_D is the derivative gain; T_f is the low pass filter time constant. And the relationship between these coefficients and the integral time constant, derivative time constant are:

$$K_i = \frac{K_p}{\tau_i} \tag{5.6.7}$$

$$K_D = K_p \tau_D \tag{5.6.8}$$

and the digital PID controller's transfer function is in the form of:

$$G_c(s) = \frac{(K_p + \frac{K_p \tau_d}{T_f})s^2 + (\frac{K_p}{T_f} + \frac{K_p}{\tau_i})s + \frac{K_p}{\tau_i T_f}}{s(s + \frac{1}{T_f})} \tag{5.6.9}$$

Using the controller design technique in continuous domain, the root locus controller design method is used. Intuitively, two zeros in the controller will be added close to poles of the exciter and the main generator [46]. And another pole in the controller is added to ensure the root locus passes through the design point. Details of the controller design procedure for the brushless generating system described in this thesis can be found in Appendix 5. The controller is designed to have a damping ratio $\zeta = 0.8$, to guarantee that there is not a large overshoot, and the natural frequency is $\omega_n = 25Hz$.

Designed controller's transfer function of the controller takes the form:

$$G_c(s) = \frac{5.611(s+19)(s+4)}{s(s+100)} \tag{5.6.10}$$

where for digital PID controller, $K_p = 1.259$, $\tau_i = 0.3$, $\tau_D = 0.035$, $T_f = 0.01$.

In order to use this continuous PID controller in computer code, Z transformations have to be made. The transfer function after Z transformations is:

$$\begin{aligned} V_r^*(t) = {} & K_c E^*(t) - (2B + C(1+e^{-aT}) - AT)E^*(t-T) + (B + Ce^{-aT} - ATe^{-aT})E^*(t-2T) \\ & + (1+e^{-aT})V_r^*(t-T) - e^{-aT}V_r^*(t-2T) \end{aligned} \tag{5.6.11}$$

where $V^*{}_r(t)$ is the output voltage of the controller, $E^*(t)$ is the error input for the controller,

$$\begin{aligned} & K_c = 5.661 \\ & A = \frac{K_c \cdot 19 \cdot 4}{100} \\ & B = K_c - C \\ & C = \frac{(K_c(19+4) - A)}{100} \\ & a = 100 \end{aligned} \tag{5.6.12}$$

sample time used in DRM simulation is 0.01s, and the details of the controller design can be found in Appendix 5.

5.7 Simulation Results of The Complete Brushless Generating System, Including AVR

With the AVR controller modelled, the complete system model for small brushless generating system can be set up with the DRM modelling technique. This section will simulate the suddenly load apply case for the system to look into the voltage dip of the system.

A reference voltage for the generated voltage of the main generator is put into the system, and numerically simulated open circuit operating condition is applied from 0s to 1.5s. Rated electrical load for the generator is applied suddenly to the generator and voltage dip happens at 1.5s in the simulation. Results are shown from figures 5.7.1 to 5.7.6.

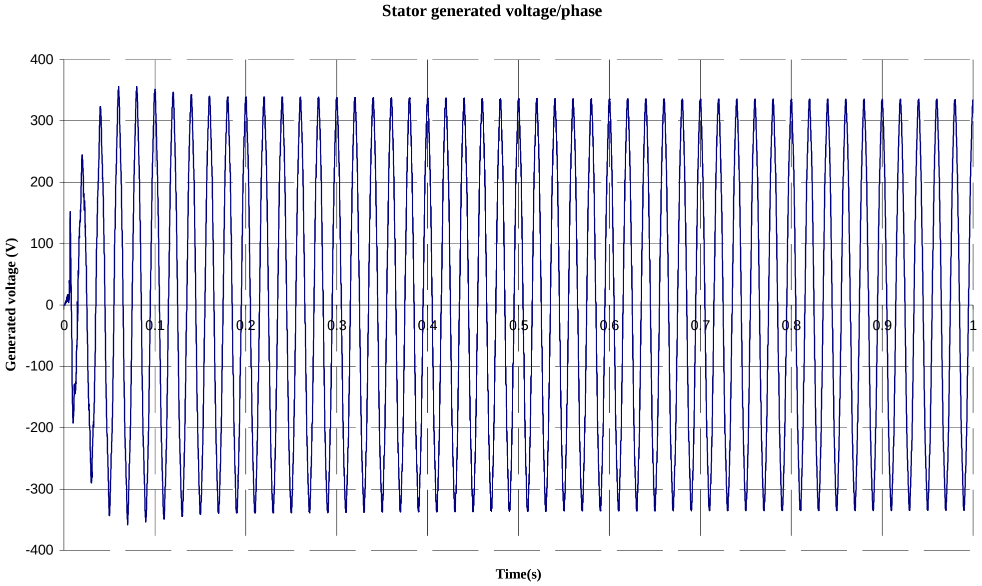

Figure 5.7.1 Generated stator per phase voltage for the complete generating system

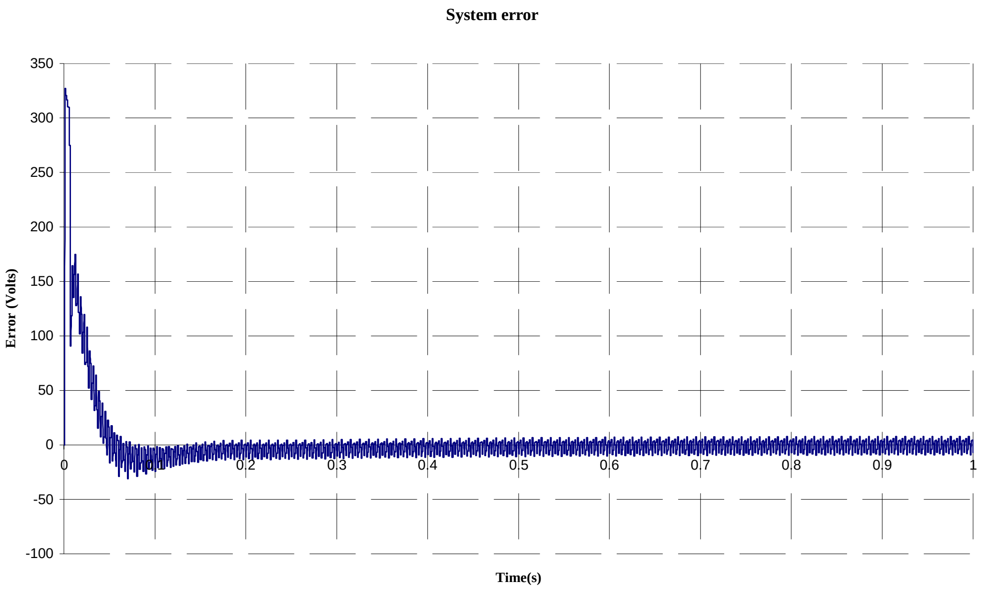

Figure 5.7.2 Error between reference voltage value and feedback voltage value

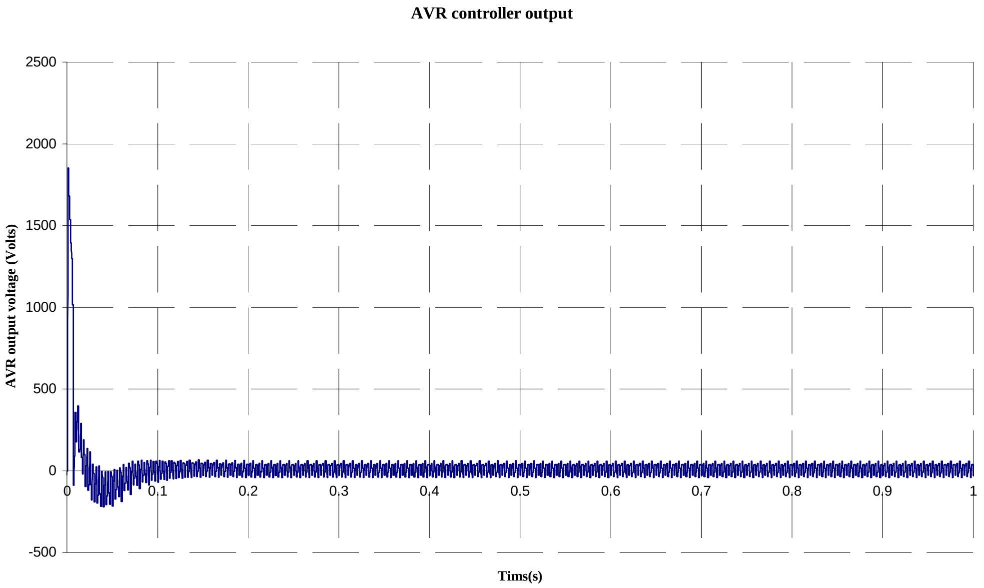

Figure 5.7.3 AVR controller output value

Figures 5.7.1-5.7.3 show the generated main generator stator voltage waveform, the system error and AVR controller output waveform in a numerically simulated open circuit case. It can be seen that the system's overshoot is small and the response time is fast.

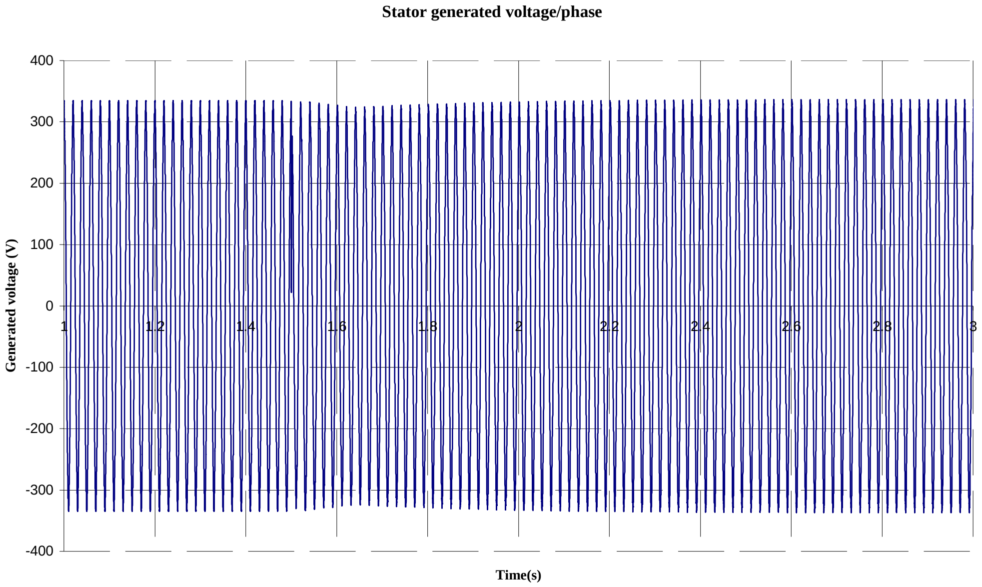

Figure 5.7.4 Generated stator per phase voltage for the complete generating system during a voltage dip

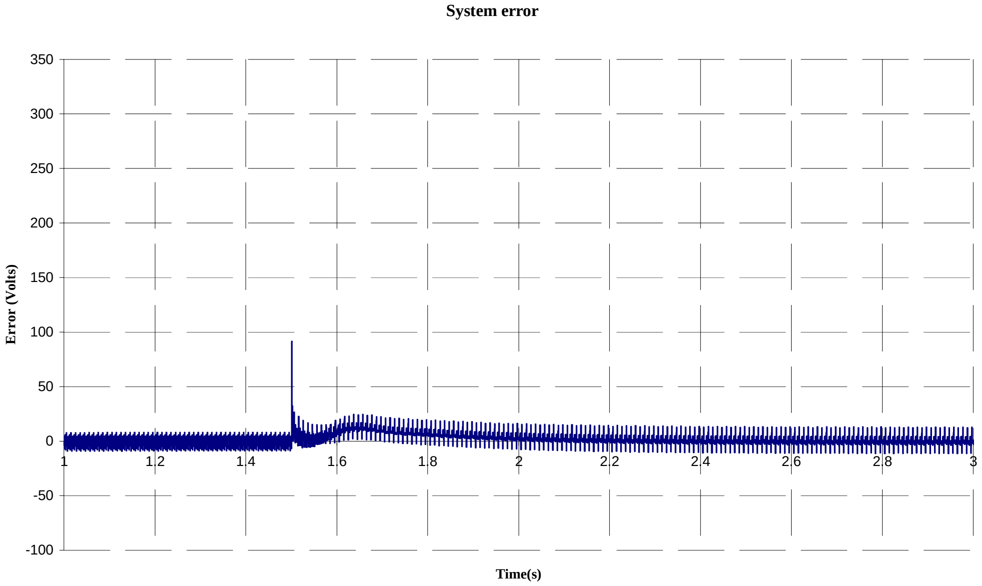

Figure 5.7.5 Error between reference voltage value and feedback value during a voltage dip

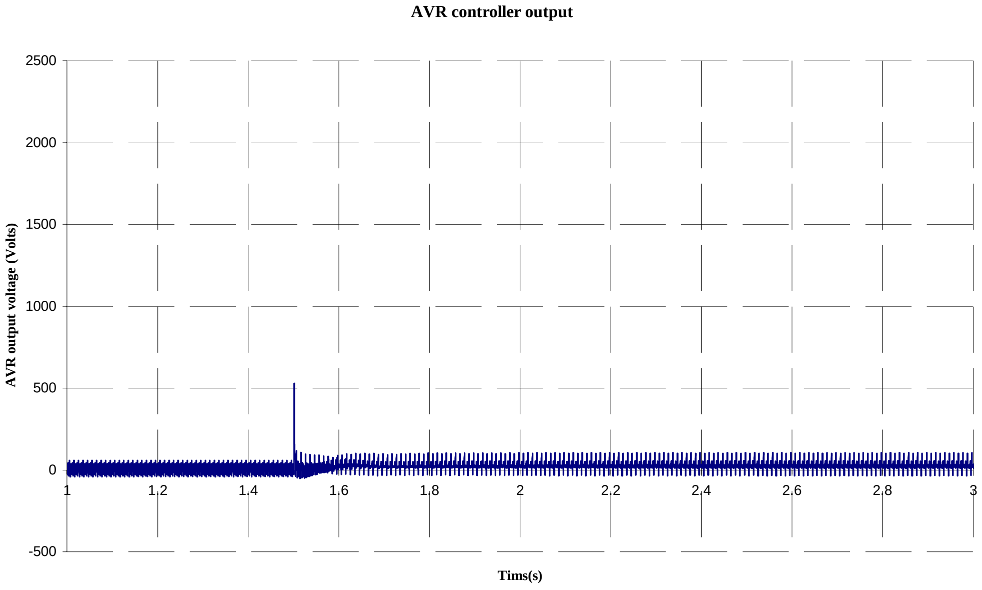

Figure 5.7.6 AVR controller output value during a voltage dip

From figures 5.7.4-5.7.6 it can be seen that during a sudden load apply, the AVR controller response fast to the load change, and remain a constant generated voltage for the complete system in steady state.

5.8 Conclusion

This chapter modelled and simulated the complete brushless generating system based upon the salient pole synchronous generator model described in chapter 4 using the DRM modelling technique of electrical machines. A brief introduction of the brushless system was given first in the beginning of this chapter, followed by the DRM model of the exciter as well as the simulation results for the exciter only. Models suitable for numerical simulation for the rectifiers and system state variables and equations describing the system's behaviour are also given. A comparison of the DRM simulation result with experiments are made and it is shown that the DRM result has an excellent agreement with experimental results.

To model the complete brushless generating system, an AVR controller is added into the system model, designed by root locus technique to be a PID controller. DRM simulations incorporating controls for the complete system are made, and results show that the AVR works fine in a voltage dip condition.

CHAPTER 6 MULTIPLE MACHINE SYSTEM-CASCADED DOUBLY FED INDUCTION MACHINE SIMULATION

6.1 Introduction

In previous chapters, DRM modelling of small salient-pole synchronous generator and the modelling of brushless generating system, including exciter, automatic voltage regulator, rotating rectifiers and the generator, has been investigated and validated. It has been shown that DRM modelling of an electrical machine is an effective and flexible method, and its application could be further extended to the simulation and investigation of multi-machine systems. Such a system is a cascaded doubly fed induction generator for use in wind energy generation.

In this chapter, the multiple-machine, system-cascaded, doubly-fed, induction generator, which is a research interest in the field of wind energy generation in recent years, will be modelled and simulated by the Dynamic Reluctance Method. Simulation results in the respect of power flow and frequency changes in the cascaded doubly fed induction machine system will be discussed. In the beginning of this chapter, some simple introduction of the application field of cascaded machine is presented.

Renewable energy, such as wind energy, hydro energy, geothermal energy and solar energy invokes great interest these years, due to the increasing concerns for the environment and finite hydrocarbon resources. These renewable energies are clean energy suitable for the next century, and have minimum environmental impact.

Among these energy sources, wind and hydro energy are the most widely adopted renewable approaches for industrial electricity generation applications. For example, more than 20% of electricity consumption in the west of

Denmark is provided by wind energy [49], and their utilization is felt to be very promising to help provide the future energy requirements. Offshore and remote regions offer great potential for exploiting wind energy. Research into cost effective solutions for such locations is currently being carried out.

Many wind energy generation systems have been proposed over the years [16] [50] [51]. Current maximum power ratings are around 5 MW [52] [53] but are increasing with time due to developments in technology. From the electrical machine point of view, wind energy generators could be classified as asynchronous generator, synchronous generators and even reluctance rotor machines. Asynchronous generators are most common for a small rating wind generating system under 2MW, and direct-driven permanent magnet synchronous machines are preferred for a larger rating.

Many types of wind generators have been proposed and validated, among them, the common type of wind generating system can be shown in figure 6.1.

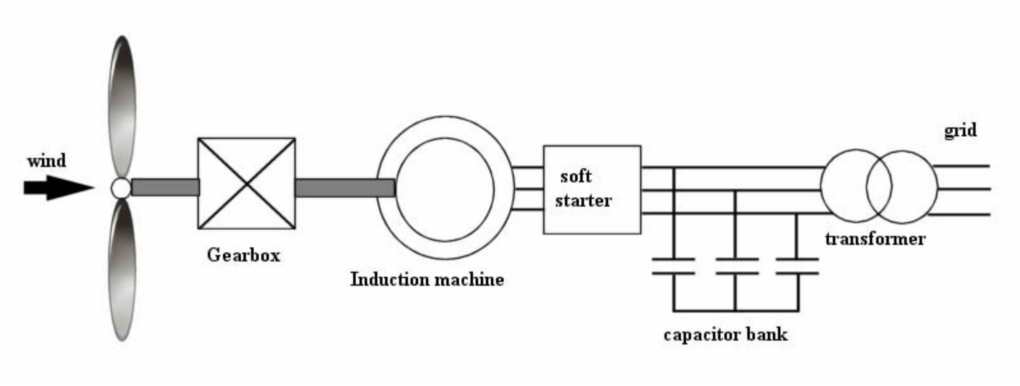

Figure 6.1.1 Fixed speed wind generating system

Figure 6.1 shows a fixed speed wind generating system, with capacitor bank staying on the stator side, between the grid and the generator, which is a widely used commercial choice due to its simplicity in design and low cost. The machine has normally two set of stator windings with different pole numbers, thus implement fixed frequency current at two different shaft speed. Although this kind of fixed speed system is reliable and simple, it limits the power output of the wind generating system because of the capacitor bank. Efficiency in power extraction from the wind is critical in defining the economic limit of application of a wind turbine.

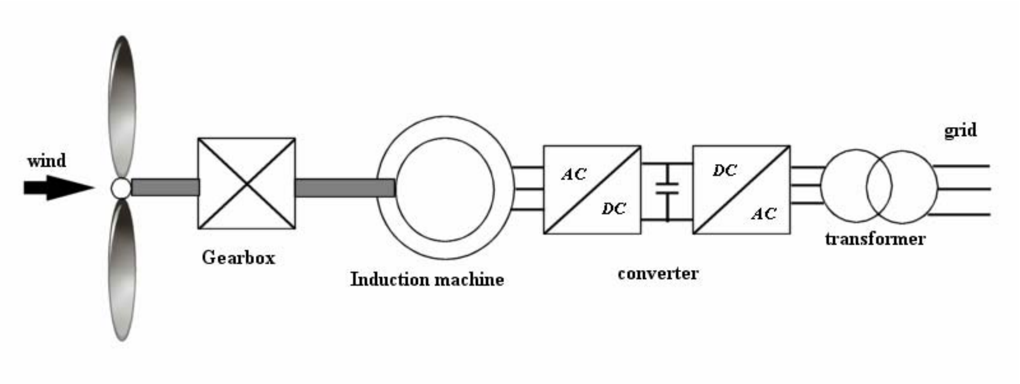

Figure 6.1.2 Variable speed wind generating system with stator side converter

For a variable speed wind generating system, figure 6.2 shows one of the system arrangements. Power of a cage rotor induction generator can be controlled and improved by a power converter connecting to generator stator, and a unity power factor operation is possible [16][51]. The stator side power converter supplies the required reactive power and also handles the full active power generated by the machine. This is also commercially available.

However, the full-power converter as shown in figure 6.1.2 has to handle all the power transmitted to the machine, and normally the converter would be big and expensive.

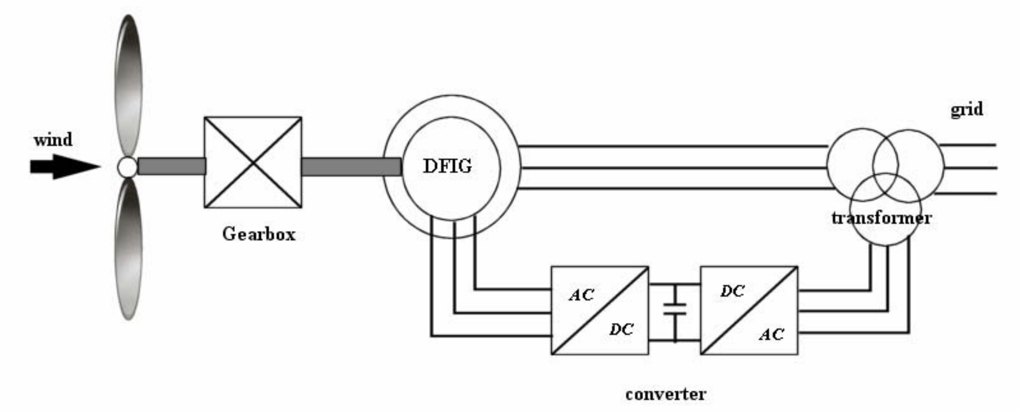

Figure 6.1.3 Variable speed wind generating system with rotor side converter

To reduce the cost and size of the power converter, nowadays research from wind energy generation is concentrated on the so-called doubly-fed induction machine, which is a three phase a.c. machine with two accessible three phase windings from which power can be fed to or extracted from. It has a back-to-back converter connected to the rotor of the generator through a slip ring, and stator connected to the grid directly. In this case, power converter rating depends on the range of the operating speed, and it only needs to handle the slip power of the machine, thus the size and cost of the whole system are reduced substantially. But, maintenance cost would be high due to the presence of slip rings and brushes.

Viable alternatives for the doubly fed induction machine have been proposed to get rid of the slip rings and brushes, which are called brushless, doubly-fed, induction machines [51]. The cascaded doubly fed induction machine, as referred to by Hopfernsperger [20] [54], is one of the alternatives.

6.2 Cascaded Doubly-fed Induction Machine in Wind Energy Technology

A single doubly fed induction machine (SDFM) [54], has the topology as shown in figure 6.1.3. The stator winding of a wound rotor induction machine is connected to a stiff voltage supply and the rotor winding is connected to a bi-directional power converter. The main drawback of this kind of arrangement is the slip ring brushes combination [20]. The brushless doubly fed induction machine is designed to take the slip ring and brushes out of the machine system. Cascaded doubly fed induction machine (CDFM) is one of the brushless arrangements.

Cascade doubly fed induction machine is the arrangement that connecting two wound rotor induction machine together, mechanically and electrically. The two machines stay on the same shaft, and one stator winding is connected to the grid, while the other stator winding is connected to the power converter. Its structure is shown in figure 6.2.1. Since the two rotors have a stiff mechanical coupling no brushes are need for the slip ring connection.

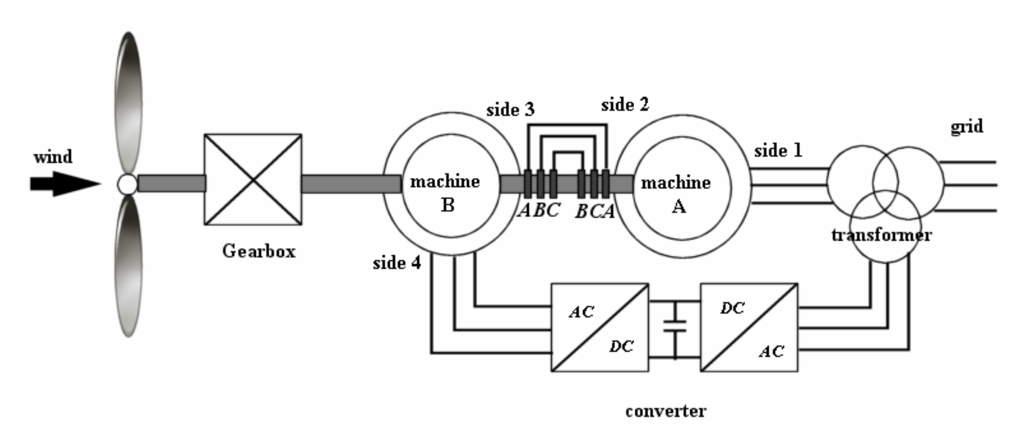

Figure 6.2.1 Cascaded doubly-fed induction machine (CDFM)

Excitation to the rotor of machine A in figure 6.2.1 is transferred between the stator of the induction machine that is connected to the converter (machine B) to the machine that is generating (machine A).

There are two kinds of electrical connection for the cascade doubly fed induction machine: positive phase sequence connection and negative phase sequence connection. Positive phase sequence results by connecting the rotor windings together with the same phase sequence. And negative phase sequence result by swapping the phase sequence on side 3 of machine B. If the two machines mechanical connected in series, as the case in figure 6.2.1, with a negative phase sequence electrical connection, the rotating flux field on the two rotor would be opposite relative to the rotor, and the developed toque for machine A and B are co-acting in this negative connection case. However, if the rotors are connected in positive connection electrically, the rotating fields have the same rotating direction. The developed torque is counter-acting for this negative sequence connection [54]. Therefore, with the two machines connected in series mechanically, only the negative phase sequence connection of real importance is under consideration in the thesis.

But, things would be different for a back-to-back machine arrangement [54]. A positive phase sequence would be appropriate for back-to-back connected cascaded machines, to generate co-acting torque on the two machines and also generate opposite direction rotor rotating flux fields relative to the rotor. In this case, the positive phase sequence is of importance and could be generating the current with the frequency that is needed.

As mentioned in reference [20][54][55], the resulting frequency relationship for a CDFM machine connected in series between machine stator current and rotor currents is:

$$f_1 = (p_A + p_B) f_m - f_4 \tag{6.2.1}$$

where f_1 and f_4 are the stator side frequencies in side 1 and side 4 for machine A and machine B in figure 6.2.1. p_A and p_B are the number of pole pairs in the two machines, f_m is the mechanical rotor frequency. In the 4 pole, cascade machine system described in this thesis, the stator of machine A is connected to the 50Hz electric grid. Side 2 and 3 are identical apart from the phases due to the negative phase sequence connections. The CDFM machine reaches the synchronous point of machine A at 750 rpm, while $f_2 = f_3 = 0$. The relationship of these frequencies is shown in figure 6.2.2.

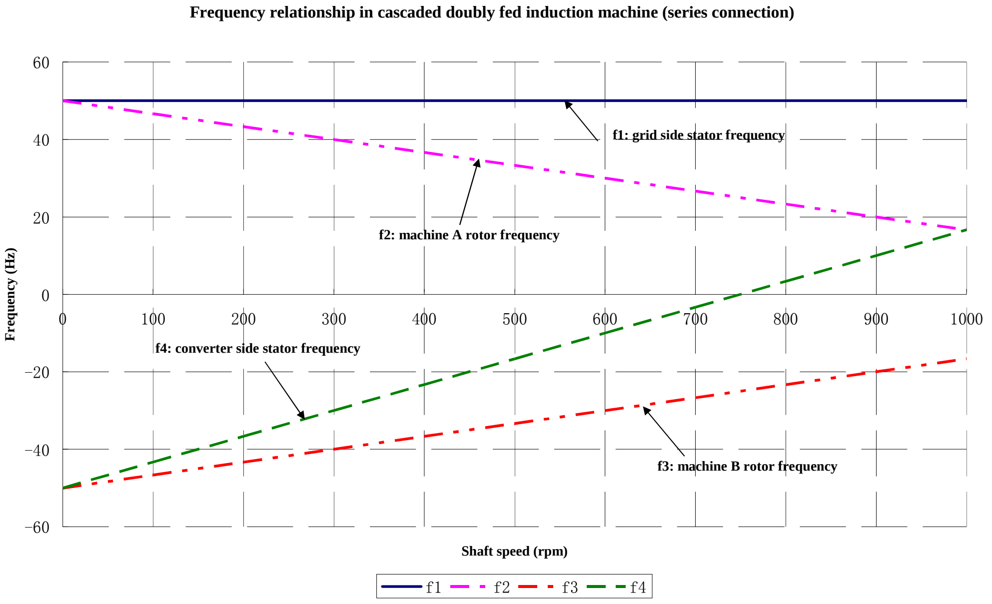

Figure 6.2.2 Frequency relationship in series connected cascaded doubly fed induction machines

As seen from figure 6.2.2, in synchronous speed, which is 750rpm in the case that is considered here, the converter stator side 4 frequency is 0, d.c. voltage is supplied to the converter side machine B, and 50Hz current should come out from the grid side stator in machine A. In other shaft speed cases, where shaft speed is above or below the synchronous speed, the frequency on stator side of grid side machine A would be changed to negative or positive according to the frequency characteristic given in figure 6.2.2. In another word, from the power pint of view, electric power flow into the cascaded doubly fed induction machine system with a shaft speed lower than synchronous speed, and flow out of the system in the higher shaft speed than synchronous speed, when f_4 is positive. P.s. assume power flowing into the cascaded machine system is negative in sign, power flowing into the grid is positive in sign.

In later simulations of cascaded machine system presented in this thesis, two typical cases: shaft speed to be 550 rpm and 950 rpm, will be considered and simulated. The frequencies in the stator terminals, rotor windings, as well as the powers that are flowing in or out of the system, will be investigated. However, the DRM modelling of cascaded machines will be described next.

The advantage of DRM modelling is that saturation, skew, phase belt harmonics and tooth harmonics can all be examined in detail and their influence on system performance assessed. These practical issues of implementing a large system might well cause problems for the control and power electronic components. It has already been demonstrated in chapter 5 that incorporation of these elements into DRM simulations can be readily achieved. It is thus possible to simulate in detail the complete wind energy recovery system and examine design changes to obtain a viable solution quite quickly. The following work however concentrates solely on the electrical machine aspects.

6.3 DRM Model of Cascaded Doubly-fed Induction Machine

Detailed DRM model of induction machines has been introduced and improved in chapter 2 and 3 separately. Here in this chapter, the concentration would be the electrical and mechanical connection of the two cascaded machines.

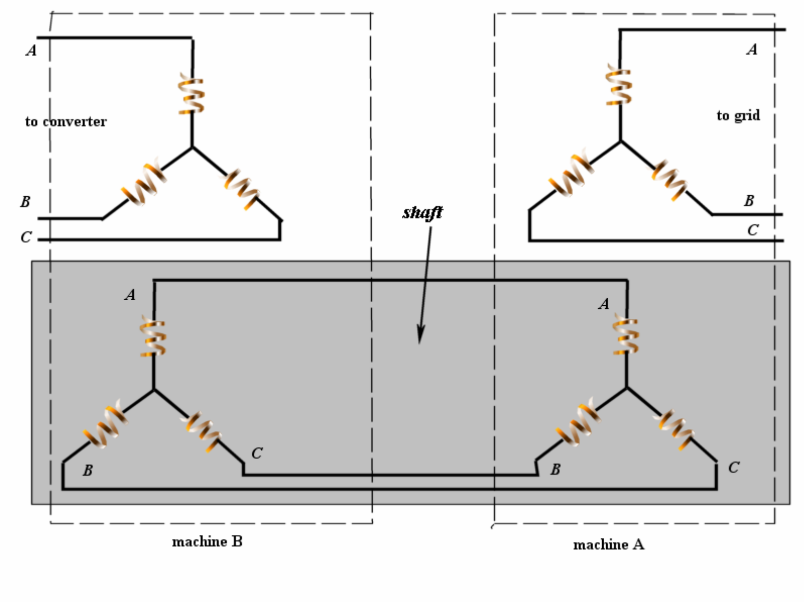

Figure 6.3.1 Electrical and mechanical connection diagram of cascaded machine system

As is shown in figure 6.3.1, machine A and machine B are connected on the same shaft, and in series sequence mechanically, different from the back-to-back mechanical connection used in reference [54]. With this mechanical connection, in order to generate constant frequency under different shaft speed, the negative phase sequence electrical connection between the two rotors has to be utilized, as mentioned in previous section in this chapter. In figure 6.3.1, phase B and phase C of the rotors for the two induction machine have been swapped, for a negative phase sequence.

The electrical loop connection between the connected rotors in the two machines is shown in figure 6.3.2. The outer loop, loop B, is the electrical loop that connects phase B in machine B and phase C in machine A. The inner loop, loop C, is the electrical loop that connects phase C in machine B and phase B in machine A.

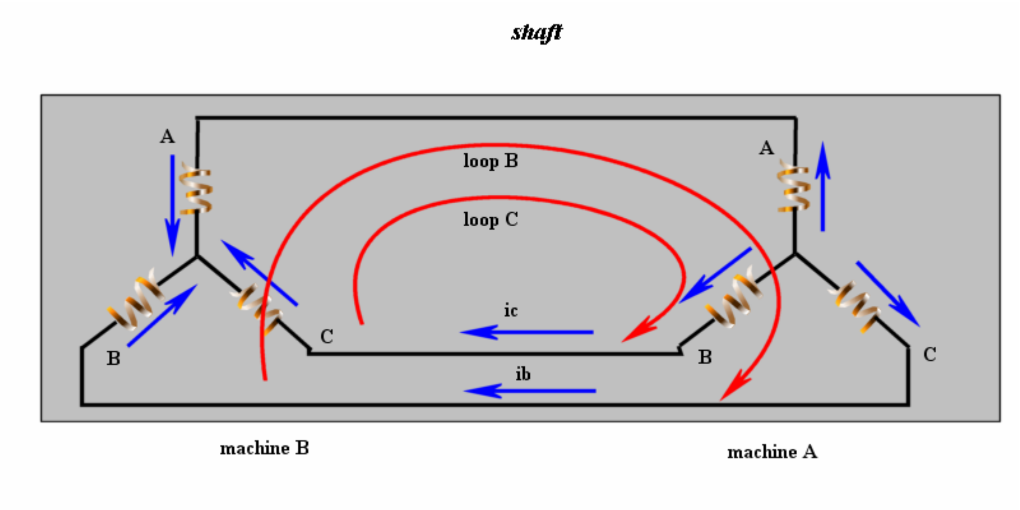

Figure 6.3.2 Electrical connection loop between the rotors in cascaded induction machines

The electrical loop equation for outer loop B is:

$$N_{1b}\frac{d\phi_{1b}}{dt}+R_{1b}i_b-N_{1a}\frac{d\phi_{1a}}{dt}+R_{1a}(i_b+i_c)+N_{2c}\frac{d\phi_{2c}}{dt}+R_{2c}i_b-N_{2a}\frac{d\phi_{2a}}{dt}+R_{2a}(i_b+i_c)=0 \tag{6.3.1}$$

and the electrical loop equation for loop C is:

$$N_{1c}\frac{d\phi_{1c}}{dt}+R_{1c}i_c-N_{1a}\frac{d\phi_{1a}}{dt}+R_{1a}(i_b+i_c)+N_{2b}\frac{d\phi_{2b}}{dt}+R_{2b}i_c-N_{2a}\frac{d\phi_{2a}}{dt}+R_{2a}(i_b+i_c)=0 \tag{6.3.2}$$

Where, subscripts 1 and 2 means the first machine, e.g. machine B, and the second machine, e.g. machine A. The two independent variables are the phase B and phase C current of machine B, as shown in figure 6.3.2.

The mechanical connection of the two machines is quite simple: they are connected to the same shaft in series, and the shaft speed is fixed numerically to a constant value during the simulation.

Therefore, the system variables for the cascaded doubly fed induction machine system are:

$$\mathbf{x}=\begin{pmatrix}\text{machine B node 0 mmf potential}\\ \cdots\\ \text{machine B node }\mathrm{N_B}-1\text{ mmf potential}\\ \text{machine B stator phase B current}\\ \text{machine B stator phase C current}\\ \text{two machines common rotor current }i_b\\ \text{two machines common rotor current }i_c\\ \text{rotor rotating angle}\\ \text{machine A node 0 mmf Potential}\\ \cdots\\ \text{machine A node }\mathrm{N_A}-1\text{ mmf Potential}\\ \text{machine A stator phase B current}\\ \text{machine A stator phase C current}\end{pmatrix} \tag{6.3.4}$$

and the equations that describe the cascade machine system are:

$$\mathbf{F(x)}=\begin{pmatrix}\text{conservation of flux in machine B at node 0}\\ \cdots\\ \text{conservation of flux in machine B at node }\mathrm{N_B}-1\\ \text{machine B phase }\mathrm{V_{AB}}\text{electrical equaiton}\\ \text{machine B phase }\mathrm{V_{AC}}\text{electrical equation}\\ \text{equation 6.3.1, loop B}\\ \text{equaiton 6.3.2, loop C}\\ \text{speed equation}\\ \text{conservation of flux in machine A at node 0}\\ \cdots\\ \text{conservation of flux in machine A at node }\mathrm{N_A}-1\\ \text{machine A phase }\mathrm{V_{AB}}\text{electrical equaiton}\\ \text{machine A phase }\mathrm{V_{AC}}\text{electrical equation}\end{pmatrix} \tag{6.3.5}$$

Having these system equations and system variables, the system state could be solved by using the globally convergent Newton-Raphson method mentioned in chapter 3. The simulation result will be shown in next section, and also some discussion of the results.

6.4 Simulation Results

In this section, the DRM simulation results of the cascaded doubly fed induction machine system will be discussed and investigated. Currents and power flow between the machines and terminals will be shown.

Three operation circumstances of the system will be considered: sub-synchronous speed, synchronous speed and super-synchronous speed. The machine system is two identical induction machines, with 4 poles each with 48 stator slots and 36 rotor slots. The coil pitch of the machine stator winding is 10 and 8 for the rotor winding. Further details can be found in appendix 2. Synchronous speed of this system is 750 rpm, as stated in the previous section. The super-synchronous operation case 950 rpm will be considered as a typical case in this section, while sub-synchronous case would be 550 rpm. The operation range of this turbine would be 0.73 p.u. to 1.26 p.u.. Rated load at 1.0pf is applied to the grid side of the machine system, and the load is star connected.

6.4.1 Sub-synchronous speed, shaft speed - 550 rpm

When the shaft is rotating at sub-synchronous speed, a low frequency a.c voltage source is applied to the stator side 4 of machine B, through the converter. Normally in a controlled cascaded doubly fed induction machine system, the frequency and the applied voltage are controlled by the converter. However, in the discussion and simulation in the thesis, a voltage source with fixed frequency and voltage value, which is decided by the shaft speed, is applied to converter side stator directly, and no control details will be discussed here. Frequency relations in sub-synchronous speed, which is 550 rpm, can be seen in figure 6.4.1.

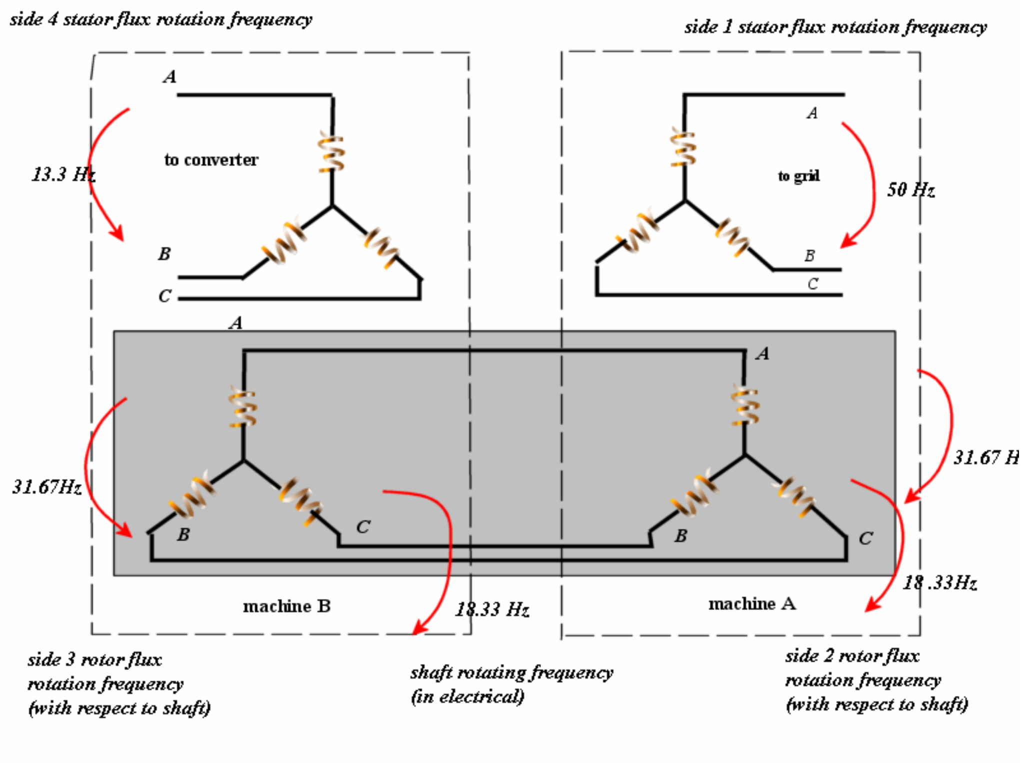

Figure 6.4.1 Frequency relations in sub-synchronous speed – 550 rpm for CDFM

As can be seen in figure 6.4.1, 13.3 Hz frequency stator voltage source is applied to the converter side stator, e.g. side 4, thus the stator flux field rotating in a counter-clockwise direction. This frequency is determined by the shaft speed (electrical) with respect to the synchronous speed of the cascaded machine system. The desired generation frequency is 50 Hz, which comes out of side 1 of machine A, considering the shaft speed is sub-synchronous speed, thus the slip frequency should be supplied by the converter. Thus, current frequency for side 4 in machine B should be $\frac{(750-550)}{750}\cdot 50Hz = 13.3Hz$.

In order to generate a steady torque in electrical machines, the stator flux field and rotor flux field have to remain stationary with respect to each other, thus the resultant rotor flux field rotating speed and direction has to be the same with that of stator. In machine B, rotor is sitting on the shaft, which rotates at the electrical frequency $\frac{2\cdot 550}{60} = 18.33Hz$ (each induction machine has 2 pole pairs), and it is opposite to rotation of stator flux field. Thus the rotor flux field rotation direction with respect to the shaft should be counter-clockwise and its frequency is $18.33 + 13.33 = 31.67Hz$. Due to the negative phase sequence connection between the two rotors of the CDFM system, rotor flux field rotation direction in machine A is clockwise, which is the same direction with the shaft rotation, as shown in figure 6.4.1. To remain the flux field in stator and rotor to be the same in machine A, stator flux field frequency will be the sum of the electrical rotation frequency of the shaft, which is 18.33Hz, and the rotor flux field rotating frequency with respect to the shaft in machine A, which is 31.67Hz. Thus, the generated stator flux field rotation frequency is 18.33Hz+31.67Hz=50Hz.

Figures 6.4.2-6.4.4 show the stator and rotor current waveforms in machine A and machine B for CDFM system in sub-synchronous speed.

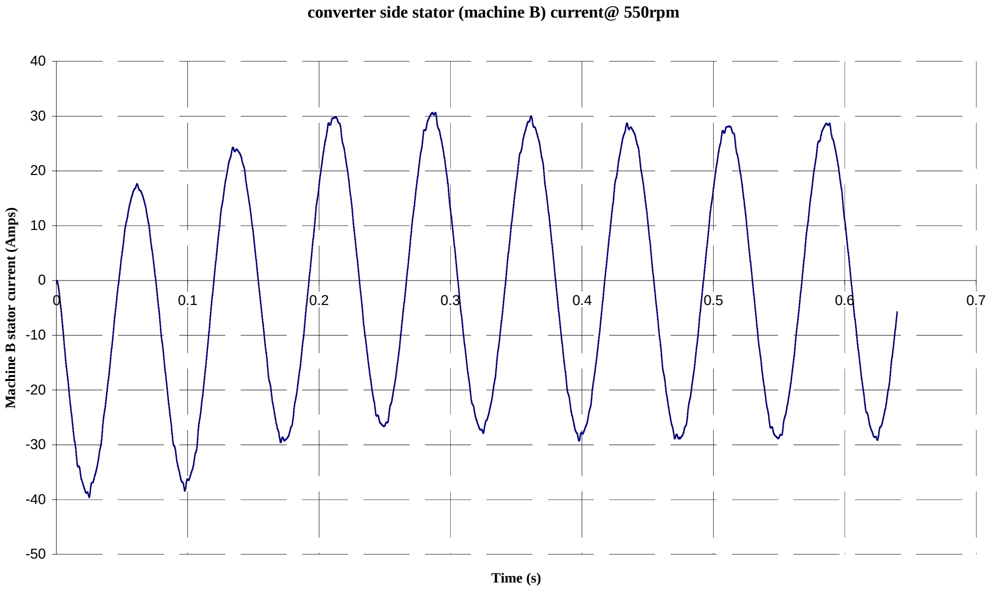

Figure 6.4.2 Converter side (side 4) induction machine stator current waveform

Current frequency in figure 6.4.2 is 13.3 Hz, as what is expected according to the analysis in previous context.

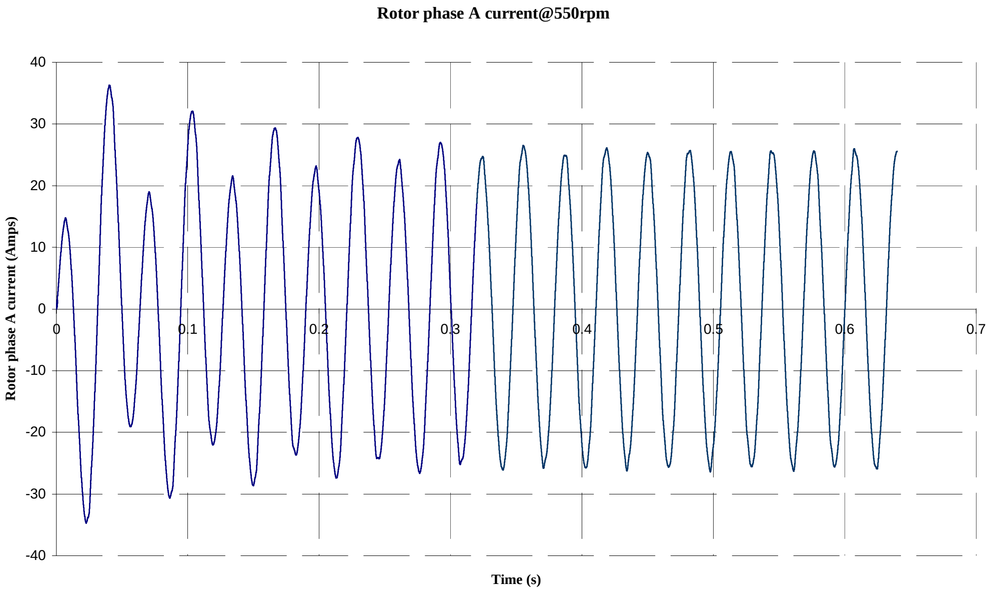

Figure 6.4.3 Cascaded machine rotor phase A current (side 2 & 3)

Rotor current frequency in figure 6.4.3 is 31.67Hz, as what is expected.

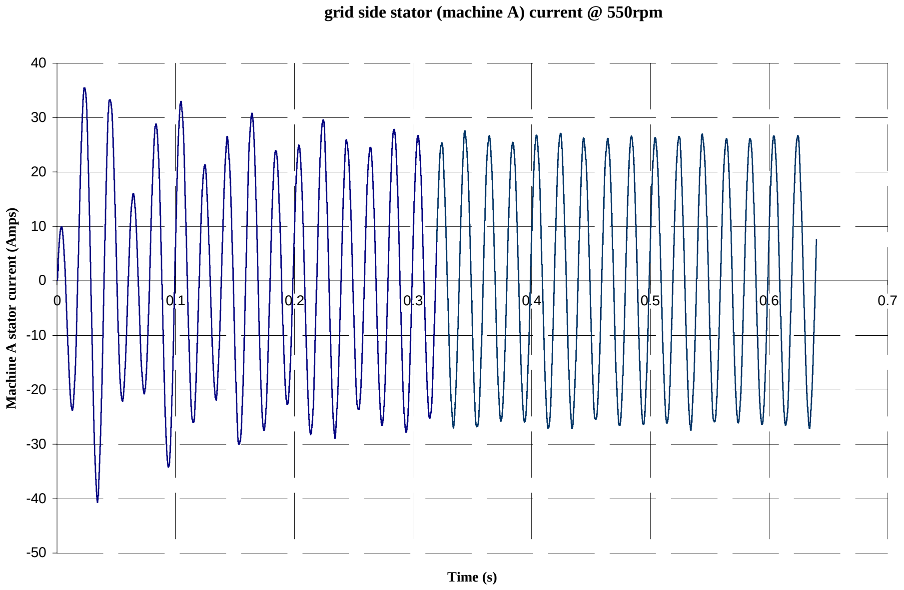

Figure 6.4.4 Grid side stator current waveform (side 1)

Figure 6.4.4 shows the generated stator current waveform for machine A, its frequency is 50 Hz, as what is expected.

From the DRM simulation result in figure 6.4.2-6.4.4, it can be shown that DRM could simulate the cascaded doubly fed induction machine system voltages and currents in both machines. Following context will show that DRM could also be used to analyse the power flow conditions in cascaded machine system.

The power flow conditions in sub-synchronous speed for CDFM are shown in figure 6.4.5.

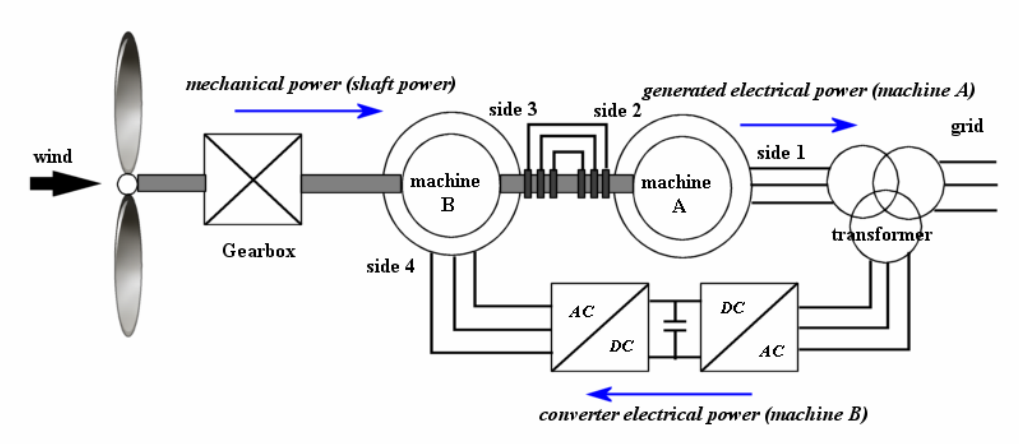

Figure 6.4.5 Power flow condition in sub-synchronous speed

Mechanical power flow into the cascaded doubly induction machine system through the shaft, and shaft speed is below the synchronous speed in this sub-synchronous speed case. Because the shaft speed is lower than the synchronous speed, converter electrical power will flow into the cascaded machine system, as shown in figure 6.4.5. Power relations for the cascaded machine system speed condition would be:

$$\left|P_{mech}\right| = P_{converter\ electrical} + P_{generated\ electrical} + \left|P_{loss}\right| \tag{6.4.1}$$

In the sub-synchronous speed case, converter electrical power would be negative (assume power flowing into the cascaded machine system and power loss is negative in sign), and generated electrical power in side 1 would be positive (assume power flowing into the grid is positive in sign). Power flow simulation by DRM method is shown in figure 6.4.6.

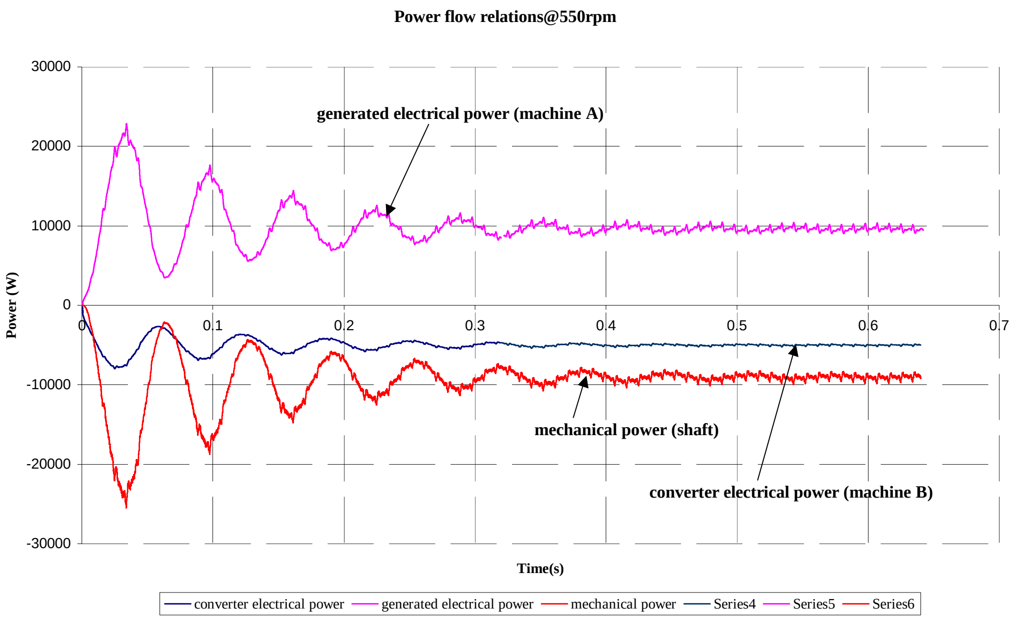

Figure 6.4.6 Power flow relationship between terminals in sub-synchronous speed

As can be seen in figure 6.4.6, the steady state mechanical power is –8.9KW, generated electrical power is 9.6KW, converter electrical power is -5KW. If no power loss is considered, the converter side machine should be coping with slip frequency power, but it is not the case in the simulations here. This is due to the induction machine simulated here is of small ratings, thus the copper loss is relatively bigger in percentage than the machine with larger ratings, and power loss have to be considered to make power transformation consistent. From equation 6.4.1, the power loss of the whole system would be around 4.3 KW. Total system copper loss from DRM simulation is shown in table 6.4.1.

Copper loss	**Stator current (peak)**	**Stator copper loss/phase (kW)**	**Stator copper loss (kW)**	**Rotor current (peak)**	**Rotor copper loss/phase(kW)**	**Rotor copper loss (kW)**	**Machine total (kW)**
Machine B	**27 A**	**0.38**	**1.14**	**25 A**	**0.326**	**0.978**	**2.118**
Machine A	**26 A**	**0.353**	**1.058**	**25 A**	**0.326**	**0.978**	**2.036**
System total			**2.198**			**1.956**	**4.154**

Table 6.4.1 Copper loss for sub-synchronous speed operating condition

The power loss difference between 4.3 KW and the copper loss, which is 4.154 KW, would be the computation errors, caused probably by the inaccurate calculation of the rms value of currents during the loss calculations as well as harmonics losses.

6.4.2 Super-synchronous speed, shaft speed - 950rpm

For super-synchronous speed, the frequency relations between the stator flux and rotor flux fields for the two induction machines are different from that of sub-synchronous speed.

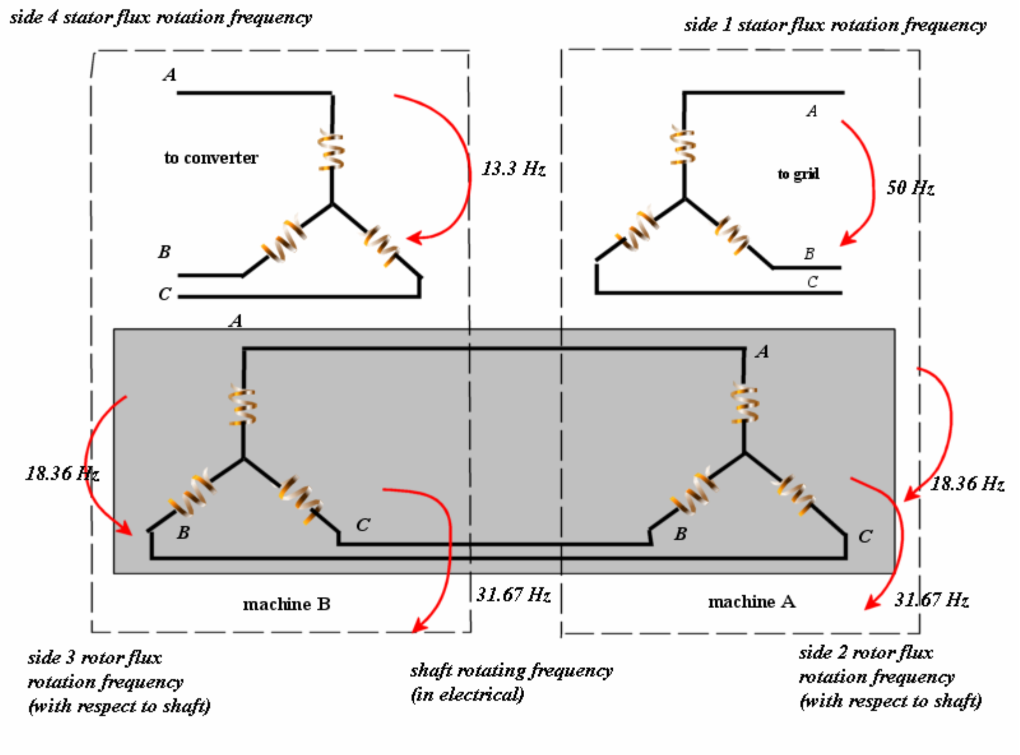

Figure 6.4.7 Frequency relations in super-synchronous speed – 950 rpm for CDFM

Figure 6.4.7 shows the frequency relations for super-synchronous speed. Flux field rotating direction for the stator flux field for converter side machine B is opposite to that of sub-synchronous speed. And such cause the machine B rotor flux field rotating frequency changed with respect to shaft. With a different mechanical speed of the shaft, and a corresponded rotor flux field frequency, 50 Hz stator current comes out of the stator terminals of the grid side induction machine, thus, a constant frequency, variable speed cascaded doubly fed induction machine system is fulfilled. Currents in stator and rotor in the cascaded machine system could be shown from figure 6.4.8 to 6.4.10.

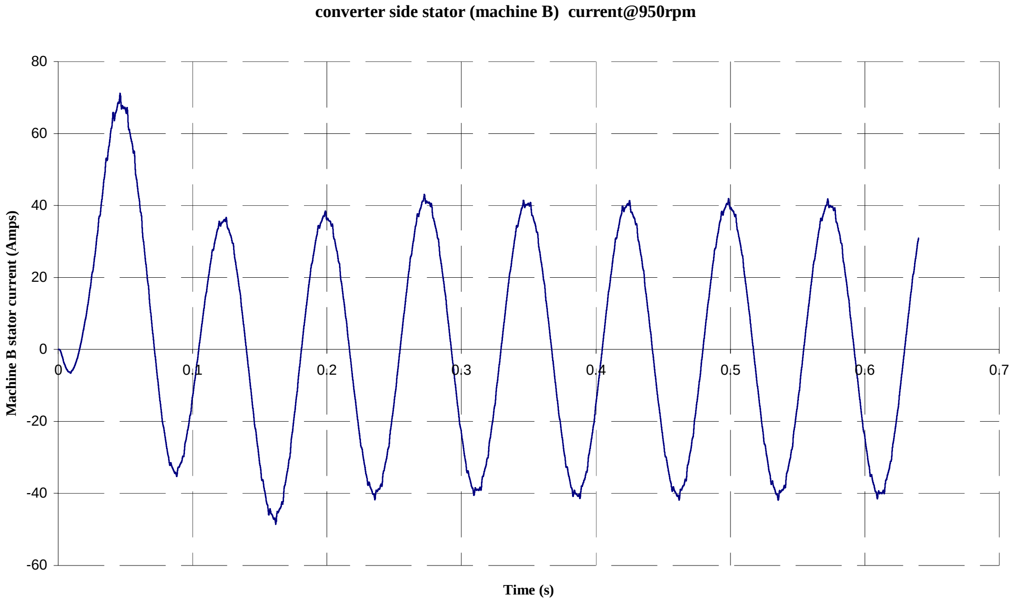

Figure 6.4.8 Converter side (side 4) induction machine stator current waveform

Stator current frequency of machine B in figure 6.4.8 is 13.3 Hz, calculated based on the running condition of the shaft speed. It is the frequency of the applied voltage through converter to machine B’s stator,.

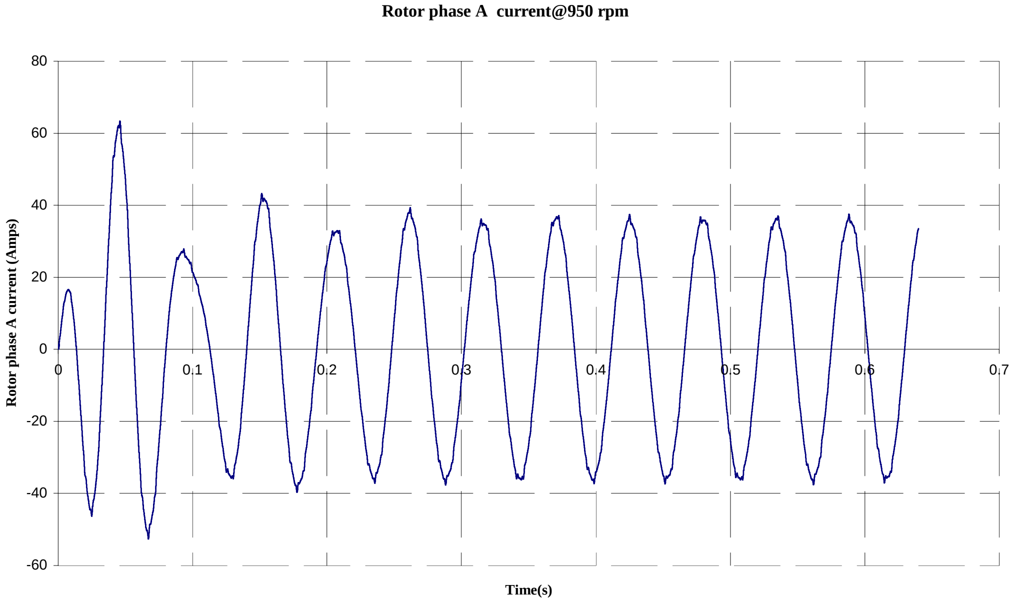

Figure 6.4.9 Rotor current waveform (side 2 & 3)

Rotor current frequency in super-synchronous speed 950 rpm in figure 6.4.9 is 18.33 Hz, as what is expected in figure 6.4.7.

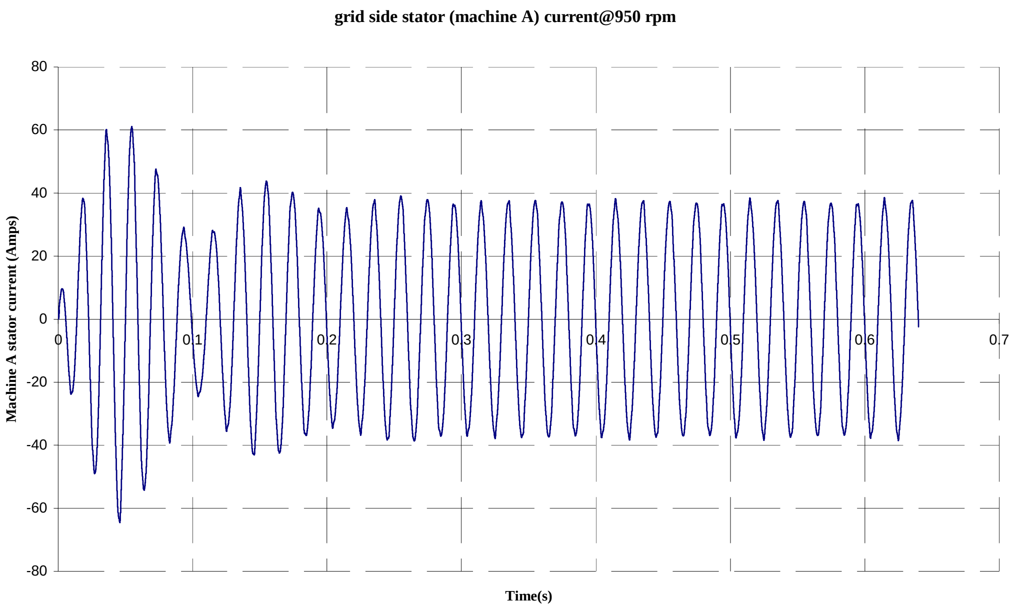

Figure 6.4.10 Grid side (side 1) induction machine generated current waveform

Figure 6.4.10 shows the generated stator current waveform for machine A, its frequency is 50 Hz, the same with theoretical value.

Power flow relations in super-synchronous speed are shown in figure 6.4.11.

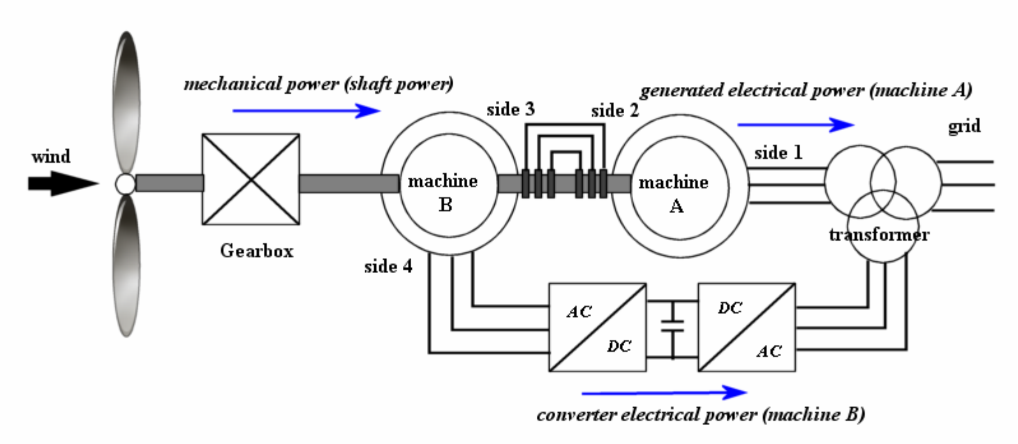

Figure 6.4.11 Power flow condition in super-synchronous speed

For super-synchronous speed running condition, power relations inside the cascaded machine system follows the same power relations as shown in equations 6.4.1. But, due to the super-synchronous speed the system is operating, converter electrical power will flow out of the machine system instead of flowing into, as shown by the arrow in figure 6.4.11. DRM simulation for power flow condition in super-synchronous running state is shown in figure 6.4.12.

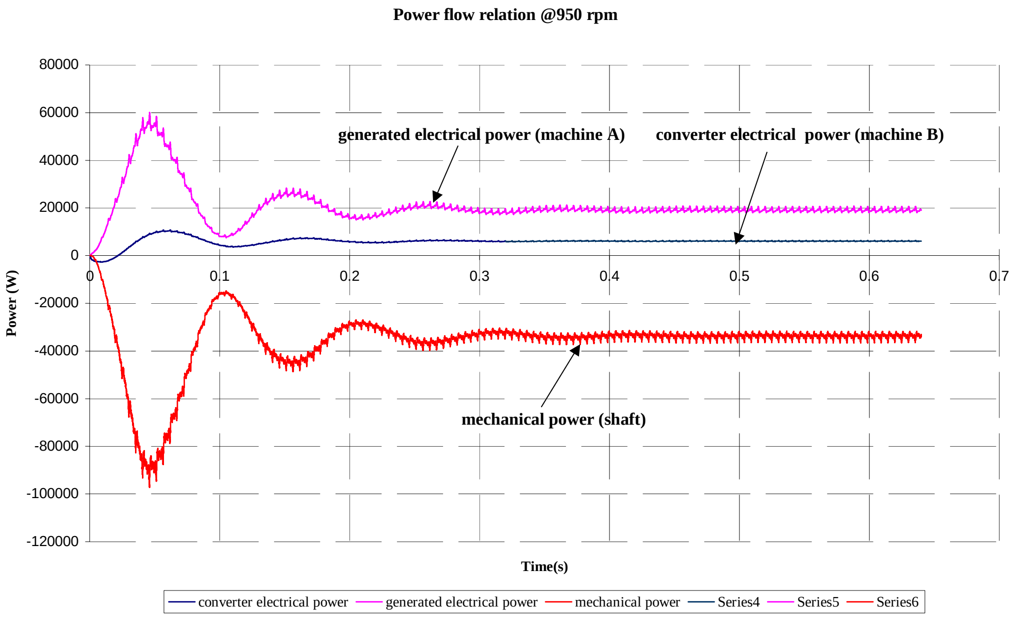

Figure 6.4.12 Grid side induction machine stator current waveform (side 1)

As can be seen from figure 6.4.12, converter electrical power changed the sign to positive, which means power is flowing out of side 4 to the grid. This is what is expected in theory. The mechanical power is -33.7KW, generated electrical power is 19.07 KW, and the converter electrical power is 6 KW. From equations 6.4.1, power loss of the whole system would be around 8.63 KW. Total system copper loss from DRM simulations for super-synchronous speed 950 rpm is shown in Table 6.4.2.

	Stator current (peak)	Stator copper loss/phase (kW)	Stator copper loss (kW)	Rotor current (peak)	Rotor copper loss/phase (kW)	Rotor copper loss (kW)	Machine total (kW)
Machine B	40 A	0.835	2.5	35.6 A	0.66	1.98	3.48
Machine A	36 A	0.676	2.03	35.6 A	0.66	1.98	4.01
System total			4.53			3.96	7.49

Table 6.4.2 Copper loss for super-synchronous speed operating condition

Power loss difference between 8.63 kW and 7.49 kW copper losses is the computational errors.

6.4.3 Synchronous speed, shaft speed - 750 rpm

In synchronous speed, d.c. voltage is applied to the stator of converter side machine, as shown in figure 6.4.13.

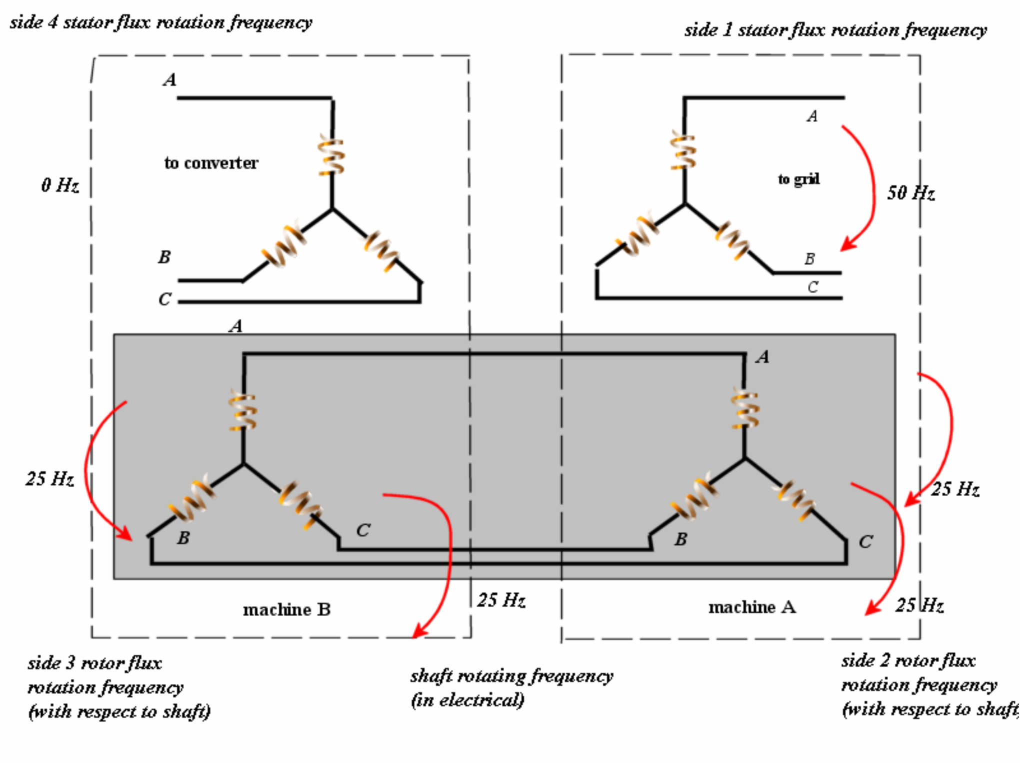

Figure 6.4.13 Frequency relations in synchronous speed – 750 rpm for CDFM

As can be seen from figure 6.4.13, stator flux field for machine B is stationary due to the d.c. voltage applied to it. To maintain the same direction and frequency of the stator flux field, rotor flux field rotating direction would be in the opposite direction to the shaft rotating direction with respect to the shaft, such that the total rotor flux field would be stationary to the frame. After machine A's rotor flux field rotating direction is changed by swapped phases, 50 Hz stator currents are generated from machine A, side 1, as shown in figure 6.4.13. Figure 6.4.14 to 6.4.16 show the current waveform of synchronous speed running condition for CDFM.

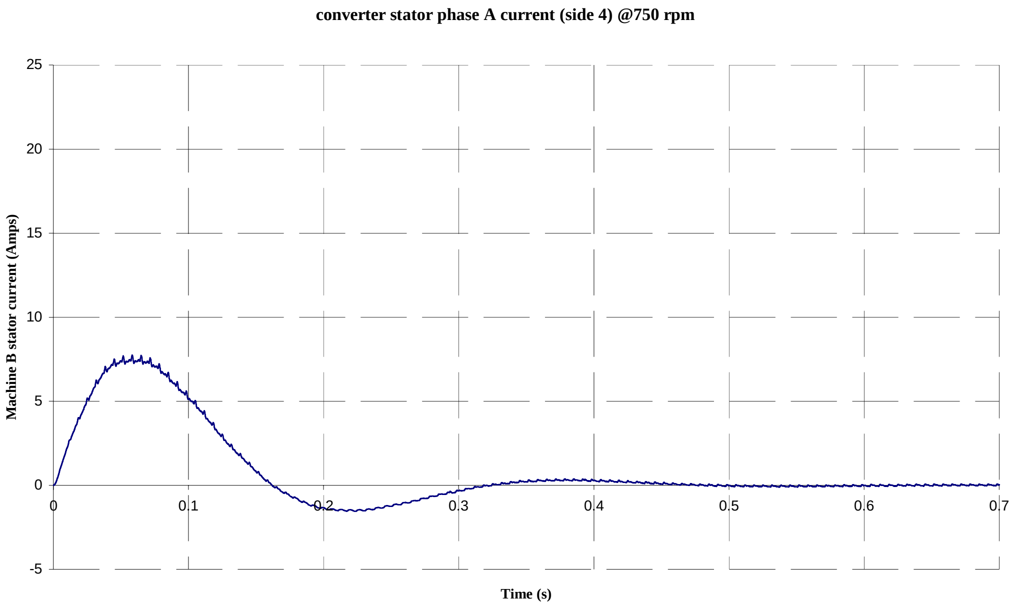
converter stator phase A current (side 4) @750 rpm
Machine B stator current (Amps)
25
20
15
10
5
0
-5
0
0.1
0.2
0.3
0.4
0.5
0.6
0.7
Time (s)

(a)

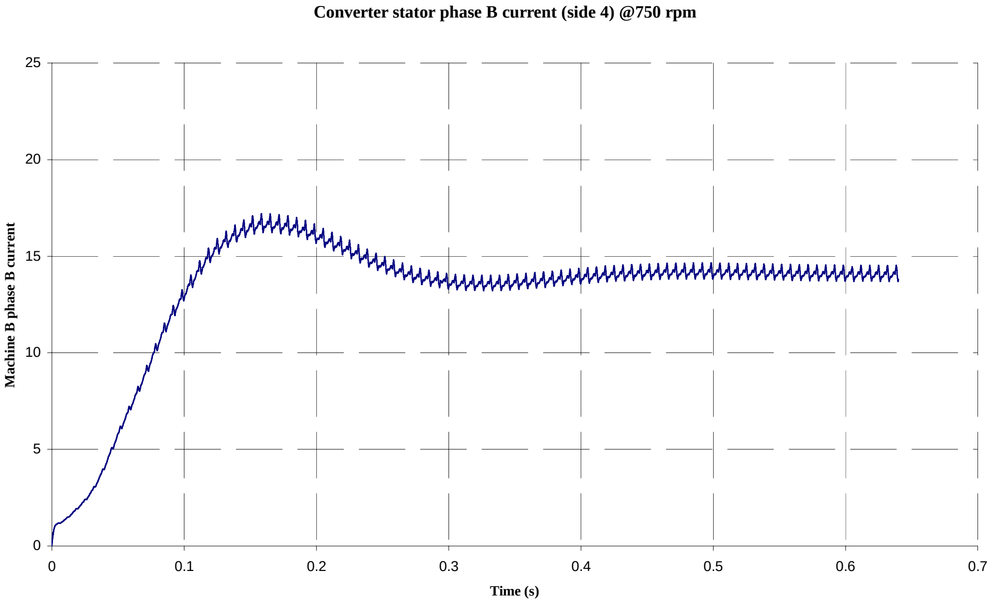
Converter stator phase B current (side 4) @750 rpm
Machine B phase B current
25
20
15
10
5
0
0
0.1
0.2
0.3
0.4
0.5
0.6
0.7
Time (s)

(b)

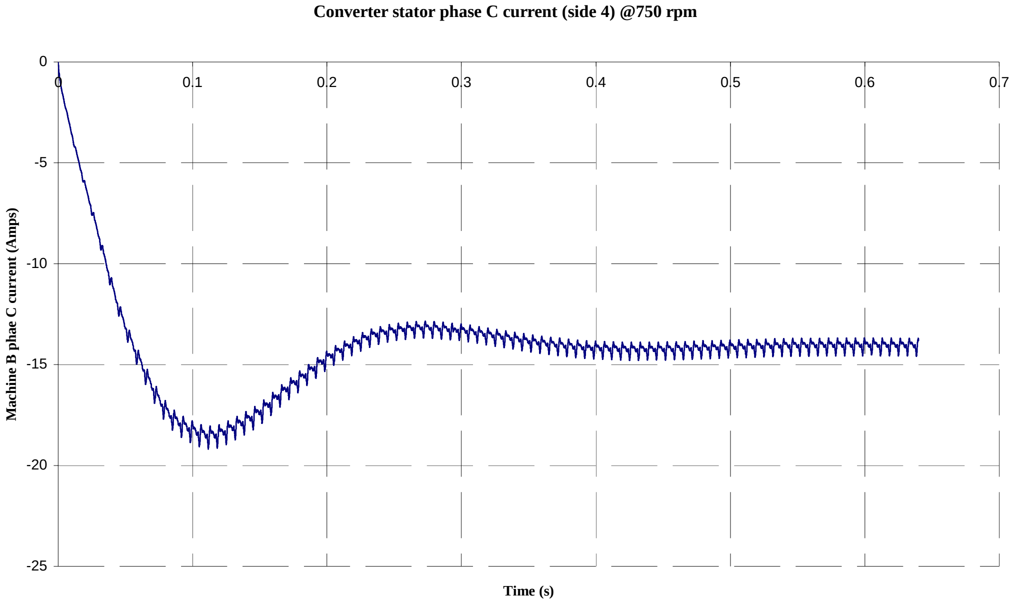

(c)

Figure 6.4.14 Converter side (side 4) stator current waveform

Figure 6.4.14 shows the three-phase stator current of machine B. Phase B and C are d.c. current practically, and phase A current is zero in steady state. This is due to the 0 frequency sinusoidal waveform applied the stator terminals in machine B.

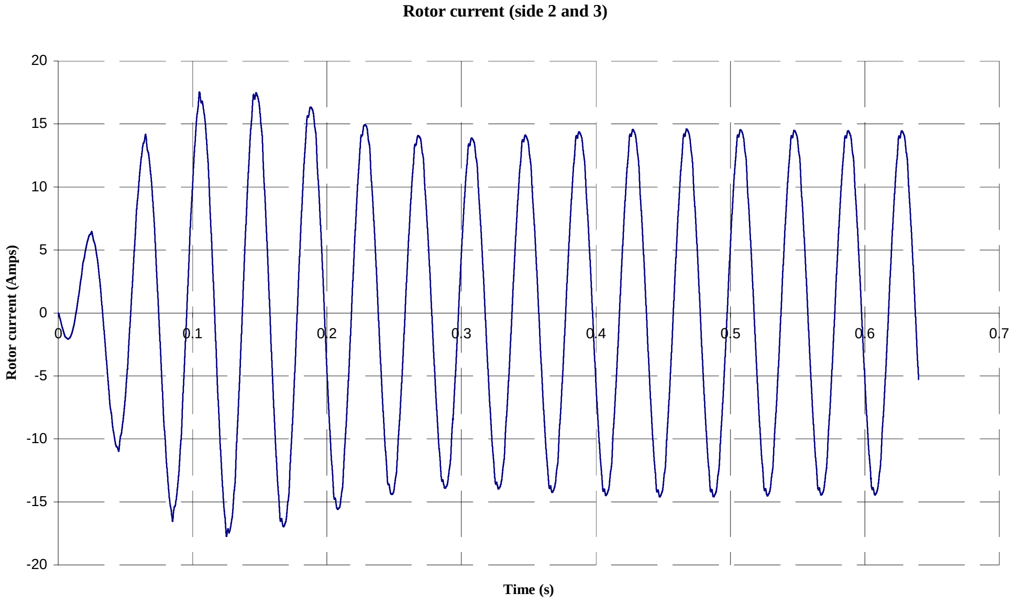

Figure 6.4.15 Cascaded machine rotor phase A current (side 2 and 3)

Rotor current frequency is 25 Hz, as what is expected in synchronous running condition.

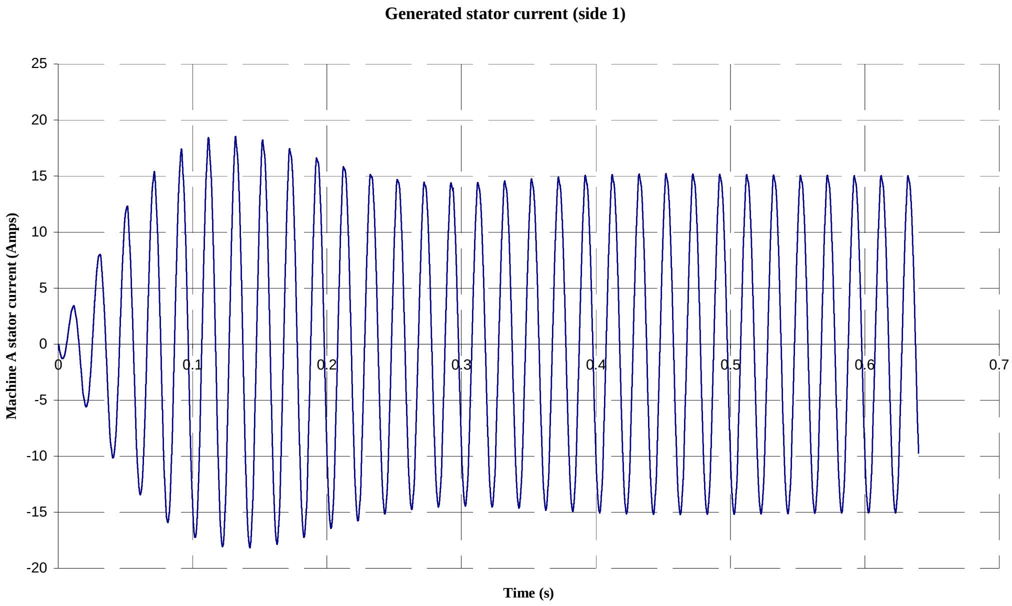

Figure 6.4.16 Generated grid side stator current waveform (side 1)

Figure 6.4.16 shows the generated stator current waveform for machine A in synchronous running condition, its frequency is 50 Hz, as what is expected.

In synchronous speed, converter power only handles the power to iron loss, as have been stated in previous sections. Power flow condition can be seen in figure 6.4.17.

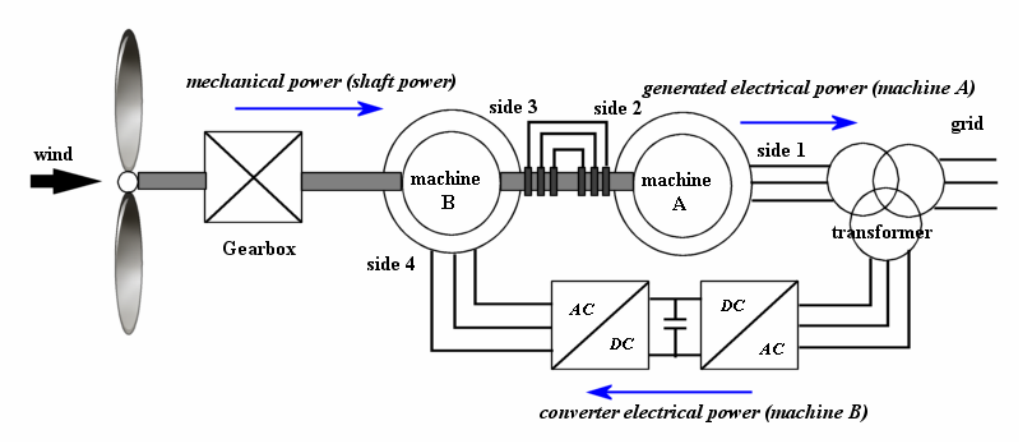

Figure 6.4.17 Power flow condition in synchronous speed for CDFM system

Converter power is supposed to be flowing into the CDFM system to compensate for the system losses. Power relations as shown in equations 6.4.1 should be satisfied. DRM simulation result for power flow is shown in figure 6.4.18.

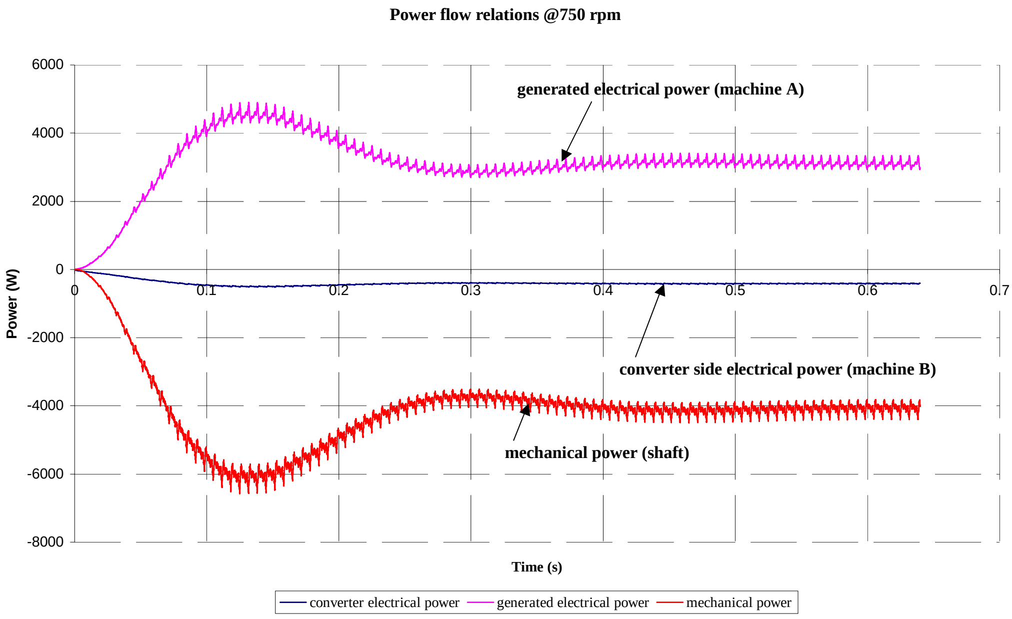

Figure 6.4.18 Power flow relationship between terminals in synchronous speed

As can be seen in figure 6.4.18, the mechanical power in steady state is 4.09 KW, generated electrical power is 3.12 kW, and converter electrical power is 0.414kW. From the calculation in equations 6.4.1, the total power loss in the system would be around 1.384 kW. Total system copper loss from DRM simulations is shown in Table 6.4.2.

	Stator current (d.c)	Stator copper loss/phase A (kW)	Stator copper loss (kW)	Rotor current (peak)	Rotor copper loss/phase (kW)	Rotor copper loss (kW)	Machine total (kW)
Machine B	14 A	0.204	0.408	14 A	0.102	0.306	0.714
Machine A	15 A	0.117	0.352	14 A	0.102	0.306	0.658
System total			0.76			0.612	1.372

Table 6.4.3 Copper loss for synchronous speed operation

The power difference between 1.372 kW for copper loss and 1.384 kW for total system loss is due to computational errors.

With the help of DRM simulation, the frequency relationship and power flow conditions in three operations state for cascaded doubly fed induction machine have been simulated and analysed. One thing needs to be pointed out is that;

obvious harmonics distortion can be spotted in power flow conditions figures for all of the three running conditions. This is due to the slot harmonics in the two machines, and might cause control problem for the controls in cascaded machine systems.

6.5 Conclusion

This chapter extends the DRM modelling method further to the modelling and simulation of the multiple-machine, system-cascaded, doubly-fed, induction machine system, which involves two cascaded induction machines to replace the slip ring in doubly fed induction generators. Simulation results are investigated considering sub-synchronous speed, super-synchronous speed and synchronous speed respectively. Power flow conditions and current frequencies are investigated as well.

There are slotting harmonic effects which show through as distortion in the current waveforms and are clearer in the power waveforms. These effects in this case are not particularly strong but could fall into the current bandwidth of the current controllers of a practical system and may well cause voltage distortion. However, the simulation here is for small power machines which are skewed thus substantially suppressing the slotting effects. Skewing is much less common in high power machines and practical designs may therefore see considerably greater slotting problems if they are not designed appropriately. The DRM approach obviously has the capability to assist fully in exploring and controlling these design problems.

CHAPTER 7 RELUCTANCE MESH TOPOLOGY INVESTIGATION IN THE DYNAMIC RELUCTANCE MESH MODELLING METHOD

7.1 Introduction

Dynamic Reluctance Mesh modelling is an effective way to model and simulate electrical machines and multiple machine systems, as have been studied and validated in chapter 4, 5 and 6. The accuracy of the simulation results from DRM model depends on many aspects, including the topology of the reluctance mesh, the numerical parameter settings as well as the solving accuracy of the solver. Among them, the topology of the reluctance mesh is a key factor.

However, the creation of the topology of reluctance mesh is determined by experience, based on the prior known knowledge of the flux distribution inside the electrical machines, both the iron part and the air gap part. Different topology of reluctance mesh will give different machine simulation behaviour; and the different modelling of the air gap region, which involves leakage flux modelling, gives the most differences.

This chapter will concentrate on the influence of reluctance mesh topology on machine simulation results. The influence of the modelling of slot leakage flux in induction machines; the discretisation of stator tooth tips in exciter and the discretisation of salient pole iron part will be investigated and discussed separately. The objective of the work in this chapter is to determine what is important in reluctance mesh creation based upon the prior knowledge of flux distribution in the machine.

7.2 Induction Machine Reluctance Mesh Investigation

As described in section 3.5, there are leakage fluxes flowing linking windings in the stator and rotor slots, thus, an additional reluctance representing leakage flux between stator and rotor teeth needs to be added, as shown in figure 7.2.1. Topologies using 1, 2 and 3 mmfs are modelled in the tooth part of the induction machine, with corresponds to 1 reluctance representing leakage flux, 2 reluctances and 3 reluctances.

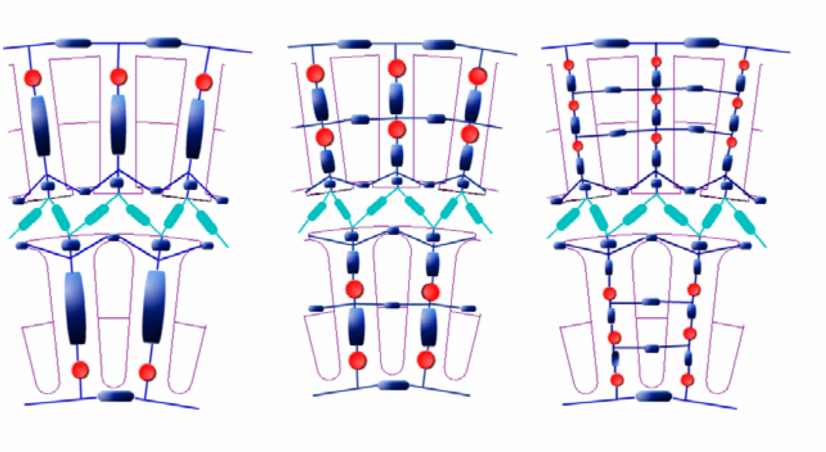

Figure 7.2.1 Induction machine reluctance mesh topology considering leakage flux across slots

In each case, if the magnetic steel of the teeth is perfect and has infinite permeability, the leakage flux values obtained will be the same. However, with finite permeability and particularly with high levels of saturation the three models will not yield the same leakage flux.

Figure 7.2.2 shows the DRM simulation results for a non-skewed rotor induction machine, with 1mmf, 2mmfs, and 3mmfs in stator and rotor reluctance mesh. Reluctances represent leakage fluxes in between stator and rotor slots and are calculated by leakage reluctance calculation method given in section 3.5.

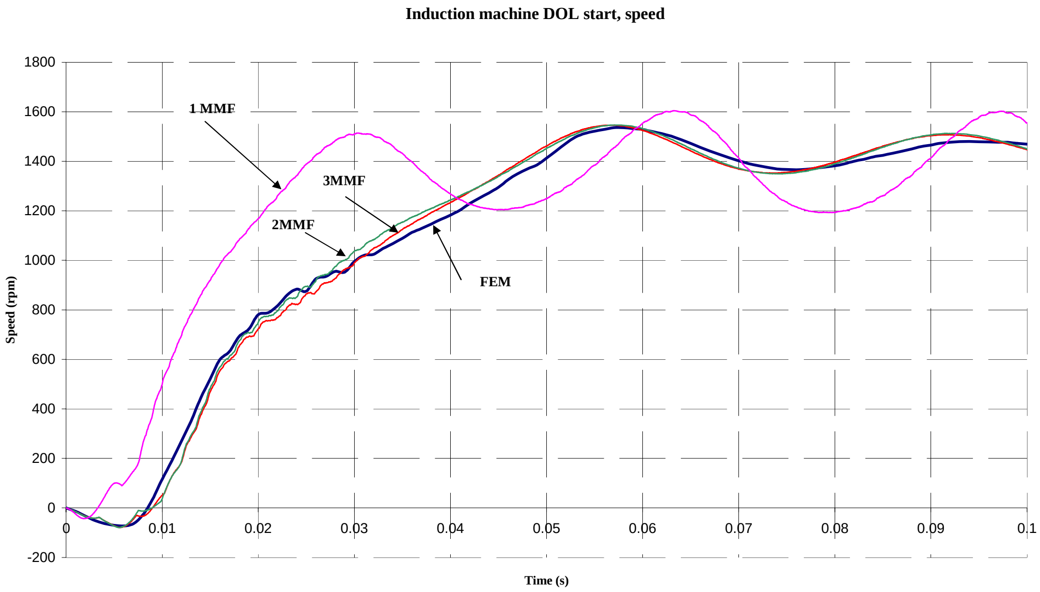

Figure 7.2.2 DRM simulation result of induction machine speed rising curve, with 1mmf, 2mmfs and 3mmfs in reluctance mesh

As can see from figure 7.2.2, the simulation results from the reluctance mesh with 2mmfs and 3mmfs give a better agreement to FEM result compared to the result given by 1mmf. The reason is that the slope of the acceleration curve of the induction machine depends on the rate of rise of flux and current inside the machine, which is influenced primarily by leakage flux. By modelling the leakage flux reluctance between stator and rotor slots for the 2mmfs and 3mmfs modelling, the leakage effects in the machine is accounted for more effectively as it is a distributed phenomena. Initially all three curves agree because there is limited winding current and the acceleration is very low. As the winding currents build up to several times the rated value saturation of the leakage flux paths in the teeth become significant and the acceleration curves diverge. Thus a better agreement of the acceleration curve compared to the FEM result occurred with the 3 mmf model which allows for this saturation effect more effectively.

Therefore, in DRM modelling, the additional reluctances representing distributed leakage flux in the machine should be created to account for leakage flux, particularly when the machine transient behaviour, which is considerably affected by leakage effects, is the research interest. Quite satisfactory results can be obtained by using 2 mmf sources per tooth though 3 would be better in critical cases. There appears to be no need to use more than 3 mmf sources per tooth in normal machines.

7.3 Exciter Reluctance Mesh Investigation

Exciters have a slightly different geometry in the respect of the relative width of the stator and rotor tooth tips in comparison to induction machines: the tooth tip widths of the stator and rotor in the induction machine are in a similar range while for an exciter, the stator tooth tip is much wider than that of the rotor. This is due to the machine type, i.e. salient pole, and a small number of armature slots for cost reasons in exciter. For the exciter, high frequency currents are generated to feed to the rotating rectifier and then to the generator field winding. The number of poles in the exciter is commonly much more than that of the induction machine. Also, d.c. is applied to the exciter stator, and the number of stator teeth is designed to be equal to the number of poles, avoiding a complicated a.c. winding to reduce manufacturing cost. Therefore, the reluctance mesh discretisation of the stator tooth tip in exciter could be the same as that of induction machine from the geometry perception, but also could be different considering the wider stator tooth tip width with respect to the rotor tooth tip width.

In this section, three different discretisations of the exciter stator tooth tip will be used in DRM simulations, shown in figure 7.3.1 to figure 7.3.3, and then their resultant machine behaviour will be examined and compared.

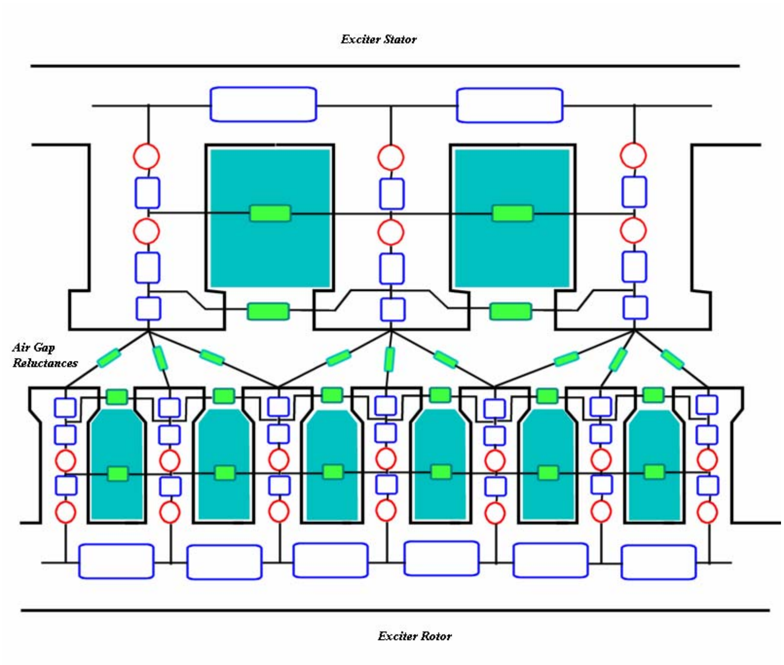

Figure 7.3.1 Reluctance mesh of the exciter, type 1: one reluctance on stator tooth tip

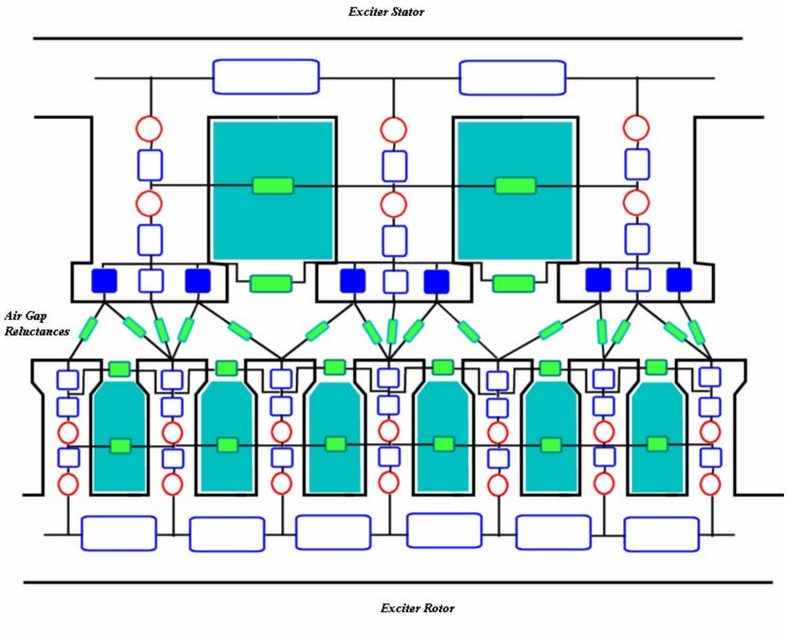

Figure 7.3.2 Reluctance mesh of the exciter, type 2: three reluctances on stator tooth tip

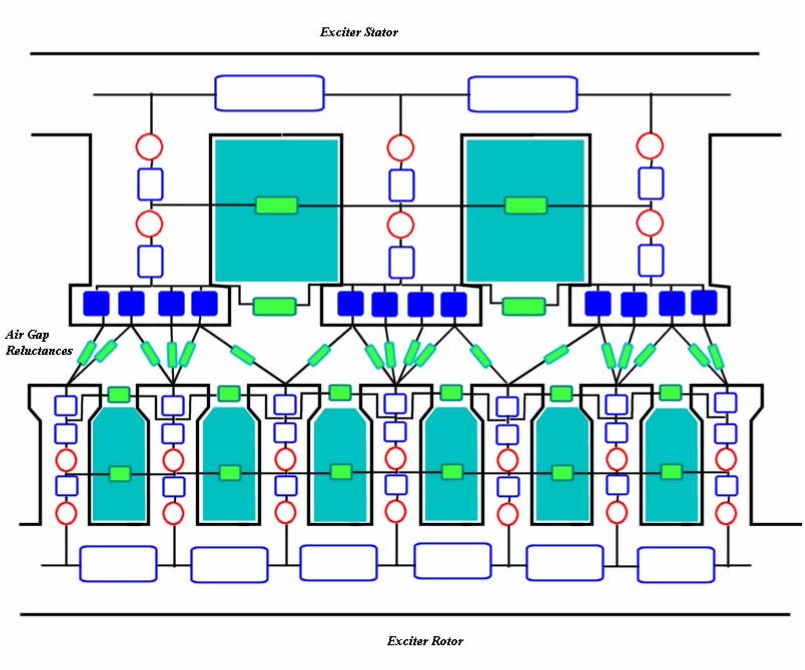

Figure 7.3.3 Reluctance mesh of the exciter, type 3: four reluctances on stator tooth tip

When comparing figure 7.3.1, figure 7.3.2 and figure 7.3.3, differences of these reluctance meshes are the number of elements in the stator tooth tip area. It can be seen that exciter stator teeth is divided into three elements in mesh type 2 and into four in type 3 respectively, but only divided to one in mesh type 1. For mesh type 2, the width of each virtual tooth in the stator is of the similar width with that of rotor. The reason why reluctance mesh type 2 and 3 are utilized is because the flux distribution is assumed to be normal to the tooth surface (constant potential surface) in mesh type one, although practically this may not be the case due to saturation reducing the relative permeability. Some of the flux distribution in the tip region of the tooth will be distorted due to the different geometry of tip area and tooth region. By dividing the tooth surface into more than one reluctance element, this flux distortion can be accounted for. In each case however, a finite element model of the air gap and teeth has been used to work out the air gap reluctances which are to be used. Air gap reluctance curves for these three types of stator tip discretisation are shown in figure 7.3.4. It can be seen that the air gap curves have different width and magnitude due to the different discretisations.

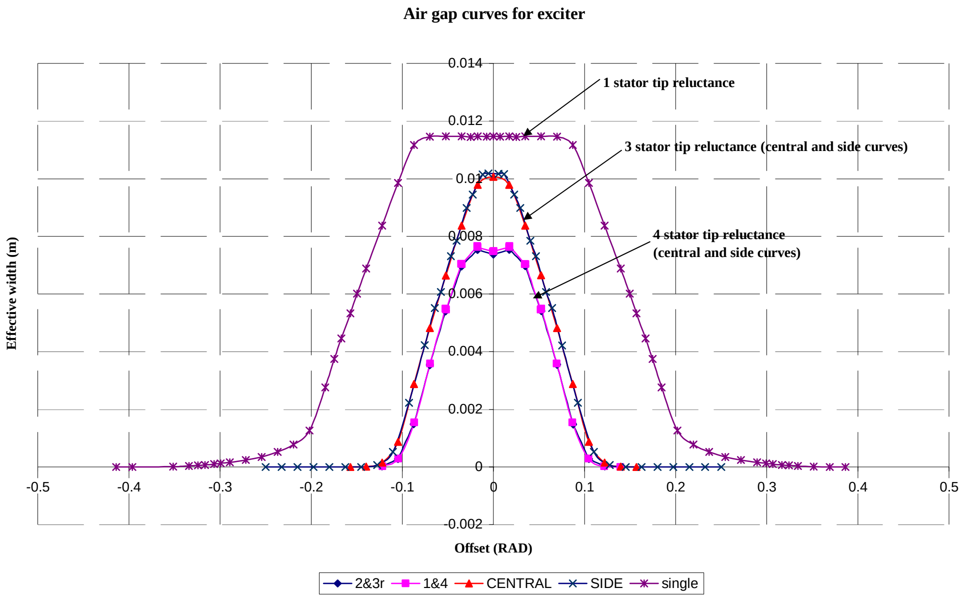

Figure 7.3.4 Air gap reluctance curves for the three discretisations for exciter stator tooth tip

The relatively wide center part of the air gap reluctance curve for 1 stator tip reluctance is explained by the much wider stator tooth tip width compared to the rotor tooth tip width. Thus a constant air gap reluctance width is expected while rotor tooth is within the stator tooth region.

Comparison of DRM simulation results for these different types of reluctance mesh in a simulated open circuit case are shown in figure 7.3.5 to 7.3.7. It can be seen that the current and voltage ripple are bigger for reluctance mesh type 2 and 3 compared to mesh type 1.

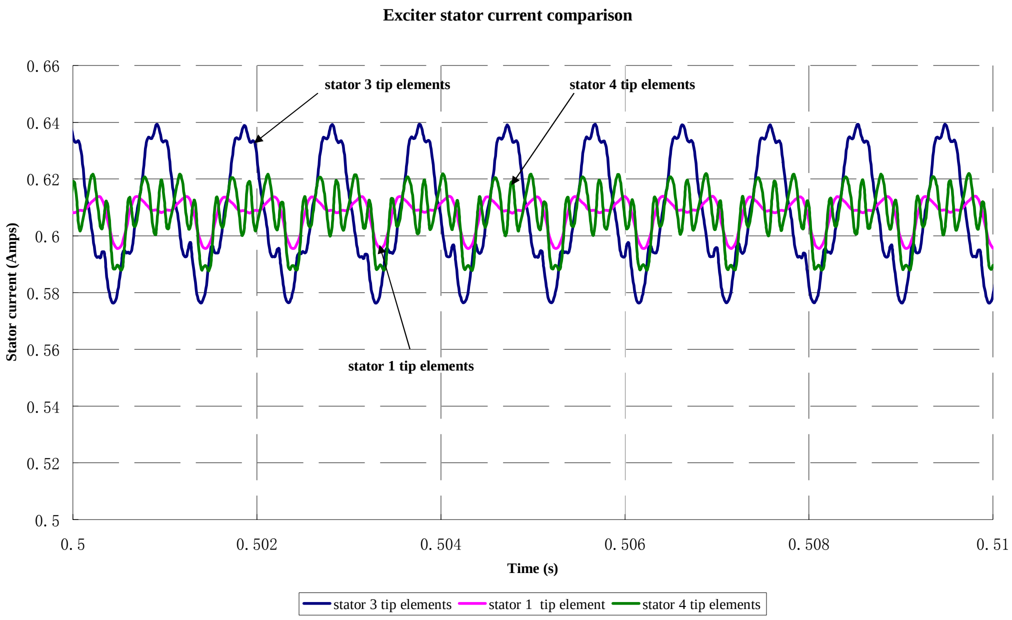

Figure 7.3.5 Exciter stator current comparisons for different reluctance meshes, mesh type 1,2&3

Stator current ripple, as shown in figure 7.3.5, has the slot harmonic ripple caused by the slot opening on the rotating rotor. Its frequency is the slot passing frequency, which is $25 \times 42 = 1050$ [28]. It can be seen that mesh 2 and mesh 3 give a bigger ripple due to the different way of modelling the tip elements that touch the air gap. More elements on tooth tip area can account for the flux non-uniform distribution in the tooth tip area but cause an effect of ripple in stator current. This is due to the division of the stator tooth producing virtual teeth on the stator. However, if there was not appreciable saturation of the stator tooth tip elements there would be no appreciable difference between the models.

Figure 7.3.6 shows the exciter rotor current for the three different kinds of reluctance meshes. It can be seen that mesh type 1 and mesh type 3 give a similar average exciter rotor current waveform, although result for mesh 3 has more harmonics, which is due to the additional discretisation on stator teeth. There are bigger exciter rotor current harmonics in the result of mesh type 2, compared to mesh type 1 and 2. It looks like mesh 2 gives a substantial cogging effect, the same as for induction machines, when the number of stator teeth equals the number of rotor teeth. In mesh type 2, the number of virtual teeth of exciter stator is 42, while the number of rotor teeth of this exciter is also 42, the same number of teeth for exciter stator virtual teeth. According to Alger [25], cogging effect due to stator and rotor having same number of teeth happens.

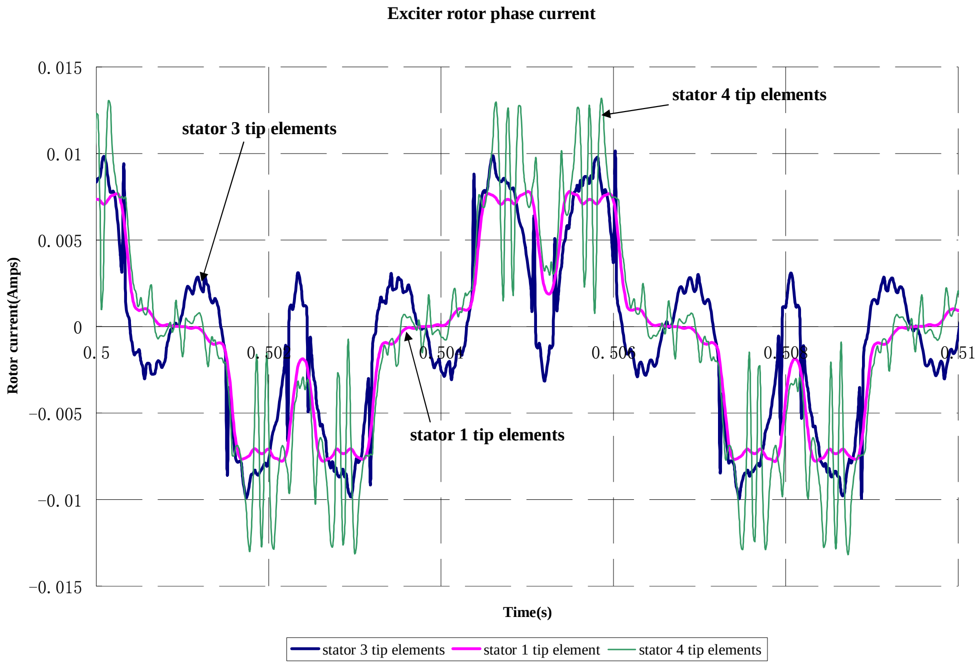

Figure 7.3.6 Exciter rotor current comparison for different reluctance meshes, mesh type 1,2&3

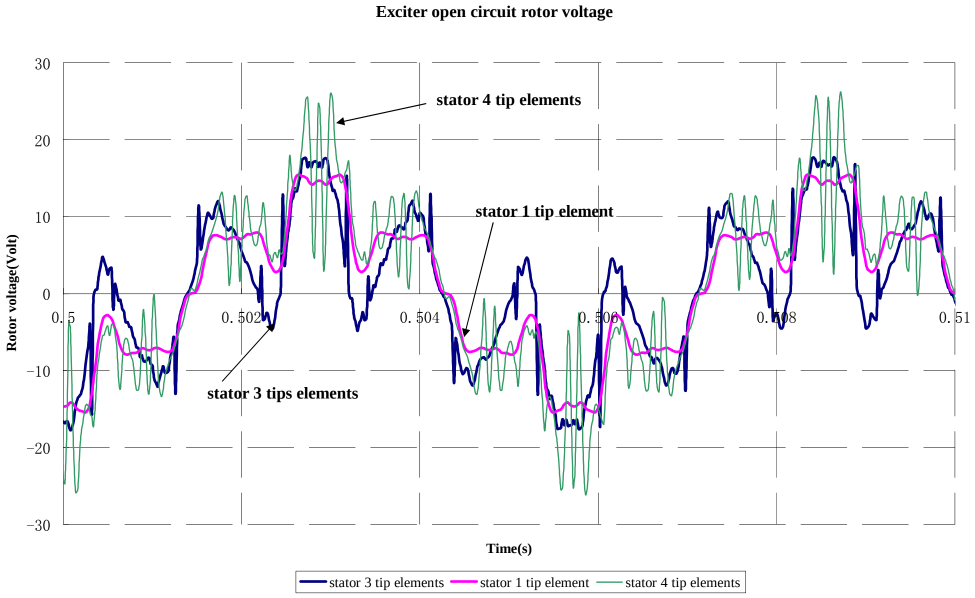

Figure 7.3.7 Exciter rotor terminal open circuit voltage comparison for mesh type 1,2&3

This cogging effect could also be seen from figure 7.3.7, the exciter open circuit rotor terminal voltage waveforms. It can be seen that compared with mesh type 1 and 3, result comes out from mesh type 2 has obvious cogging.

With different discretisation approaches for the stator tooth tip in the exciter, different currents and voltage waveforms for the stator and rotor could be achieved. Each of them reflects real machine behaviour in some aspect, and tooth harmonics effects could be simulated. However, the only real difference between the models is the stator tooth tip reluctance elements. If the tooth tip elements of the models 2 and 3 become zero then these models reduce to model 1. This would suggest that there is a fair degree of saturation in the tooth tips of the exciter under normal operating conditions.

The conclusion here is that not only is it necessary to apply the concept of virtual teeth with salient pole forms of machine but it is also necessary to model the air gap reluctances and tooth tip reluctances effectively. This is particularly true for machines with saturated salient pole tips under normal or faulty operating conditions.

7.4 Salient Pole Synchronous Generator Reluctance Mesh Investigation

Considering the reluctance mesh for salient pole synchronous generator, two types of reluctance mesh will be investigated in this section: one with 6 virtual teeth on the central pole, while the other one with doubled the virtual teeth in the central part of the salient pole. The geometry of the salient pole examined in this section has a stepped airgap in the middle of the salient pole, specifications of this machine is detailed in Appendix 6. The two reluctance meshes to be investigated are shown in figure 7.4.1 & 7.4.2, referenced as DRM case 1 and DRM case 2.

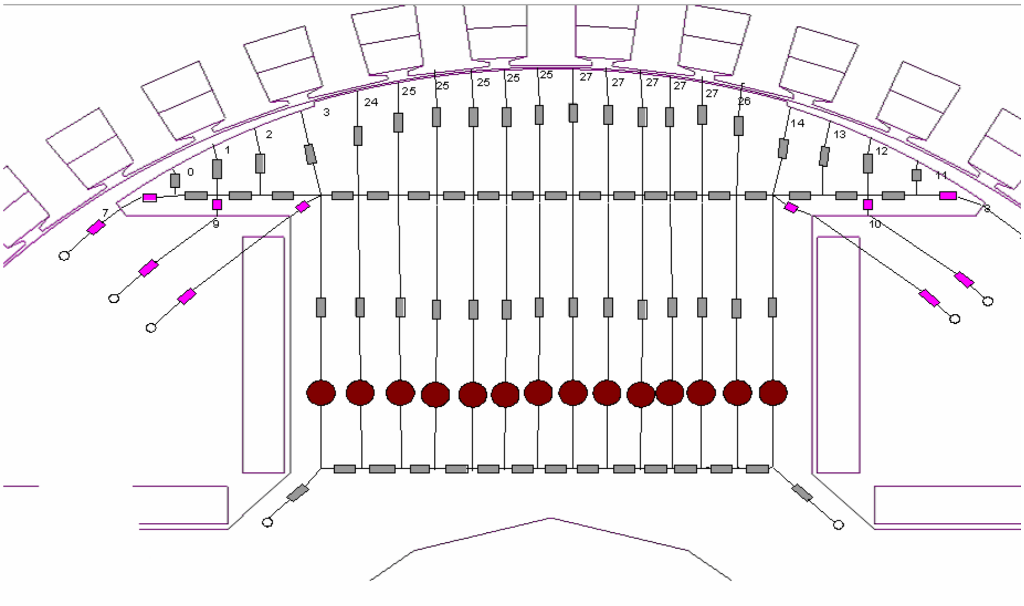

Figure 7.4.1 Dynamic reluctance mesh type 1 for salient pole synchronous machine

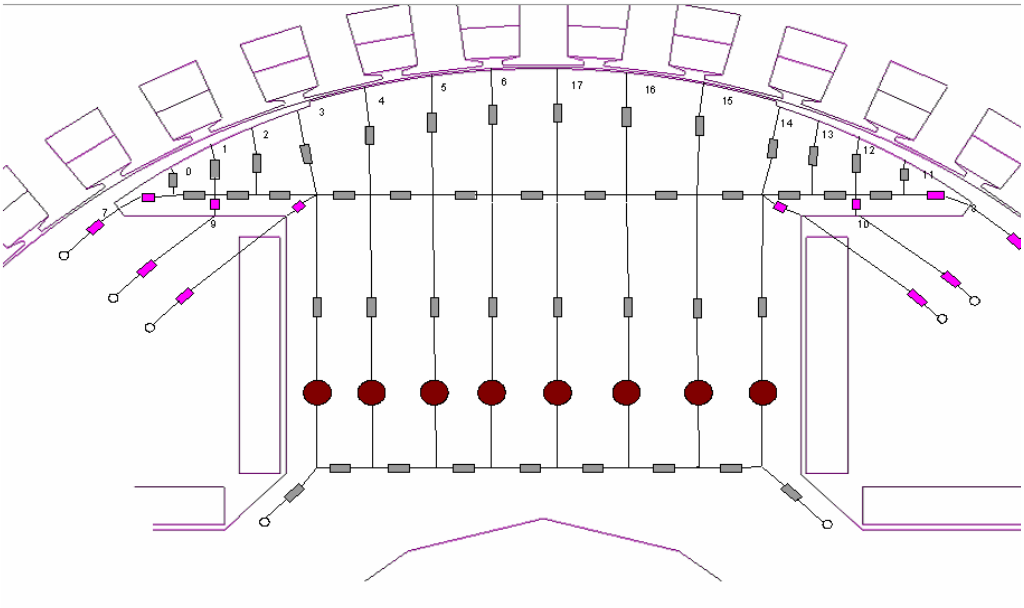

Figure 7.4.2 Dynamic reluctance mesh type 2 for salient pole synchronous machine

The static field inductance of the generator model with the two kinds of meshes would be calculated by the DRM simulation results. Inductance is calculated by the rotor flux linkage divided by the rotor field current, shown in equation 7.4.1.

$$L_r = \frac{\lambda_r}{i_f} \tag{7.4.1}$$

where L_r , λ_r and i_f are the rotor inductance, flux linkage and field current respectively. Flux linkage is derived from the DRM simulation by summing the flux in all the reluctances that are effectively sitting vertically on rotor surface.

These inductance calculation results from the two reluctance meshing methods of the salient pole are then compared to the inductance calculated from FE model, with different element sizes and for specific iron permeability. Results can be shown in figure 7.4.3. The field modelling accuracy of the finite element result depends on the element size in the finite element discretisation. The smaller the element size, the higher the accuracy of the field models but the greater the potential for rounding errors in computation. In the results comparison below, two inductance calculation results from finite element will be presented: one is the inductance calculated from automatic discretisation meshing, the other is calculated from the discretisation that allocates the maximum element size in the machine to be 0.3mm.

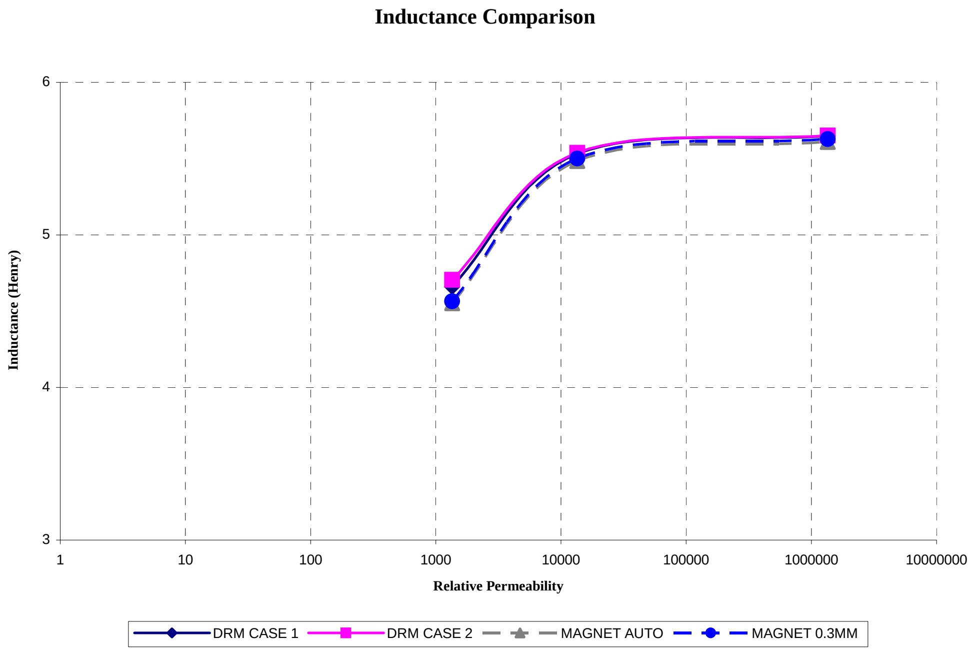

Figure 7.4.3 Inductance comparison from DRM and FE method

And the error with respect to FE model is shown in figure 7.4.4.

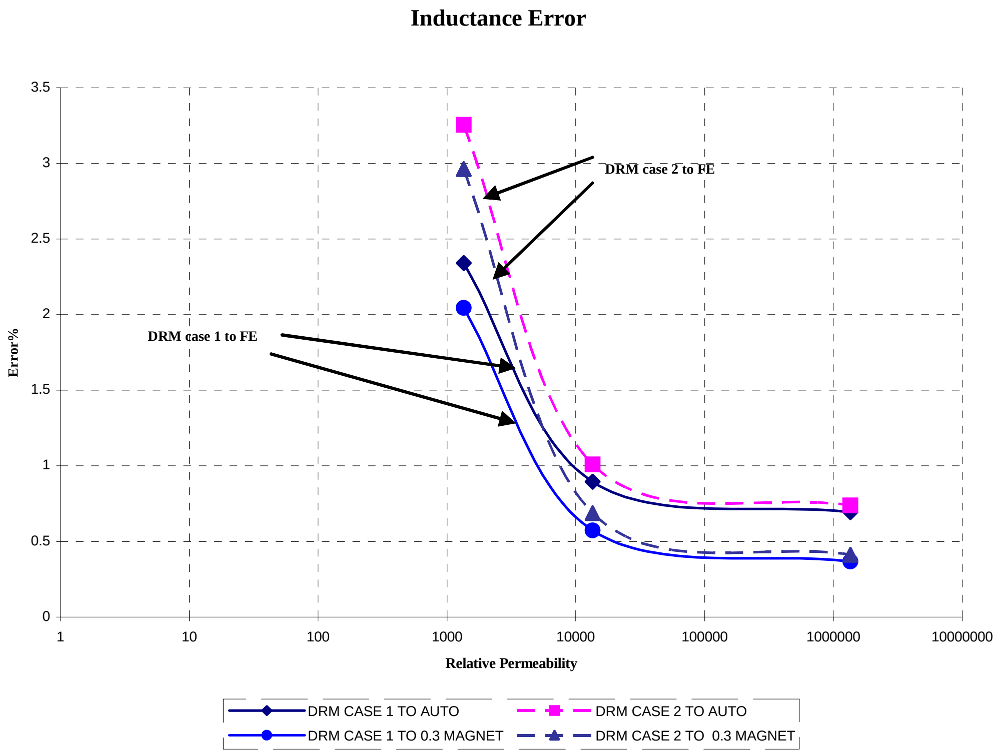

Figure 7.4.4 Inductance comparison error for DRM with respect to FE

It can be seen that DRM case 1 produces less error compared to finite element results, than DRM case 2, which means that the more number of iron elements discretised, the more accurate the result would be, even for the central salient pole part which conducts main flux in machine's magnetic circuit. All the errors decrease with the increase of the iron permeability. Permeability is involved in the result sheet is because the air gap overlap curve that has been used in the salient pole synchronous machine DRM simulation is derived from a simplified FE model with a very big permeability ($\mu_r = 135000$), while in the DRM simulations in this section, the iron permeability used in DRM simulation is not that big, and this will result in a discrepancy between the DRM and FE simulation results, shown in figure 7.4.4. The larger the iron permeability used in DRM simulations, the closer the simulation result will be to the FE result.

It can also be seen that the smaller the element size in the FE model, the smaller the errors, which proves the rule that the smaller elements size makes a more accurate field model.

In this section, by comparing different ways of discretising iron elements in a salient pole, the effect of iron discretisation has been investigated. It is shown from the result that the discretisation in unsaturated iron doesn't influence the simulation result a lot, from the inductance point of view.

7.5 Influence of the Reluctance Mesh in a Single Machine to Multiple Machine System

In previous sections, different reluctance mesh topologies for induction machines, exciters and salient pole synchronous machines have been investigated individually. In this section, the influence of the reluctance mesh for one machine in a multiple machine system will be examined.

This section will look at the mesh discretisation influence in DRM simulations for the brushless generating system that has been simulated and investigated in chapter 5. Different exciter stator reluctance meshes are applied, and the whole system open circuit curves will be derived and comparison will be made to experimental results. Different reluctance mesh for exciter is applied here instead of for salient pole rotor is because the exciter is non-skewed, thus a saturation effect is prominent and could be spotted easily.

By applying the exciter stator reluctance model type 1 and 2, the open circuit curve of the whole system is shown below in Figure 7.5.1.

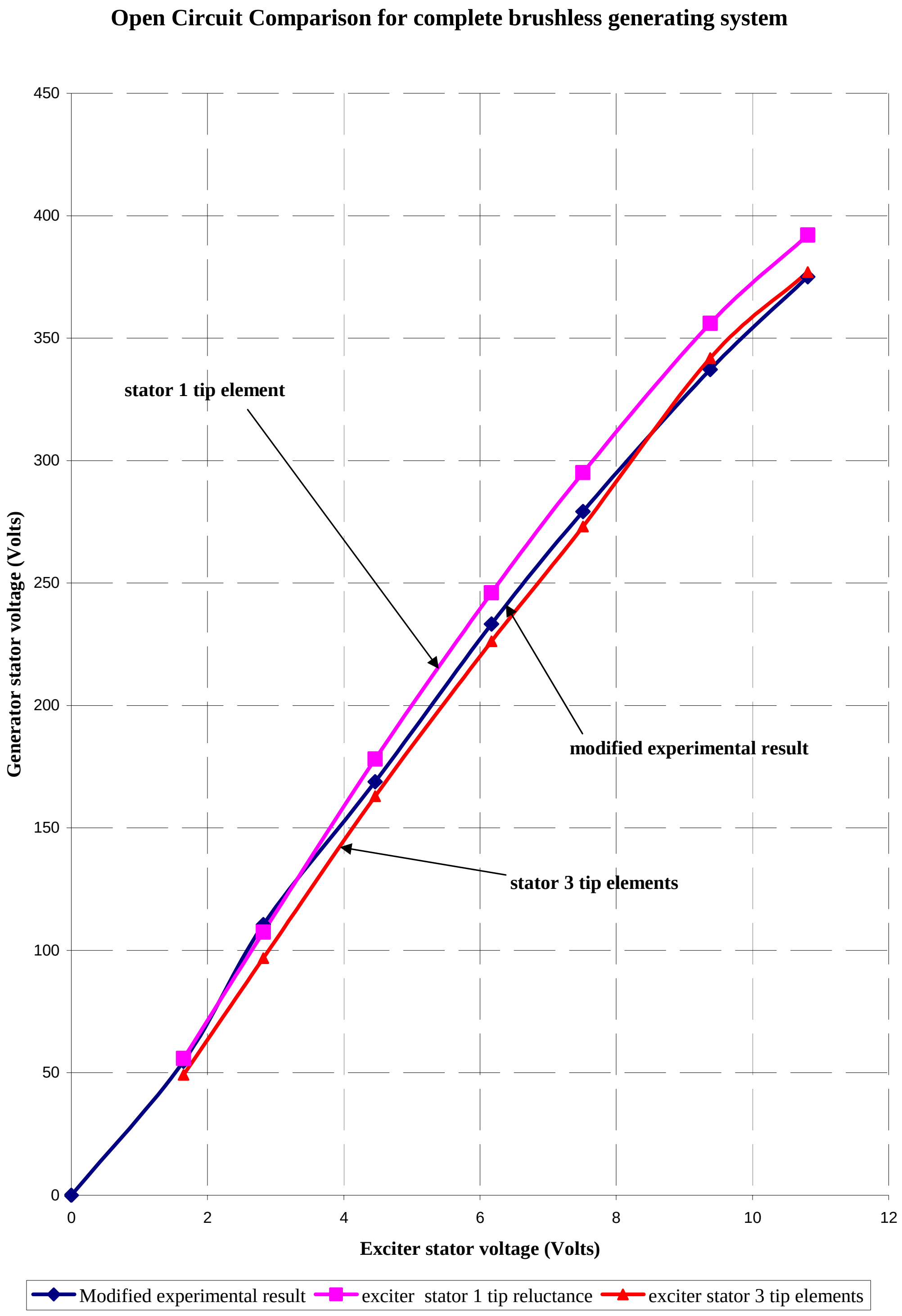

Figure 7.5.1 Open circuit test simulation result comparison for generating system, with different reluctance mesh of exciter

Clearly the greater discretisation of the exciter stator poles not only influences the harmonic content of the rotor current waveform as seen in the previous section, but also alters the shape of the open circuit curve for the brushless generator. It is clear that the exciter must have saturated pole tips and suffer from armature reaction since increasing the number of virtual stator teeth increases the agreement between experimental and simulated results. Armature reaction increases with exciter load current and reduces the net flux in the exciter producing a lower field current in the main generator. The results show better agreement between the models at low generator output voltage and thus low load and low armature reaction conditions in the exciter. As generator output voltage increases the open circuit curves of the different models diverge and the lower discretisation models which cannot evaluate armature reaction in the exciter effectively, become increasingly in error.

It is quite difficult to obtain experimentally the rotor current waveforms of the exciter when it is operating as part of a brushless generator set simply because the signals are on the rotating rotor. However, the overall system performance yields sufficient information when the additional component models have already been verified as accurate. It appears that to obtain sufficient accuracy, the number of virtual teeth on each stator pole has to be similar to, or slightly greater than the actual number of teeth on the rotor since 3 virtual teeth gives very good results for a rotor with 3 teeth per pole in this case.

7.6 Conclusion

The accuracy of DRM modelling technique depends partly on the topology of the reluctance mesh. The topology of the reluctance mesh is decided by the prior knowledge of the flux distribution in the machine. This chapter investigated the influence of the different reluctance mesh forms on the DRM simulation results, taking the exciter machine, salient pole generator and the whole generating system as examples. The objective was to examine what is important in terms of this prior knowledge.

The research has confirmed the importance of modelling in detail the leakage reluctances in a machine where high winding currents under transient conditions cause saturation of leakage flux paths. There is also a need to use virtual teeth with salient pole machines if saturation of the pole is to be considered as is almost inevitable due to armature reaction. This has been clearly demonstrated with the open circuit curves for the brushless generator when different virtual teeth numbers have been examined for the exciter. The results show that a similar number of virtual teeth are required to the actual number of teeth carrying the armature winding.

A further conclusion is that when using the finite element models to evaluate the air gap reluctance values it is best to use permeance values for the iron parts of the machine which approximate to the values likely to be found under normal operating conditions associated with the main flux path.

CHAPTER 8 CONCLUSION AND FUTURE WORK

8.1 Introduction

This chapter summarizes the main conclusions drawn from the thesis and discusses relevant future work of this research area.

8.2 Conclusion

This thesis developed and validated a computationally efficient, detailed, modelling method for electrical machine simulations derived from field behaviour. It is suitable for machines with both uniform and non uniform air gaps such as induction motors and salient pole synchronous generators respectively. It is particularly suitable for modelling multiple machine systems which may include nonlinear power electronic components and control schemes. The method is based on and extends greatly, simple, traditional, finite difference, lumped reluctance, machine models. Comparison of results between DRM simulations and those obtained using finite elements as well as those obtained experimentally have shown that this method gives excellent agreement within engineering accuracies. Furthermore, this method can also be applied to other related systems with complicated control and power electronic schemes in place.

The modelling approach developed in this thesis sits between system modelling using SIMULINK and idealised dq machine models and the finite element modelling of individual machines. Commercial finite-element models are just beginning to include control systems but they still do not include multiple machine systems and control. In its current form the DRM program does not have the flexibility of SIMULINK but it includes saturation of main and leakage flux paths, slotting and space harmonic effects in detail in the machine models which dq analysis can not do. While the DRM machine models evaluate effectively all of the major factors which make machines non ideal, they are not as comprehensive as a full finite element model developed specifically for a particular machine. However, being computationally efficient they take far less time to solve than FEM models offering iterative design procedures not only for the machine but also for the system.

A summery of the research work and detailed conclusions is presented in each of the relevant chapters. However, the main conclusions are summarized as follows:

In the modelling of electrical machines, a more accurate method of modelling the air gap reluctance in the DRM method, called air gap overlap curves, was proposed based upon the simulation results from FE calculations. This air gap overlap curve method extracts the useful information about the flux distribution between the stator and rotor in the machines which takes fringing effects into account and thus a more accurate model of the air gap flux connection is achieved. This method can be used in induction machines but it is particularly useful for salient pole synchronous machine which have non-uniform air gap geometry where it is difficult for the original air gap reluctance creation rules of the DRM to be applied effectively. This thesis detailed the method of deriving the air gap overlap curve for the salient pole synchronous generator in chapter 4, and results from open circuit test and short circuit test as well as the air gap flux density distribution have shown that they agree well with both the FE result and experiments. However, this air gap overlap curve derived from FE only works accurately for a moderately nonlinear iron; for a heavily saturated iron, flux distribution as well as the overlap curves between the stator and rotor will be slightly different.

Detailed DRM models for electrical machines, such as slot leakage modelling in induction machine and inter pole flux modelling and damper bar modelling in salient pole synchronous machines, were also addressed in the thesis. The discretisation method of the solid rotor pole is also described, because it is different from the reluctance mesh creation for induction machine previously applied. Comparison of the DRM results to FE and experiments have shown that when these measures are included, the DRM can supply simulation results with a very good accuracy from the engineering perspective.

A key part of any finite difference or FE program is the non linear equation solver. The Newton-Raphson solver originally used for the DRM software was further improved to overcome the nonconverge problems when solving system with great nonlinearity. A globally convergent NR solver was proposed introducing line searching schemes to identify a proper Newton step. This improvement increased the stability of the solving process thus enabling more complicated system simulations which have significant nonlinearities and control schemes will be tackled more easily. This expanded the field of application of the DRM method.

This thesis also applied the DRM modelling technique to the simulation and investigations of multiple machine systems, namely, the small brushless generating system and the cascaded doubly fed induction generators used in the wind generation industry. This is a significant advance on conventional methods of simulating machine systems. Normally, system models are analysed through traditional winding coil models. These machine models are very limited and neglect many saturation, harmonic and slotting effects inherent in a practical system. With the DRM machine modelling technique, the complete system incorporating multiple machines and power electronic components as well as control schemes can be simulated with the entire practical machine features modelled. All this is achieved within a reasonable computation time. This is a task which commercial FE could not cope with nowadays.

To complete the research of the DRM modelling technique, the influence of different reluctance mesh topologies on the machine behaviour was investigated in chapter 7. Results comparison for different reluctance mesh forms of calculated and experimental results show that more refined reluctance mesh models may be needed where the iron is heavily saturated by main or leakage fluxes. That is in deep stator slots where leakage fluxes contribute to tooth saturation it is not sufficient to model the slot leakage in one reluctance linking the tooth tips. Dividing the slots and teeth into two or three sections along the length of the teeth introduces additional slot leakage flux paths across the slots which share out this leakage flux and reduce excessive tooth saturation. Two sections are adequate in most cases but three sections give very good results. Additionally, it was shown that salient poles should be treated as a number of parallel virtual teeth and that even in very heavily saturated machines the number of virtual teeth should be similar, but not exactly equal to, the number of teeth on the armature.

The findings above have fulfilled the original aims of the research program and have widened the knowledge of multiple machine simulation techniques, and also expanded the application field of the dynamic reluctance modelling technique.

8.3 Suggestions for Future Work

There are a number of suggestions for future work which can extend the understanding and application of the dynamic reluctance modelling method and increase the DRM modelling accuracy. These are:

1. Air gap reluctance models in the machines can be improved to accommodate heavily saturated iron. This could be implemented by applying different air gap overlap curves depending on the saturation degree, e.g. the flux density value in the stator or rotor teeth. Thus, different flux distributions which depend upon the saturation of the iron can be accounted for. This is particularly useful in the simulations where saturation phenomena are important to the electrical machine's behaviour.
2. More realistic models and complex control schemes for the AVR controller can be applied to the simulation model of small brushless generating systems, other than the simplest PID controller currently simulated in the thesis. Their performance could be evaluated by the modified DRM simulation tool in the thesis.
3. This modified DRM machine simulation tool might be applied to other machines or machine system simulation fields, where various control schemes and machine designs need to be evaluated but with a reasonable simulation time. Such a case might be a full, doubly fed wind generator system.

APPENDIX 1 SALIENT POLE SYNCHRONOUS GENERATING SYSTEM SPECIFICATIONS

1.1 Main generator technical details

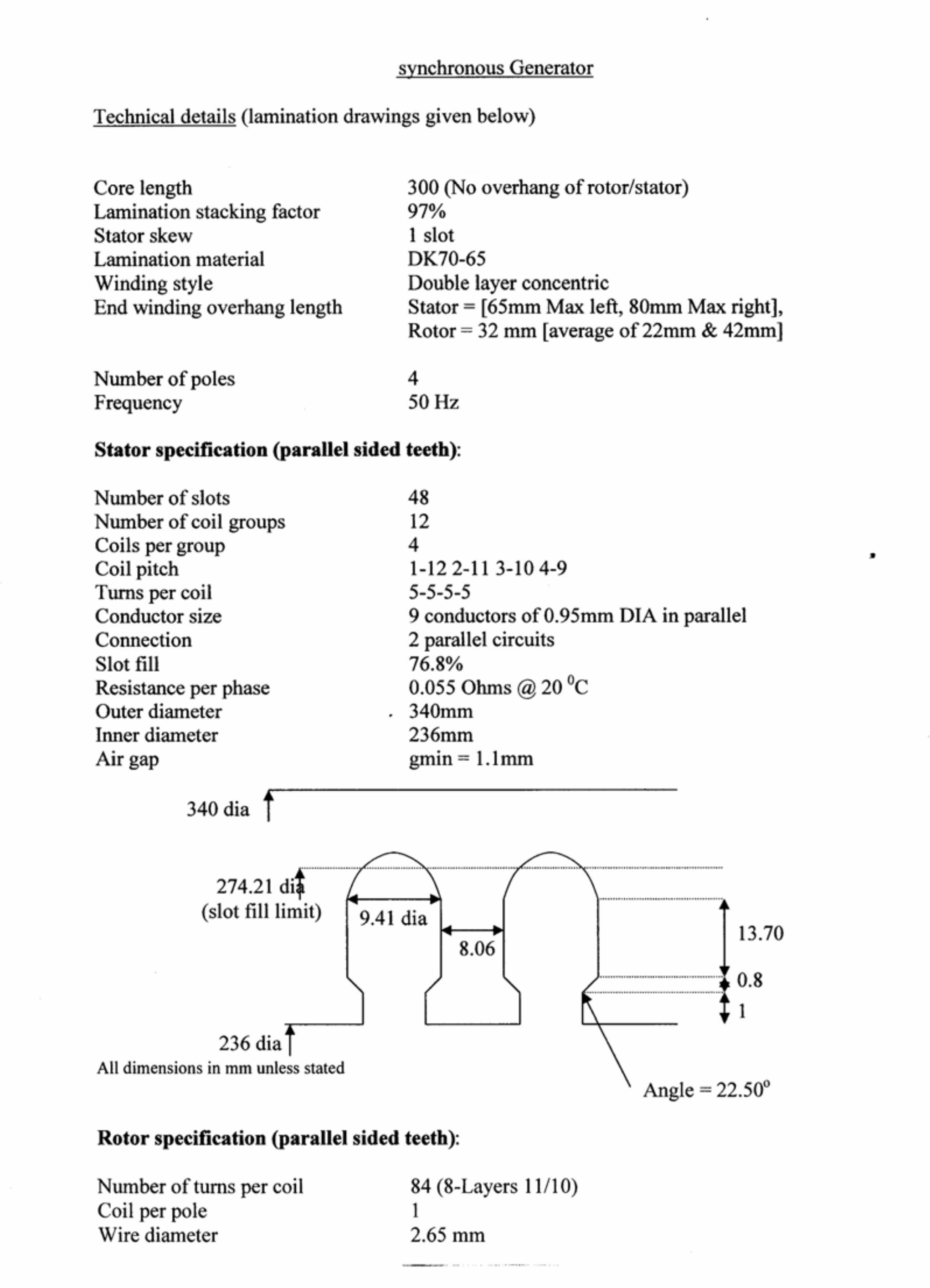

synchronous Generator

Technical details (lamination drawings given below)

Core length	300 (No overhang of rotor/stator)
Lamination stacking factor	97%
Stator skew	1 slot
Lamination material	DK70-65
Winding style	Double layer concentric
End winding overhang length	Stator = [65mm Max left, 80mm Max right], Rotor = 32 mm [average of 22mm & 42mm]
Number of poles	4
Frequency	50 Hz

Stator specification (parallel sided teeth):

Number of slots	48
Number of coil groups	12
Coils per group	4
Coil pitch	1-12 2-11 3-10 4-9
Turns per coil	5-5-5-5
Conductor size	9 conductors of 0.95mm DIA in parallel
Connection	2 parallel circuits
Slot fill	76.8%
Resistance per phase	0.055 Ohms @ 20 ^{0}C
Outer diameter	340mm
Inner diameter	236mm
Air gap	gmin = 1.1mm

All dimensions in mm unless stated

Rotor specification (parallel sided teeth):

Number of turns per coil	84 (8-Layers 11/10)
Coil per pole	1
Wire diameter	2.65 mm

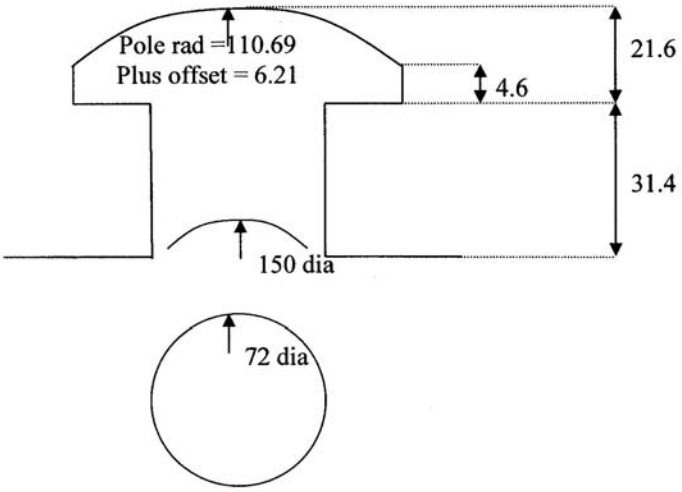

ll dimensions in mm unless stated

1.2 Main generator rotor lamination drawings

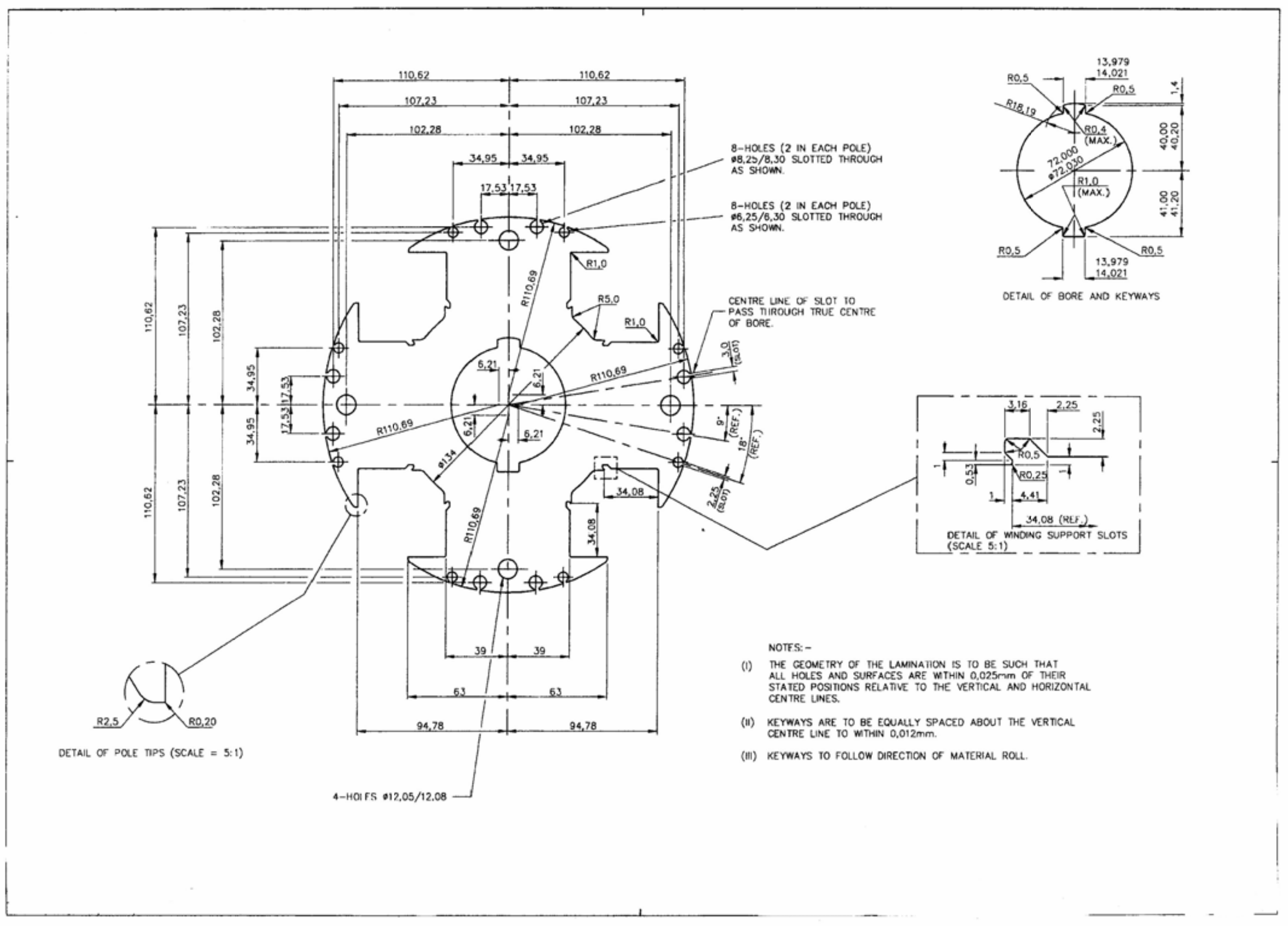

NOTES: –

(I) THE GEOMETRY OF THE LAMINATION IS TO BE SUCH THAT ALL HOLES AND SURFACES ARE WITHIN 0,025mm OF THEIR STATED POSITIONS RELATIVE TO THE VERTICAL AND HORIZONTAL CENTRE LINES.

(II) KEYWAYS ARE TO BE EQUALLY SPACED ABOUT THE VERTICAL CENTRE LINE TO WITHIN 0,012mm.

(III) KEYWAYS TO FOLLOW DIRECTION OF MATERIAL ROLL.

Figure A1.2.1 Rotor lamination drawings

1.3 Main generator stator and rotor details

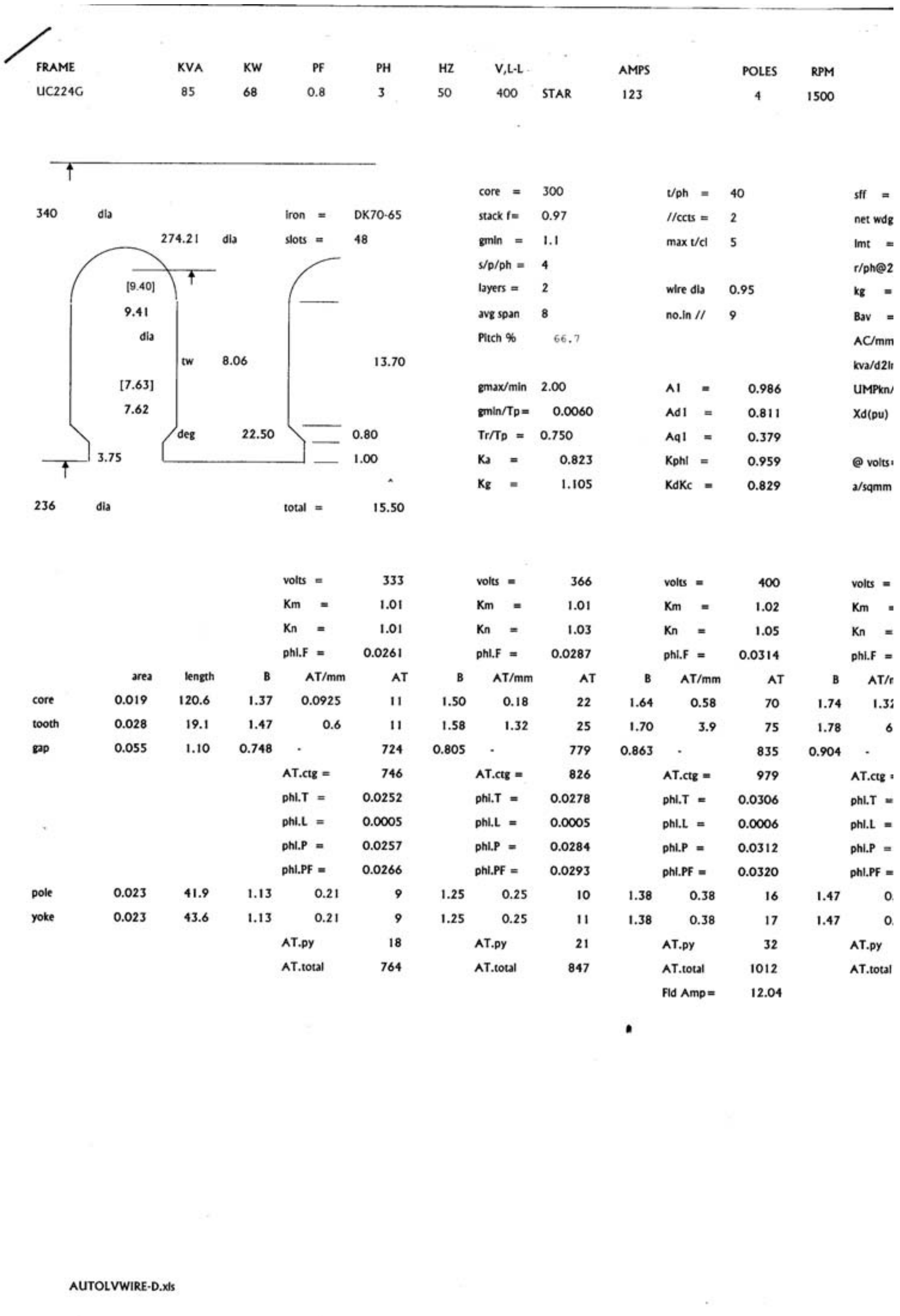

FRAME	KVA	KW	PF	PH	HZ	V,L-L		AMPS	POLES	RPM
UC224G	85	68	0.8	3	50	400	STAR	123	4	1500

340 dia
274.21 dia
[9.40]
9.41
dia
tw 8.06
13.70
[7.63]
7.62
deg 22.50
0.80
1.00
3.75
236 dia

iron = DK70-65
slots = 48
total = 15.50

core = 300
stack f= 0.97
gmin = 1.1
s/p/ph = 4
layers = 2
avg span 8
Pitch % 66.7
gmax/min 2.00
gmin/Tp= 0.0060
Tr/Tp = 0.750
Ka = 0.823
Kg = 1.105

t/ph = 40
//ccts = 2
max t/cl 5
wire dia 0.95
no.in // 9
A1 = 0.986
Ad1 = 0.811
Aq1 = 0.379
Kphi = 0.959
KdKc = 0.829

sff =
net wdg
lmt =
r/ph@2
kg =
Bav =
AC/mm
kva/d2l
UMPkn/
Xd(pu)
@ volts
a/sqmm

	area	length	B	AT/mm	AT	B	AT/mm	AT	B	AT/mm	AT	B	AT/r
				volts =	333		volts =	366		volts =	400		volts =
				Km =	1.01		Km =	1.01		Km =	1.02		Km =
				Kn =	1.01		Kn =	1.03		Kn =	1.05		Kn =
				phi.F =	0.0261		phi.F =	0.0287		phi.F =	0.0314		phi.F =
core	0.019	120.6	1.37	0.0925	11	1.50	0.18	22	1.64	0.58	70	1.74	1.3
tooth	0.028	19.1	1.47	0.6	11	1.58	1.32	25	1.70	3.9	75	1.78	6
gap	0.055	1.10	0.748	-	724	0.805	-	779	0.863	-	835	0.904	-
				AT.ctg =	746		AT.ctg =	826		AT.ctg =	979		AT.ctg =
				phi.T =	0.0252		phi.T =	0.0278		phi.T =	0.0306		phi.T =
				phi.L =	0.0005		phi.L =	0.0005		phi.L =	0.0006		phi.L =
				phi.P =	0.0257		phi.P =	0.0284		phi.P =	0.0312		phi.P =
				phi.PF =	0.0266		phi.PF =	0.0293		phi.PF =	0.0320		phi.PF =
pole	0.023	41.9	1.13	0.21	9	1.25	0.25	10	1.38	0.38	16	1.47	0.
yoke	0.023	43.6	1.13	0.21	9	1.25	0.25	11	1.38	0.38	17	1.47	0.
				AT.py	18		AT.py	21		AT.py	32		AT.py
				AT.total	764		AT.total	847		AT.total	1012		AT.total
										Fld Amp=	12.04		

AUTOLVWIRE-D.xls

Figure A1.3.1 Stator details

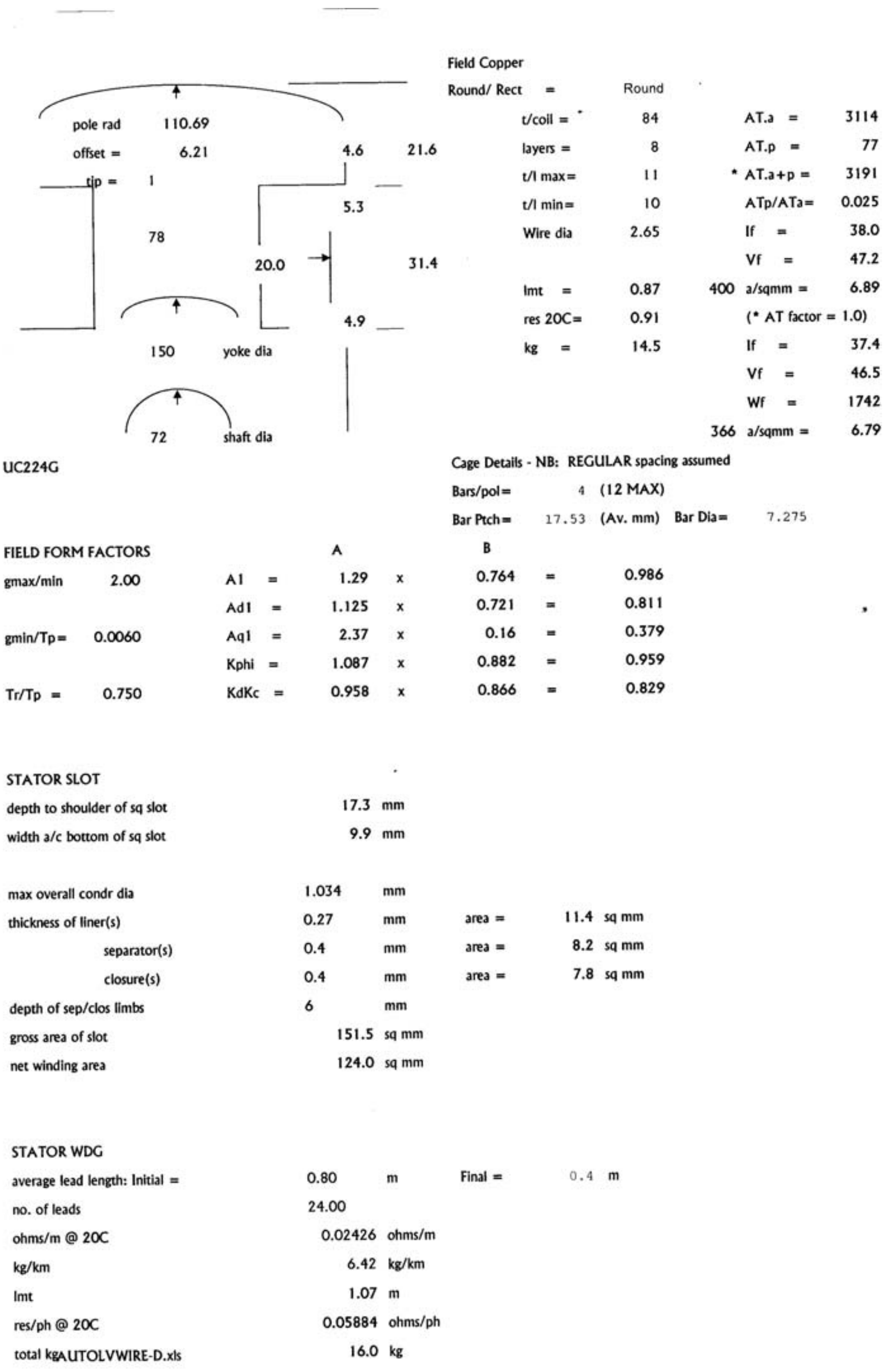

pole rad 110.69
offset = 6.21
tip = 1
78
20.0
150 yoke dia
72 shaft dia
4.6 21.6
5.3
31.4
4.9

UC224G

Field Copper
Round/ Rect = Round
t/coil = 84
layers = 8
t/l max= 11
t/l min= 10
Wire dia 2.65
lmt = 0.87
res 20C= 0.91
kg = 14.5

AT.a = 3114
AT.p = 77
* AT.a+p = 3191
ATp/ATa= 0.025
If = 38.0
Vf = 47.2
400 a/sqmm = 6.89
(* AT factor = 1.0)
If = 37.4
Vf = 46.5
Wf = 1742
366 a/sqmm = 6.79

Cage Details - NB: REGULAR spacing assumed
Bars/pol= 4 (12 MAX)
Bar Ptch= 17.53 (Av. mm) Bar Dia= 7.275

FIELD FORM FACTORS				A		B		
gmax/min	2.00	A1	=	1.29	x	0.764	=	0.986
		Ad1	=	1.125	x	0.721	=	0.811
gmin/Tp=	0.0060	Aq1	=	2.37	x	0.16	=	0.379
		Kphi	=	1.087	x	0.882	=	0.959
Tr/Tp =	0.750	KdKc	=	0.958	x	0.866	=	0.829

STATOR SLOT
depth to shoulder of sq slot 17.3 mm
width a/c bottom of sq slot 9.9 mm

max overall condr dia 1.034 mm
thickness of liner(s) 0.27 mm area = 11.4 sq mm
separator(s) 0.4 mm area = 8.2 sq mm
closure(s) 0.4 mm area = 7.8 sq mm
depth of sep/clos limbs 6 mm
gross area of slot 151.5 sq mm
net winding area 124.0 sq mm

STATOR WDG
average lead length: Initial = 0.80 m Final = 0.4 m
no. of leads 24.00
ohms/m @ 20C 0.02426 ohms/m
kg/km 6.42 kg/km
lmt 1.07 m
res/ph @ 20C 0.05884 ohms/ph
total kgAUTOLVWIRE-D.xls 16.0 kg

Figure A1.3.2 Rotor details

1.4 Exciter machine details

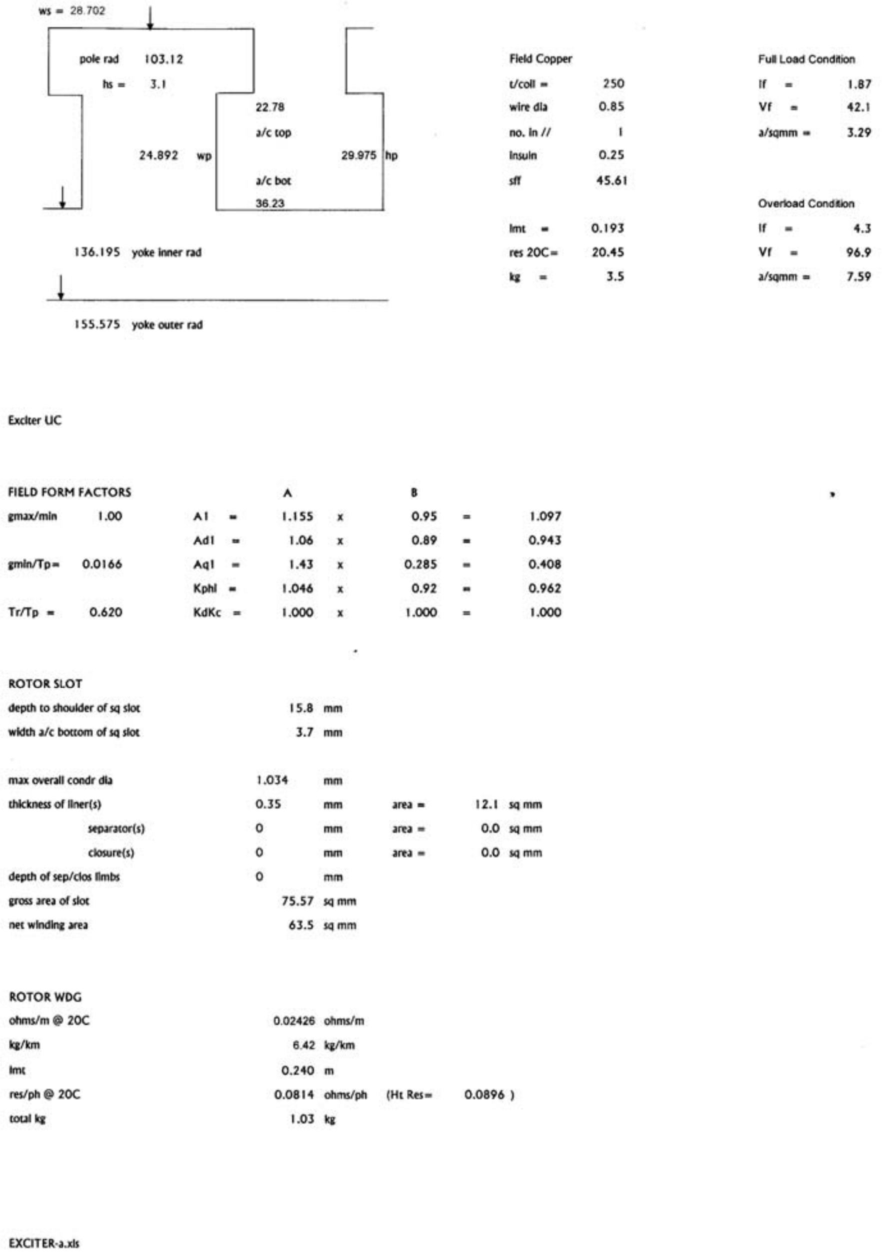

Field Copper	
t/coil =	250
wire dia	0.85
no. in //	1
insuln	0.25
sff	45.61
lmt =	0.193
res 20C=	20.45
kg =	3.5

Full Load Condition	
If =	1.87
Vf =	42.1
a/sqmm =	3.29

Overload Condition	
If =	4.3
Vf =	96.9
a/sqmm =	7.59

Exciter UC

FIELD FORM FACTORS				A		B		
gmax/min	1.00	A1	=	1.155	x	0.95	=	1.097
		Ad1	=	1.06	x	0.89	=	0.943
gmin/Tp=	0.0166	Aq1	=	1.43	x	0.285	=	0.408
		Kphi	=	1.046	x	0.92	=	0.962
Tr/Tp =	0.620	KdKc	=	1.000	x	1.000	=	1.000

ROTOR SLOT				
depth to shoulder of sq slot	15.8	mm		
width a/c bottom of sq slot	3.7	mm		
max overall condr dia	1.034	mm		
thickness of liner(s)	0.35	mm	area =	12.1 sq mm
separator(s)	0	mm	area =	0.0 sq mm
closure(s)	0	mm	area =	0.0 sq mm
depth of sep/clos limbs	0	mm		
gross area of slot	75.57	sq mm		
net winding area	63.5	sq mm		

ROTOR WDG				
ohms/m @ 20C	0.02426	ohms/m		
kg/km	6.42	kg/km		
lmt	0.240	m		
res/ph @ 20C	0.0814	ohms/ph	(Ht Res=	0.0896)
total kg	1.03	kg		

EXCITER-a.xls

Figure A1.4.1 Exciter stator details

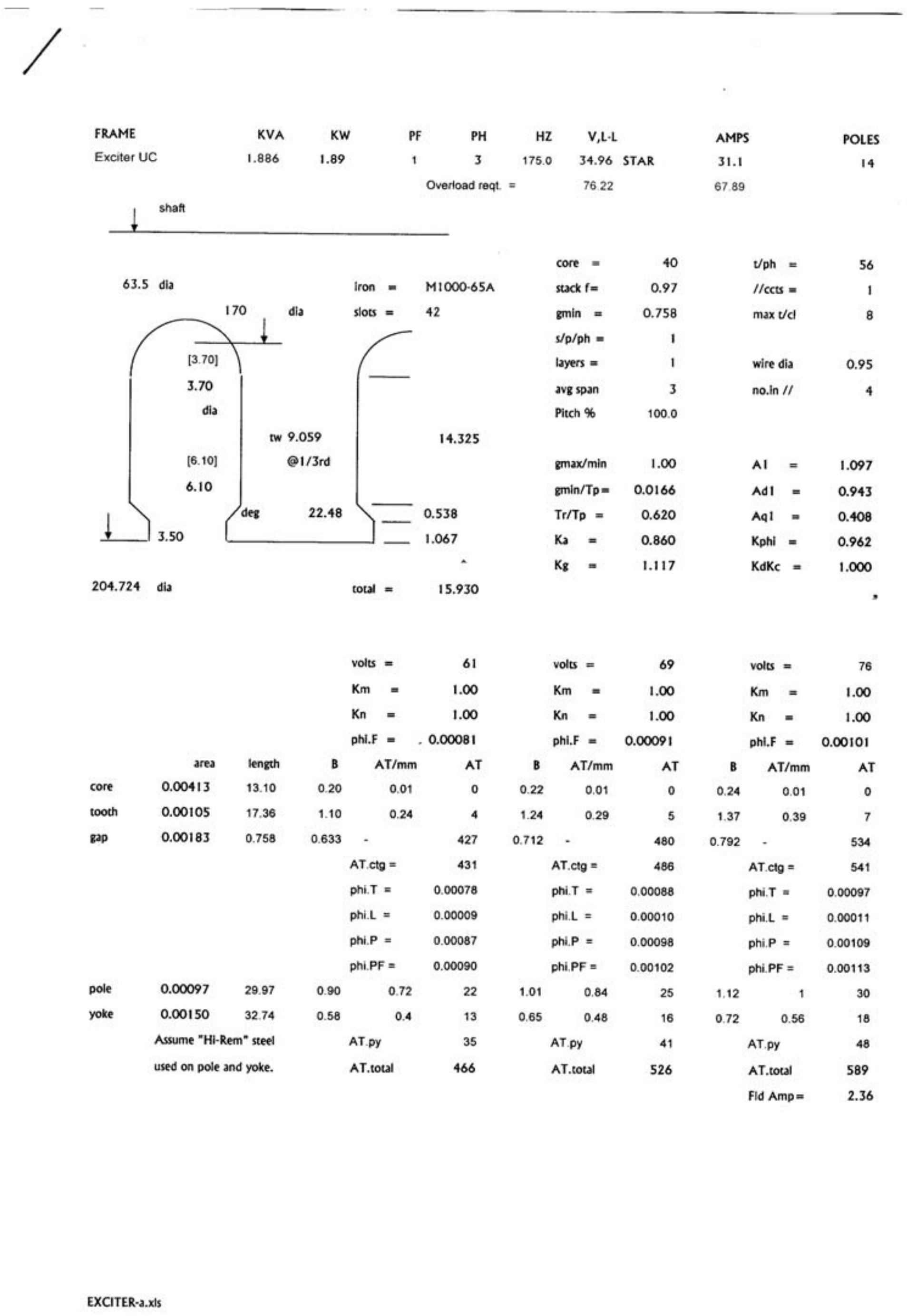

FRAME	KVA	KW	PF	PH	HZ	V,L-L	AMPS	POLES
Exciter UC	1.886	1.89	1	3	175.0	34.96 STAR	31.1	14
				Overload reqt. =		76.22	67.89	

iron = M1000-65A
slots = 42
total = 15.930

core = 40
stack f= 0.97
gmin = 0.758
s/p/ph = 1
layers = 1
avg span 3
Pitch % 100.0

gmax/min 1.00
gmin/Tp= 0.0166
Tr/Tp = 0.620
Ka = 0.860
Kg = 1.117

t/ph = 56
//ccts = 1
max t/cl 8

wire dia 0.95
no.in // 4

A1 = 1.097
Ad1 = 0.943
Aq1 = 0.408
Kphi = 0.962
KdKc = 1.000

				volts =	61		volts =	69		volts =	76
				Km =	1.00		Km =	1.00		Km =	1.00
				Kn =	1.00		Kn =	1.00		Kn =	1.00
				phi.F =	. 0.00081		phi.F =	0.00091		phi.F =	0.00101
	area	length	B	AT/mm	AT	B	AT/mm	AT	B	AT/mm	AT
core	0.00413	13.10	0.20	0.01	0	0.22	0.01	0	0.24	0.01	0
tooth	0.00105	17.36	1.10	0.24	4	1.24	0.29	5	1.37	0.39	7
gap	0.00183	0.758	0.633	-	427	0.712	-	480	0.792	-	534
				AT.ctg =	431		AT.ctg =	486		AT.ctg =	541
				phi.T =	0.00078		phi.T =	0.00088		phi.T =	0.00097
				phi.L =	0.00009		phi.L =	0.00010		phi.L =	0.00011
				phi.P =	0.00087		phi.P =	0.00098		phi.P =	0.00109
				phi.PF =	0.00090		phi.PF =	0.00102		phi.PF =	0.00113
pole	0.00097	29.97	0.90	0.72	22	1.01	0.84	25	1.12	1	30
yoke	0.00150	32.74	0.58	0.4	13	0.65	0.48	16	0.72	0.56	18
	Assume "Hi-Rem" steel			AT.py	35		AT.py	41		AT.py	48
	used on pole and yoke.			AT.total	466		AT.total	526		AT.total	589
										Fld Amp=	2.36

EXCITER-a.xls

Figure A1.4.2 Exciter rotor details

APPENDIX 2 INDUCTION MACHINE SPECIFICATIONS

Nameplate data:

Manufacture	Brook Crompton
Phases	3
Connection	Delta
Poles	4
Power	15 kw
Volts	415 v
Frequency	50 Hz
Current	27.08 A
Speed	1454 rpm
Torque	99.5 Nm
Efficiency	0.891

Construction details

Stator	Figure 2.1
Rotor	Figure 2.2
Inertia	086713 Kgm2
Core Length	14.605 cm
Air gap length	0.05842 cm
Stator slots	48
Rotor slots	36

Stator winding details

Conductors per slot	22
Layers per slot	2
Configuration	three tier concentric
Coil pitch	9 slots

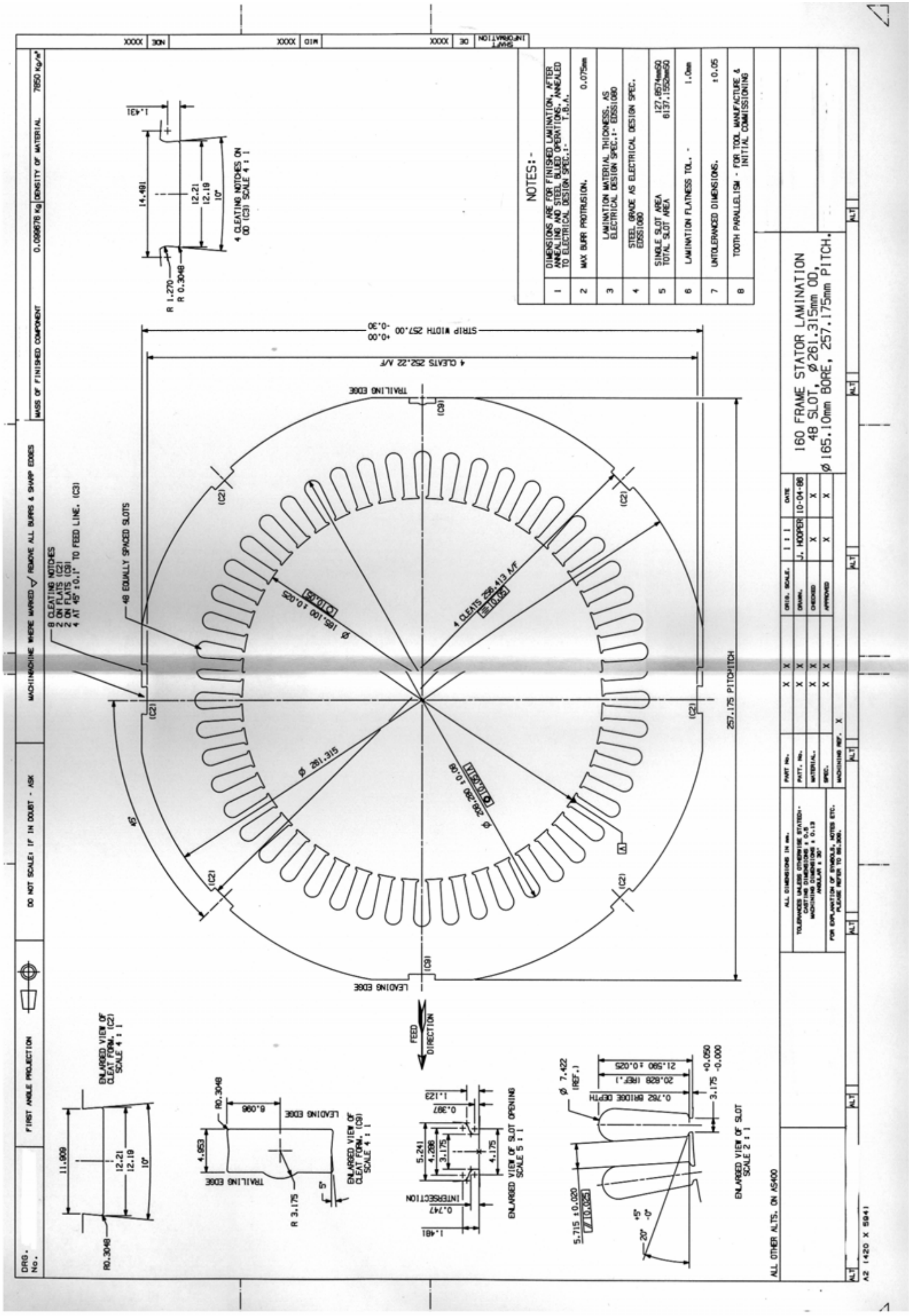

Figure A2.1 Stator details

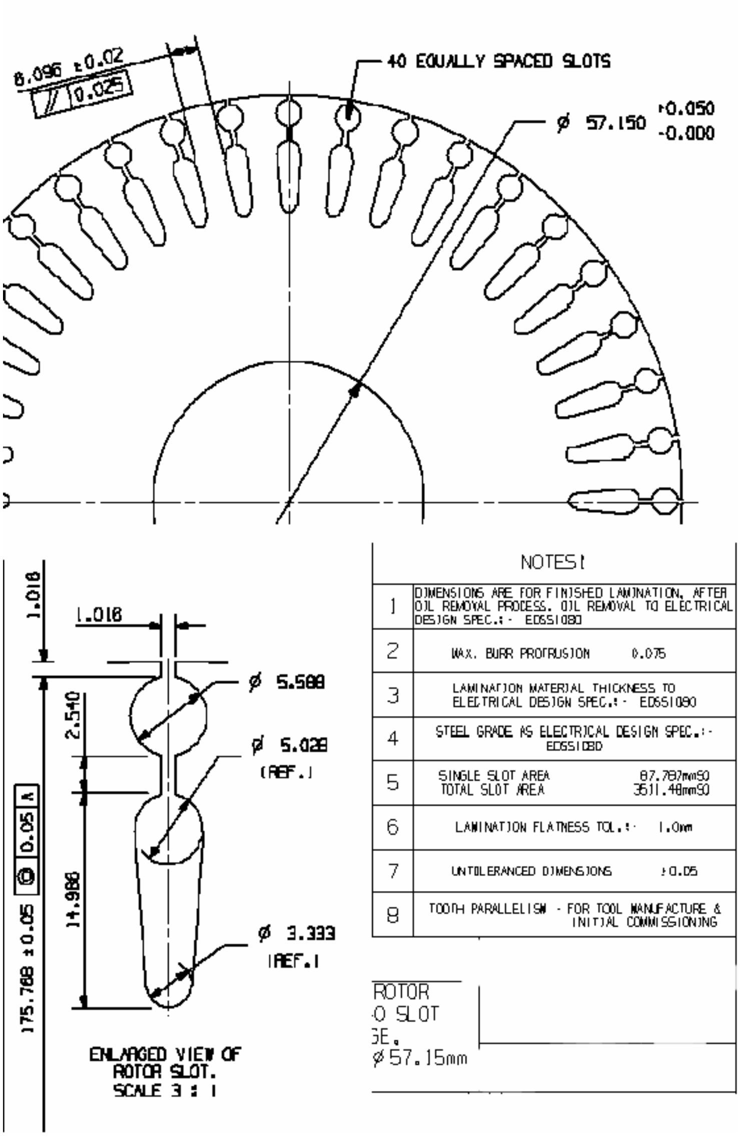

NOTES:

1	DIMENSIONS ARE FOR FINISHED LAMINATION, AFTER OIL REMOVAL PROCESS. OIL REMOVAL TO ELECTRICAL DESIGN SPEC.:- EDSS1080
2	MAX. BURR PROTRUSION 0.075
3	LAMINATION MATERIAL THICKNESS TO ELECTRICAL DESIGN SPEC.:- EDSS1090
4	STEEL GRADE AS ELECTRICAL DESIGN SPEC.:- EDSS1080
5	SINGLE SLOT AREA 87.787mmSQ TOTAL SLOT AREA 3511.48mmSQ
6	LAMINATION FLATNESS TOL.:- 1.0mm
7	UNTOLERANCED DIMENSIONS ±0.05
8	TOOTH PARALLELISM - FOR TOOL MANUFACTURE & INITIAL COMMISSIONING

Figure A2.2 Rotor details

APPENDIX 3 RELUCTANCE CALCULATION METHOD FOR SALIENT POLE ROTOR

This appendix will introduce how the iron reluctances in salient rotor pole are calculated. Figure A3.1 shows the reluctance map for a salient rotor pole. Reluctances in the left side of the rotor.

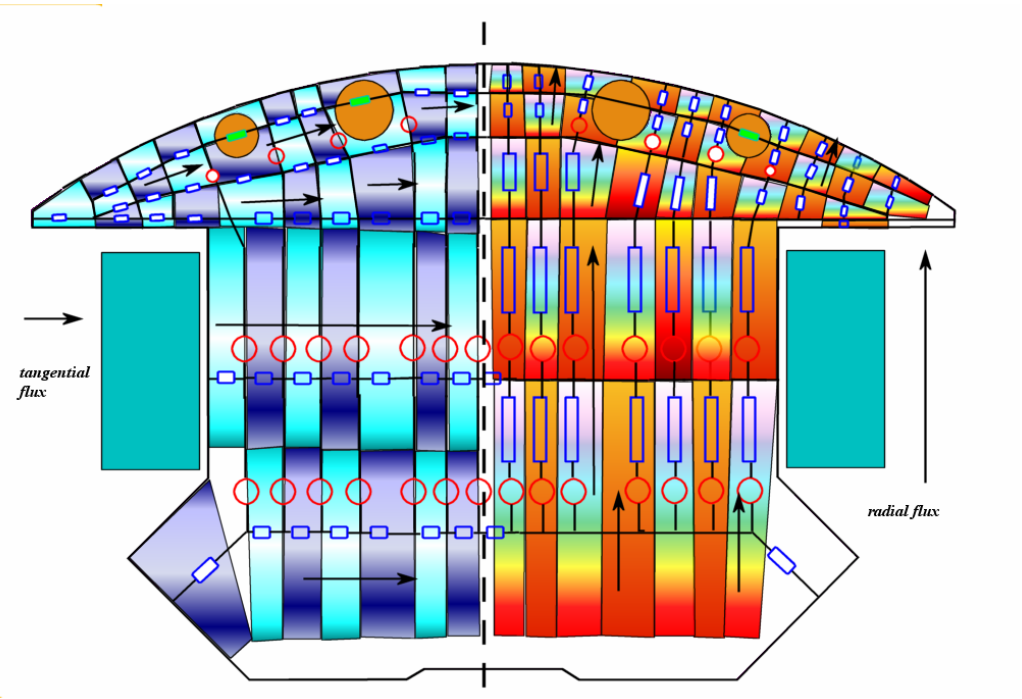

Figure A3.1 Salient pole reluctance mesh calculation graph

The left side of the salient rotor reluctance mesh in figure A3.1shows the discretisation of the tangential flux inside the salient pole, and the right part shows the discretisation of the radial flux inside the salient pole. Because the symmetry of the pole, only half of the reluctance mesh for tangential flux and radial flux is sufficient.

The area of each the reluctance in figure A3.1 is shown by the shadowed area around the reluctance. Given the geometry of the salient pole, these reluctance width, length and depth can be calculated as shown by figure A3.1.

APPENDIX 4 FULL WAVE BRIDGE RECTIFIER

In Industrial applications, where three-phase a.c. voltages are available, it is preferable to use three-phase rectifier circuits, compared to single-phase rectifiers, because of their low ripple content in the waveform and a higher power-handling capability. The three-phase, six-pulse, full-bridge diode rectifier shown in figure A4.1 is a commonly used circuit arrangement.

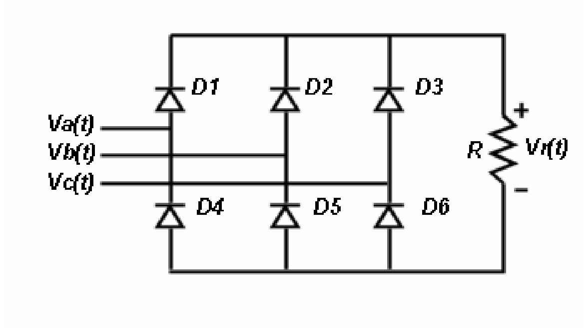

Figure A4.1 Six diodes full wave three-phase bridge rectifier

The voltage waveforms for the circuit shown in figure A4.1 are shown in figure A4.2, where the solid lines are the voltage across the resistance.

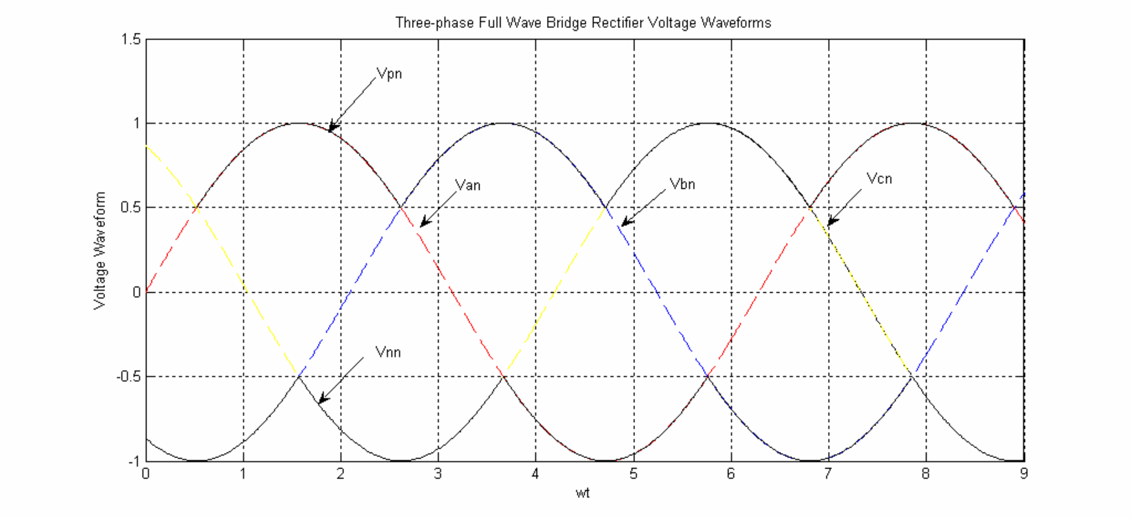

Figure A4.2 Voltage across resistance load in a full waveform bridge rectifier

In figure A4.2, v_{pn} is the voltage of point P with respect to the a.c. voltage neutral point n, and v_{nn} is point N’s voltage, which is the negative d.c. terminal voltage, with respect to neutral point. D.c. voltage across the resistance load would be: (N is the neutral voltage, ie zero and P is the positive terminal of the resistive load or rectifier positive output. N is alos the negative voltage output from the rectifier ie two separate things, hence Vnn is the voltage between negative and neutral. Vd is the effective output voltage across the resistive load which moves up and down with respect to the neutral voltage)

$$v_d = v_{pn} - v_{nn} \tag{A4.1}$$

as shown in figure A4.3.

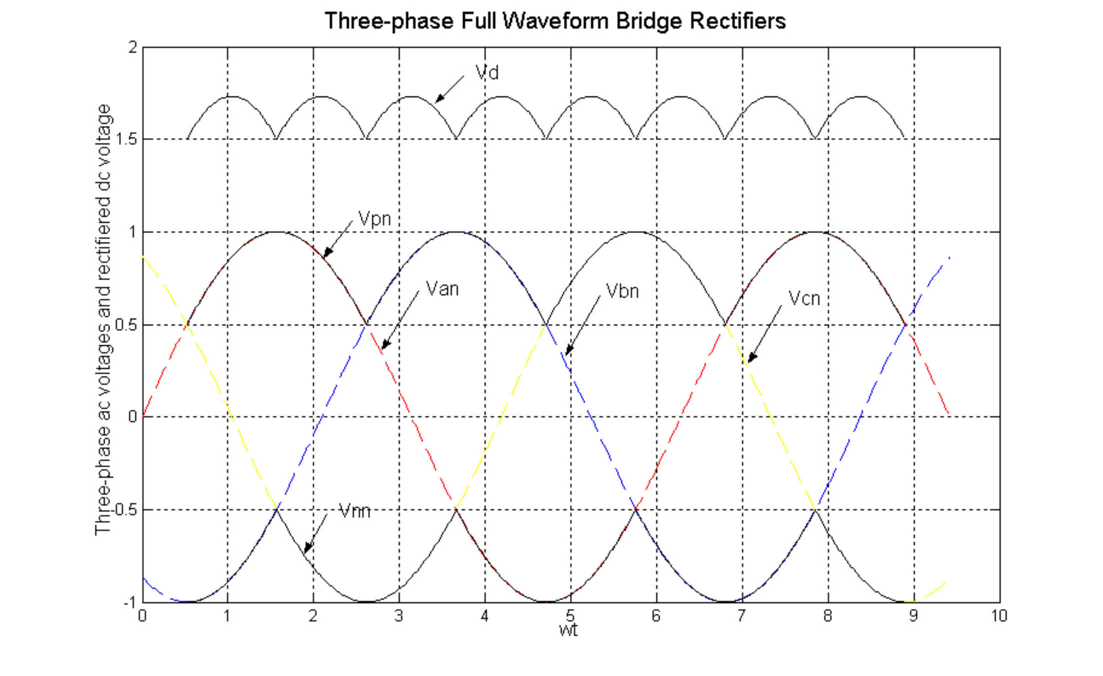

Figure A4.3 D.c voltage waveform of three phase full wave voltage rectifiers

By integrating v_d , which has ripple in its waveform; we could derive the average d.c. voltage v_{do} :

$$v_{do} = \frac{1}{\pi/3}\int_{-\pi/6}^{\pi/6} \sqrt{2}V_{LL}\cos\omega t\, d(\omega t) = \frac{3}{\pi}\sqrt{2}V_{LL} = 1.35V_{LL} \tag{A4.2}$$

and by using the definition of rms current in the phase current waveform, which is a sinusoidal waveform, the rms value of line current i_s in this idealized case is :

$$I_s = \sqrt{\frac{2}{3}}I_d = 0.816I_d \tag{A4.3}$$

and fundamental-frequency component i_{s1} of ac line current has an rms value:

$$I_{s1} = \frac{1}{\pi}\sqrt{6}I_d = 0.78I_d \tag{A4.4}$$

where I_d is the current flowing through the resistive load.

In this kind of full wave bridge rectifier, each diode conducts for 120’, as shown in figure A4.4.

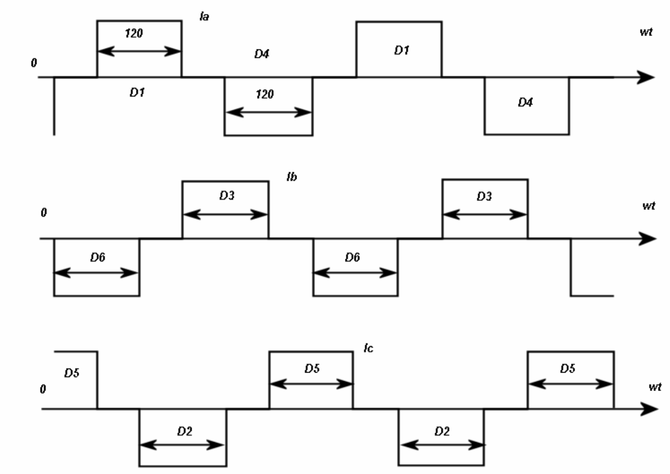

Figure A4.4 Time sequence of conducting of each diode in full wave bridge rectifier

APPENDIX 5 ROOT LOCUS DESIGN OF AVR CONTROLLER

The system response requirements of the excitation control system are: a desired damping ratio $\zeta = 0.8$, to guarantee that there is not a big overshoot. The natural frequency is $\omega_n = 25Hz$. Thus the desired close loop root would be:

$$s_{1,2} = -\zeta\omega_n \pm \omega_n\sqrt{\zeta^2 - 1} = -20 \pm 15j \tag{5.1}$$

In designing the controller, the corresponded time constant for a digital PID controller, such the integral time constant τ_i, derivative time constant τ_D and the low pass filter time constant have to be considered meanwhile. Especially for the integral time constant τ_i, which will affect the error reducing in the system response. Too big τ_i will cause the system error reduce too slow to notice.

After adjusting the parameters in analogue PID controller, which is in the form in equation 5.2.

$$G_c(s) = \frac{K_c(s+b)(s+c)}{s(s+a)} \tag{5.2}$$

the final controller is in the form:

$$G_c(s) = \frac{5.611(s+19)(s+4)}{s(s+100)} \tag{5.3}$$

and corresponded digital PID controller parameters are:

$K_p = 1.259$,

$\tau_i = 0.3$

$\tau_D = 0.035$

$T_f = 0.01$.

The system's response in simulation is satisfied. The root locus of the system is shown in figure A5.1.

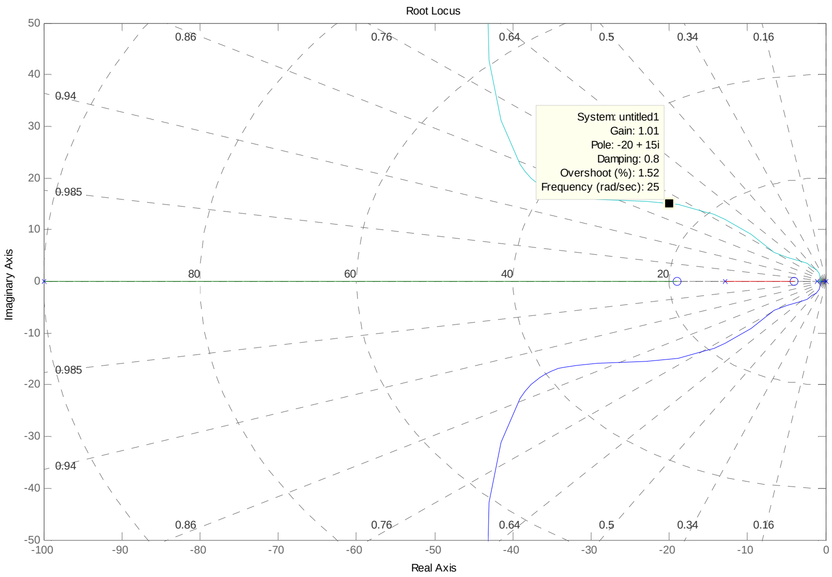

Figure A5.1 Root locus of AVR controller

It can be seen that the root locus of the system pass the design point, thus the design requirements are satisfied.

Once the transfer function of the controller in frequency domain is derived, in order to use the controller in the digitally sampled system of the DRM model, it has to be transformed to z domain. The transformed z transfer function is:

$$G_c(z) = \frac{AT}{z-1} + \frac{B(z-1)}{z-e^{-aT}} + C \tag{5.4}$$

where A, B and C are constants derived from K_c and poles of controller:

$$A = \frac{K_c * 12.85347044 * 1.048987727}{a} \tag{5.5}$$

$$B = K_c - C \tag{5.6}$$

$$C = \frac{K_c(12.85347044 + 1.048987727) - A}{16} \tag{5.7}$$

thus, the final digital control signal to the exciter field voltage is:

$$\begin{aligned} V_r(z) = {} & (K_c - (2B + C(1+e^{-aT}) - AT)z^{-1} + (B + Ce^{-aT} - ATe^{-aT})z^{-2})E(z) \\ & + ((1+e^{-aT})z^{-1} - e^{-aT}z^{-2})V_r(z) \end{aligned} \tag{5.8}$$

taking the inverse z-transform, the numerical algorithm for the computer signal for controller output $V_r^*(t)$ is:

$$\begin{aligned} V_r^{\,*}(t) &= K_c E^*(t) - (2B + C(1+e^{-aT}) - AT)E^*(t-T) + (B + Ce^{-aT} - ATe^{-aT})E^*(t-2T) \\ &\quad + (1+e^{-aT})V_r^{\,*}(t-T) - e^{-aT}V_r^{\,*}(t-2T) \end{aligned} \tag{5.9}$$

this is the final PID controller that has been used in brushless generating system DRM simulations.

APPENDIX 6 SALIENT POLE SYNCHRONOUS GENERATOR WITH A STEP IN THE SALIENT ROTOR SPECIFICATIONS

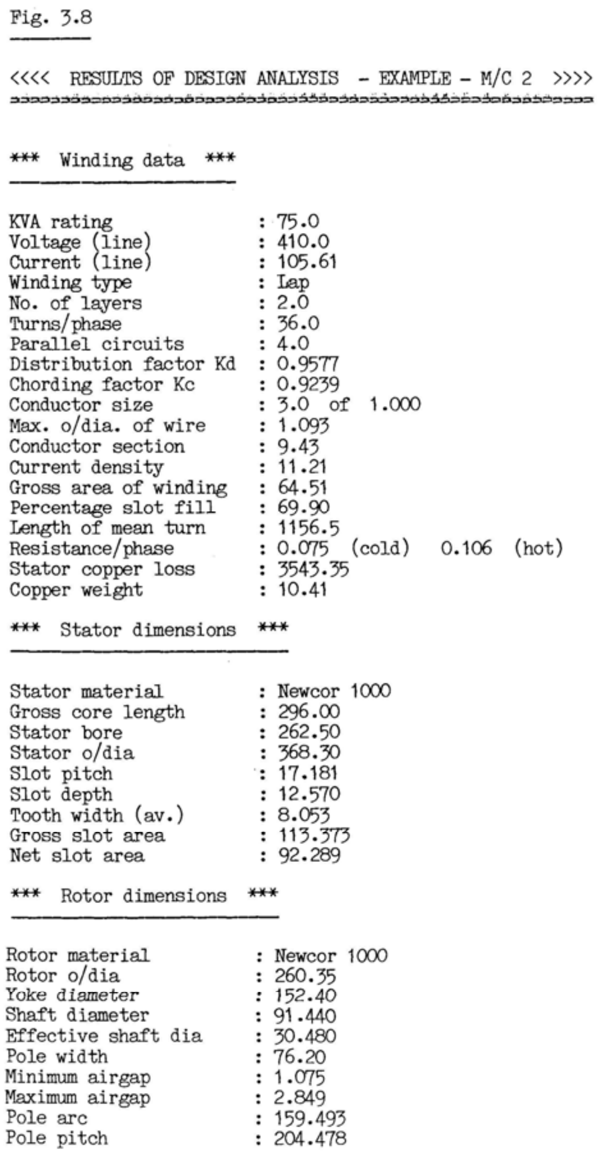

```
Fig. 3.8
--------

<<<<  RESULTS OF DESIGN ANALYSIS  - EXAMPLE - M/C 2  >>>>
==========================================================


***  Winding data  ***
----------------------

KVA rating              : 75.0
Voltage (line)          : 410.0
Current (line)          : 105.61
Winding type            : Lap
No. of layers           : 2.0
Turns/phase             : 36.0
Parallel circuits       : 4.0
Distribution factor Kd  : 0.9577
Chording factor Kc      : 0.9239
Conductor size          : 3.0  of  1.000
Max. o/dia. of wire     : 1.093
Conductor section       : 9.43
Current density         : 11.21
Gross area of winding   : 64.51
Percentage slot fill    : 69.90
Length of mean turn     : 1156.5
Resistance/phase        : 0.075  (cold)   0.106  (hot)
Stator copper loss      : 3543.35
Copper weight           : 10.41

***  Stator dimensions  ***
---------------------------

Stator material         : Newcor 1000
Gross core length       : 296.00
Stator bore             : 262.50
Stator o/dia            : 368.30
Slot pitch              : 17.181
Slot depth              : 12.570
Tooth width (av.)       : 8.053
Gross slot area         : 113.373
Net slot area           : 92.289

***  Rotor dimensions  ***
--------------------------

Rotor material          : Newcor 1000
Rotor o/dia             : 260.35
Yoke diameter           : 152.40
Shaft diameter          : 91.440
Effective shaft dia     : 30.480
Pole width              : 76.20
Minimum airgap          : 1.075
Maximum airgap          : 2.849
Pole arc                : 159.493
Pole pitch              : 204.478
```

Fig.3.8 cont.

```
***  Rotor winding details  ***

Field turns/pole        : 335.0
Field L.M.T.            : 976.00
Conductor size (wire)   : 2.0  of  1.060
Conductor section       : 1.76
Total resistance        : 12.60  (cold)  17.76  (hot)
Copper weight           : 20.4

***  Magnetic areas and lengths  ***

                 Pole      Yoke      Gap       Tooth     Core
Areas          : 0.0217    0.0346    0.0608    0.0275    0.0229
Lengths        : 53.975    35.908    1.0750    12.570    128.79

***  Constants  ***

Gmax/Gmin               : 2.6502
Gmin/Pole pitch         : 0.00526
Pole arc/Pole pitch     : 0.7800
Wiesemans coeff. A1     : 0.9367
Wiesemans coeff. KO     : 0.9640
Wiesemans coeff. Ad1    : 0.7811
Wiesemans coeff. Aq1    : 0.3563
Ka (=ratio Ad1/A1)      : 0.8339
Carters coeff. Kg       : 1.0176

***  Pole permeance and flux  ***

Pole permeance          : 0.8875E-06
Total flux              : 0.03227
Leakage flux            : 0.00076
Pole flux               : 0.03303

***  Reactances  ***

Leakage reactance       : 0.1204  ohms    0.0537  p.u.
D-axis mag. reactance   : 5.2829  ohms    2.3570  p.u.
D-axis synch. reactance : 5.4033  ohms    2.4107  p.u.
Q-axis mag. reactance   : 2.4098  ohms    1.0752  p.u.
Q-axis synch. reactance : 2.5302  ohms    1.1289  p.u.
Ratio Xsd/Xsq           : 2.1355
```

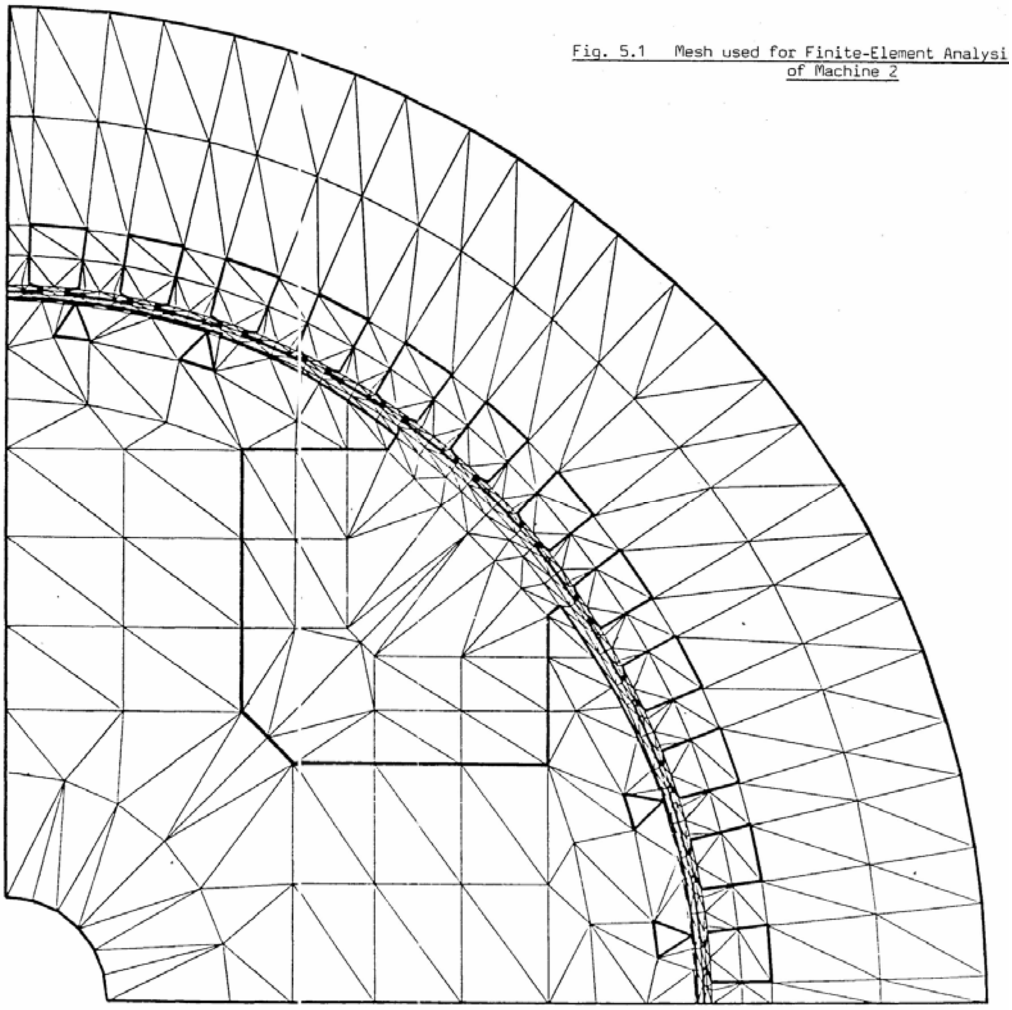

Fig. 5.1 Mesh used for Finite-Element Analysi of Machine 2

REFERENCES

[1]: M.J. Carpenter, Magnetic Equivalent Circuits, *Proceedings IEE*, Vol. 115 (10), 1968, pp.1503-1511.

[2]: L. Haydock, *The systematic development of equivalent circuits for synchronous machines*, Ph.d Thesis, University of London, 1986.

[3]: P. Sewell, K.J. Bradley, J.C. Clare, P.W. Wheeler, A. Ferrah, R. Magill, Efficient dynamic models for induction machines, *International Journal of Numerical Modelling: Electronic Networks, Devices and Fields*, (1999), Vol. 12, pp. 449-464.

[4]: J.L. Coulomb, G. Meunier, Finite element implementation of virtual work principle for magnetic or electric force and torque computation, *IEEE Transactions on Magnetics*, (1984), Vol. 20, No. 5, pp. 1894-1896.

[5]: J. Mizia, K. Adamiak, A. R. Eastham, and G. E. Dawson, Finite element force calculation: Comparison of methods for electric machines, *IEEE Transactions on Magnetics*, (1988), Vol. 24, No. 1, pp.447-450.

[6]: V. Ostovic', A method for evaluation of transient and steady state performance in saturated squirrel cage induction machines, *IEEE Transactions on Energy Conversion*, (1986), Vol. **1**, No. 3, pp. 190-197.

[7]: V. Ostovic', A simplified approach to magnetic equivalent-circuit modelling of induction machines, *IEEE Transactions on Industry Applications*, (1988), Vol.24, No. 2, pp. 308-316.

[8]: V. Ostovic', A novel method for evaluation of transient states in saturated electric machines, *IEEE Transactions on Inustry Applications*, (1989), Vol. 25, No. 1, pp. 96-100.

[9]: M.J. Carpenter, D.C. Macdonald, Circuit representation of inverter-fed synchronous motors, *IEEE Transactions on Energy Conversion*, (1989), Vol. **4**, No. 3, pp. 531-537.

[10]: H. Roisse, M. Hecquet, P. Brochet, Simulation of synchronous machines using a electric-magnetic coupled network model, *IEEE Transactions on magnetics*, (1998), Vol. **34**, No. 5, pp. 3656-3659.

[11]: V. Ostovic', J.M. Miller, V.K. Garg, R.D. Schultz, S.H. Swales, A

magnetic-equivalent-circuit-based performance computation of a Lundell alternator, *IEEE Transactions on Industry Applications*, (1999), Vol. **35**, No. 4, pp. 825-830.

[12]: Slides, *Impact of excitation system on power system stability*, ABB Industrie AG.

[13]: Paul Breeze, *Power generation technology*, Elsevier, Oxford, 2005.

[14]: S. Smith, R. Todd, M. Barnes, P. Tavner, Improved energy conversion for doubly-fed wind generators, *IEEE annual meeting Industrial Application Society (IAS)*, 2-6 October, 2005, Hong Kong.

[15]: M.G. Simoes, B.K. Bose, R.J. Spiegel, Fuzzy logic based intelligent control of a variable speed cage machine wind generation system, *IEEE Transactions on Power electronics*, (1997), Vol. **12**, No. 5, pp. 87-95.

[16]: R. Datta, V.T. Ranganathan, Variable speed wind power generation using doubly fed wound rotor induction machine-a comparison with alternative schemes, *IEEE Transactions on Energy Conversion*, (2002), Vol. **17**, No. 3, pp. 414-421.

[17]: S. Muller, M. Deicke, R.W. De Donker, Doubly fed induction generator systems for wind turbines, *IEEE Industry Applications Magzine*, (2002), May/June, pp. 26-33.

[18]: L. Morel, H. Godfroid, A. Mirzaian, J. Kauffmann, Double-fed induction machine: converter optimisation and field oriented control without position sensor, *IEE Proceedings Electric Power Applications*, (1998) vol. **145**, No. 4, pp. 360–368, July.

[19]: L. Xu and C. Wei, Torque and reactive power control of a doubly fed induction machine by position sensorless scheme, *IEEE Transactions on Industry Applications*, (1995) Vol. **31**, No. 3, May/June, pp. 636–642.

[20]: B. Hopfensperger, D.J. Atkinson, Doubly-fed a.c. machines: classification and comparsion, *Proc. Power Electronics and Applications (EPE)*, Graz, Austria, Aug., 27–29, 2001.

[21]: A.B.J. Reece, T.W. Preston, *Finite element methods in electrical power Engineering,*

[22]: James L. Kirtley Jr., *Electric Machines Lecture Notes*, Massachusetts Institute of Technology, Feburary 11, 2004.

[23]:W.H. Press, Saul A. Teukolsky, William T. Vetterling, Brian P. Flannery,

Numerical Recipes in C++: The Art of Scientific Computing, Cambridge University Press, 2nd Edition, 2002.

[24]: A.E. Fitzgerald, Charles Kingsley, Jr., Stephen D. Umans, *Electric machinery*, McGraw-Hill Higher Education, New York, 6th Edition, 2002.

[25]: P. L. Alger, *Induction machines: their behaviour and uses*, Gordon and Breach, (1995), Basel, Switzerland.

[26]: K.J. Bradley, A. Tami, Reluctance mesh modelling of induction motors with healthy and faulty rotors, *31st IEEE Industrial Application Conference*, San Diego, Oct. 6-10, 1996, pp.625-632.

[27]: Y. Saad, *Iterative methods for sparse linear systems*, PWS, Boston, 1996.

[28]: M.G. Say, *Alternating Current Machines*, Longman Science & Technological, 5th edition, 1983.

[29]: Anisa, Ungku Anisa Ungku Amirulddin, *Analysis and simulation of vector controlled bearingless induction motors*, Ph.d thesis, University of Nottingham, 2005.

[30]: R.E. Steven, *Electrical Machines and Power Electronics*, Van Nostrand Reinhold Co. Ltd, England, 1983.

[31]: F. Saccomanno, *Electric power system analysis and control*, IEEE Press series on power engineering, Willey Interscience, 2003.

[32]: R.H. Park, Two-reaction theory of synchronous machines-generalized methods of analysis-part 1, *AIEE transaction*, Vol. **48**, July 1929, pp. 716-727.

[33]: J. Arrillaga, C. P. Arnold, *Computer analysis of power systems*, John Wiley & Sons, 1990.

[34]: Stephen J. Chapman, *Electric Machinery Fundamentals*, 3rd Edition, McGraw-Hill, 1998.

[35]: Peter P. Silvester, R.L. Ferrari, *Finite Elements for electrical engineers*, 3rd Edition, Cambridge University Press, 1996.

[36]: A. Darabi, C. Tindall, S. Ferguson, Finite-element time-step coupled Generator, load, AVR, and brushless exciter modelling, *IEEE Transactions on Energy Conversion*, (2004), Vol. 19, No. 1, pp. 73-80.

[37]: Ralph J. Smith, Richard C. Dorf, *Circuits, devices and systems*, 5th Edition, John Wiley & Sons Inc.

[38]: Karl J. Astrom, Bjorn Wittenmark, *Computer Controlled System Theory and Design*, Prentice-hall information and system sciences series, 1984.

[39]: Norman S. Nice, *Control System Engineering*, 4th Edition, John Wiley & Son, 2004, New York.

[40]: Charles L. Phillips, H. Troy Nagle, *Digital control system analysis and design*, 2nd Edition, Prentice-Hall International, 1990.

[41]: J. Machowski, J.W. Bialek, S. Robak, J.R. Bumby, Excitation control system for use with synchronous generators, *IEE Proceedings, Generation, Transmission and Distribution.*, Vol. 145, No.5, September 1998.

[42]: A. Darabi, C.E. Tindall, Analogue AVR model for use in real time transient simulation of small salient pole alternators, *Power electronics, machines and drives*, Conference Publications No. 487, 16-18 April 2002, IEE2002

[43]: P.M. Anderson, A.A. Fouad, *Power system control and stability*, IEEE Press, 2nd edition, 2002.

[44]: M.L. Crenshaw et al., Excitation system models for power system stability studies, IEEE committee report, *IEEE transactions on power apparatus and system*, Vol. PAS-100, No. 2 February 1981.

[45]: R. C. Shaw, *Modelling and Simulating Automatic Voltage Regulators for Newage AVK SEG Generators*, MENG Hons Project Report Part 2 HSP 1876

[46]: Kiyong Kim, Richard C. Schaefer, Tuning a PID Controller for a Digital Excitation Control System, *IEEE Transactions on Industry Applications*, Vol. 41, No. 2 March/April 2005.

[47]: A. Godhwani, M.J. Basler, K. Kim, T.W. Eberly, Commissioning Experience with a Modern Digital Excitation System, *IEEE Transactions on Energy Conversion*, Vol. 13, No. 2 June 1998.

[48]: M.G. McArdle, D.J. Morrow, P.A.J. Calvert, O. Cadel, Implementation of a Digital AVR for Small Alternators, *Proceedings of International Conference on Electric Utility Deregulation and Restructuring and Power Technologies*, City University, London, 4-7 April 2000.

[49]: Danish wind industry association, information available at: http://www.windpower.org/en/news/articles

[50]: Anderson Peterson, Analysis, Modelling and Control of Doubly-fed Induction Generators for Wind Turbines, *Ph.D thesis in Chalmes University of Technology*, Goteborg, Sweden, 2005.

[51]: A. Miller, E. Muljadi, and D. S. Zinger, a variable speed wind turbine power control, *IEEE. Trans. Energy Conversion*, vol. 12, pp. 181-187, June 1997.

[52]: http://www.istis.sh.cn/list/list.asp?id=1980

[53]: http://www.repower.de/index.php?id=12&L=1

[54]: B. Hopfensperger, D.J.Atkinson, R.A. Lakin, Stator flux oriented control of a cascaded doubly-fed induction machine, *IEE proceedings Electric Power Application*, vol. 146, No.6, November 1999.

[55]: B. Hopfensperger, D.J.Atkinson, R.A. Lakin, combined magnetising flux oriented control of the cascaded doubly fed induction machine, *IEE proceedings Electric Power Application*, vol. 148, No.4, July 2001.

[56]: [F-7]: B. Hopfensperger, D.J.Atkinson, R.A. Lakin, The application of field oriented control to a cascaded doubly fed induction machine, *Power Electronics and Variable Speed Drives, 18-19 September 2000*, Conference Publication No. 475.